

UNIVERSITE CATHOLIQUE DE LOUVAIN

Faculté des Sciences

Département de Physique

Unité de Physique Théorique et de Physique Mathématique



Light deflection experiments as a test of relativistic theories of gravitation

Dissertation présentée en vue
de l'obtention du grade de
Docteur en Sciences
(Groupe des Sciences Physiques)

par

Sophie PIREAUX

Supervisor:

Professor **Jean-Marc GERARD**

September 2002

Composition of the jury:

- **Professor Jean-Pierre ANTOINE,**
Unité de Physique Théorique et Mathématique (FYMA),
Université catholique de Louvain (UCL),
BELGIUM,
- **Professor Jean-Marc GERARD,**
Unité de Physique Théorique et Mathématique (FYMA),
Université catholique de Louvain (UCL),
BELGIUM,
- **Professor Jacques WEYERS,**
Unité de Physique Théorique et Mathématique (FYMA),
Université catholique de Louvain (UCL),
BELGIUM,
- **Professor Jan GOVAERTS,**
Unité de Physique Nucléaire (FYNU),
Université catholique de Louvain (UCL),
BELGIUM,
- **Professor Jean SURDEJ,**
Institut d'Astrophysique et de Géophysique,
Université de Liège (Ulg),
BELGIUM,
- **Professor François MIGNARD,**
Centre d'Etudes et de Recherches en Géodynamique et Astrométrie (CERGA),
Observatoire de la Côte d'Azur (OCA),
FRANCE.

Acknowledgements

We wish to thank our nearest and dearest for their support and their encouragements ; Professor Jean Govaerts, Professor Jean Surdej and the late Professor Jacques Demaret, for their readiness to spare some of their time answering our questions. Also the help from those persons who kindly read this work and helped improve the English is highly appreciated.

Finally, we are in debt to the members of our jury (and particularly to our supervisor, Professor Jean-Marc Gérard) for their judicious comments; those initiated further reflections and teased our curiosity.

Contents

Contents	1
Introduction	5
Refractive versus gravitational light deflection	5
Why alternative theories to General Relativity?	7
Importance of light deflection tests	9
Light bending as a test for alternative theories of gravitation	9
The structure and main results of this thesis	11
Chapter 1: Selected alternative theories to General Relativity (GR)	13
1.1 Scale Invariant Tensor Scalar theory (SITS)	13
1.2 Tensor Scalar theories (TS/BD/STRINGS)	14
1.2.1 Jordan frame	14
1.2.2 Einstein frame	16
1.3 Minimal Tensor Scalar theory (MTS)	18
1.4 Large Extra-Dimension theories (LED)	18
1.4.1 Metric reduction and Brans-Dicke effective action	20
1.4.2 Effective field content of the gravitational sector in 4-dimensions	22
1.4.3 Weak field limit	23
1.5 The Weyl theory (W)	24
1.6 Eddington-Robertson-Schiff parameters	27
1.6.1 General	27
1.6.2 MTS isotropic solution	28
1.6.3 SITS isotropic solution	28
1.6.4 TS (or BD, STRINGS) isotropic solutions	28
1.6.5 Eddington-Robertson-Schiff parameters for selected theories	30
Chapter 2: TS cosmological estimation of the PN parameter γ	33

2.1	Cosmological equations	33
2.1.1	Formulation in terms of the Hubble parameter	33
2.1.2	A notion of quintessence	34
2.2	The case of a null cosmological constant	35
2.2.1	Conditions for an attractor mechanism towards GR	36
2.2.2	Solutions that admit GR as an attractor	38
2.2.3	A confrontation with SNIa results	40
2.2.4	Solutions in a flat radiation universe	42
2.2.5	Solutions in a flat dust universe	44
2.2.6	Values for the integration constants	49
2.2.7	Our model and the attractor mechanism	50
2.2.8	Evaluation of the observables	51
2.3	The case of a <i>non</i> null cosmological constant	55
2.3.1	Solutions that admit GR as an attractor	55
2.3.2	A confrontation with SNIa results	56
2.3.3	Impact of the cosmological constant on γ -predictions	56
2.4	Impact of the scalar potential and initial conditions on γ -predictions	59
2.5	Summary of the main results	63
2.5.1	Main properties of our model	63
2.5.2	Predicted value of the PN parameter γ	63
Chapter 3:	Light deflection angle in the solar system: general considerations	65
3.1	First order measurement	65
3.1.1	Why the solar system, and especially the Sun?	65
3.1.2	Present and future constraints on γ	66
3.2	Second order measurement	67
3.2.1	Relevance of the impact parameter b	67
3.2.2	Measurability of the impact parameter b and asymptotic deflection angle $\hat{\alpha}$	72
3.2.3	Other effects: non sphericity of the gravitational source, angular momentum	74
3.2.4	Orders of magnitude of the different contributions	78
3.2.5	Further remarks on “corrective” effects	83
3.2.6	Current state of the art	84
Chapter 4:	Testing alternative theories in the solar system using the light deflection angle?	85
4.1	Relevant (P)PN parameters at first and second order in light deflection	85

4.2	Theories leading to first order corrections	86
4.2.1	TS theories	86
4.2.2	LED theories	87
4.3	Theories leading to second order corrections	93
4.3.1	Effective geodesic potential for light	93
4.3.2	Asymptotic weak field second order and finite distance deflection angle for MTS/SITS theories	95
4.4	Theories leading to a modification of the Newtonian potential	96
4.4.1	Effective geodesic potential for the Weyl theory	96
4.4.2	Asymptotic deflection angle for the Weyl theory	99
4.5	Summary of the main results	109
4.5.1	TS theories	109
4.5.2	LED theories	109
4.5.3	MTS/SITS theories	109
4.5.4	The Weyl theory	109
Chapter 5:	Gravitational lensing/microlensing	111
5.1	Present and future of microlensing/gravitational lensing	111
5.2	Brief summary of the phenomenon	112
5.2.1	Asymptotic first and second order light deflection angle	112
5.2.2	Lens equation	112
5.2.3	Amplifications	115
5.2.4	Microlensing	116
5.3	Testing alternative theories of gravitation with microlensing/gravitational lensing?	117
5.3.1	Parameters of the simulations	117
5.3.2	TS theories	118
5.3.3	MTS/SITS theories	123
5.3.4	The Weyl theory	133
5.4	Summary of the main results of this chapter	143
5.4.1	TS theories	143
5.4.2	MTS/SITS theories	143
5.4.3	The Weyl theory	143
Conclusions and perspectives		145
	TS theories	145
	MTS/SITS theories	147

LED theories	148
The Weyl theory	149
General	151
Perspectives	151
Bibliography	153
APPENDIX A: Conventions	I
APPENDIX B: Fact sheets of γ-tests through light deflection and other experiments	III
In the optical waveband	IV
In the radio waveband	XVIII
Other experiments measuring γ	XXIV
APPENDIX C: Light deflection angle in the framework of field theory	XXV
Feynman rules from the linearized LED gravitational action	XXV
Light deflection process in LED theories	XXVIII
Cross-section of LED light - massive scalar-field scattering	XXXII
Light deflection angle in LED theories	XXXIII

Introduction

1 Refractive versus gravitational light deflection

Everyone is familiar with the fact that light is refracted as it travels through different media (glass, water, air...). This well-known phenomenon accounts for many different observations: a stick halfway in water appears to be bent, the fish is not exactly where you see it, the mirages in the desert form far from the real objects, etc. Mirages are explained by light rays propagating through layers of warm air of different refractive index, and bending towards regions of colder (i.e. denser) air. This refractive light deflection may significantly affect our view of distant earth objects. For example, we could see two (or more) images (one direct and one inverted lower image) of the lights of a distant car travelling on a sun heated road (Figure 0.1). Furthermore, the images are often deformed, or the car may seem to be closer as its lights appear brighter. Indeed, the so-called atmospheric lensing causes the multiplication of images, image deformation, or light amplification of distant unresolved objects.

Any of these “optical illusions” are simply due to the fact that light is deflected if the medium is inhomogeneous. As we are aware that the stick in the water is not truly bent, and as, when we aim at a fish, we slightly compensate for the offset, we all know that the image of the sky on the desert sand must not be mistaken for a pound of water. Mankind even took advantage of refractive light bending, and among others, built optical lens telescopes to observe the sky.

In 1915, Albert Einstein linked the fate of space-time with the presence of matter. Indeed, in General Relativity (GR), space-time can be compared with a mattress which is flat when no object lies on it. The presence of massive bodies on that mattress deforms (or we should say forms) it; the heavier the body, the more pronounced the dip. Consequently, a small marble originally travelling freely on a straight line on its surface, will now be following a curved trajectory. The closer the marble rolls from the massive body, the more deflected it will be from its originally straight path. So do the photons (particles of light) as they follow curves, called geodesics, of our space-time shaped by the presence of gravitational masses (Figure 0.2).

The effect of space-time on light trajectories in General Relativity is exactly the same as for an inhomogeneous medium in classical optics. The only difference is that General Relativity is simpler in a sense because there is no dispersion since the effective deflection index does not depend on the light frequency.

In analogy with refractive light deflection, what is called gravitational light deflection leads us to see a light source, like a star, slightly offset from its true position (just like the fish in water). It can also significantly affect our view of distant universe sources as a result of image multiplication, deformation, or light amplification. Again, Nature is trying to fool us as we scrutinize the solar system and the Universe through our telescopes! However, corrections to our tricked view can be calculated in the framework of General Relativity. Moreover, astrophysicists have new natural telescopes at their disposal, using now large mass distributions as lenses to observe distant objects too faint to be seen otherwise. In this work, we propose to investigate another application of gravitational light deflection: instead of trying to model our Universe through General Relativity, we will explore the possibility to use experimental data to test a set of alternative theories beyond General Relativity.

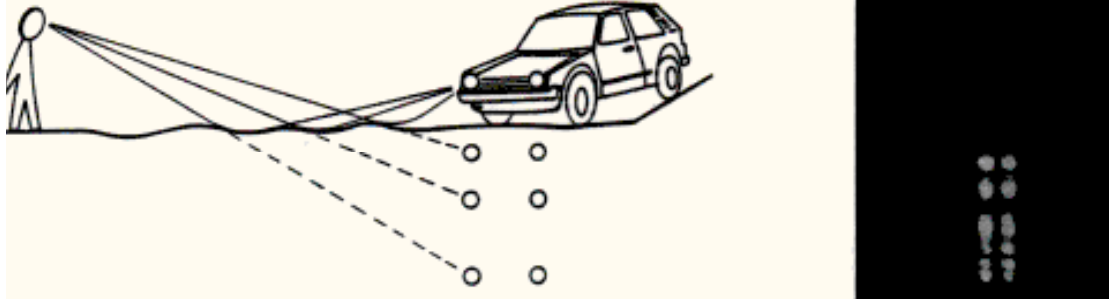


Fig. 0.1 Propagation of light rays above a heated ground between a distant car and an observer (left). Atmospheric lensing causes the formation of multiple images (right). With the courtesy of J. Surdej.

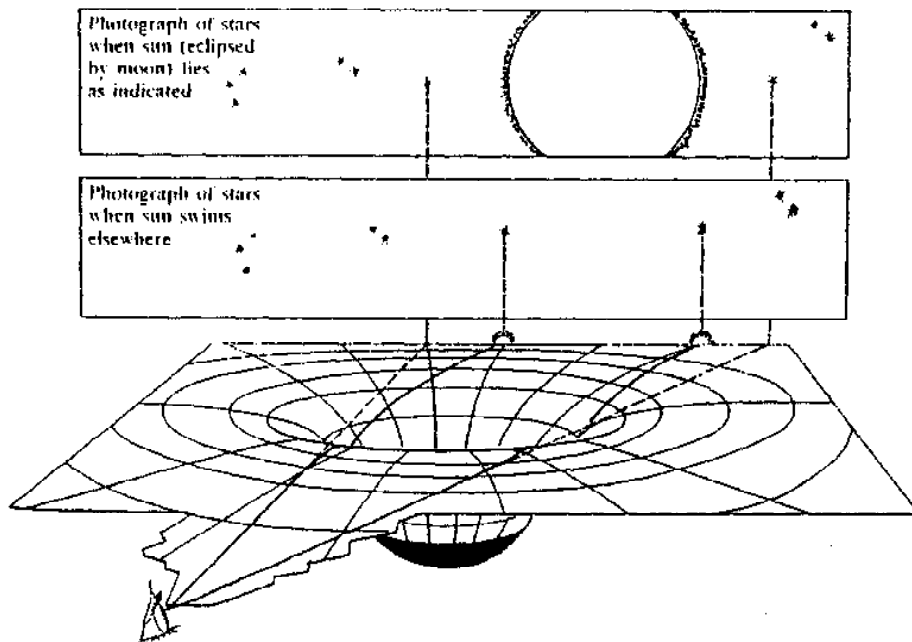


Fig. 0.2 The lowest part of this drawing illustrates how the solar gravitational potential deforms space-time, and how photons follow curved geodesics. The upper part of the drawing shows the resulting apparent position of the star, slightly offset from its true position, due to the presence of the Sun. The intermediate drawing shows the true position of the star, as seen when the Sun is not present in this part of the sky.

2 Why alternative theories to General Relativity?

General Relativity, this monumental theory elaborated by Albert Einstein, is a pure tensor theory which simply reduces to Newton's theory in the weak field limit. It agrees, so far, with all the observations made in our solar system and has to be taken into account in modern technologies like the Global Positioning System (GPS) [20] or when computing orbits. Nevertheless, the theory of General Relativity cannot be the final theory of gravitation for the following reasons.

First of all, **from a theoretical point of view**, General Relativity is characterized by the requirement that the gravitational interaction be mediated solely by a massless helicity-2 particle, the graviton, corresponding to the metric. Let us express the underlying consequences of such an assumption at the level of the total action:

$$I_{GR} = I_{GR \text{ gravitation}} + I_{GR \text{ matter}} .$$

1/From the point of view of the dynamics of the gravitational field, the action describing the propagation and self-interaction of the gravitons is the Hilbert-Einstein action which contains only the metric $g_{\mu\nu}$ and the scalar curvature R associated with it:

$$I_{GR \text{ gravitation}}(g_{\mu\nu}) = \int dx^{(4)} \sqrt{-g} \left\{ -\frac{1}{2\kappa} R \right\} \quad \text{with } \kappa \equiv 8\pi G_N/c^4 .$$

A first remark is that the minimal choice of the Hilbert-Einstein action is not based on any fundamental principle. Or to express it in another way, it is evident that covariance and Newtonian field approximation alone do not determine uniquely the gravitational action. For example, quadratic, or cubic terms... in the curvature tensor could also be considered. Furthermore, nothing guarantees that the Newtonian potential is valid on very short, or very long distances. Moreover, when elaborating his theory of General Relativity in order to unify Special Relativity with the Newtonian law of gravitation, Einstein kept the gravitational coupling unchanged. The Newtonian constant, G_N , is not dimensionless ($[G_N] = \text{mass}^{-2}$ in units $\hbar = c = 1$) though, unlike for example the electro-weak coupling constant. This means that Einstein's theory of gravitation cannot be properly described by quantum field perturbation theory. Indeed, an expansion in powers of the coupling constant leads to divergences in this case, and those divergences cannot be absorbed by the renormalization of a finite number of parameters.

Consequently, General Relativity cannot be perturbatively¹ quantized and this makes it impossible to unify it with other fundamental interactions.

Also, General Relativity is not invariant under conformal transformations. However, if we wish to achieve the unification of gravitation with particle physics, in which conformal invariance plays a crucial role, we might consider a theory of gravitation that incorporates this property.

2/From the point of view of the coupling of gravitation to matter fields, General Relativity is a Metric theory (Metric coupling) and its coupling is universal (the same for any matter field). A Metric coupling of gravitation to matter means that it depends only on a symmetric metric and on its first order derivatives, with freely-falling test (point-like) particles following the geodesics of this *same* metric. In terms of the matter action,

$$I_{GR \text{ matter}}(g_{\mu\nu}) = \int dx^{(4)} \mathcal{L}_m(g_{\mu\nu}, \psi_m) ,$$

a universal Metric coupling simply corresponds to replacing the flat Minkowskian metric, $\eta_{\mu\nu}$, by $g_{\mu\nu}(x^\sigma)$ in the Standard Model of fundamental interactions.

A Metric theory of gravity preserves the Einstein Equivalence Principle (EEP). The latter one postulates

¹ Fifteen years ago, a new approach to quantum gravity was proposed. Loop gravity, also called Quantum General Relativity and now fairly well developed [21, 118], is a tentative theory, just like String theories. Direct or indirect corroboration of those theories is lacking, because Planck-scale physics is not experimentally accessible yet.

Loop gravity, however, is not as ambitious as String theories: it does not aim, like the latter, at unifying all known fundamental physics into one single theory. The main differences between Loop gravity and String theories, though, are that the loop approach is non-perturbative and provides a background independent quantification of General Relativity.

1. the equivalence between inertial and gravitational masses for test (point-like) particles, independently of their mass and composition.

The consequence of this postulate, called the Weak Equivalence Principle (WEP) is the well-known Universality of Free Fall for particles with negligible gravitational binding energy.

2. the equivalence, locally, of any free-falling reference frame with a reference frame at rest in empty space, from the point of view of all *non*-gravitational experiments for particles with negligible gravitational binding energy.

To analyze the physical implications of this principle, it is easier to reformulate it as the two following requirements:

- (a) In a freely-falling reference frame, locally, the result of any *non*-gravitational experiment is independent of the velocity of the reference frame. This constitutes the Local Lorentz Invariance Principle (LLIP).

This principle implies the isotropy of the speed of light: there are no preferred referential rest frames.

- (b) In a freely-falling reference frame, locally, the result of any *non*-gravitational experiment is independent of the space-time point where this experiment is made. This last postulate is the Local Positional Invariance Principle (LPIP).

A consequence of this principle is the constancy of Standard Model “constants”: they depend only on the coupling constants and mass scales entering the Standard Model. A second consequence of LPIP is the universality of the gravitational redshift. When two identical clocks are located at different positions in a static external Newtonian potential, they show, independently of their nature and constitution, a difference in clock rate when compared thanks to electromagnetic signals; and it is, at first order in $1/c^2$, proportional to the difference of the Newtonian potential at the two space-time points.

From the experimental point of view, the physical consequences of the assumed Metric coupling are well tested (see Will [143] and references therein). The Universality of Free Fall (WEP) is now verified within $4 \cdot 10^{-13}$ by sophisticated torsion balances, comparing the accelerations of various materials towards local topography on the Earth, movable laboratory masses, the Sun and the Galaxy. Any anisotropy of space that would have a direct incidence on the energy levels in atomic nuclei is banned at the 10^{-21} level (LLIP). Sharp constraints have also been set on the variability of Standard Model constants using very different data sources (spectral lines in galaxies, a natural fission reactor active in Gabon two billion years ago...): for example, the most stringent limit is on the fine structure constant with $|\dot{\alpha}/\alpha| < 10^{-15} \text{ years}^{-1}$ (time LPIP). As far as the gravitational redshift is concerned, it was tested by hydrogen-maser clocks at the 10^{-4} level (space LPIP).

It is the dynamical part of Einstein’s General Theory of Relativity which is the less strongly constrained. The Newtonian weak field limit potential has only been verified down to the millimeter scale by laboratory experiments [18]. Even though Einstein’s theory passed so far all the relevant solar system tests (light bending, time delay, perihelion shift of Mercury) within the experimental errors (see Will [143] and in particular Table 4), we recall that General Relativity cannot reproduce the flat velocity distributions in the vicinity of galaxies without using copious amounts of dark matter. The Newtonian potential would indeed predict a decreasing distribution.

We are thus confronted with the following dilemma: either we assume the existence of a huge amount of dark matter, or we modify the potential for galactic distances. This second solution would immediately invalidate General Relativity with a null cosmological constant.

Note that the solution to the “dark matter dilemma” could also be a combination of the two solutions mentioned here above, thus requiring a more acceptable amount of dark matter.

Finally, **from a cosmological point of view**, the Standard Big Bang Model deduced from General Relativity suffers from several weaknesses. It is indeed based on particular hypotheses like isotropy, flatness, and a very small cosmological constant. These constitute as many initial conditions/parameters that it would be desirable to deduce from the dynamics in the setting of a new theory. Equally, linked to those particular initial conditions, come out the discussions about the horizon, the curvature and the age of the universe.

It must now be clear why, from the theoretical, experimental and cosmological point of view, an alternative theory of gravitation is highly desirable. A “new” theory would even be preferable to General Relativity, if it agrees with laboratory and solar system gravitational experiments (with maybe some departures from the Einsteinian theory on larger distance scales), while encompassing properties like renormalizability or scale invariance at some level. Hopefully too, the alternative theory might provide further dynamical insight on the cosmological evolution of our universe.

3 Importance of light deflection tests

When testing alternative theories of gravitation in the solar system, the (Post-)Post-Newtonian formalism ((P)PN) is very convenient. In the case of Metric theories of gravity, and if we furthermore restrict ourselves to Fully Conservative theories, *i.e.* theories preserving not only the total energy and momentum but also the total angular momentum, only three PN parameters have to be considered. Moreover, in this work, we only treat Purely Dynamical theories. That is to say Metric theories whose gravitational fields have their structure and evolution determined by coupled differential equations. In this framework, only two PN parameters are relevant: the first one, γ , characterizes the “amount of curvature per unit rest mass” and the second one, β , the “non-linearity in the superposition law of gravity” [142, 143]. Throughout this work, we will be mostly interested in the first of these parameters, γ .

There are presently four solar system experiments² available, with sufficient accuracy, to significantly constrain gravitational theories: the time-delay and light bending tests, the Lunar Nordtvedt test, and the precession of the perihelion of Mercury. However, unlike **time delay and light bending which are clean tests**, in the sense that they provide a direct estimation of γ , the other tests are truly only sensitive to combinations of the Post-Newtonian parameters β , γ and other parameters, so that it is necessary to combine results from several tests to isolate γ .

Historically, the spectacular phenomenon of light deflection by a gravitational source (namely the Sun) was the trigger to the success of Einstein’s theory. Today, the arrival of new detection techniques allows not only for the precise measurement of the light deflection angle (change in the apparent position of a light source) due to the Sun or planets in our solar system, but also for the observation of microlensing events (variation of the received light flux) at the scale of our galaxy, and of gravitational mirages (multiple images) or weak lensing (distorted images) at extragalactic distance scales. Let us state the characteristics of these effects.

The light deflection angle due to the gravitational field of the Sun was the very first prediction of General Relativity which originally confirmed this theory within a 20% error margin. Today, with modern techniques operating in the radio-waveband, the precision has reached about 0.01%, allowing the planets of our solar system to be considered as potential deflectors too. Nevertheless, changes in the apparent light source position only constitute a test of General Relativity **in our solar system**.

The microlensing effect predicted by General Relativity is usually used to search for dark matter **in the vicinity of our galaxy and also in external galaxies**. This phenomenon, due to a small object with a mass characteristic of planet or a star, could also be used as a test to exclude some extensions of General Relativity, on the basis of their predictions at galactic distance scales.

At extra-galactic distance scales, one would rather use the gravitational mirage criteria (examples of such phenomenon are presented in Figure 0.3) or weak lensing. At such distances, galaxies or clusters do actually act as lenses. There, alternative theories can depart from the Einsteinian theory, but their predictions must in any case stay in agreement with the observations verified by General Relativity at shorter distances.

So light deflection experiments allow us to test the universality of relativistic theories of gravitation over different distance scales by considering successively a close star, a galaxy or a distant quasar... as light sources that will be lensed by a solar system body, a star of the galactic halo, a galaxy or a cluster.

4 Light bending as a test for alternative theories of gravitation

The aim of this thesis is thus to investigate predictions regarding light deflection within some chosen alternative theories to General Relativity, in order to confront them with present or future constraints from observations.

However, **in view of the blooming business of alternative theories**, we know that it is impossible here to consider every alternative theory of gravitation. So, we shall restrict ourselves to a few promising ones.

Concerning theories reconsidering the Metric coupling inherent to the matter part of the general relativistic action, we will only give one example, namely the Kaluza-Klein type of theories used in Large Extra Dimensions (LED) developments. In such theories, gravitation is described by a $(4 + d)$ -dimensional gravitational action. However, particles

² In the future, this set will be enlarged. See the last table in Annex B for some examples.

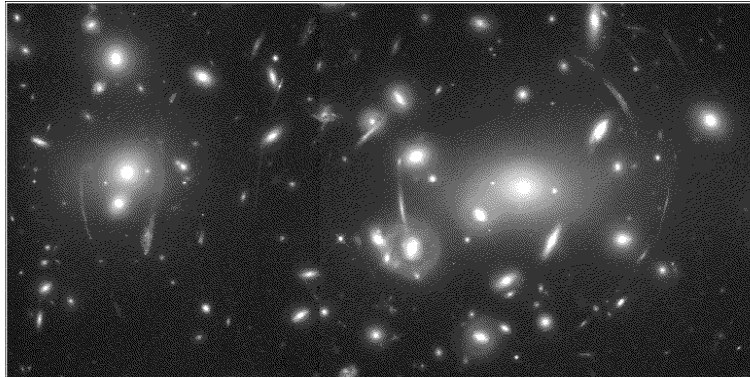


Fig. 0.3 Gravitational lens in Abell 2218. Picture obtained with the Hubble Space telescope (WFPC2), April 5, 1995, NASA.

only couple to gravitation in 4-dimensions and hence do not follow the geodesics of the 4-dimensional induced metric, obtained after compactification of the extra-dimensions. In addition to the usual massless graviton mode, the physical gravitational sector in the 4-dimensional picture now includes massless tensor and scalar modes, as well as tensor and scalar massive modes. Furthermore, the massless scalar mode induces a coupling of gravitation to matter which is too strong to account for solar system tests of gravitation. Given that the Weak Equivalence Principle is already violated in any case, a mass is simply given by hand to this otherwise massless scalar mode.

The WEP, LLIP and LPIP consequences of a Metric coupling principle being checked with such an astonishing precision, we will mostly concentrate on Metric theories of gravity and alter only the dynamical part of the total general relativistic action.

When extending the gravitational sector, the most popular way is to add massless scalar degrees of freedom. We will consider the minimal example, where only one massless scalar field is added in the gravitational action and the Newtonian gravitational coupling constant, G_N , is kept. That is, the gravitational scalar does not couple to matter. From the gravitational part of the Minimal Tensor Scalar theory (MTS) action (1.27) so obtained, we can recover the Scale Invariant Tensor Scalar theory (SITS) (1.1), in which the scalar field does not couple to matter either, but which has a non-minimal coupling of the metric to the scalar field (mixed $(R\phi)$ -term in the gravitational action).

On the other hand, the class of so called Tensor Scalar theories (TS) (1.4) allows for the existence of massless scalar gravitational fields which couple to matter with a gravitational strength only. The corresponding gravitational “constant” is no longer Newton’s constant, but is rather determined by the inverse of a scalar field. Thus Tensor Scalar theories interestingly provide a possible route to a renormalization/quantization of gravity. Finally, such theories are strongly motivated by String theories which, besides the usual Einstein tensor metric field, contain massless scalars that are crucial for the coupling and may play an important role also in an effective action at low energies.

Finally, we will explore another type of alternative to the first postulate of General Relativity, and consider the example of the purely conformal tensorial theory, namely the Weyl theory (W) (1.49). The Weyl approach introduces higher order derivatives of the metric in the gravitational Lagrangian, as a combination of scalars formed with the Riemann, Ricci and the squared curvature tensor. One of its interesting features is of course its conformal invariance. In addition, the gravitational coupling is dimensionless, because the curvature scalars present in the gravitational action are now of dimension four in mass (in units $\hbar = c = 1$), allowing for renormalization.

Now, **from the point of view of light deflection**, we realized that, because of the unknown mass distribution of the deflector (which is often inferred from the observations assuming General Relativity), some phenomena like gravitational mirages, weak lensing or microlensing might not always be efficient for testing alternative theories. This is why this thesis is mostly centered on the light deflection angle and the change in apparent position. Qualitatively different lensing configurations are, however, emphasized but weak lensing is omitted.

Nevertheless, this option might need to be revised in the future, light deflection being a fast developing field. If so, a complementary study of these tests would be interesting.

5 The structure and main results of this thesis

This work is divided into five chapters, in addition to this introduction and to the conclusions.

In **Chapter 1**, we shall summarize the main properties of the theories of gravitation listed above. For theories allowing a parametrized (Post-)Post-Newtonian ((P)PN) expansion, the corresponding parameters will be derived. In particular, for Tensor Scalar theories, we present a new efficient way to derive the (P)PN parameters by means of a conformal transformation of the Schwarzschild Minimal Tensor Scalar solution.

In **Chapter 2**, we give an original particular but exact and analytical class of cosmological solutions to Tensor Scalar theories. This class of solutions to the dust era admits General Relativity as an attractor and is naturally inferred from the radiation-era evolutionary equations. It is used to obtain an estimate of the present value of the Post-Newtonian parameter γ , for Tensor Scalar theories, as needed to discuss the predictions regarding light deflection. The influence of a cosmological constant added to this model, so as to agree with Supernovae of type A (SNIa) results, as well as the dependence of γ -estimate on the model are also discussed.

In **Chapter 3**, general considerations on the measurement of the light deflection angle in the weak field limit are underlined. First of all, the precision of the past, present, and future experiments, as well as the role of the impact parameter in the formulation of the second order deflection angle are evoked. The important effects to be considered at second order are enumerated and orders of magnitude given. The second order contribution to the light deflection angle is crucial to untangle Minimal Tensor Scalar and Scale Invariant Tensor Scalar theories from General Relativity.

In **Chapter 4**, we approach the question of weak field limit angular displacement predictions for the different theories we have selected.

In Large Extra-Dimension theories, when a mass is given to the zero-mode scalar field, the minimal coupling is restored and the deviations from General Relativity become less spectacular and in reasonable agreement with experiments. However, the massive tensor modes will contribute at third order in light deflection with a signature that could be looked for in future experiments. Indeed, not only is this additional term a function of the mass of the gravitational deflector and of the observation angle with respect to the deflector, but it is also a function of the number d of extra-dimensions and of the mass scale M_s of the theory. Additionally, it exhibits a strong quadratic dependence in the energy of the photons, *i.e.* in the frequency of observations. Thanks to these features, we shall see that if the present lower bound on M_s obtained from collider physics, $\sim 3 \text{ TeV}/c^2$, is safe from the point of view of observations in the radio waveband, in the visible band, experiments push it higher to above $\sim 28 \text{ TeV}/c^2$ for $d = 2$. Observations made at higher frequencies, for example in the UV band, would allow more stringent constraints on (d, M_s) . Such a task might be achievable with the astrometric satellite GAIA.

For the Minimal Tensor Scalar theory, Scale Invariant Tensor Scalar theory and Weyl gravity, the analysis of the geodesic light deflection potential allows us to define critical values of the free parameter of the theory at which the traditional Schwarzschild black hole potential changes drastically, or to discuss the existence of a critical closest approach distance under which no deflection can take place. In the Weyl theory, there even exists a maximum closest approach value beyond which light orbits are bound (if the additional linear contribution to the Newtonian potential is negative).

In this same chapter, the asymptotic behavior of the Weyl theory is carefully discussed with respect to the sign of the linear term in the gravitational potential. The exact conformal transformation to asymptotic Minkowski flat space is provided.

Also, light deflection in the solar system allows us to put strong constraints on the Weyl linear parameter, but does not help us to settle its sign.

In **Chapter 5**, we are interested in microlensing and gravitational mirages. For Tensor Scalar theories, neither microlensing nor gravitational mirages seem to provide a useful test. For example, if the lens mass is unknown, the Tensor Scalar microlensing amplification curve can be rescaled to that of General Relativity. As far as the Weyl theory is concerned, on the contrary, the shape of the amplification curve is modified according to a factor function of the free parameter of the theory and of the distances involved in the microlensing event. Within the limits of our approximation, we were allowed to discuss the case of a negative linear parameter. It leads to a larger microlensing amplification than in General Relativity, but the corrective factor is already constrained to be very close to 1. Hence, the deviation from the general relativistic predictions might be irrelevant.

For the Weyl theory, gravitational mirages constitute more appropriate tests of gravitation, as the distances involved

correspond to those at which the characteristic linear contribution to the gravitational potential becomes significant. They allowed us to further reduce our solar system bound on the absolute value of a negative linear parameter by about three orders of magnitude. Such an analysis could yet be refined... The gravitational mirage test might also be useful for Minimal Tensor Scalar and Scale Invariant Tensor Scalar theories because some ranges of the MTS/SITS parameter and some lensing configurations allow predictions qualitatively different from General Relativity. More precisely, a systematic analysis of the image parity is an interesting test in the case of mirages. For microlenses, very small values of the MTS/SITS parameter could lead to an extinction of the light source; whereas the predictions are analogous to the general relativistic ones for larger values of the parameter.

Finally, **in the conclusion**, we summarize our results and comment on a few perspectives.

Note that the reader can consult our conventions in **Appendix A**, while **Appendix B** provides the necessary information and references on light deflection experiments; **Appendix C** gives a detailed calculation of light deflection in Large Extra-Dimension theories, together with the required Feynman rules.

Chapter 1:

Selected alternative theories to General Relativity (GR)

Several extensions and alternatives to General Relativity have been suggested, aiming to answer the objections that General Relativity is facing: theories including several additional (scalar) degrees of freedom, and higher order (in the metric derivatives) tensor theories...

In this first chapter, we recall the main characteristics of some selected alternative theories to GR. The corresponding Eddington-Robertson-Schiff parameters are then derived for the theories admitting a parametrized Post-Newtonian expansion, since those parameters are crucial to discuss light deflection predictions in the next chapters.

1.1 Scale Invariant Tensor Scalar theory (SITS)

The so-called Scale Invariant Tensor Scalar (SITS) theory for a massless scalar field ϕ is defined by the following action:

$$I_{SITS} = \int dx^{(4)} \sqrt{-g} \left\{ -\frac{1}{2\kappa} R + \frac{1}{2} \phi^{|\mu} \phi_{|\mu} + \frac{1}{12} R \phi^2 + \mathcal{L}_m(g_{\mu\nu}, \psi_m) \right\} \quad (1.1)$$

with

$$\kappa \equiv 8\pi G/c^4.$$

The non-minimal coupling of the massless scalar ϕ to the curvature invariant ensures the vanishing of the trace of the scalar-field stress tensor, so that the scalar sector of the gravitational action is conformally invariant [30, 47]. The SITS theory is a Metric theory in which the scalar field does not couple to matter. Consequently, the Weak Equivalence Principle is preserved and we can identify G with the measured Newtonian constant G_N .

Applying the variational principle to the SITS action, with respect to the metric, leads to the following field equations [30, 47, 48]:

$$\frac{1}{\kappa} \left[1 - \frac{\kappa}{6} \phi^2 \right] G^{\mu\nu} = T_\phi^{\mu\nu} + T_m^{\mu\nu} \quad \text{with} \quad \left\{ \begin{array}{l} G^{\mu\nu} \equiv R^{\mu\nu} - \frac{1}{2} R g^{\mu\nu} \\ \equiv \text{the Einstein tensor,} \\ T_\phi^{\mu\nu} \equiv \phi^{|\mu} \phi^{|\nu} - \frac{1}{2} g^{\mu\nu} \phi^{|\sigma} \phi_{|\sigma} + \frac{1}{6} \left\{ g^{\mu\nu} \square \phi^2 - (\phi^2)^{|\mu|\nu} \right\} \\ \equiv \text{the scalar energy-momentum tensor.} \end{array} \right. \quad (1.2)$$

On the other hand, the variational principle with respect to the scalar field gives the scalar-field equation:

$$\square \phi = \frac{1}{6} R \phi. \quad (1.3)$$

1.2 Tensor Scalar theories (TS/BD/STRINGS)

String theories are the only consistent approach, known so far, to quantize perturbatively gravitation. They possess a 2D conformal invariance and lead to an effective action containing additional degrees of freedom in comparison with General Relativity. A minimal version of these consists in the tensor scalar theory first suggested by **Brans and Dicke** [28] in 1961: a single massless scalar field with a constant coupling to matter is proposed. GR is recovered when the scalar coupling to matter vanishes.

This theory was first introduced by the two authors, as explicitly mentioned in the title of their article, to implement Mach's principle in a relativistic theory of gravitation. This goal had soon to be abandoned though, as it requires a large scalar coupling constant to matter, totally excluded by the classical tests of gravitation in the solar system. Nevertheless, the theory of Brans and Dicke (BD) still represents an interesting possible low energy limit of Strings if the scalar coupling to matter is space-time dependent.

What we shall call **Tensor Scalar theories** (TS) in this work are generalizations of the Brans-Dicke action, with a single scalar field³. Specific scalar coupling time-dependences admit an attractor mechanism of the theory towards General Relativity without a strong dependence on initial conditions, thus allowing to nicely fit the present observations. The cosmological evolution of the scalar coupling to matter will be studied in detail in Chapter 2, in one particular model.

Those BD-like theories can be expressed in two different frames, the original Jordan/String frame or the Einstein/Pauli frame, which are physically equivalent (one simply has to be cautious about expressing the final result in terms of measurable quantities). The Einstein frame appears more convenient for cosmological calculations (analysis and cosmological evolution of equations of the Friedman-Lemaître type). The Jordan frame is probably better suited to relativistic calculations (light deflection, perihelion advance, particle motion...) as particles follow the geodesics of the corresponding Jordan metric, which is not the case in the Einstein frame.

1.2.1 Jordan frame

Let us recall the TS action [28], as it was formulated originally, in the Jordan frame:

$$I_{TSJ} = \int dx^{(4)} \sqrt{-g} \left[\frac{-1}{2\kappa} \left\{ R - \frac{\varpi(\Phi)}{\Phi^2} \Phi^{|\mu} \Phi_{|\mu} \right\} + \mathcal{L}_m(g_{\mu\nu}, \psi_m) \right] \quad (1.4)$$

where

$$\kappa \equiv 8\pi G/c^4, \quad G \equiv \frac{1}{\Phi},$$

and $\varpi(\Phi)$ is the TS parameter, function of the scalar field Φ .

The coupling of gravitation to matter is Metric which implies that the WEP is verified.

The equations of motion in the Jordan frame are given by

$$\begin{aligned} G^{\mu\nu} &= +\frac{\varpi(\Phi)}{\Phi^2} [\Phi^{|\mu} \Phi^{|\nu} - \frac{1}{2} g^{\mu\nu} \Phi^{|\sigma} \Phi_{|\sigma}] + \frac{1}{\Phi} [\Phi^{|\mu|\nu} - g^{\mu\nu} \Phi^{|\sigma}{}_{|\sigma}] + \frac{8\pi}{\Phi c^4} T_m^{\mu\nu}, \\ \square\Phi &= \frac{1}{2\varpi(\Phi)+3} \left[-\frac{d\varpi}{d\Phi} \Phi^{|\sigma} \Phi_{|\sigma} + \frac{8\pi}{c^4} T_m \right], \end{aligned} \quad (1.5)$$

where

$$T_m = g_{\mu\nu} T_m^{\mu\nu}.$$

An approximative solution to the field equations can be found in the Newtonian (present-time) limit, after linearization of the field equations. We first linearize the theory in the Jordan frame according to

$$g_{\mu\nu} = \eta_{\mu\nu} + h_{\mu\nu}$$

³ It has been shown that the (positive energy definite) multiscalar case does not bring essentially new features with respect to the monoscalar case [40].

and

$$\Phi = \Phi_0 (1 + \varphi) ,$$

where Φ_0 is a constant background value.

Owing to the cosmological timescale for the variation of the scalar field and its coupling, with respect to the timescale for gravitational experiments, the solution we will derive is static. Furthermore, in Chapter 2, we shall see that the present-time value of the scalar field, of its derivative and of its coupling to matter must be small.

Accordingly, we write the metric equation as

$$\square h_{\mu\nu} \simeq -2\kappa \left[T_{m\ \mu\nu} - \frac{1}{2}\eta_{\mu\nu} T_m + \frac{1}{2}\alpha_{TS}^2 T_m \eta_{\mu\nu} \right] , \quad (1.6)$$

where

$$\alpha_{TS} \equiv \frac{1}{\sqrt{2\varpi(\Phi) + 3}} . \quad (1.7)$$

Note that to obtain this compact expression (1.6), we chose a gauge ($H^\mu{}_\mu = H^{\mu\nu}{}_{|\mu} = H^{ij}{}_{|j} = 0$, keeping only the three physical polarizations for the graviton) in which the following tensor,

$$H_{\mu\nu} \equiv h_{\mu\nu} - \frac{1}{2}\eta_{\mu\nu} h - \eta_{\mu\nu} \varphi \quad \text{with } h \equiv \eta^{\mu\nu} h_{\mu\nu} ,$$

is traceless and transverse.

For the scalar field, the resulting equation

$$\square\varphi \simeq \alpha_{TS}^2 \kappa T_m$$

shows that α_{TS} can be identified as the field dependent scalar coupling to matter.

At first order in $1/c^2$, the energy-momentum tensor in a dust universe is given by $T_m^{\mu\nu} = \varrho_m c^2 u^\mu u^\nu$ where ϱ_m is the matter density. The field equations thus become

$$\begin{aligned} \square h_{00} &\simeq - [1 + \alpha_{TS}^2] \kappa \varrho_m c^2 , \\ \square h_{ii} &\simeq - [1 - \alpha_{TS}^2] \kappa \varrho_m c^2 , \\ \square\varphi &\simeq + [\alpha_{TS}^2] \kappa \varrho_m c^2 . \end{aligned}$$

The solutions with respect to a cosmological constant background (noted with a subscript “0”), up to first order in $1/c^2$ for a spherically symmetric static metric, are thus

$$h_{00} \simeq -2 [1 + \alpha_{TS0}^2] \frac{GM}{rc^2} , \quad (1.8)$$

$$h_{ii} \simeq -2 [1 - \alpha_{TS0}^2] \frac{GM}{rc^2} , \quad (1.9)$$

$$\varphi \simeq +2 \alpha_{TS0}^2 \frac{GM}{rc^2} . \quad (1.10)$$

In the Jordan frame, if we apply the variational principle with respect to the metric $g_{\mu\nu}$ to the matter action

$$I_{TS\ m\ J} = \int M c\ ds , \quad (1.11)$$

we see that particles follow geodesics of the metric, owing to the Metric coupling:

$$\frac{d^2 x^\mu}{dk^2} + \Gamma_{\nu\rho}^\mu \frac{dx^\nu}{dk} \frac{dx^\rho}{dk} = 0 \quad \text{where } dk = c\ d\tau \text{ and } k \text{ is the affine parameter for } g_{\mu\nu} .$$

This equation can be expanded up to $\mathcal{O}(1/c^2)$. For a static spherically symmetric metric, this gives

$$\frac{dt^2}{d\tau^2} \simeq 0$$

and

$$\frac{d^2 r}{dt^2} \simeq (1 + \alpha_{TS0}^2) \frac{GM}{r^2}. \quad (1.12)$$

To recover the Newtonian law, the effective potential (for a unitary mass m) in the Jordan frame must be

$$V_{TS}(r) = - (1 + \alpha_{TS0}^2) \frac{GM}{r} \quad \text{with } F_{TS}(r) = -\partial_r V_{TS}(r). \quad (1.13)$$

Consequently, we could write, for the present value of the gravitational “constant”,

$$G = \frac{1}{1 + \alpha_{TS0}^2} G_N. \quad (1.14)$$

1.2.2 Einstein frame

The conformal factor

$$A^2(\Sigma) \equiv \frac{G}{\tilde{G}} \equiv \frac{1}{\tilde{G}\Phi} \quad \text{with } \alpha_{TS} \equiv \frac{\partial}{\partial \Sigma} \ln A(\Sigma) \quad (1.15)$$

transforms the metric of the Jordan frame, $g_{\mu\nu}$, into the so-called Einstein metric, $\tilde{g}_{\mu\nu} = A^{-2}(\Sigma) g_{\mu\nu}$. The TS theory now reads

$$\tilde{I}_{TS E} = \int dx^{(4)} \sqrt{-\tilde{g}} \left[\frac{-1}{2\tilde{\kappa}} \left\{ \tilde{R} - 2 \Sigma^{\tilde{\mu}} \Sigma_{\tilde{\mu}} \right\} + \mathcal{L}_m(A^2(\Sigma) \tilde{g}_{\mu\nu}, \psi_m) \right] \quad (1.16)$$

where

$$\tilde{\kappa} \equiv 8\pi\tilde{G}/c^4. \quad (1.17)$$

In this frame, the Metric coupling is not explicit because particles do not follow the geodesics of $\tilde{g}_{\mu\nu}$.

Notice that the coupling of gravitation to matter is now non-minimal ($A^2(\Sigma) \neq 1$), and thus the gravitational constant \tilde{G} cannot be identified with the Newtonian value.

Moreover, masses in the Einstein frame (\tilde{M}) are no longer constant but related to the masses in the Jordan frame (M) by

$$\tilde{M} = A(\Sigma) M. \quad (1.18)$$

This can be easily understood when looking at the conformal transformation of the Jordan matter action (1.11) into the Einstein matter action,

$$\tilde{I}_{TS m E} = \int \tilde{M} c \tilde{d}s. \quad (1.19)$$

Finally, notice that the effective String action for a massless scalar field Σ appears as one particular case of the BD theory (ϖ constant) with ϖ equal to -1 . In this particular case, the conformal factor is explicitly given by

$$A_{STRINGS}^2(\Sigma) = e^{2\Sigma}. \quad (1.20)$$

The equations of motion⁴ in the Einstein frame are

$$\tilde{G}^{\mu\nu} = \tilde{\kappa} \tilde{T}_m^{\mu\nu} + 2 \Sigma^{|\mu} \Sigma^{|\nu} - \tilde{g}^{\mu\nu} \Sigma_{|\sigma} \Sigma^{|\sigma}, \quad (1.21)$$

and for the scalar field,

$$\tilde{\square} \Sigma = -\frac{\tilde{\kappa}}{2} \alpha_{TS}(\Sigma) \tilde{T}_m. \quad (1.22)$$

In this frame also an approximative solution to the field equations around the present time can be found, after linearization in the Newtonian limit. Using

$$\tilde{g}_{\mu\nu} = \eta_{\mu\nu} + \tilde{h}_{\mu\nu}$$

and

$$\Sigma = \Sigma_0 + \sigma, \quad (1.23)$$

where Σ_0 is a constant background value, we get

$$\tilde{\square} \tilde{h}_{\mu\nu} \simeq -2\tilde{\kappa} \left(\tilde{T}_m^{\mu\nu} - \frac{1}{2} \eta_{\mu\nu} \tilde{T}_m \right),$$

in the gauge where the tensor

$$\tilde{H}_{\mu\nu} \equiv \tilde{h}_{\mu\nu} - \frac{1}{2} \eta_{\mu\nu} \tilde{h} \quad \text{with } \tilde{h} \equiv \eta^{\mu\nu} \tilde{h}_{\mu\nu}$$

is traceless and transverse.

The equation for the scalar field is given by

$$\tilde{\square} \sigma = -\frac{\tilde{\kappa}}{2} \alpha_{TS} \tilde{T}_m.$$

Particularizing these equations to a dust universe and retaining only the first order in $1/c^2$ ($\tilde{T}_m^{\mu\nu} \simeq \tilde{\varrho}_m c^2 \tilde{u}^\mu \tilde{u}^\nu$), the field equations become

$$\begin{aligned} \tilde{\square} \tilde{h}_{00} &\simeq -\tilde{\kappa} \tilde{\varrho}_m c^2, \\ \tilde{\square} \tilde{h}_{ii} &\simeq -\tilde{\kappa} \tilde{\varrho}_m c^2, \\ \tilde{\square} \sigma &\simeq -\left[\frac{1}{2} \alpha_{TS} \right] \tilde{\kappa} \tilde{\varrho}_m c^2. \end{aligned}$$

Up to first order in $1/c^2$, the solutions are

$$\tilde{h}_{00} \simeq -2 \frac{\tilde{GM}}{rc^2}, \quad (1.24)$$

$$\tilde{h}_{ii} \simeq -2 \frac{\tilde{GM}}{rc^2}, \quad (1.25)$$

$$\sigma \simeq -\alpha_{TS0} \frac{\tilde{GM}}{rc^2}, \quad (1.26)$$

with respect to a cosmological constant background and for a spherically symmetric static metric.

⁴ If a cosmological constant is added to the Lagrangian (1.16), $\tilde{I}_{TS \text{ gravitation } E} = \int dx^{(4)} \sqrt{-\tilde{g}} \frac{1}{2\tilde{\kappa}} \left[\tilde{R} - \Lambda - 2 \Sigma^{|\mu} \Sigma_{|\mu} \right]$, equation (1.21) reads $\tilde{G}^{\mu\nu} - \Lambda \tilde{g}^{\mu\nu} = \tilde{\kappa} \tilde{T}_m^{\mu\nu} + 2 \Sigma^{|\mu} \Sigma^{|\nu} - \tilde{g}^{\mu\nu} \Sigma_{|\sigma} \Sigma^{|\sigma}$.

1.3 Minimal Tensor Scalar theory (MTS)

If one imposes the minimal coupling of gravitation to matter ($A^2 \equiv 1$) in the Einstein frame, the Minimal Tensor Scalar gravitational action (MTS) is obtained and the corresponding gravitational constant can be identified with the measured Newtonian constant, $G = G_N$. It is the simplest way to modify the Hilbert-Einstein action of GR, taking into account the possible effect of one massless scalar field:

$$I_{MTS} = \int dx^{(4)} \sqrt{-g} \left\{ -\frac{1}{2\kappa} R + \frac{1}{2} \Psi^{|\mu} \Psi_{|\mu} + \mathcal{L}_m(g_{\mu\nu}, \psi_m) \right\} \quad (1.27)$$

with

$$\kappa \equiv 8\pi G/c^4.$$

The most general static, spherically symmetric and asymptotically flat *exact* solution to the corresponding equations of motion,

$$G^{\mu\nu} = \kappa (T_{\Psi}^{\mu\nu} + T_m^{\mu\nu}) \quad \text{with} \quad \begin{cases} T_{\Psi}^{\mu\nu} & \equiv \Psi^{|\mu} \Psi^{|\nu} - \frac{1}{2} g^{\mu\nu} \Psi^{|\sigma} \Psi_{|\sigma} \\ & \equiv \text{the scalar energy-momentum tensor,} \end{cases} \quad (1.28)$$

$$\square \Psi = 0,$$

is given in vacuum by

$$ds^2 = A^2(r) c^2 dt^2 - B^2(r) dr^2 - D^2(r) r^2 (d\theta^2 + \sin^2 \theta d\varphi^2)$$

$$\text{with} \quad A^2(r) = B^{-2}(r) = \left(1 - \frac{2GM}{\Upsilon r c^2}\right)^{\Upsilon} \quad (1.29)$$

$$D^2(r) = \left(1 - \frac{2GM}{\Upsilon r c^2}\right)^{1-\Upsilon}$$

for the metric in Schwarzschild-like coordinates [69, 135, 145]; and for the scalar field, by

$$\Psi = \Psi_0 \pm \left(\frac{1 - \Upsilon^2}{2\kappa}\right)^{\frac{1}{2}} \ln \left(1 - \frac{2GM}{\Upsilon r c^2}\right). \quad (1.30)$$

As we shall see later, this solution is useful to obtain the Eddington-Robertson-Schiff parameters not only of MTS theory, but also of SITS and TS theories.

Note that for this MTS theory with a minimal coupling of gravitation to matter, M is a constant gravitational mass. From (1.29), one must have

$$0 < \Upsilon \leq 1$$

to ensure the correct sign for the attractive Newtonian potential (with gravitational coupling $\frac{G}{\Upsilon}$) in the weak field limit. We recover the standard Schwarzschild solution of General Relativity when Υ is 1.

1.4 Large Extra-Dimension theories (LED)

The idea of extra-dimensions is not new: first introduced by Kaluza and Klein in the 1920's [94], it was revived with the concept of compactification used in many recent String theories scenarios. This time, the compactification radius is assumed to be much larger than the Planck length, but still under the millimeter scale⁵, in order to explain why

⁵ One therefore needs more than one extra-dimension, because the size of the extra-dimensions is given by

$$R \sim \frac{M_{\text{Planck}}^{2/d}}{M_s^{(d+2)/2}} \frac{\hbar}{c} \quad \text{and for } M_s \sim \text{TeV}/c^2, \quad R \sim \begin{cases} 10^{+13} \text{ m} & \text{for } d = 1 \\ 10^{-3} \text{ m} & \text{for } d = 2 \\ \dots & \dots \end{cases}$$

it has stayed hidden to experiments so far [18]. One of the attractive features of these Large Extra-Dimension theories is that they could provide a solution to the mass hierarchy problem [19] if the new low fundamental mass scale M_s is at the TeV/c^2 range. Also, LED theories predict a certain number of experimental signatures for collider physics, and deviation from Newton's law at submillimeter distances⁶.

The central idea in LED theories is simple: gravitation consists of pure General Relativity but in $(4+d)$ -dimensions (the so-called "Bulk", where gravity propagates), coupled to Standard Model fields constrained to live in our 4-dimensional world (the "3-brane"). The hypothesis is a coupling of all matter fields to the induced 4-dimensional metric. Additionally, compactification of all extra-dimensions on a torus is here assumed. The total LED action reads

$$I_{LED} = \int dx^{(4+d)} \sqrt{-\hat{g}} \frac{-1}{2\hat{\kappa}} \hat{R} + \int dx^{(4)} \sqrt{-g} \mathcal{L}_m(g_{\mu\nu}, \psi_m) \quad (1.31)$$

where

$$\hat{\kappa} \equiv 8\pi\hat{G}/c^4$$

and any quantity in $(4+d)$ -dimensions is designated by a " $\hat{\quad}$ ". For example, \hat{g} is the determinant of the metric field \hat{g}_{uv} (with indices $u, v = 0, 1, 2, 3, \dots, 3+d$) and \hat{R} is the corresponding curvature scalar in $(4+d)$ -dimensions. The metric $g_{\mu\nu}$ (with indices $\mu, \nu = 0, 1, 2, 3$) is the induced metric in 4-dimensions from the $(4+d)$ -metric: $g_{\mu\nu} = \hat{g}_{\mu\nu}$, and g is its determinant.

A $(4+d)$ -perturbation around a Minkowskian background,

$$\hat{g}_{uv} = \eta_{uv} + \sqrt{2\hat{\kappa}} \hat{h}_{uv}, \quad (1.32)$$

gives the linearized gravitational action (only quadratic terms are kept),

$$\hat{I}_{LED \text{ gravitation}}^{quadratic} = \int dx^{(4+d)} \left[\frac{1}{4} \partial_w \hat{h}^{uv} \partial^w \hat{h}_{uv} - \frac{1}{4} \partial_w \hat{h} \partial^w \hat{h} + \frac{1}{2} \partial^u \hat{h} \partial^w \hat{h}_{wu} - \frac{1}{2} \partial_w \hat{h}^{wu} \partial^v \hat{h}_{uv} \right], \quad (1.33)$$

where $\hat{h} \equiv \hat{h}^u_u$.

Like in electromagnetism, the introduction of a gauge symmetry breaking term is needed in order to avoid the appearance of singularities in the corresponding quantum field theory. Thus, adding

$$\left[+\frac{1}{2} \partial_w (\hat{h}^{wu} - \frac{1}{2} \eta^{wu} \hat{h}) \partial^v (\hat{h}_{uv} - \frac{1}{2} \eta_{uv} \hat{h}) \right]$$

to (1.33) leaves us with the following Lagrangian⁷

$$\hat{I}_{LED \text{ gravitation}}^{quadratic} = \int dx^{(4+d)} \left[\frac{1}{4} \partial_w \hat{h}^{uv} \partial^w \hat{h}_{uv} - \frac{1}{8} \partial_w \hat{h} \partial^w \hat{h} \right]. \quad (1.34)$$

Looking at the way gravity couples to matter fields constrained to our 4-dimensional world (by hypothesis), we of course recover the Standard Model on a Minkowski space-time, at zero order in the gravitational perturbation (1.32). However, the expansion at first order now gives the linearized interaction between gravitation and Standard Model fields,

$$I_{LED \text{ interaction}}^{quadratic} = -\sqrt{\frac{\hat{\kappa}}{2}} \int d^4x [h^{\mu\nu} T_{m \mu\nu}], \quad (1.35)$$

where $h^{\mu\nu}$ is the corresponding gravitational perturbation to the induced metric $g^{\mu\nu}$ in 4-dimensions.

As we shall see, a direct consequence of this coupling hypothesis is that only 4-dimensional indices contribute to the propagation of gravitation (as an intermediate state at least).

⁶ For a review on the subject, consult Perez-Lorenzana [98] and references therein.

⁷ Note that the normalization is defined in such a way that a 4-dimensional kinetic term in the induced perturbation (kinetic term hidden in (1.33)) would be correctly normalized to $(\frac{1}{4} \dots)$.

1.4.1 Metric reduction and Brans-Dicke effective action

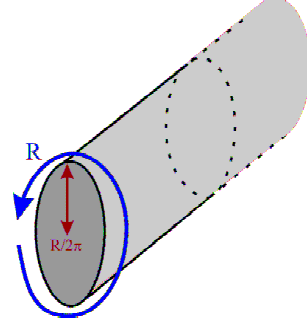


Fig. 1.1 Compactification of all extra-dimensions on a torus is here assumed, with all radii fixed to a unique value, $R/(2\pi)$, for simplicity. The size of the extra-dimensions is thus R and the extra-dimension coordinates are given by $0 \leq y^{\bar{\mu}} \leq R$.

The classical approach to understand the predictions of LED theories consists in the Kaluza-Klein reduction of the $(4 + d)$ -dimensional metric. As this approach has already been thoroughly investigated, the reader may refer to [65], in which all the phenomenology arising from the compactification of large extra-dimensions is deduced via this method. For our purposes, one may drop the massive modes as their masses are defined in such a way that they do not contribute to the gravitational interaction above one millimeter.

Let us remind the reader of the metric decomposition from $(4 + d)$ to 4 dimensions^{8, 9}:

$$\eta_{\mu\nu} + \sqrt{2\kappa} \hat{h}_{\mu\nu} = \eta_{\mu\nu} + \sqrt{2\kappa} \begin{bmatrix} h_{\mu\nu} + \alpha_{LED} \eta_{\mu\nu} \Phi & A_{\mu\bar{\nu}} \\ A_{\bar{\mu}\nu} & -2 \alpha_{LED} \Phi_{\bar{\mu}\bar{\nu}} \end{bmatrix},$$

where $h_{\mu\nu}$, $A_{\mu\bar{\nu}}$ and $\Phi_{\bar{\mu}\bar{\nu}}$ (with indices $\bar{\mu}, \bar{\nu} = 3+1, \dots, 3+d$) are respectively the metric perturbation in 4-dimensions, the vector and scalar perturbations. We call the trace on these scalar fields: $\Phi = \eta^{\bar{\mu}\bar{\nu}} \Phi_{\bar{\mu}\bar{\nu}}$. This decomposition can be introduced in the $(4 + d)$ -linearized theory (equations (1.33) and (1.35)). If we remember that the compactification is made on a torus (see Figure 1.1), with all radii fixed to a unique value, $R/(2\pi)$, for simplicity ($0 \leq y^{\bar{\mu}} \leq R$), the fields admit a decomposition in Fourier modes (\vec{n}) as

$$\begin{aligned} h_{\mu\nu}(\hat{x}) &= h_{\mu\nu}(x^\mu, y^{\bar{\mu}}) = \sum_{n_{\bar{\mu}}=-\infty}^{n_{\bar{\mu}}=+\infty} h_{\mu\nu}^{(\vec{n})}(x^\mu) e^{i \frac{2\pi}{R} \vec{n} \cdot \vec{y}}, \\ A_{\mu\bar{\nu}}(\hat{x}) &= A_{\mu\bar{\nu}}(x^\mu, y^{\bar{\mu}}) = \sum_{n_{\bar{\mu}}=-\infty}^{n_{\bar{\mu}}=+\infty} A_{\mu\bar{\nu}}^{(\vec{n})}(x^\mu) e^{i \frac{2\pi}{R} \vec{n} \cdot \vec{y}}, \\ \Phi_{\bar{\mu}\bar{\nu}}(\hat{x}) &= \Phi_{\bar{\mu}\bar{\nu}}(x^\mu, y^{\bar{\mu}}) = \sum_{n_{\bar{\mu}}=-\infty}^{n_{\bar{\mu}}=+\infty} \Phi_{\bar{\mu}\bar{\nu}}^{(\vec{n})}(x^\mu) e^{i \frac{2\pi}{R} \vec{n} \cdot \vec{y}}. \end{aligned}$$

Such a decomposition allows to separate $I_{LED}^{quadratic} \equiv I_{LED}^{quadratic}{}_{gravitation} + I_{LED}^{quadratic}{}_{interaction}$ in zero ($\vec{n} = 0$) and nonzero modes ($\vec{n} \neq 0$) contributions. From the field equations corresponding to action (1.34), zero modes can be shown to be nonmassive modes (corresponding to an equation of state $\square \cdot = 0$), while nonzero modes correspond to massive particles (corresponding to an equation of state $(\square + m_n^2 c^2) \cdot = 0$ with $m_n^2 c^2 = 4\pi^2 \vec{n}^2 \hbar^2 / R^2$). This will become more evident in the next subsection.

⁸ with different signs than in equation (6) of reference [65] in order to be consistent with our sign convention for the metric.

⁹ Note that this decomposition is purely arbitrary, but it is chosen in such a way that the resulting kinetic terms in the Lagrangian be correctly decoupled and normalized. The free parameter α_{LED} will be fixed by the normalization.

The zero mode action, corresponding to equation (23) in reference [65], is given by

$$I_{LED}^{quadratic} (\bar{n}=0) = \int dx^{(4)} \left[\left(\frac{1}{4} \partial_\mu h^0 \alpha^\beta \partial^\mu h_{\alpha\beta}^0 - \frac{1}{4} \partial_\mu h^0 \partial^\mu h^0 + \frac{1}{2} \partial^\rho h^0 \partial^\mu h_{\mu\rho}^0 - \frac{1}{2} \partial_\mu h^0 \nu^\mu \partial^\rho h_{\nu\rho}^0 \right) \right. \\ \left. + \left(\frac{\alpha_{LED}^2}{2} \partial_\mu \Phi^0 \partial^\mu \Phi^0 + \alpha_{LED}^2 \partial_\mu \Phi_{ij}^0 \partial^\mu \Phi^{0ij} \right) - \left(\frac{1}{4} \sum_{i=1}^d F_{\mu\nu i}^0 F_i^{0\mu\nu} \right) \right. \\ \left. - \sqrt{\frac{\kappa}{2}} (h_{\mu\nu}^0 T_m^{\mu\nu}) - \alpha_{LED} \sqrt{\frac{\kappa}{2}} \Phi^0 T_m \right] \quad (1.36)$$

with

$$\kappa \equiv 8\pi G/c^4,$$

where $F_{\mu\nu \bar{\rho}} \equiv \partial_\mu A_{\nu\bar{\rho}} - \partial_\nu A_{\mu\bar{\rho}}$ and $T_m \equiv \eta_{\mu\nu} T_m^{\mu\nu}$.

The vector fields may be dropped as by construction they propagate freely without interacting with the Standard Model fields ψ_m , see (1.35). At this stage however, the kinetic term for the only scalar field coupling to matter, Φ^0 , is not properly normalized, as the $\Phi_{\bar{\mu}\bar{\nu}}$ fields are not traceless. The trace may be extracted with the use of the following relation

$$\Phi_{\bar{\mu}\bar{\nu}} = \Phi_{\bar{\mu}\bar{\nu}}^{(0)} + \frac{1}{d} \eta_{\bar{\mu}\bar{\nu}} \Phi,$$

where $\Phi_{\bar{\mu}\bar{\nu}}^{(0)}$ are the traceless parts of the $\Phi_{\bar{\mu}\bar{\nu}}$. This leaves a kinetic term for the trace, Φ^0 , which may be normalized to the usual factor $\frac{1}{2}$ by fixing

$$\alpha_{LED}^2 = \frac{d}{d+2}. \quad (1.37)$$

All remaining kinetic terms for the traceless fields may also be dropped as they do not couple to matter either. Consequently, one is just left with a linearized Brans-Dicke theory of gravitation in the Jordan frame ($\eta_{\mu\nu} + \sqrt{2\kappa} h_{\mu\nu}^0, \Phi^0$), with a particularly strong scalar coupling constant α_{LED} . The effective action for null modes thus reads¹⁰:

$$I_{LED}^{effective} (\bar{n}=0) = \int dx^{(4)} \left[\left(\frac{1}{4} \partial_\mu h^0 \alpha^\beta \partial^\mu h_{\alpha\beta}^0 - \frac{1}{4} \partial_\mu h^0 \partial^\mu h^0 + \frac{1}{2} \partial^\rho h^0 \partial^\mu h_{\mu\rho}^0 - \frac{1}{2} \partial_\mu h^0 \nu^\mu \partial^\rho h_{\nu\rho}^0 \right) \right. \\ \left. - \sqrt{\frac{\kappa}{2}} (h_{\mu\nu}^0 T_m^{\mu\nu}) + \left(\frac{1}{2} \partial_\mu \Phi^0 \partial^\mu \Phi^0 \right) - \alpha_{LED} \sqrt{\frac{\kappa}{2}} \Phi^0 T_m \right]. \quad (1.38)$$

In terms of the Brans-Dicke parameter ϖ defined by (1.7), this corresponds to

$$\varpi = \frac{1-d}{d}. \quad (1.39)$$

The particular value $\varpi \rightarrow \infty$, recovered for $d=0$, logically leads us back to GR; while ϖ runs from 0 for $d=1$, to -1 for $d \rightarrow +\infty$. This last value of ϖ happens to correspond to that associated with String theories.

The nonzero mode action is a lot more lengthy to obtain with this method, as the corresponding fields require a redefinition. But the effective action eventually reads [141]:

$$\sum_{\bar{n}} I_{LED}^{effective} (\bar{n} \neq 0) = \sum_{\bar{n}} \int dx^{(4)} \left[\frac{1}{4} \partial_\mu h^{(\bar{n})\alpha\beta} \partial^\mu h^{(\bar{n})\alpha\beta} - \frac{1}{4} \partial_\mu h^{(\bar{n})} \partial^\mu h^{(\bar{n})} + \frac{1}{2} \partial^\rho h^{(\bar{n})} \partial^\mu h^{(\bar{n})}{}_{\mu\rho} \right. \\ \left. - \frac{1}{2} \partial_\mu h^{(\bar{n})\nu\mu} \partial^\rho h^{(\bar{n})}{}_{\nu\rho} + \frac{1}{4} m_n^2 c^2 h^{(\bar{n})} h^{(\bar{n})} - \frac{1}{4} m_n^2 c^2 h^{(\bar{n})}{}_{\mu\nu} h^{(\bar{n})\mu\nu} \right. \\ \left. - \sqrt{\frac{\kappa}{2}} (h^{(\bar{n})}{}_{\mu\nu} T_m^{\mu\nu}) \right. \\ \left. + \left(\frac{1}{2} \partial_\mu \Phi^{(\bar{n})} \partial^\mu \Phi^{(\bar{n})} - \frac{1}{2} m_n^2 c^2 \Phi^{(\bar{n})2} \right) - \beta_{LED} \sqrt{\frac{\kappa}{2}} (\Phi^{(\bar{n})} T_m) \right] \quad (1.40)$$

with for the massive scalar coupling¹¹

$$\beta_{LED}^2 = \frac{2d-1}{3d+2}. \quad (1.41)$$

¹⁰ The normalization between kinetic terms and couplings is defined in agreement with (1.35).

¹¹ As noticed in references [62, 141], the scalar terms obtained in reference [65] have to be properly normalized in order to find out the correct scalar couplings.

1.4.2 Effective field content of the gravitational sector in 4-dimensions

Instead of using the common Kaluza-Klein decomposition, one may simply compute the propagator of the helicity-2 graviton in $(4 + d)$ -dimensions. The basic hypotheses of compactification on a torus and 4-dimensional matter couplings are then applied, to deduce all the effective couplings necessary to deal with higher dimensional gravity. This method shall allow us rapidly to understand the field content of the 4-dimensional gravitational sector [60]. Indeed, the vacuum field $(4 + d)$ -equations corresponding to (1.34) are

$$\frac{1}{2} \hat{\square} \left[\hat{h}^{uv} - \frac{1}{2} \eta^{uv} \hat{h} \right] = 0.$$

The graviton propagator, defined as the Green function $\hat{G}_{uv,sw}$ for the motion operator,

$$\frac{1}{4} \hat{\square} [\eta^{up} \eta^{vq} + \eta^{uq} \eta^{vp} - \eta^{uv} \eta^{pq}] \hat{G}_{uv,sw}(\hat{x} - \hat{x}') = -\frac{1}{2} (\delta_s^p \delta_w^q + \delta_w^p \delta_s^q) \hat{\delta}(\hat{x} - \hat{x}'),$$

then reads in the $(4 + d)$ -momentum space,

$$\hat{G}^{uv,sw}(\hat{q}) = \frac{\eta^{us} \eta^{vw} + \eta^{uw} \eta^{vs} - \frac{2}{2+d} \eta^{uv} \eta^{sw}}{\hat{q}^2 + i\varepsilon}. \quad (1.42)$$

Let us consider as an example a gravitational scattering process for matter fields (Ψ_{m1} and Ψ_{m2}) described by stress-energy tensors $T_m^{(\Psi_{m1})}(\vec{p}_1, \vec{p}_2)$ and $T_m^{(\Psi_{m2})}(\vec{k}_1, \vec{k}_2)$ in (1.35). Using (1.42), the scattering amplitude (in the 4-momentum space) will then be proportional to

$$\begin{aligned} \mathcal{M} &\sim G T_m^{(\Psi_{m1})} \cdot \frac{\eta^{\mu\alpha} \eta^{\nu\beta} + \eta^{\mu\beta} \eta^{\nu\alpha} - \frac{2}{2+d} \eta^{\mu\nu} \eta^{\alpha\beta}}{\hat{q}^2 + i\varepsilon} \cdot T_m^{(\Psi_{m2})} \\ &\sim G T_m^{(\Psi_{m1})} \cdot G^{\mu\nu, \alpha\beta}(\hat{q}) \cdot T_m^{(\Psi_{m2})}. \end{aligned} \quad (1.43)$$

Using the fact that the compactification is made on a torus with all radii fixed to the unique value $R/(2\pi)$, the $(4 + d)$ -metric perturbations admit a Fourier decomposition in the extra-dimensions:

$$\hat{h}_{uv}(\hat{x}) = \hat{h}_{uv}(x^\mu, y^{\vec{\mu}}) = \sum_{n_{\vec{\mu}}=-\infty}^{n_{\vec{\mu}}=+\infty} \hat{h}_{uv}^{(\vec{n})}(x^\mu) e^{i \frac{2\pi}{R} \vec{n} \cdot \vec{y}},$$

and the $(4 + d)$ -dimensional momentum either reduces to the 4-dimensional momentum for zero modes ($\vec{n} = 0$),

$$\hat{q}^2 \mapsto q^2,$$

or splits into the 4-dimensional momentum plus a mass term for nonzero modes ($\vec{n} \neq 0$):

$$\hat{q}^2 \mapsto q^2 - m_n^2 c^2 \quad \text{where } m_n^2 c^2 = \frac{4\pi^2 \vec{n}^2 \hbar^2}{R^2}. \quad (1.44)$$

At this level, one may understand that gravitation propagates in 4-dimensions through one massless mode and an infinite tower of massive modes, all exhibiting the same tensor structure expressed in (1.43). Let us now identify the corresponding massless and massive 4-dimensional fields.

For massless fields/modes ($\vec{n} = 0$), we may extract the propagator of a massless helicity-2 graviton from the whole tensor structure (1.42). The remaining term couples, like a massless gravitational scalar field, to the trace of the energy-momentum tensor:

$$\mathcal{M}_{(\vec{n}=0)} \sim G T_m^{(\Psi_{m1})} \cdot \frac{\eta^{\mu\alpha} \eta^{\nu\beta} + \eta^{\mu\beta} \eta^{\nu\alpha} - \frac{2}{2+d} \eta^{\mu\nu} \eta^{\alpha\beta}}{q^2 + i\varepsilon} \cdot T_m^{(\Psi_{m2})}$$

$$\begin{aligned}
&= G T_m^{(\Psi_{m\ 1})} \cdot \frac{\eta^{\mu\alpha}\eta^{\nu\beta} + \eta^{\mu\beta}\eta^{\nu\alpha} - \eta^{\mu\nu}\eta^{\alpha\beta}}{q^2 + i\varepsilon} \cdot T_m^{(\Psi_{m\ 2})} \\
&\quad + [\alpha_{LED}^2 G] T_m^{(\Psi_{m\ 1})} \cdot \frac{1}{q^2 + i\varepsilon} \cdot T_m^{(\Psi_{m\ 2})}. \quad (1.45)
\end{aligned}$$

The scalar coupling reduction factor $\alpha_{LED}^2 = d/(d+2)$ corresponds to the zero mode scalar coupling found by the traditional Kaluza-Klein reduction (1.37). The effective theory which naturally corresponds to this propagator is of course (1.38).

Similarly, **for the massive fields/modes** ($\vec{n} \neq \mathbf{0}$), after extraction of the massive spin-2 graviton propagator, one is left with a term which now corresponds to a massive gravitational scalar field,

$$\begin{aligned}
\mathcal{M}_{(\vec{n} \neq \mathbf{0})} &\sim G T_m^{(\Psi_{m\ 1})} \cdot \frac{\eta^{\mu\alpha}\eta^{\nu\beta} + \eta^{\mu\beta}\eta^{\nu\alpha} - \frac{2}{2+d}\eta^{\mu\nu}\eta^{\alpha\beta}}{q^2 - m_n^2 c^2 + i\varepsilon} \cdot T_m^{(\Psi_{m\ 2})} \\
&= G T_m^{(\Psi_{m\ 1})} \cdot \frac{\eta^{\mu\alpha}\eta^{\nu\beta} + \eta^{\mu\beta}\eta^{\nu\alpha} - \frac{2}{3}\eta^{\mu\nu}\eta^{\alpha\beta}}{q^2 - m_n^2 c^2 + i\varepsilon} \cdot T_m^{(\Psi_{m\ 2})} \\
&\quad + [\beta_{LED}^2 G] T_m^{(\Psi_{m\ 1})} \cdot \frac{1}{q^2 - m_n^2 c^2 + i\varepsilon} \cdot T_m^{(\Psi_{m\ 2})}, \quad (1.46)
\end{aligned}$$

with the massive scalar reduction factor $\beta_{LED}^2 = 2/3 (d-1)/(d+2)$ found earlier, by classical means, as the nonzero mode scalar coupling (1.41) in the effective action (1.40).

We have seen that gravitation is mediated by one massless helicity-2 graviton like in GR, plus one massless scalar and an infinite tower of massive Kaluza-Klein fields. Indeed, at each level \vec{n} , there are 1 spin-2, $(d-1)$ spin-1, plus $d(d-1)/2$ spin-0 states, all with a degenerated mass m_n , among which the vector fields (spin-1) do not couple to Standard Model matter fields.

1.4.3 Weak field limit

We now need to understand how G and the Newtonian constant G_N are related. To do so, we take the classical limit of the theory, meaning the nonrelativistic limit of the Fourier transform of the scattering amplitude mediated by the gravitational interaction of LED (1.43):

$$\begin{aligned}
\mathcal{M}_{LED} &\sim \mathcal{M}_{(\vec{n}=\mathbf{0})} + \sum_{\vec{n}} \mathcal{M}_{(\vec{n} \neq \mathbf{0})} \\
&\stackrel{(1.46), (1.45)}{\sim} G T_m^{(\Psi_{m\ 1})} \cdot \left(\eta^{\mu\alpha}\eta^{\nu\beta} + \eta^{\mu\beta}\eta^{\nu\alpha} - \frac{2}{2+d}\eta^{\mu\nu}\eta^{\alpha\beta} \right) \left[\frac{1}{q^2} + \sum_{\vec{n}} \frac{1}{q^2 - m_n^2 c^2} \right] \cdot T_m^{(\Psi_{m\ 2})}.
\end{aligned}$$

The massive states lead to Yukawa contributions to the classical interaction potential

$$V_{massive}(r) \propto \frac{e^{-\frac{m_n c}{\hbar} r}}{r}; \quad (1.47)$$

but such contributions are ruled out for distances above one millimeter by current experiments. These experimental constraints can be implemented in LED theories by choosing large enough masses $m_n (\gtrsim 10^{-3} \text{ eV}/c^2)$ for the Kaluza-Klein fields. Hence, as we want to recover the Newtonian constant in this regime, we may drop the contribution of all massive state propagators. Accordingly, the scattering amplitude reduces to

$$\mathcal{M}_{LED} \stackrel{(1.45)}{\sim} G T_m^{(\Psi_{m\ 1})} \cdot \left(\eta^{\mu\alpha}\eta^{\nu\beta} + \eta^{\mu\beta}\eta^{\nu\alpha} - \eta^{\mu\nu}\eta^{\alpha\beta} + \alpha_{LED}^2 \eta^{\mu\nu}\eta^{\alpha\beta} \right) \frac{1}{q^2} \cdot T_m^{(\Psi_{m\ 2})}.$$

One could make the whole computation of the corresponding Feynman diagrams, by introducing the adequate energy-momentum tensor for the fields associated to matter. However, our purpose is to recover the effective gravitational potential. We may then consider solely classical matter particles, for which the stress tensor is given by $T_m^{(i)\ \mu\nu}(x) = \varrho_m c^2 u_\mu u_\nu$ with $\varrho_m c^2$ the energy density of the particle and $m_i \delta^3(\vec{x} - \vec{x}_i)$ its mass. To the leading order, we may

neglect the currents and consider $T_m^{(i)}{}_{\mu\nu}(x) \sim \varrho_m c^2 \delta_\mu^0 \delta_\nu^0$. The amplitude then reduces to

$$\mathcal{M}_{LED} \sim (1 + \alpha_{LED}^2) G \frac{m_1 m_2}{\bar{q}^2},$$

the Fourier transform of which gives the effective gravitational potential. The same considerations within General Relativity would lead us to

$$\mathcal{M}_{GR} \sim G_N \frac{m_1 m_2}{\bar{q}^2}.$$

In order to recover the exact Newtonian law with the Newtonian constant, one has set the ratio of those two amplitudes to 1. We thus obtain the relation between G and G_N :

$$G = \frac{1}{1 + \alpha_{LED}^2} G_N, \quad (1.48)$$

as we could have guessed from equation (1.14), knowing that the linearized zero-mode action (1.38) can be related to the Brans-Dicke one.

1.5 The Weyl theory (W)

The preceding alternative theories included gravitational scalar degrees of freedom. The Weyl theory (W) [83, 85, 87, 88] is on the contrary purely tensorial, still with a Metric coupling of gravitation to matter, but with higher order derivatives of the metric in the dynamical sector. A particularity of this theory is to be conformally invariant (under transformations $g_{\mu\nu} \mapsto \chi^2(x) g_{\mu\nu}$ with $\chi^2(x)$ a finite, positive, nonvanishing, continuous real function), which makes it attractive since renormalizable perturbatively [56, 129] and asymptotically free [55, 72] in a way similar to the theory of strong interactions.

The Weyl gravitational action given by

$$\begin{aligned} I_W \text{ gravitation} &= \int d^4x \sqrt{-g} W^{\mu\nu\rho\sigma} W_{\mu\nu\rho\sigma} \\ &= \int d^4x \sqrt{-g} \left\{ R^{\mu\nu\rho\sigma} R_{\mu\nu\rho\sigma} - 2 R^{\mu\nu} R_{\mu\nu} + \frac{1}{3} R^2 \right\} \end{aligned} \quad (1.49)$$

is conformally invariant since

$$W_{\mu\nu\rho\sigma} \mapsto \chi^2(x) W_{\mu\nu\rho\sigma}.$$

The geodesics for massive particles are obviously not conformally invariant, but the way to implement this symmetry breaking is still obscure. However, light geodesics are conformally invariant, see Subsection 4.4.1, so that any gravitational test based on the trajectories of photons (like the light deflection and the radar echo delay) should not carry this ambiguity.

In vacuum, the variational principle applied to action (1.49) with respect to the metric leads to the Bach equations [107]

$$B^{\mu\nu} \equiv R_{\alpha\beta} W^{\mu\alpha\nu\beta} + 2 W^{\alpha\mu\beta\nu}{}_{|\alpha|\beta} = 0. \quad (1.50)$$

The vacuum solutions of GR ($R_{\alpha\beta} = 0$) are also vacuum solutions of the Weyl theory thanks to the well-known Bianchi identities. Thus, the Schwarzschild metric is a particular solution of the spherically symmetric Bach equations.

The generalized Birkhoff theorem proves that there exists a three parameter (β_W, γ_W, k_W , all constants) family of static and spherically symmetric solutions to those Bach equations. Any of these solutions can be recast, thanks to conformal and coordinate transformations into a canonical line element [107]. It provides the general solution to the Bach equations,

$$ds^2 = g_{\mu\nu} dx^\mu dx^\nu$$

$$= \chi^2(r) \cdot \left\{ \begin{array}{l} + \left[1 - \beta_W \frac{(2-3\beta_W \gamma_W)}{r} - 3 \beta_W \gamma_W + \gamma_W r - k_W r^2 \right] c^2 dt^2 \\ - \left[1 - \beta_W \frac{(2-3\beta_W \gamma)}{r} - 3 \beta_W \gamma_W + \gamma_W r - k_W r^2 \right]^{-1} dr^2 - r^2 d\Omega^2 \end{array} \right\} \quad (1.51)$$

which is static for $\left[1 - \beta_W \frac{(2-3\beta_W \gamma)}{r} - 3 \beta_W \gamma_W + \gamma_W r - k_W r^2 \right] > 0$ and contains, as expected, the Schwarzschild line element as a particular case ($\beta_W = \frac{G_N M}{c^2}$ and $\gamma_W = k_W = 0$). The conformal factor $\chi^2(r)$ is arbitrary unless a conformal symmetry breaking mechanism is specified.

The corresponding potential for gravitation is not Newtonian anymore. **If choosing $\chi^2(r) \equiv 1$ (or choosing a constant χ^2 , in which case r and t are rescaled by a constant factor),** this is the so-called Weyl gravitational potential:

$$V_W(r) = \underbrace{-\frac{\beta_W}{2} \frac{(2-3\beta_W \gamma_W)}{r} c^2}_{\text{Newtonian term}} \underbrace{-\frac{3}{2} \beta_W \gamma_W c^2}_{\text{constant term}} \underbrace{+\frac{\gamma_W}{2} r c^2}_{\text{galactic term}} \underbrace{-\frac{k_W}{2} r^2 c^2}_{\text{cosmological term}}. \quad (1.52)$$

It presents a constant ($\beta_W \gamma_W$)-term in addition to the traditional Newtonian term, so that the solution cannot, with any conformal transformation, be brought to a Minkowskian space, even asymptotically. It contains also a linear term that might dominate at galactic distance scales, as well as a quadratic term that should become significant only at cosmological distances of the gravitational source. When γ_W is null (classical Schwarzschild solution), k_W is proportional to the cosmological scalar curvature of a de Sitter background [87].

When fitting the experimental galactic rotation curves (see Figure 1.2) with the gravitational Weyl potential (Newtonian plus galactic term only), without the assumption of any dark matter, Mannheim and Kazanas [82, 84, 87] provided the following constraints on the parameters β_W and γ_W of the theory:

$$\begin{aligned} \gamma_W &\sim +10^{-26} \text{ m}^{-1}, \\ \beta_W &\simeq \frac{G_N M}{c^2} \Big|_{M_{\text{Galaxy}}} \sim +10^{+14} \text{ m}^{+1}. \end{aligned} \quad (1.53)$$

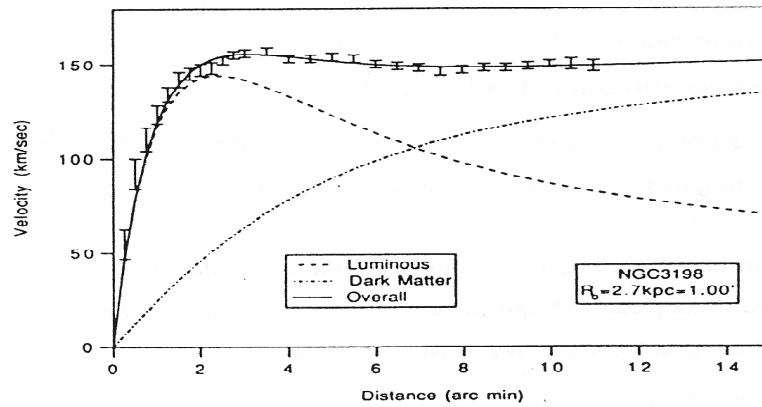


Fig. 1.2 Rotation curve for the galaxy NGC3198 of radius R_0 .

The dash curve represents the contribution of the Newtonian potential ($\partial V_N / \partial r \propto v^2 / r$) corresponding to the luminous mass, *i.e.* the “observed” matter. The solid line is the Newtonian contribution plus an *ad hoc* amount of dark matter so to verify experimental data given by the error bars. The dotted curve models the contribution of dark matter alone. The experimental data can also be fitted without any dark matter, by using the Weyl gravitational potential ($\partial V_W / \partial r \propto v^2 / r$) and adjusting properly its parameters.

This picture is extracted from Mannheim’s article [85].

On radial distances (r) smaller than the parsec, the $(\beta_W \gamma_W)$ - and k_W -contributions can be neglected in the effective potential (1.52).

The explanation of the flattening of rotation curves on galactic distance scales given by Mannheim and Kazanas requires γ_W to be positive. The order of magnitude of γ_W , close to the inverse of the Hubble length, was noted as an interesting coincidence. However, we have to keep in mind that the Mannheim-Kazanas parametrization (1.53) is based on the specific choice¹² $\chi^2(r) \equiv 1$, while any gravitational test or measurement requiring a distance/time scale depends on the conformal factor.

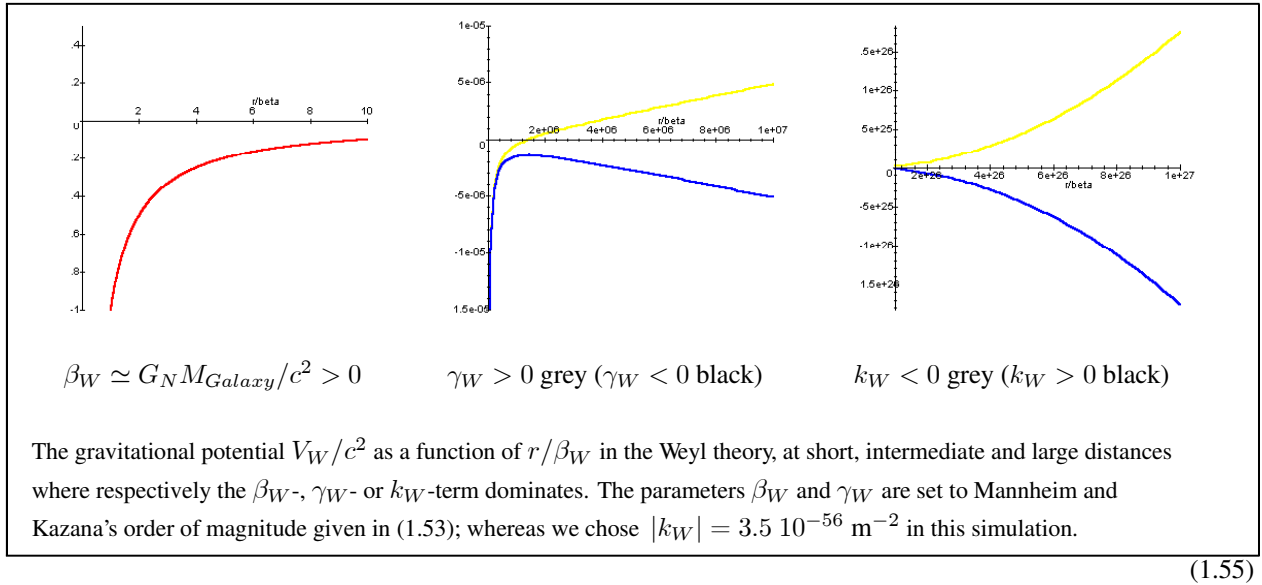
It is important to note here the radial distance scale at which the Weyl gravitational potential can be considered to be a weak field ($2 V_W(r)/c^2 \ll 1$), for $\beta_W \simeq G_N M/c^2$ with gravitational mass M , and neglecting the k_W -term. We find, for either the Sun (M_{Sun}), the Galaxy ($M_{Galaxy} \sim 10^{11} M_{Sun}$) or a cluster ($M_{cluster} \sim 10^{13} - 10^{15} M_{Sun}$),

$$r_{weak\ field} \ll \frac{3\beta_W \gamma_W \pm 1 \pm \sqrt{1 \pm \begin{Bmatrix} +14 \\ -2 \end{Bmatrix} \beta_W \gamma_W - 3(\beta_W \gamma_W)^2}}{2\gamma_W} \quad (1.54)$$

$$\begin{aligned} & \stackrel{(\beta_W \gamma_W)\text{-term neglected}}{\sim} \pm \frac{1}{\gamma_W} \\ & \stackrel{(1.53)}{\sim} +10^{26} \text{ m if } \chi^2(r) = 1, \end{aligned}$$

with upper sign and number for $\gamma_W > 0$ and lower sign and number for $\gamma_W < 0$. The last line is written assuming the order of magnitude of parameter γ_W given by (1.53).

The following graphs (1.55) of the gravitational potential for a galaxy in Weyl gravity are plotted according to the Mannheim-Kazanas parametrization (1.53).



¹² In a private communication [86], Mannheim advocated that "all mass is dynamical" in his theory. In other words, both the test particle and the gravitational source would get their mass from the same Higgs field, such that all massive particles possess the same conformal factor, $\chi^2(r)$, which makes it unobservable.

However, it is known that there should exist at least two different symmetry breaking mechanisms generating the ordinary matter mass. For example, the electron gets its mass from the Higgs mechanism of the Standard Electroweak Model, whereas the mass of the proton is mainly due to the Quantum Chromodynamics. Hence, we claim that it is not allowed to attribute a common conformal factor $\chi^2(r)$ to all types of particles.

1.6 Eddington-Robertson-Schiff parameters

For an alternative theory, when the corresponding weak field potential vanishes asymptotically, the Post-Newtonian formalism proves to be very convenient to write the gravitational tests in a generic manner. But, as explained in the introduction of this work, we shall mainly consider here Metric theories of gravity, and so, *we will use a somewhat simplified formalism*. We recall that Metric theories of gravity are theories based on the hypothesis of the universal Metric coupling which preserves the Weak Equivalence Principle together with the Local Lorentz Invariance Principle and the Local Positional Invariance Principle; that is to say that they verify the Einstein Equivalence Principle. In terms of the ten Post-Newtonian (PN) parameters, according to a theorem of Lee *et al.* [79], every Lagrangian-based Metric theory of gravity has all parameters describing violations of the conservation of the total energy and momentum equal to zero. This means that the theory is at least Semi-Conservative and in the most general framework of the PN formalism developed by Will and his collaborators [142], $\alpha = 1$ and $\alpha_3 = \zeta_1 = \zeta_2 = \zeta_3 = \zeta_4 = 0$. We will further restrict ourselves to theories that additionally conserve the angular momentum, the so-called Fully Conservative theories, *i.e.* $\alpha_1 = \alpha_2 = 0$. For this last type of theories, only three PN parameters have to be considered: γ , β and ξ . The first one characterizes the “amount of curvature per unit rest mass”, the second one the “non-linearity in the superposition law of gravity” and the last one the “preferred location effects” [142, 143]. However, all the theories that we analysed in this work are Purely Dynamical theories, in other words, Metric theories whose gravitational fields have their structure and evolution determined by coupled differential equations. In this framework, ξ equals 0 and we are left with γ and β , originally introduced by Eddington (1922), Robertson (1962) and Schiff (1967).

1.6.1 General

In the weak field approximation, we use the standard Eddington-Robertson-Schiff parametrization defined in the isotropic coordinates, for a general line element

$$ds^2 = A^2(\rho)c^2 dt^2 - B^2(\rho) [d\rho^2 + \rho^2(d\theta^2 + \sin^2\theta d\varphi^2)] , \quad (1.56)$$

but go one order further in the potential expansion:

$$\begin{aligned} A^2(\rho) &\simeq 1 + 2\alpha \left(\frac{V}{c^2}\right) + 2\beta \left(\frac{V}{c^2}\right)^2 + \frac{3}{2}\epsilon \left(\frac{V}{c^2}\right)^3 , \\ B^2(\rho) &= D^2(\rho) \\ &\simeq 1 - 2\gamma \left(\frac{V}{c^2}\right) + \frac{3}{2}\delta \left(\frac{V}{c^2}\right)^2 . \end{aligned} \quad (1.57)$$

It is crucial to realize that $V \equiv V(\rho)$ is *the effective weak field gravitational potential* expressed in terms of the isotropic radial coordinate ρ ; this potential appears in the weak field limit of the considered theory to reproduce the Newtonian law of motion:

$$\vec{F}_{\text{gravitation on } m \text{ due to } M} = m * \vec{a} \quad \text{with} \quad \vec{F}_{\text{gravitation on } m \text{ due to } M} \equiv -m * \overrightarrow{\text{grad}}(V) . \quad (1.58)$$

Notice that we have normalized the coefficients in this weak field expansion in such a way that all the parameters are equal to 1 for GR.

We shall now recover the Eddington-Robertson-Schiff parameters corresponding to the alternative theories mentioned in the preceding sections. To do so, we must use the general isotropic solution to the corresponding field equations for each of them. The idea is to take the *exact* MTS solution transposed into isotropic coordinates first to obtain the MTS Eddington-Robertson-Schiff parameters, then to reach SITS and TS Eddington-Robertson-Schiff parameters through conformal transformations from the MTS isotropic solution. Note that the Weyl theory does not allow of an expansion of its metric in powers of $V_N(r)/c^2$, because the corresponding weak field gravitational potential is not Newtonian anymore. Furthermore, the Weyl potential blows up at infinity. Also, LED theories do not admit a (P)PN expansion because they are based on a $(4 + d)$ -metric (that eventually couples to 4-dimensional matter fields through an effective 4-metric).

1.6.2 MTS isotropic solution

Applying the following coordinate transformation,

$$\boxed{\begin{array}{l} \text{Schwarzschild : } r \mapsto \text{isotropic : } \rho \\ r = \frac{GM}{2\Upsilon c^2} \left[\frac{\left(1 + \frac{GM}{2\Upsilon \rho c^2}\right)^2}{\frac{GM}{2\Upsilon \rho c^2}} \right] \end{array}} \quad (1.59)$$

to the asymptotically flat and spherically symmetric MTS solution given in equation (1.29), it is easy to recover the isotropic formulation of the metric,

$$\begin{aligned} A^2(\rho) &= \left[\frac{1 - \frac{GM}{a\rho c^2}}{1 + \frac{GM}{a\rho c^2}} \right]^a, \\ B^2(\rho) &= D^2(\rho) = \left[1 + \frac{GM}{a\rho c^2} \right]^4 \left[\frac{1 - \frac{GM}{a\rho c^2}}{1 + \frac{GM}{a\rho c^2}} \right]^{2-a}, \\ \text{with } a &= 2\Upsilon \in]0; 2], \end{aligned} \quad (1.60)$$

as well as the scalar-field solution,

$$\Psi = \Psi_0 \pm \left(\frac{4 - a^2}{2\kappa} \right)^{\frac{1}{2}} \ln \left(\frac{1 - \frac{GM}{a\rho c^2}}{1 + \frac{GM}{a\rho c^2}} \right). \quad (1.61)$$

It is now straightforward to expand the MTS isotropic metric in terms of its effective weak field gravitational potential $V_{MTS}(\rho) \equiv -\frac{GM}{\rho}$, with $G = G_N$, in order to obtain the corresponding Eddington-Robertson-Schiff parameters in Table (1.67).

1.6.3 SITS isotropic solution

It is well-known [30, 48] that an appropriate rescaling of the metric

$$g_{\mu\nu} \text{ SITS} \mapsto \frac{1}{\kappa} \left[1 - \frac{\kappa}{6} \phi^2 \right] g_{\mu\nu} \text{ SITS} = g_{\mu\nu} \text{ MTS} \quad (1.62)$$

together with a redefinition of the scalar field

$$\phi = \left(\frac{6}{\kappa} \right)^{\frac{1}{2}} \tanh \left[\left(\frac{\kappa}{6} \right)^{\frac{1}{2}} \Psi \right] \quad (1.63)$$

and $\kappa_{MTS} = \kappa_{SITS} = \kappa$, recast the gravitational part of the SITS action into the MTS form.

The SITS isotropic solution is thus easily recovered from the MTS isotropic solution (1.60), using (1.62) and noting that for both theories $G_{MTS} = G_{SITS} = G_N$ and $M_{MTS} = M_{SITS} = M$ is constant.

The expansion of the SITS isotropic solution in terms of the corresponding effective weak field gravitational potential, $V_{SITS}(\rho) \equiv -\frac{GM}{\rho}$, to recover the Eddington-Robertson-Schiff parameters in Table (1.67) is then trivial.

1.6.4 TS (or BD, STRINGS) isotropic solutions

The MTS solution for the metric is given by expressions (1.60) and (1.29), respectively in the isotropic and Schwarzschild coordinates, with G equal to the Newtonian constant.

If we compare the gravitational actions of the MTS (1.27) and the TS (Einstein frame) theories (1.16), we realize that

the TS solution in the Einstein frame ($\tilde{g}_{\mu\nu}$) is given by the same expressions as cited above when replacing

$$(g_{\mu\nu}, M, \kappa)|_{MTS} \mapsto (\tilde{g}_{\mu\nu}, \tilde{M}, \tilde{\kappa})|_{TS E}$$

and noting that

$$\Sigma = \sqrt{\frac{\kappa_{MTS}}{2}} \Psi. \quad (1.64)$$

In the TS case however, \tilde{G} is different from G_N as the coupling of matter to gravity is non-minimal ($A^2(\Sigma)$).

The TS solution in the Jordan frame ($g_{\mu\nu} = A^2(\Sigma) \tilde{g}_{\mu\nu}$) is now recovered thanks to the conformal transformation (1.15) applied on the solution in the Einstein frame ($\tilde{g}_{\mu\nu}$). The scalar coupling to matter ($G \neq G_N$) makes the search for the Eddington-Robertson-Schiff parameters in the Jordan frame somewhat less trivial though, as we shall show. In this case indeed, we first need to expand the conformal factor in isotropic coordinates:

$$\begin{aligned} \frac{A^2(\Sigma)}{A^2_0} &\equiv \frac{A^2(\Sigma)}{A^2(\Sigma_0)} \simeq 1 + \frac{1}{A_0^2} \left. \frac{\partial A^2}{\partial \Sigma} \right|_{\Sigma_0} (\Sigma - \Sigma_0) + \frac{1}{2A_0^2} \left. \frac{\partial^2 A^2}{\partial \Sigma^2} \right|_{\Sigma_0} (\Sigma - \Sigma_0)^2 + \frac{1}{6A_0^2} \left. \frac{\partial^3 A^2}{\partial \Sigma^3} \right|_{\Sigma_0} (\Sigma - \Sigma_0)^3 \\ &\simeq 1 + 2\alpha_{TS0} (\Sigma - \Sigma_0) + \left(2\alpha_{TS0}^2 + \alpha'_{TS0} \right) (\Sigma - \Sigma_0)^2 \\ &\quad + \frac{1}{3} \left(4\alpha_{TS0}^3 + 6\alpha_{TS0} \alpha'_{TS0} + \alpha''_{TS0} \right) (\Sigma - \Sigma_0)^3. \end{aligned}$$

In the above expression, Σ can be replaced using the expansion of the MTS solution for the scalar field in isotropic coordinates ($\Sigma = \sqrt{\frac{\kappa_{MTS}}{2}} \Psi$ together with (1.61)),

$$\Sigma \simeq \Sigma_0 + \frac{\sqrt{4-a^2}}{2} \left[\frac{2}{a} \left(-\frac{\tilde{G}\tilde{M}}{\rho c^2} \right) + \frac{2}{3a^3} \left(-\frac{\tilde{G}\tilde{M}}{\rho c^2} \right)^3 \right].$$

On the other side, the expansion of the MTS solution found for the scalar field in Schwarzschild coordinates ((1.64) together with (1.30)),

$$\Sigma \simeq \Sigma_0 + \frac{\sqrt{4-a^2}}{a} \left(-\frac{\tilde{G}\tilde{M}}{rc^2} \right),$$

can be compared to the solution of the Newtonian limit of the TS scalar-field equation (1.26) with (1.23),

$$\Sigma \simeq \Sigma_0 + \alpha_{TS0} \left(-\frac{\tilde{G}\tilde{M}}{rc^2} \right),$$

to yield a value for the integration constant a :

$$\frac{1}{a^2} = \frac{1}{4} (1 + \alpha_{TS0}^2). \quad (1.65)$$

The conformal factor

$$\begin{aligned} \frac{A^2(\Sigma)}{A^2_0} &\simeq 1 + 2\alpha_{TS0}^2 \left(-\frac{\tilde{G}\tilde{M}}{\rho c^2} \right) + \alpha_{TS0}^2 \left(2\alpha_{TS0}^2 + \alpha'_{TS0} \right) \left(-\frac{\tilde{G}\tilde{M}}{\rho c^2} \right)^2 \\ &\quad + \left[\frac{1}{3} \left(4\alpha_{TS0}^3 + 6\alpha_{TS0} \alpha'_{TS0} + \alpha''_{TS0} \right) \alpha_{TS0}^2 + \frac{1}{6} \alpha_{TS0}^2 (1 + \alpha_{TS0}^2) \right] \left(-\frac{\tilde{G}\tilde{M}}{\rho c^2} \right)^3 \end{aligned}$$

so obtained can be used to transform the expansion of the Einstein TS solution into the the Jordan one:

$$\begin{aligned} g_{tt} &\simeq \frac{A^2(\Sigma)}{A_0^2} \left\{ 1 + 2 \left(-\frac{\widetilde{GM}}{\rho c^2} \right) + 2 \left(-\frac{\widetilde{GM}}{\rho c^2} \right)^2 + \frac{2}{3} \left[2 + \frac{1}{4} (1 + \alpha_{TS0}^2) \right] \left(-\frac{\widetilde{GM}}{\rho c^2} \right)^3 \right\}, \\ -g_{\rho\rho} &\simeq \frac{A^2(\Sigma)}{A_0^2} \left\{ 1 - 2 \left(-\frac{\widetilde{GM}}{\rho c^2} \right) + 2 \left[1 - \frac{1}{4} (1 + \alpha_{TS0}^2) \right] \left(-\frac{\widetilde{GM}}{\rho c^2} \right)^2 \right\}. \end{aligned}$$

Nevertheless, as mentioned earlier in this section, in order to provide the Eddington-Robertson-Schiff parameters, the expansion has to be made in terms of the corresponding *effective weak field gravitational potential* in the Jordan frame (1.13), which can be rewritten, using (1.13), (1.15) and (1.18) as

$$V_{TS}(\rho_J) = - (1 + \alpha_{TS0}^2) \frac{(A_0^2 G) (A_0^{-1} M)}{(A_0 \rho_J)} = - (1 + \alpha_{TS0}^2) \frac{\widetilde{GM}}{\rho_E}.$$

According to this remark, we finally get the expansion of the Jordan metric providing the appropriate Eddington-Robertson-Schiff parameters listed in Table (1.67).

We remark that when applying this result to Strings ($\varpi = -1 \Leftrightarrow \alpha_{TS0} = 1$), we find the corresponding Eddington-Robertson-Schiff parameters for the String model with one massless scalar field. This could also be found when expanding the conformal factor particular to Strings (1.20) and rewriting the final expansion of the metric in terms of the appropriate effective weak field gravitational potential, $V_{STRINGS}(\rho_J) = -2 \frac{\widetilde{GM}}{\rho_E}$.

Notice that this method to obtain the (P)PN parameters for TS theories is faster than developing the total action or Lagrangian (as it is done by Damour *et al.* [38]). Indeed, to obtain the parameter β , one must go one order further in the linearized theory ($g_{\mu\nu} = \eta_{\mu\nu} + h_{\mu\nu}$) keeping the cubic terms of the total action ($I_{TS\ total\ J} = I_{TS\ gravitation\ J} + I_{TS\ matter\ J}$) in the slow motion limit.

1.6.5 Eddington-Robertson-Schiff parameters for selected theories

The Eddington-Robertson-Schiff parameters of the theories mentioned in this chapter can be read from Table (1.67), where

$$\begin{aligned} \alpha_{TS0} &= \alpha_{TS}(\Sigma_0), \\ \alpha'_{TS0} &= \partial\alpha_{TS}/\partial\Sigma|_{\Sigma_0}, \end{aligned} \tag{1.66}$$

and Σ_0 denotes the cosmologically determined value of the scalar field at present time, far away from the solar system.

The alternative theories selected here all verify the Weak Equivalence Principle (WEP) as $\alpha = 1$ for all those theories. Consequently, it is clear that the PN parameter γ will be the most important one when studying light deflection which is proportional to the combination $(\alpha + \gamma)$ at first order. Moreover, α is strongly constrained to 1 through the different tests of the Einstein Equivalence Principle (EEP) as described in the introduction, for any theory of gravitation. As far as the second order is concerned, we would like to emphasize here that there exists no general principle stating that Post-PN deviations from GR ($1 - \varepsilon$ and $1 - \delta$) must be smaller than any PN deviations from GR ($1 - \alpha$, $1 - \beta$ and $1 - \gamma$).

The MTS theory illustrates this, as deviation from GR only shows up at the Post-PN order, for any prediction in the weak field limit.

As far as light deflection is concerned (as well as time-delay experiments, or experiments involving only α and γ at first PN order), **the SITS theory** too only differs from GR at the Post-PN order.

We shall see in Section 3.2.1 that only the PPN parameter δ is involved in light deflection. In **Tensor Scalar theories of gravity (TS)**, of which BD and Strings are particular cases, this parameter can be rewritten as a combination of the PN parameters β and γ , as can be seen from Table (1.67). We remark also that in those theories, $1 - \gamma$ is always positive; the first order term in light deflection will thus always be weaker than in GR, see (3.1). On the contrary, $1 - \beta$ can have a priori either sign.

	PN:			Post- PN:	
	$1 - \alpha$	$1 - \beta$	$1 - \gamma$	$1 - \varepsilon$	$1 - \delta$
<i>MTS</i> : $a = 2\Upsilon \in]0; 2]$ $G = G_N$	0	0	0	$\frac{a^2-4}{9a^2}$	$-\frac{a^2-4}{3a^2}$
<i>SITS</i> : $a = 2\Upsilon \in]0; 2]$ $G = G_N$	0	$\frac{a^2-4}{6a^2}$	0	$+\frac{5(a^2-4)}{9a^2}$	$-\frac{a^2-4}{9a^2}$
<i>TS</i> <i>Jordan frame</i> : $a = 2/\sqrt{1 + \alpha_{TS0}^2}$ G	0	$-\frac{\alpha_{TS0}^2 \alpha'_{TS0}}{2(1+\alpha_{TS0}^2)^{3/2}}$	$\frac{2\alpha_{TS0}^2}{1+\alpha_{TS0}^2}$	$+\frac{\alpha_{TS0}^2}{9(1+\alpha_{TS0}^2)}$ $-\frac{4}{3} \frac{\alpha_{TS0}^2 \alpha_{TS0}}{(1+\alpha_{TS0}^2)^{3/2}}$ $-\frac{2}{9} \frac{\alpha_{TS0}^3}{(1+\alpha_{TS0}^2)^{3/2}}$	$+\frac{4}{3}(1-\beta) + \frac{15-8(1-\gamma)}{6}(1-\gamma)$
<i>STRINGS</i> <i>Jordan frame</i> : $a = \sqrt{2}$ \Downarrow $\alpha_{TS} = 1$ G	0	0	1	$\frac{1}{18}$	$\frac{7}{6}$
<i>GR</i> : $a = 2\Upsilon = 1$ \Downarrow $\alpha_{TS} = 0$ $G = G_N$	0	0	0	0	0

(1.67)

Chapter 2:

TS cosmological estimation of the PN parameter γ

In this chapter, we will exclusively concentrate on Tensor Scalar theories (TS) with one scalar field and time-dependent coupling. We will study a model of cosmological evolution in the Einstein frame. From the radiation-era cosmological equations, we will, naturally, derive a particular *exact* analytical solution to the matter dominated era, which admits General Relativity as an attractor. Evolving this solution leads to a prediction for the present value of γ , the Eddington-Robertson-Schiff (PN) parameter, fundamental to test light deflection. Furthermore, we will consider adding a cosmological constant to the theory in order to be in agreement with SNIa results, and see its influence on the predicted value of γ . In the last section of this chapter, our exact analytical solution and its predictions will be confronted with other evolutionary models proposed in the literature.

2.1 Cosmological equations

We shall write the equations for a spatially flat ($\tilde{\mathbf{k}} = \mathbf{0}$) or non spatially flat ($\tilde{\mathbf{k}} \neq \mathbf{0}$) metric. However, when looking for a particular class of solutions that admit GR as an attractor, we will only consider the flat case¹³.

2.1.1 Formulation in terms of the Hubble parameter

Consider a Robertson-Walker metric in the Einstein frame, in Schwarzschild-like coordinates,

$$\tilde{d}s^2 = c^2 d\tilde{t}^2 - \left[\frac{1}{1 - \tilde{\mathbf{k}}r^2/\tilde{\mathcal{R}}^2} dr^2 + r^2 d\Omega^2 \right], \quad (2.1)$$

for a perfect fluid with pressure \tilde{P}_m and matter¹⁴ density $\tilde{\varrho}_m$, with $\tilde{u}_\mu \tilde{u}^\mu = 1$ and $\tilde{u}^\mu \equiv \dot{x}^\mu \equiv \frac{dx^\mu}{cd\tilde{\tau}}$:

$$\tilde{T}_{\mu\nu m} = (\tilde{\varrho}_m c^2 + \tilde{P}_m) \tilde{u}_\mu \tilde{u}_\nu - \tilde{P}_m \tilde{g}_{\mu\nu} \quad \text{where } \tilde{\varrho}_m > 0. \quad (2.2)$$

In the Einstein frame, the field equations (1.21) and (1.22) with a cosmological constant read separately as

$$-3 \frac{\ddot{\tilde{\mathcal{R}}}}{c^2 \tilde{\mathcal{R}}} = +2 \frac{\dot{\tilde{\Sigma}}^2}{c^2} + \frac{\tilde{\kappa}}{2} \tilde{\varrho}_m c^2 (1 + 3\lambda_m) + \Lambda c^2,$$

¹³ The spatial curvature ($\tilde{\mathbf{k}}$) is written in bold, so that the corresponding terms can be easily removed to recover the flat universe case ($\tilde{\mathbf{k}} = 0$).

¹⁴ Massive particles plus radiation.

$$2 \left(\frac{\dot{\tilde{\mathfrak{R}}}}{c\tilde{\mathfrak{R}}} \right)^2 + \frac{\ddot{\tilde{\mathfrak{R}}}}{c^2\tilde{\mathfrak{R}}} + \frac{2\tilde{\mathbf{k}}}{\tilde{\mathfrak{R}}^2} = +\frac{\tilde{\kappa}}{2}\tilde{\varrho}_m c^2 (1 - \lambda_m) + \Lambda c^2,$$

$$\frac{\ddot{\tilde{\Sigma}}}{c^2} + 3\frac{\dot{\tilde{\mathfrak{R}}}}{c\tilde{\mathfrak{R}}}\frac{\dot{\tilde{\Sigma}}}{c} = -\alpha_{TS} (1 - 3\lambda_m) \frac{\tilde{\kappa}}{2}\tilde{\varrho}_m c^2,$$

for the temporal (first equation) or spatial (second equation) components of the metric field and for the scalar field (third equation), where

$$\begin{aligned} \Sigma &= \Sigma(t) \text{ is supposed to be spatially homogeneous,} \\ \dot{} &= \frac{d}{dt}, \end{aligned}$$

and the composition of the universe is encoded in the variable

$$\lambda_m \equiv \tilde{P}_m / (\tilde{\varrho}_m c^2) \in \left] \lambda_{m \text{ inf}} = -1; \lambda_{m r} = \frac{1}{3} \right]. \quad (2.3)$$

The notation $\lambda_{m \text{ inf}}$ corresponds to the inflation era and $\lambda_{m r}$ to the radiation era. The dust era is given by $\lambda_{m d} = 0$.

We can combine the first two equations to get rid of the $(\ddot{\tilde{\mathfrak{R}}}/\tilde{\mathfrak{R}})$ -term. Furthermore, if we use the Hubble parameter

$$\tilde{H} \equiv \tilde{H}(\tilde{t}) = \frac{\dot{\tilde{\mathfrak{R}}}}{\tilde{\mathfrak{R}}}, \quad (2.4)$$

the resulting cosmological equations are

$$\begin{aligned} -3\dot{\tilde{H}} - 3\tilde{H}^2 &= +2\dot{\tilde{\Sigma}}^2 + \left(\frac{1+3\lambda_m}{2}\right)\tilde{\kappa}\tilde{\varrho}_m c^4 - \Lambda c^4, \\ 3\tilde{H}^2 &= +\dot{\tilde{\Sigma}}^2 + \tilde{\kappa}\tilde{\varrho}_m c^4 - \frac{3\tilde{\mathbf{k}}c^2}{\tilde{\mathfrak{R}}^2} + \Lambda c^4, \\ \ddot{\tilde{\Sigma}} + 3\tilde{H}\dot{\tilde{\Sigma}} &= -\frac{1}{2}\alpha_{TS} (1 - 3\lambda_m)\tilde{\kappa}\tilde{\varrho}_m c^4. \end{aligned} \quad (2.5)$$

An equivalent system is

$$\begin{aligned} \dot{\tilde{H}} + 3\tilde{H}^2 + \frac{2\tilde{\mathbf{k}}c^2}{\tilde{\mathfrak{R}}^2} &= +\left(\frac{1-\lambda_m}{2}\right)\tilde{\kappa}\tilde{\varrho}_m c^4 + \Lambda c^4, \\ \dot{\tilde{H}} + \frac{3}{2}(1 + \lambda_m)\tilde{H}^2 &= -\left(\frac{1-\lambda_m}{2}\right)\dot{\tilde{\Sigma}}^2 - \frac{1}{2}(1 + 3\lambda_m)\frac{\tilde{\mathbf{k}}c^2}{\tilde{\mathfrak{R}}^2} + \frac{1}{2}(1 + \lambda_m)\Lambda c^4, \\ \dot{\tilde{\varrho}}_m + 3(1 + \lambda_m)\tilde{\varrho}_m\tilde{H} &= +\alpha_{TS} (1 - 3\lambda_m)\tilde{\varrho}_m\dot{\tilde{\Sigma}}, \end{aligned} \quad (2.6)$$

where the first equation stems from the spatial component of the metric-field equations, the second equation is the combination of the temporal and spatial components to get rid of the $(\tilde{\kappa}\tilde{\varrho}_m c^4)$ -term, while the last equation describes the non-conservation of the energy-momentum tensor.

Whichever of the systems we use, the three equations are coupled, non-linear functions of four unknowns: $\tilde{\varrho}_m$, α_{TS} or $A(\Sigma)$, Σ , and \tilde{H} . The system is thus a priori undetermined and one has to provide an additional constraint.

2.1.2 A notion of quintessence

We would like here to recall the notion of quintessence that will be useful in the following.

Quintessence models were historically introduced to provide some dynamical insight on the coincidence of the present matter density with the present density of the cosmological constant. Indeed, the two densities have a totally different evolution as a function of the scale factor $\tilde{\mathfrak{R}}$. However, if the present SNIa observations favor an accelerating universe

and hence a non null cosmological constant, they do not demonstrate that the cosmological “constant” is truly time-independent! The idea was thus to replace it by a cosmological scalar potential, and to endow the theory with some “tracker mechanism”: the cosmological-potential density tracks the matter density.

To make the connection with quintessence, we shall use the following notations.

For an action given by

$$\tilde{I}_{extended\ quintessence} = \int d^4x \sqrt{-\tilde{g}} \left[\frac{-1}{2\tilde{\kappa}} \left\{ \tilde{R} - 2 \tilde{g}_{\mu\nu} \Sigma^{\tilde{\mu}} \Sigma_{\tilde{\mu}} - \tilde{V}^*(\Sigma) \right\} + L_m(A^2(\Sigma) \tilde{g}_{\mu\nu}, \Psi_m) \right], \quad (2.7)$$

the equations of motion replacing system (2.5) would be

$$\begin{aligned} -3 \dot{\tilde{H}} - 3\tilde{H}^2 &= + \left(\frac{1+3\lambda_\Sigma}{2} \right) \tilde{\kappa} \tilde{\varrho}_\Sigma c^4 + \left(\frac{1+3\lambda_m}{2} \right) \tilde{\kappa} \tilde{\varrho}_m c^4, \\ 3\tilde{H}^2 &= + (\tilde{\varrho}_\Sigma + \tilde{\varrho}_m + \tilde{\varrho}_k) \tilde{\kappa} c^4, \\ \ddot{\Sigma} + 3\tilde{H} \dot{\Sigma} &= -\frac{1}{2} \frac{d\tilde{V}(\Sigma)}{d\Sigma} - \frac{1}{2} \frac{d\tilde{V}^*(\Sigma)}{d\Sigma}, \end{aligned}$$

where $\tilde{V}^*(\Sigma)$ is the quintessence potential that does not cancel when Σ is constant;
 $\frac{d\tilde{V}(\Sigma)}{d\Sigma} \equiv \alpha_{TS} (1 - 3\lambda_m) \tilde{\kappa} \tilde{\varrho}_m c^4$ vanishes when Σ is constant because it only contains derivatives of the scalar field;

$$\begin{aligned} \tilde{\varrho}_\Sigma &\equiv \frac{\dot{\Sigma}^2}{\tilde{\kappa} c^4} + \frac{\tilde{V}^*(\Sigma)}{\tilde{\kappa} c^4} \text{ is the scalar-field density;} \\ \tilde{P}_\Sigma &\equiv \frac{\dot{\Sigma}^2}{\tilde{\kappa} c^4} - \frac{\tilde{V}^*(\Sigma)}{\tilde{\kappa} c^4} \text{ is the pressure associated with the scalar field;} \\ \tilde{\varrho}_k &\equiv \frac{-3\mathbf{k}e^2}{\mathfrak{R}^2 \tilde{\kappa} c^4} \text{ is the curvature density.} \end{aligned}$$

Let us compare this action with the action $\tilde{I}_{TS\ E}$ (1.16) that we use in this section. In the case of $\tilde{I}_{TS\ E}$, we have a non trivial coupling to matter ($A^2(\Sigma) \neq 1$) with (1.15), but no quintessence potential, $\tilde{V}^*(\Sigma) = 0$. Consequently, the ratio of the scalar pressure to the scalar density is fixed: $\lambda_\Sigma \equiv \tilde{P}_\Sigma / (\tilde{\varrho}_\Sigma c^2) = +1$. On the contrary, for quintessence models, the coupling is usually trivial ($A^2(\Sigma) = 1$) in the corresponding action $\tilde{I}_{quintessence}$, which means that $\tilde{V}(\Sigma) = 0$, and a cosmological constant can be retrieved when $\lambda_\Sigma = -1$. Indeed, when the scalar field is constant, $\tilde{I}_{quintessence}$ is analog to

$$\tilde{I}_{GR+\Lambda} \equiv \int d^4x \sqrt{-\tilde{g}} \left[\frac{-1}{2\tilde{\kappa}} \left\{ \tilde{R} + 2\Lambda \right\} + L_m(\tilde{g}_{\mu\nu}, \Psi_m) \right]$$

because we can define a cosmological-constant contribution $\Lambda \equiv \tilde{V}^*(\Sigma_{est})$ and its associated density $\tilde{\varrho}_\Lambda \equiv \frac{\Lambda}{\tilde{\kappa}}$ to get $\lambda_\Lambda \equiv \tilde{P}_\Lambda / (\tilde{\varrho}_\Lambda c^2) = -1$.

We thus see that the scalar field can never play the role of a cosmological constant in our cosmological model deriving from $\tilde{I}_{TS\ E}$.

2.2 The case of a null cosmological constant

To particularize the preceding equations to a null cosmological constant, we will alternatively choose different sets of variables to express the cosmological equations. This will enlighten us on the different characteristics of the type of cosmological solutions we are looking for, namely, models that admit General Relativity as an attractor and will pass solar system tests of gravitation at least as successfully as GR does so far.

2.2.1 Conditions for an attractor mechanism towards GR

To discuss whether a TS cosmological model converges towards General Relativity, it is interesting to write the cosmological equations in terms of a set of new variables $x(\tilde{t})$ and $\vartheta(\tilde{t})$.

A/ Definition of new variables

It has been shown by Gérard and Mahara [58, 59] that it is possible, with an adequate change of variables, to solve the second formulation of the cosmological equations (2.6) by quadrature, in terms of one simple arbitrary function. Indeed, let us replace

$$\tilde{H}(\tilde{t}) \equiv \frac{1}{x(\tilde{t})} \quad \text{with } x(\tilde{t}) \neq 0 \quad (2.8)$$

in the second system of equations (2.6). We find

$$\begin{aligned} \dot{\tilde{x}} - 3 + \frac{(1 - \lambda_m)}{2} \tilde{\kappa} \tilde{\varrho}_m c^4 x^2 - \frac{2\tilde{\mathbf{k}}c^2}{\tilde{\mathfrak{R}}^2} x^2 &= 0, \\ \dot{\tilde{x}} - \frac{3}{2}(1 + \lambda_m) - \frac{(1 - \lambda_m)}{2} \frac{\dot{\tilde{\Sigma}}^2}{\tilde{\Sigma}} x^2 - \frac{(1 + 3\lambda_m)\tilde{\mathbf{k}}c^2}{2\tilde{\mathfrak{R}}^2} x^2 &= 0, \\ \dot{\tilde{\varrho}}_m + 3(1 + \lambda_m)\tilde{\varrho}_m \frac{1}{x} &= \alpha_{TS}(1 - 3\lambda_m)\tilde{\varrho}_m \frac{\dot{\tilde{\Sigma}}}{\tilde{\Sigma}}. \end{aligned}$$

Comparing the first two equations, we obtain

$$\frac{\tilde{\kappa}\tilde{\varrho}_m c^4}{3} x^2 + \frac{1}{3} \frac{\dot{\tilde{\Sigma}}^2}{\tilde{\Sigma}} x^2 - \frac{\tilde{\mathbf{k}}c^2}{\tilde{\mathfrak{R}}^2} x^2 = 1.$$

When $\tilde{\mathbf{k}} = 0$, this last equation and the fact that the matter density is always positive make it possible to define a new variable $\vartheta(\tilde{t})$ [58]:

$$\begin{aligned} \frac{\dot{\tilde{\Sigma}}}{\tilde{\Sigma}} x &= \sqrt{3} \sin \vartheta, \\ \tilde{\kappa}\tilde{\varrho}_m c^4 x^2 &= 3 \cos^2 \vartheta, \end{aligned} \quad (2.9)$$

and thus the system nicely reduces to

$$\begin{aligned} \dot{\tilde{x}} &= \frac{3}{2}(1 + \lambda_m) + \frac{3}{2}(1 - \lambda_m) \sin^2 \vartheta, \\ \dot{\tilde{\varrho}}_m + 3(1 + \lambda_m)\tilde{\varrho}_m \frac{1}{x} &= \alpha_{TS}(1 - 3\lambda_m)\tilde{\varrho}_m \frac{\dot{\tilde{\Sigma}}}{\tilde{\Sigma}}. \end{aligned} \quad (2.10)$$

When $\tilde{\mathbf{k}} \neq 0$, or later, when we shall study the role of a cosmological constant, this change in the variables does not seem to be wise. It is then more appropriate and natural to rewrite the equations in terms of densities (see Section 2.2.3).

B/ About the general solution when $\tilde{\mathbf{k}} = 0$:

Let us now recall the general features of flat TS cosmologies analyzed in [58].

In the case of General Relativity, we have $\Sigma \equiv \Sigma_{cst}$, which implies in equation (2.9) that $\vartheta_{GR} = n\pi$, where n is an integer.

When excluding the case of General Relativity with $\lambda_m = -1$, the solutions $x(\tilde{t})$ are monotonous for $\lambda_m \in [-1, \frac{1}{3}]$, since $\dot{\tilde{x}} > 0$ for all \tilde{t} . Then, the function $x(\tilde{t})$ only goes at most once through zero, let us say at a time called \tilde{t}^* . If $\vartheta(\tilde{t})$ is defined on the interval $[\tilde{t}_1, \tilde{t}_2]$ containing \tilde{t}^* with $\tilde{t}^* \neq \tilde{t}_1$ and $\tilde{t}^* \neq \tilde{t}_2$, we can consider two separate intervals $[\tilde{t}_1, \tilde{t}^*]$ [and] $[\tilde{t}^*, \tilde{t}_2]$, so that we have two solutions for $x(\tilde{t})$, one on each interval, one positive and one negative. Equally, because of the definition of $x(\tilde{t})$ given by (2.8), we get two solutions for $\tilde{H}(\tilde{t})$, one on each interval. The function $\vartheta(\tilde{t})$ being arbitrary, the cosmological solutions $(\tilde{\varrho}_m, \alpha_{TS}$ or $A(\Sigma), \Sigma, \tilde{H})$ are thus defined only on a finite interval of time.

We can write the general solution for $x(\tilde{t})$ as expressed in reference [58],

$$x(\tilde{t}) = \frac{3}{2}(1 + \lambda_m)\tilde{t} + \frac{3}{2}(1 - \lambda_m) \int_0^{\tilde{t}} \sin^2 \vartheta(\iota) d\iota \quad \text{for all } \tilde{t} > 0, \quad (2.11)$$

with $x(\tilde{t}) \in \left[x_{\min} = \frac{3}{2}(1 + \lambda_m)\tilde{t}, x_{\max} = 3\tilde{t} \right],$

where the minimum and the maximum are reached when $\vartheta = \vartheta_{GR} = n\pi$ and $\vartheta = (2n + 1)\pi/2$, respectively. Once $x(\tilde{t})$ is known, we can recover $\tilde{\varrho}_m$ from the second equation of (2.9), α_{TS} or $A(\Sigma)$ using (1.7) and the third equation of (2.10), $\Sigma(\tilde{t})$ by the first equation of (2.9), and finally \tilde{H} by (2.8).

To analyze the asymptotic behavior (when $\tilde{t} \rightarrow +\infty$) of the solutions for the tensor scalar theories, we need to assume that the function $\vartheta(\tilde{t})$ exists on the whole real time axis. To do so, we shall translate the different time intervals where $\vartheta(\tilde{t})$ exists. And if $\vartheta(\tilde{t})$ is well defined, so is $x(\tilde{t})$ too.

When the time variable goes to infinity, we see from (2.11) and the first equation of (2.9) that the time derivative of the scalar field tends to zero. However, it does not mean that all the cosmological solutions to Tensor Scalar theories admit General Relativity as an attractor [58, 41 page 2218 for some counter-examples]. In fact, GR is defined by $\Sigma_{GR} = \Sigma_{cst}$ and $\alpha_{GR} = 0$ (which means no coupling of the scalar field to matter fields) at any time, that is to say, $A(\Sigma)_{GR} = cst \neq 0$. So, in order to select cosmological solutions to Tensor Scalar theories that admit General Relativity as an attractor, we must first integrate the second equation of (2.10) to find α_{TS} and then $A(\Sigma)$ using (1.7). Secondly, we shall verify that $A(\Sigma) \rightarrow cst \neq 0$ when $\tilde{t} \rightarrow +\infty$.

C/ A general equation when $\tilde{\mathbf{k}} = \mathbf{0}$:

It is possible to obtain a general equation for $x(\tilde{t})$ and $\vartheta(\tilde{t})$ only [58]. Let us replace the time derivative of the scalar field from the first equation of (2.9) as well as the matter density and its time derivative from the second equation of (2.9) into the second equation of (2.10). After some simplification, we find

$$\sqrt{3} \left[\frac{2}{3} \frac{\dot{\vartheta} x}{\cos \vartheta} + (1 - \lambda_m) \sin \vartheta \right] = -(1 - 3\lambda_m) \alpha_{TS}(\Sigma) \quad \text{for all } \lambda_m, \text{ when } \tilde{\mathbf{k}} = \mathbf{0}. \quad (2.12)$$

This key equation will be used later in analogy with a mechanical oscillator in terms of other variables.

D/ Discussion of the asymptotic behavior of the solutions when $\tilde{\mathbf{k}} = \mathbf{0}$:

Equation (1.7) can be rewritten as

$$\frac{\dot{A}}{A} = \alpha_{TS} \dot{\Sigma},$$

in which we can substitute $\dot{\Sigma}$ from the first equation of (2.9), and then α_{TS} from (2.12) in order to integrate $A(\tilde{t})$:

$$\begin{aligned} \frac{1}{A(\tilde{t})} \frac{dA}{dt} &= -\frac{\sqrt{3}}{(1-3\lambda_m)} \frac{\sqrt{3} \sin \vartheta}{x} \left[\frac{2}{3} \frac{\dot{\vartheta} x}{\cos \vartheta} + (1 - \lambda_m) \sin \vartheta \right] \\ \Leftrightarrow \frac{A(\tilde{t})^{(1-3\lambda_m)}}{\cos^2 \vartheta(\tilde{t})} &= \frac{A_{eq}^{(1-3\lambda_m)}}{\cos^2 \vartheta_{eq}} \exp \left[-3(1 - \lambda_m) \int_{\tilde{t}_{eq}}^{\tilde{t}} \frac{\sin^2 \vartheta(\iota)}{x(\iota)} d\iota \right] \quad \text{for all } \tilde{t} \text{ and } \lambda_m \quad \text{when } \tilde{\mathbf{k}} = \mathbf{0}. \quad (2.13) \end{aligned}$$

We have set the integration constant by imposing $A(\tilde{t}^*) \equiv A_{eq}$, $\vartheta(\tilde{t}^*) \equiv \vartheta_{eq}$ and $x(\tilde{t}^*) = 0$ at the equilibrium time $\tilde{t}_{eq} = \tilde{t}^*$, where \tilde{t}_{eq} , the end of the radiation era, corresponds to $\tilde{\varrho}_{rad} = \tilde{\varrho}_{dust}$.

Taking the limit $\tilde{t} \rightarrow +\infty$ in this last expression, we have that $x(\tilde{t}) \geq x(\tilde{t})_{\min} \rightarrow +\infty$ while $\sin^2 \vartheta$ is bounded. Accordingly, the convergence of expression (2.13) only depends on the behavior of the integral for $\lambda_m < 1$, while it is necessarily convergent for $\lambda_m = 1$. Studying equation (2.13), we can summarize the asymptotic cosmological

behavior of TS theories as follows [58]:

$$\begin{array}{l}
 \int_{\tilde{t}_{eq}}^{\tilde{t}} \frac{\sin^2 \vartheta(t)}{x(t)} dt \text{ is convergent when } \tilde{t} \rightarrow \infty \Rightarrow \vartheta(\tilde{t}) \xrightarrow{\tilde{t} \rightarrow \infty} n\pi \\
 \lambda_m = 1 \Rightarrow A(\tilde{t}) \xrightarrow{\tilde{t} \rightarrow \infty} A_{eq} \frac{\cos \vartheta_{eq}}{\cos \vartheta(t=\infty)} = cst \Rightarrow \text{GR is an attractor} \\
 \left\{ \begin{array}{l} \lambda_m \neq 1 \\ \int_{\tilde{t}_{eq}}^{\tilde{t}} \frac{\sin^2 \vartheta(t)}{x(t)} dt \text{ is convergent when } \tilde{t} \rightarrow \infty \end{array} \right\} \Rightarrow A(\tilde{t}) \xrightarrow{\tilde{t} \rightarrow \infty} cst \Rightarrow \text{GR is an attractor} \\
 \left\{ \begin{array}{l} \lambda_m \neq 1 \\ \int_{\tilde{t}_{eq}}^{\tilde{t}} \frac{\sin^2 \vartheta(t)}{x(t)} dt \text{ is divergent when } \tilde{t} \rightarrow \infty \end{array} \right\} \Rightarrow \begin{cases} \lambda_m = 1/3 : & A(\tilde{t}) \text{ is not determined} \\ \lambda_m > 1/3 : & A(\tilde{t}) \xrightarrow{\tilde{t} \rightarrow \infty} \infty \Rightarrow \text{GR is not an attractor} \\ \lambda_m < 1/3 : & A(\tilde{t}) \xrightarrow{\tilde{t} \rightarrow \infty} 0 \Rightarrow \text{GR is not an attractor} \end{cases}
 \end{array}$$

Thus, we see that GR acting as an attractor is not a generic case.

2.2.2 Solutions that admit GR as an attractor

Once we wish to characterize solutions that admit GR as an attractor and study their evolution, shifting to another set of variables $(\tilde{\Sigma}(\tilde{t}), \tilde{\mathfrak{R}}(\tilde{t}))$ seems appropriate. Indeed, we should not forget our aim: to evolve a particular solution of this class, from time \tilde{t} to present time \tilde{t}_0 , in order to obtain an estimate for the present value of the PN parameter γ . This γ is linked to the Brans-Dicke parameter $\varpi(\tilde{t})$, which itself can be rewritten in terms of the coupling $\alpha_{TS}(\tilde{t})$. We thus need to find an evolution equation for $\alpha_{TS}(\tilde{t})$, which can depend on the time evolution of the scalar field.

A/ Definition of the cosmological parameter

The cosmological parameter $\tilde{p}(\tilde{t})$ [41] will be an alternative to the time variable, \tilde{t} :

$$\tilde{p}(\tilde{t}) = \ln \tilde{\mathfrak{R}}(\tilde{t}) + cst_1 \quad \text{and } \tilde{p}_{eq} = 0 \text{ at the end of the radiation era.} \quad (2.14)$$

We can choose to set the value of the cosmological parameter at equilibrium time to zero, as it only consists in a choice for the origin on the ladder of time. Moreover, we shall impose $cst_1 \equiv 0$, which is equivalent to say that $\tilde{\mathfrak{R}}_{eq}$ is scaled to the reference value of 1.

Noting $\dot{\tilde{p}} \equiv \frac{d}{d\tilde{p}}$, we rewrite the equation system for cosmological evolution (2.5) as

$$\begin{aligned}
 -3 \dot{\tilde{H}} - 3\tilde{H}^2 &= +2\tilde{H}^2 \tilde{\Sigma}'^2 + \left(\frac{1+3\lambda_m}{2}\right) \tilde{\kappa} \tilde{\varrho}_m c^4, \\
 3\tilde{H}^2 + \frac{3\tilde{\kappa} c^2}{\tilde{\mathfrak{R}}^2} &= +\tilde{H}^2 \tilde{\Sigma}'^2 + \tilde{\kappa} \tilde{\varrho}_m c^4, \\
 \tilde{H}^2 \tilde{\Sigma}' + \dot{\tilde{H}} \tilde{\Sigma}' + 3\tilde{H}^2 \tilde{\Sigma}' &= -\alpha_{TS} \left(\frac{1-3\lambda_m}{2}\right) \tilde{\kappa} \tilde{\varrho}_m c^4.
 \end{aligned} \quad (2.15)$$

B/ The mechanical oscillator equation

Remember that we are aiming at an equation for $(\alpha_{TS}, \tilde{\Sigma})$. To achieve this, we isolate the time derivative of the Hubble parameter in system (2.15) by combining the first and the second equation,

$$\dot{\tilde{H}} = \frac{-\frac{1}{3} \left[-\frac{3\tilde{\kappa} c^2}{\tilde{\mathfrak{R}}^2} \left(3 + 2\tilde{\Sigma}'^2\right) + \tilde{\kappa} \tilde{\varrho}_m c^4 \left(\frac{1+3\lambda_m}{2}\right) \left(3 - \tilde{\Sigma}'^2\right) + \tilde{\kappa} \tilde{\varrho}_m c^4 \left(3 + 2\tilde{\Sigma}'^2\right) \right]}{\left(3 - \tilde{\Sigma}'^2\right)},$$

and the Hubble parameter itself from the second equation of (2.15),

$$\tilde{H}^2 = \frac{\tilde{\kappa} \tilde{\varrho}_m c^4 - \frac{3\tilde{\kappa} c^2}{\tilde{\mathfrak{R}}^2}}{\left(3 - \tilde{\Sigma}'^2\right)},$$

finally to replace those expressions in the third equation.

We can make an analogy between the expression obtained for $(\Sigma^{\tilde{t}}, \Sigma^{\tilde{r}}, \alpha_{TS})$ and the equation of an oscillator in point mechanics:

$\frac{\frac{2}{3} \left[1 - \frac{3\tilde{\mathbf{k}}}{\tilde{\mathcal{R}}^2 \tilde{\kappa} \tilde{\varrho}_m c^2} \right]}{\left[1 - \Sigma^{\tilde{r}2}/3 \right]}$	$\Sigma^{\tilde{r}}$	$+$	$\left[\frac{4\tilde{\mathbf{k}}}{\tilde{\mathcal{R}}^2 \tilde{\kappa} \tilde{\varrho}_m c^2} + (1 - \lambda_m) \right]$	$\Sigma^{\tilde{r}}$	$=$	$\underbrace{-(1 - 3\lambda_m)}_{\substack{\text{forcing coefficient} \\ \text{depending on } \lambda_m}}$	$\alpha_{TS}(\Sigma)$
\downarrow	\downarrow		\downarrow	\downarrow		\downarrow	
<p>mass $m(\Sigma^{\tilde{r}})$ depending on the speed $\Sigma^{\tilde{r}}$ plus, when $\tilde{\mathbf{k}} \neq \mathbf{0}$, on the curvature \tilde{k}, the gravitational constant via $\tilde{\kappa}$ and the density $\tilde{\varrho}_m$.</p>	<p>a c c e l e r a t i o n</p>		<p>viscosity coefficient depending on λ_m plus when $\tilde{\mathbf{k}} \neq \mathbf{0}$, on the curvature \tilde{k}, the gravitational constant via $\tilde{\kappa}$ and the density $\tilde{\varrho}_m$.</p>	<p>v e l o c i t y</p>		<p>e x t e r n a l f o r c e</p>	<p>(2.16)</p>
<p>with $\Sigma(\tilde{p})$ the “displacement”.</p>							

Let us now discuss this equation.

When $\tilde{\mathbf{k}} = \mathbf{0}$, we recover the expression given in reference [41]. We notice that this “mechanical oscillator equation” for the scalar field, is exactly equation (2.12) expressed in terms of the variables $(\Sigma(\tilde{\mathbf{t}}), \tilde{\mathbf{p}}(\tilde{\mathbf{t}}))$ instead of $(\vartheta(\tilde{\mathbf{t}}), \mathbf{x}(\tilde{\mathbf{t}}))$. We also see that the coupling of $\Sigma^{\tilde{r}}$ to matter ($\tilde{\varrho}_m$) interestingly disappears in the particular case of flat cosmology.

Whichever the value of $\tilde{\mathbf{k}}$ is, the “mass” depends on the velocity, which makes it difficult to find exact solutions except for some special values of λ_m . Moreover, the “mass” reaches an infinite value when $\Sigma^{\tilde{r}2} \rightarrow 3$.

We also remark that the force term derives from a potential because of the relation between the scalar coupling and the conformal factor (1.15):

$$\begin{aligned} \tilde{F}(\Sigma) &= -\frac{d\tilde{V}}{d\Sigma} \equiv -(1 - 3\lambda_m) \alpha_{TS}(\Sigma) \\ \Leftrightarrow \tilde{V}(\Sigma) &\equiv +(1 - 3\lambda_m) \ln A(\Sigma). \end{aligned} \tag{2.17}$$

Since $\lambda_m \in]-1, 1/3[$, the forcing coefficient, $-(1 - 3\lambda_m)$, is always negative; hence, the corresponding contribution is a damping term. We thus distinguish between two cases:

$$\begin{aligned} \text{if } A(\tilde{t}) \xrightarrow{\tilde{t} \rightarrow \infty} cst \neq 0, & \quad \text{then } \tilde{V}(\Sigma) \rightarrow \tilde{V}_{\min} \text{ because } \frac{d\tilde{V}}{d\Sigma} = +(1 - 3\lambda_m) \frac{1}{A} \frac{dA(\Sigma)}{d\Sigma}, \\ \text{if } A(\tilde{t}) \xrightarrow{\tilde{t} \rightarrow \infty} 0, & \quad \text{then } \tilde{V}(\Sigma) \text{ is unbounded from below,} \\ & \quad \text{there is no asymptotical minimum to the potential.} \end{aligned} \tag{2.18}$$

These considerations about the existence of a minimum to the potential are primordial to us, because we are looking for particular solutions to the cosmological equations that admits GR as an attractor. Indeed, we see that this particular class of solutions (see conditions given in Section 2.2.1) automatically drives the scalar field to the minimum of its potential. This corresponds to a decrease of the coupling $\alpha_{TS}(\tilde{t}) \xrightarrow{\tilde{t} \rightarrow +\infty} \alpha_{GR} \equiv 0$.

2.2.3 A confrontation with SNIa results

To discuss the cosmological characteristics of Tensor Scalar theories with one scalar field, no cosmological constant and a non constant coupling, we can rewrite the cosmological equations in terms of the usual density variables $\tilde{\Omega}_m(\tilde{t})$, $\tilde{\Omega}_\Sigma(\tilde{t})$ and $\tilde{\Omega}_k(\tilde{t})$.

A/ Definition of the density variables and notion of quintessence

Remembering Einstein's critical universe, with the critical density $\tilde{\varrho}_c \equiv \frac{3\tilde{H}^2}{8\pi G}$ required to close the universe, the matter-density parameter is defined as

$$\tilde{\Omega}_m \equiv \tilde{\Omega}_{dust} + \tilde{\Omega}_{rad} \equiv \frac{\tilde{\varrho}_m}{\tilde{\varrho}_c} = \frac{8\pi G \tilde{\varrho}_m}{3\tilde{H}^2}, \quad (2.19)$$

which is always positive as $\tilde{\varrho}_m > 0$ for all \tilde{t} . This density contains both the density of massive and nonmassive particles, namely the so-called dust matter and radiation.

By analogy with the matter density, we define the scalar-field density

$$\tilde{\Omega}_\Sigma \equiv \frac{\dot{\tilde{\Sigma}}^2}{3\tilde{H}^2} = \frac{\tilde{\Sigma}^{\dot{\gamma}2}}{3}, \quad (2.20)$$

which is always positive. We remind the reader that, when the scalar field is constant, we do not recover a cosmological constant ($\tilde{\Omega}_{\Sigma cst} \neq \tilde{\Omega}_\Lambda$).

As usual, the curvature-density parameter is given by

$$\tilde{\Omega}_k \equiv \frac{-\tilde{\mathbf{k}}c^2}{\tilde{\mathfrak{R}}^2 \tilde{H}^2}. \quad (2.21)$$

When expressing the second equation of the cosmological system for evolution (2.5) in terms of densities, we obtain the usual equation:

$$1 = \tilde{\Omega}_\Sigma + \tilde{\Omega}_m + \tilde{\Omega}_k \quad \text{for all } \tilde{t}. \quad (2.22)$$

Finally, the deceleration parameter is also often used,

$$\tilde{q} \equiv -\frac{\dot{\tilde{H}}}{\tilde{H}^2} - 1, \quad (2.23)$$

and it indicates either an accelerated ($\tilde{q} < 0$), decelerated ($\tilde{q} > 0$), or constantly expanding universe ($\tilde{q} = 0$).

B/ Link to the previous variables

The density variables that we just introduced can be easily connected to the variables $x(\tilde{t})$, $\vartheta(\tilde{t})$ described earlier. First notice that, according to (2.8),

$$\dot{x} = 1 + \tilde{q}.$$

When $\tilde{\mathbf{k}} = 0$, we see why the variables $\vartheta(\tilde{t})$ and $x(\tilde{t})$ are natural. The first equation of (2.9) leads us to

$$\tilde{\Omega}_\Sigma = \sin^2 \vartheta, \quad (2.24)$$

which lies within the range $[0, 1]$; while the second equation gives

$$\tilde{\Omega}_m = \cos^2 \vartheta \quad (2.25)$$

which is bounded in a likewise manner. Equation (2.22) is then naturally recovered.

Also, the first equation of system (2.10) given in terms of $x(\tilde{t})$ and $\vartheta(\tilde{t})$ can be reformulated in an interesting way:

$$\begin{aligned} \tilde{q} &= \frac{1}{2} (1 + 3\lambda_m) \left(1 - \tilde{\Omega}_k\right) + \frac{3}{2} (1 - \lambda_m) \tilde{\Omega}_\Sigma \quad \text{for all } \tilde{t} \\ \stackrel{(2.22)}{\Leftrightarrow} \tilde{q} &= \frac{1}{2} (1 + 3\lambda_m) \tilde{\Omega}_m + \frac{1}{2} (1 + 3\lambda_\Sigma) \tilde{\Omega}_\Sigma \quad \text{with } \lambda_\Sigma = +1. \end{aligned} \quad (2.26)$$

As a consequence, using equations (2.26), (2.24) and (2.25), we are led to the following constraint

$$\frac{1}{2} (1 + 3\lambda_m) \leq \tilde{q} \leq 2.$$

The best model for our present-time (\tilde{t}_0) universe is the dust model ($\lambda_m = 0$) with $\tilde{k} = 0$, an hypothesis strongly encouraged by experiments like BOOMERANG, favoring flat cosmologies. However, in our model, this type of universe is characterized by a constraint in conflict with the supernovae predictions which favor an accelerating universe, that is, they tend to predict $\tilde{q}_0 \equiv \tilde{q}(\tilde{t}_0) < 0$.

And even if we consider $\tilde{k} \neq 0$, the predictions of our model given by (2.26) with $\lambda_m = 0$ still lead to a positive present value of \tilde{q} , in disagreement with the supernovae experiments.

A solution to this problem might be to add artificially a cosmological constant Λ to the action in the Einstein frame,

$$\tilde{I}_{TS E + \Lambda} = \int dx^{(4)} \sqrt{-\tilde{g}} \left[\frac{-1}{2\tilde{\kappa}} \left\{ \tilde{R} - 2 \Sigma^{\tilde{\mu}} \Sigma_{\tilde{\mu}} + 2\Lambda \right\} + L_m(A^2(\Sigma) \tilde{g}_{\mu\nu}, \Psi_m) \right],$$

or alternatively, to add a potential $\tilde{V}^*(\Sigma)$ which would not cancel as Σ tends towards a constant, but would provide a dynamical “cosmological constant” like in quintessence models. This type of model (2.7) is often called “extended quintessence” and is usually expressed in the Jordan frame:

$$I_{extended \ quintessence} = \int dx^{(4)} \sqrt{-g} \left[\frac{-1}{2\kappa} \left\{ R - \frac{\varpi(\Sigma)}{\Phi^2} \Phi^{|\mu} \Phi_{|\mu} - V^*(\Phi) \right\} + L_m(g_{\mu\nu}, \Psi_m) \right].$$

The density variables can also be used to provide further insight on the “mechanical oscillator” analogy. Inserting the density variables into the “mechanical oscillator equation” (2.16), we find

$$\frac{\frac{2}{3} \left[1 + \frac{\tilde{\Omega}_k}{\tilde{\Omega}_m} \right]}{\left[1 - \tilde{\Omega}_\Sigma \right]} \Sigma^{\tilde{\eta}} + \left[\frac{4}{3} \frac{\tilde{\Omega}_k}{\tilde{\Omega}_m} + (1 - \lambda_m) \right] \Sigma^{\tilde{\gamma}} = -(1 - 3\lambda_m) \alpha_{TS}(\Sigma).$$

When $\tilde{k} = 0$, we see that the “mass” tends towards infinity as $\tilde{\Omega}_\Sigma \rightarrow 1$ (which corresponds to $\tilde{\Sigma}^{\tilde{\eta}2} \rightarrow 3$, in terms of the variables $\tilde{p}(\tilde{t})$ and $\Sigma(\tilde{t})$). However, if we use the additional constraint provided by (2.22) and the definitions (2.19) and (2.20), we see that $\tilde{\Omega}_\Sigma$ can never reach this critical value of 1. Hence, the mass is always finite for $\tilde{k} = 0$.

When $\tilde{k} \neq 0$, in the preceding “mechanical oscillator equation”, it is not straightforward to interpret the factor in front of $\Sigma^{\tilde{\eta}}$ as a mass. What is its sign? Is it divergent or not? This seems to depend on the sign and value of \tilde{k} . So, using (2.22), we prefer to rewrite the “mechanical oscillator equation” as

$$\boxed{\frac{\frac{2}{3}}{\tilde{\Omega}_m} \Sigma^{\tilde{\eta}} + \left[\frac{4}{3} \frac{\tilde{\Omega}_k}{\tilde{\Omega}_m} + (1 - \lambda_m) \right] \Sigma^{\tilde{\gamma}} = -(1 - 3\lambda_m) \alpha_{TS}(\Sigma)}. \quad (2.27)$$

Now we clearly see that the mass term is always positive (as $\tilde{\Omega}_m$ always is) and that its evolution with time follows the inverse evolution of the matter density¹⁵. Moreover, we realize that we have to be more cautious about our interpretation of the second term of the equation as a viscous contribution that slows down the motion. Indeed, we

¹⁵ It is easier to think about a “mass” varying with the inverse of the matter density in time, than to think of a mass that varies with the velocity $\tilde{\Sigma}^{\tilde{\eta}}$! Indeed, in an expanding universe, the matter will dilute in the volume, so that the matter density will correspondingly decrease and the mechanical oscillator will become more and more inertial.

have to distinguish two situations according to the sign and value of $\frac{\tilde{\Omega}_k}{\tilde{\Omega}_m}$:

- if $\frac{\tilde{\Omega}_k}{\tilde{\Omega}_m} > -\frac{3}{4}(1 - \lambda_m)$ then the second term is the usual viscous coefficient (slowing down the motion),
 if $\frac{\tilde{\Omega}_k}{\tilde{\Omega}_m} < -\frac{3}{4}(1 - \lambda_m)$ then the second term is a force proportional to the speed (accelerating the motion).

However, $-\frac{3}{4}(1 - \lambda_m) \in]-\frac{3}{2}, -\frac{1}{2}]$ owing to the range of values for λ_m given by (2.3). Thus in the case of a flat or negative curvature universe ($\tilde{k} \leq 0$), we always have a viscous coefficient slowing down the motion. What happens for positive curvature universes depends on the relative amount of curvature and matter densities.

In the following sections, we will restrict ourselves to a flat universe and look for a particular exact analytical solution to the cosmological equations that admits GR as an attractor.

2.2.4 Solutions in a flat radiation universe

In a radiation universe, $\lambda_m = 1/3$ and thus $\tilde{Q}_m \equiv \tilde{Q}_{m,r}$, where the subscript “ r ” stands for the radiation era. We choose here to work with the variables $\Sigma_r(\tilde{t})$ and $p_r(\tilde{t})$, following Damour and Nordtvedt [42], but one could alternatively work with the equations in terms of $x_r(\tilde{t})$ and $\vartheta_r(\tilde{t})$.

During the radiation era, the “mechanical oscillator equation” (2.16) simply reads

$$\frac{1}{[1 - \Sigma_r^2/3]} \Sigma_r'' + \Sigma_r' = 0. \quad (2.28)$$

Thus, for purely radiative matter, the coupling α_{TS} disappears from the Einstein frame equations (2.15) and from the “mechanical oscillator equation” (2.28). We have no constraint on the coupling.

We simply integrate to find

$$\Sigma_r'(\tilde{p}) = \sqrt{3} \frac{\text{sg}(\Sigma_{eq}^{\tilde{r}}) \text{cst}_3 e^{-\tilde{p}}}{\sqrt{1 + \text{cst}_3^2 e^{-2\tilde{p}}}} \quad \text{with } \text{sg}(\Sigma_{eq}^{\tilde{r}}) \equiv \text{the sign of } \Sigma_{eq}^{\tilde{r}}, \quad (2.29)$$

in which we express cst_3 , chosen to be positive, by taking the above expression at $\tilde{p} = 0 \equiv \tilde{p}_{eq}$:

$$\text{cst}_3 \equiv \frac{\text{sg}(\Sigma_{eq}^{\tilde{r}}) \Sigma_{eq}^{\tilde{r}}}{\sqrt{3 - \Sigma_{eq}^2}} \quad \text{with } \Sigma_{eq}^{\tilde{r}} = \Sigma^{\tilde{r}}(\tilde{p} = 0). \quad (2.30)$$

A second integration of the “mechanical oscillator equation” with respect to \tilde{p} gives

$$\Sigma_r(\tilde{p}) = -\sqrt{3} \text{sg}(\Sigma_{eq}^{\tilde{r}}) \text{arcsinh} \left(\text{cst}_3 e^{-\tilde{p}} \right) + \text{cst}.$$

The integration constant is obtained by taking this expression¹⁶ at $\tilde{p} = 0 \equiv \tilde{p}_{eq}$:

$$\begin{aligned} \Sigma_r(\tilde{p}) - \Sigma_{eq} &= -\sqrt{3} \text{sg}(\Sigma_{eq}^{\tilde{r}}) \left[\text{arcsinh} \left(\text{cst}_3 e^{-\tilde{p}} \right) - \text{arcsinh} \left(\text{cst}_3 \right) \right] \quad \text{where } \Sigma_{eq} \equiv \Sigma(\tilde{p} = 0) \\ \Leftrightarrow \Sigma_r(\tilde{p}) - \Sigma_{eq} &= -\sqrt{3} \text{sg}(\Sigma_{eq}^{\tilde{r}}) \left[\ln \left(\text{cst}_3 e^{-\tilde{p}} + \sqrt{1 + \text{cst}_3^2 e^{-2\tilde{p}}} \right) - \ln \left(\text{cst}_3 + \sqrt{1 + \text{cst}_3^2} \right) \right] \end{aligned} \quad (2.31)$$

The expression for $\tilde{\Omega}_{\Sigma,r}$ follows from its definition (2.20) and (2.29) with (2.14); $\tilde{H}_r(\tilde{p})$ and $\tilde{Q}_{m,r}$ are calculated from

¹⁶ We recover the same solution as Damour and Nordtvedt in reference [42]. The only difference is that we take $\Sigma_{eq} \equiv \Sigma(\tilde{p}_{eq} = 0)$ as integration constant and $\tilde{p}_{eq} \equiv 0$ while they rather choose $\Sigma_\infty \equiv \Sigma(\tilde{p} = \infty)$ and the cosmological parameter at the beginning of the radiation era $\tilde{p}_l \equiv 0$. The conversion is easy:

$$\Sigma_\infty = \Sigma_{eq} + \sqrt{3} \text{sg}(\Sigma_{eq}^{\tilde{r}}) \ln \left(\text{cst}_3 + \sqrt{1 + \text{cst}_3^2} \right).$$

the first two equations of system (2.15) with $\tilde{\Lambda} = \tilde{k} = 0$ and (2.29); $\tilde{\Omega}_{m r}$ is obtained by introducing expressions found for $\tilde{H}_r(\tilde{p})$ and $\tilde{\varrho}_{m r}$, together with (2.14) in definition (2.19):

$$\begin{aligned}\tilde{H}_r(\tilde{p}) &= H_{eq} e^{-2\tilde{p}} \left(\frac{1 + cst_3^2 e^{-2\tilde{p}}}{1 + cst_3^2} \right)^{1/2} \quad \text{where } \tilde{H}_{eq} \equiv \tilde{H}(\tilde{p}_{eq} \equiv 0), \\ \tilde{\varrho}_{m r}(\tilde{\mathfrak{R}}_r) &= \tilde{\varrho}_{m eq} e^{-4cst_1} \tilde{\mathfrak{R}}_r^{-4} \quad \text{with } \tilde{\varrho}_{m eq} \equiv \frac{3\tilde{H}_{eq}^2}{\tilde{\kappa}c^4(1 + cst_3^2)}, \\ \tilde{\Omega}_{\Sigma r}(\tilde{\mathfrak{R}}_r) &= \frac{cst_3^2 e^{-2cst_1} \tilde{\mathfrak{R}}_r^{-2}}{1 + cst_3^2 e^{-2cst_1} \tilde{\mathfrak{R}}_r^{-2}}, \\ \tilde{\Omega}_{m r}(\tilde{\mathfrak{R}}_r) &= \frac{1}{1 + cst_3^2 e^{-2cst_1} \tilde{\mathfrak{R}}_r^{-2}}.\end{aligned}$$

From these equations, we conclude we are in presence of a standard black-body radiation, $\tilde{\varrho}_{m r} \sim \tilde{\mathfrak{R}}_r^{-4}$; this allows us to define a Cosmic Microwave Background Temperature (\tilde{T}_{CMB}^o) to confront with the observations.

Let us come back to the ‘‘mechanical oscillator equation’’ which is the most useful and straightforward way to find a natural relation for the scalar coupling. For any value of λ_m , the ‘‘mechanical oscillator equation’’ (2.16) can be rewritten as:

$$\frac{2}{3} \left[\frac{1}{[1 - \Sigma^{\tilde{r}2}/3]} \Sigma^{\tilde{r}} + \Sigma^{\tilde{r}} \right] = -(1 - 3\lambda_m) \alpha_{TS}(\Sigma) - \frac{1}{3} (1 - 3\lambda_m) \Sigma^{\tilde{r}}.$$

As we have just seen in (2.28), the left-hand side of this equation is exactly null during the radiation era.

Arguing for a smooth transition from the radiation to the matter era, we obtain a natural constraint for α_{TS} during the radiation era. Indeed, taking the limit $\lambda_m \rightarrow \lambda_{m r} = 1/3$ in this last equation, we find

$$\alpha_{TS}(\Sigma) = -\frac{1}{3} \Sigma^{\tilde{r}}. \quad (2.32)$$

The underlying assumption is that $\alpha_{TS}(\Sigma)$ is independent of λ_m .

If we now replace $\Sigma_r^{\tilde{r}}$ by its solution found in (2.29), we get

$$\alpha_{TS r}(\tilde{p}) = -\frac{1}{\sqrt{3}} \frac{\text{sg}(\Sigma_{eq}^{\tilde{r}}) cst_3 e^{-\tilde{p}}}{\sqrt{1 + cst_3^2 e^{-2\tilde{p}}}}. \quad (2.33)$$

We could also directly rewrite the scalar coupling in terms of the scalar field: expressions (2.31) and (2.33), plus the fact that

$$\frac{\sinh[\]}{\sqrt{1 + \sinh^2[\]}} = \tanh[\]$$

lead us to

$$\alpha_{TS}(\Sigma_r) = -\frac{1}{\sqrt{3}} \text{sg}(\Sigma_{eq}^{\tilde{r}}) \tanh \left[-\frac{\Sigma_r(\tilde{p}) - \Sigma_{eq}}{\sqrt{3} \text{sg}(\Sigma_{eq}^{\tilde{r}})} + \text{arcsinh}(cst_3) \right]. \quad (2.34)$$

We now have in hand a complete evolutionary solution during the radiation era which we shall use in the next section to infer a solution for the dust era.

2.2.5 Solutions in a flat dust universe

Today, the matter of our universe is clustered in stars, galaxies, clusters and gas clouds... with a lot of empty space in between. This can be modeled by a universe solely composed of dust, namely the galaxies, with proper motions¹⁷ negligible with respect to the speed of light, so that their kinetic energies are negligible with regard to their mass energy. We can then say that

$$\tilde{P}_{m d} = 0 \Rightarrow \lambda_m \simeq \frac{\tilde{P}_{m d}}{\tilde{\rho}_{m d}} = 0,$$

where the subscript “ d ” stands for a dust universe.

Our aim in this subsection is to find a solution to the cosmological equations defined in Section 2.1 for a dust universe, that admits GR as an attractor. Again, we only have three equations with four unknowns, and thus need to impose by hand a constraint, for example, on the coupling constant α_{TS} (that is to say A_d). We will first recall the rather arbitrary choice made by Damour and Nordtvedt [36] and their approximate solution to the field equations. Then, we shall suggest a natural, furthermore exact and analytical, dust-era solution exploiting the radiation-era solution that we just derived.

2.2.5.1 An arbitrary choice of the cosmological potential (Damour and Nordtvedt’s method)

Damour and Nordtvedt [41, 36] impose the conformal factor $A_d(\Sigma)$ to be:

$$\begin{aligned} A_d(\Sigma) &= e^{\frac{1}{2}N \Sigma_d^2} \\ \Leftrightarrow \alpha_{TS}(\Sigma_d) &= N \Sigma_d, \end{aligned} \quad (2.35)$$

where N is a positive constant, and the scalar coupling depends linearly on the scalar field. The potential (2.17) involved in the “mechanical oscillator equation” (2.16) is a parabolic well that possesses a minimum at $\Sigma_d = 0$. The constant N then characterizes the curvature of this potential:

$$\tilde{V}(\Sigma_d) = +\frac{1}{2}N \Sigma_d^2. \quad (2.36)$$

It is now important to understand the connection between N and the Post-Newtonian parameters for TS theories, $\gamma(\alpha_{TS 0})$ and $\beta(\alpha_{TS 0}, \partial\alpha_{TS}/\partial\Sigma|_0)$ given in Table (1.67). Indeed, if a generic dust-era cosmological potential (2.17) is expanded around the present-time (small) value of the scalar field Σ_0 , using (1.7), we find

$$\tilde{V}(\Sigma_d) \simeq \tilde{V}(\Sigma_0) + \alpha_{TS 0}(\Sigma_d - \Sigma_0) + \frac{1}{2} \partial\alpha_{TS}/\partial\Sigma_d|_0 \cdot (\Sigma_d - \Sigma_0)^2 + O\left((\Sigma_d - \Sigma_0)^3\right).$$

Comparing this expansion with the Damour-Nordtvedt model (2.36), we see how $N = \partial\alpha_{TS}/\partial\Sigma_d|_0$ is relevant to the PN parameter $1 - \beta = -N/8 \cdot (1 - \gamma) \cdot (1 + \gamma)$ and why, in this particular model, $1 - \beta$ is restricted to be always negative. Remember that $1 - \beta$ could have either sign a priori.

In the case of a flat dust universe, this chosen conformal factor leads to the following “mechanical oscillator equation” with only one unknown (Σ_d) and the scalar coupling contributing as an elastic force with elastic coefficient N :

$$\frac{2}{\left[3 - \tilde{\Sigma}_d'^2\right]} \tilde{\Sigma}_d'' + \tilde{\Sigma}_d' + N \Sigma_d = 0.$$

This equation has no analytical solution. So Damour *et al.* made the following approximation: they neglected the dependence on the velocity in the mass term, supposing that $\tilde{\Sigma}_d'^2$ (which is always < 3) is close to GR null value,

$$\frac{2}{3} \tilde{\Sigma}_d'' + \tilde{\Sigma}_d' + N \Sigma_d \simeq 0.$$

¹⁷ with respect to the Roberston-Walker metric expressed in the frame that has been chosen to be the physical one.

This simplified equation allows now for analytical solutions classified according to the value of the constant N :

if $N \in]0, 3/8[$:

$$\Rightarrow \Sigma_d(\tilde{p}) = \left[+\frac{2}{3} \frac{\tilde{\Sigma}_{eq}}{s_+} + \frac{1}{2} \left(1 + \frac{1}{s_+}\right) \Sigma_{eq} \right] e^{\frac{3}{4}(-1+s_+)\tilde{p}} + \left[-\frac{2}{3} \frac{\tilde{\Sigma}_{eq}}{s_+} + \frac{1}{2} \left(1 - \frac{1}{s_+}\right) \Sigma_{eq} \right] e^{\frac{3}{4}(-1-s_+)\tilde{p}},$$

if $N = 3/8$:

$$\Rightarrow \Sigma_d(\tilde{p}) = \Sigma_{eq} \left[1 + \left(\frac{\tilde{\Sigma}_{eq}}{\Sigma_{eq}} + \frac{3}{4} \right) \tilde{p} \right] e^{-\frac{3}{4}\tilde{p}},$$

if $N \in]3/8, \infty[$:

$$\begin{aligned} \Rightarrow \Sigma_d(\tilde{p}) &= \left[\Sigma_{eq}^2 + \frac{1}{s_-^2} \left(\frac{4}{3} \tilde{\Sigma}_{eq} + \Sigma_{eq} \right)^2 \right]^{1/2} \sin \left[\left(\frac{3}{4} s_- \tilde{p} \right) + \arctan \left(\frac{\Sigma_{eq} s_-}{\frac{4}{3} \tilde{\Sigma}_{eq} + \Sigma_{eq}} \right) \right] e^{-\frac{3}{4}\tilde{p}} \\ &= \left[\Sigma_{eq} \cos \left(\frac{3}{4} s_- \tilde{p} \right) + \frac{\left(\frac{4}{3} \tilde{\Sigma}_{eq} + \Sigma_{eq} \right)}{s_-} \sin \left(\frac{3}{4} s_- \tilde{p} \right) \right] e^{-\frac{3}{4}\tilde{p}}, \end{aligned}$$

$$\text{where } s_{\pm} \equiv \left(\pm 1 \mp \frac{8}{3} N \right)^{1/2}.$$

(2.37)

Going further, Damour and Nordvedt set the integration constant $\tilde{\Sigma}_{eq}$ to zero, arguing that, if the radiation era lasts long enough, the speed should be (almost) vanishing¹⁸ by the end of the radiation era. The attractor mechanism is thus mostly efficient during the radiation era. In our model, on the contrary, the attractor mechanism is still active during the dust era, as we shall see.

The above argument leads to the following solutions:

if $N \in]0, 3/8[$: overdamped monotonic motion towards the local minimum

$$\begin{aligned} \Rightarrow \Sigma_d(\tilde{p}) &= \frac{1}{2} \left(1 + \frac{1}{s_+}\right) \Sigma_{eq} e^{\frac{3}{4}(-1+s_+)\tilde{p}} + \frac{1}{2} \left(1 - \frac{1}{s_+}\right) \Sigma_{eq} e^{\frac{3}{4}(-1-s_+)\tilde{p}} \\ &\xrightarrow{\tilde{p} \rightarrow \infty} \frac{1}{2} \left(1 + \frac{1}{s_+}\right) \Sigma_{eq} e^{\frac{3}{4}(-1+s_+)\tilde{p}} \text{ and if } N \ll 3/8, \sim \Sigma_{eq} e^{-N\tilde{p}}, \end{aligned}$$

if $N = 3/8$: critical damped monotonic motion towards the local minimum

$$\Rightarrow \Sigma_d(\tilde{p}) = \Sigma_{eq} \left[1 + \frac{3}{4} \tilde{p} \right] e^{-\frac{3}{4}\tilde{p}}, \quad (2.38)$$

if $N \in]3/8, \infty[$: damped oscillatory motion around and towards the local minimum

$$\begin{aligned} \Rightarrow \Sigma_d(\tilde{p}) &= \Sigma_{eq} \left[1 + \frac{1}{s_-^2} \right]^{1/2} \sin \left[\left(\frac{3}{4} s_- \tilde{p} \right) + \arctan(s_-) \right] e^{-\frac{3}{4}\tilde{p}} \\ &= \Sigma_{eq} \left[\cos \left(\frac{3}{4} s_- \tilde{p} \right) + \frac{1}{s_-} \sin \left(\frac{3}{4} s_- \tilde{p} \right) \right] e^{-\frac{3}{4}\tilde{p}}. \end{aligned}$$

In these three categories of solution, $\Sigma_d(\tilde{p})$ is decreasing with time and is thus compatible with a solution corresponding to an important scalar-field contribution at the beginning of the universe, that vanishes asymptotically as $\tilde{p} \rightarrow +\infty$. Only the third category of solution is oscillating though, and so is compatible with a scalar field that would oscillate down a potential well.

However, these solutions are only valid for the dust era. They furthermore stem from an arbitrary conformal factor chosen so to lead to a potential well for $\lambda_m \in]-1, 1/3]$, with an approximation that neglects the dependence on the speed in the mass term.

¹⁸ We shall see in the next paragraph that such a choice of the integration constant is not compatible with *our* model because if the speed is zero at one time during the radiation era in our model, then not only is it always zero during this era, according to (2.29) and (2.30), but it will always be so in the dust era!

2.2.5.2 Solving the equations in fixed λ_m universe. A natural cosmological potential...

In our approach, when looking for a solution to the cosmological evolutionary equations for a dust universe, we *do not impose an arbitrary shape for the conformal factor* $A_q(\Sigma)$. Instead we try to deduce it naturally from the exact analytical solution found for the radiation universe, as the evolution of our universe has been from a radiation era (starting at \tilde{t}_l or \tilde{p}_l and ending at \tilde{t}_{eq} or \tilde{p}_{eq}) to a dust (matter dominated) era (starting at \tilde{t}_{eq} or \tilde{p}_{eq}) until now (\tilde{t}_0 or \tilde{p}_0). We do so by imposing some reasonable condition on the scalar coupling, α_{TS} . The attractor mechanism we find is analytical, exact, simple and efficient throughout the dust era.

A/ In terms of $(\Sigma(\tilde{t}), \tilde{p}(\tilde{t}))$: a smooth exit from the radiation era

Let us work with the equations in terms of $\Sigma(\tilde{t})$ and of the cosmological parameter $\tilde{p}(\tilde{t})$, for any λ_m . Again, we make the assumption that the exit from the radiation era towards the matter era is smooth, so that $\Sigma_r(\tilde{p})$, derived in earlier Section 2.2.4, must be close to the exact solution when we slightly leave the radiation era. We furthermore assume that the coupling $\alpha_{TS}(\Sigma)$ given by (2.32) is unchanged. We shall show that, in fact, the exact solution $\Sigma(\tilde{p}) \equiv \Sigma_r(\tilde{p})$ (2.31) is still an exact solution for a universe of arbitrary λ_m with no cosmological constant and zero curvature, provided that the coupling is given by (2.32) or (2.34); that is to say

$$\begin{aligned} \alpha_{TS}(\tilde{\Sigma}) &= -\frac{1}{3}\tilde{\Sigma}' \\ &= -\frac{1}{\sqrt{3}} \frac{\text{sg}(\Sigma'_{eq}) \text{cst}_3 e^{-\tilde{p}}}{\sqrt{1 + \text{cst}_3^2 e^{-2\tilde{p}}}} \\ &= -\frac{1}{\sqrt{3}} \text{sg}(\Sigma'_{eq}) \tanh \left[-\frac{\Sigma(\tilde{p}) - \Sigma_{eq}}{\sqrt{3} \text{sg}(\Sigma'_{eq})} + \text{arcsinh}(\text{cst}_3) \right]. \end{aligned} \quad (2.39)$$

Prior to the demonstration of the above statement, let us comment on these coupling and scalar-field functions. The scalar coupling only depends on the initial condition Σ_{eq} , that we can determine by fixing $\alpha_{TS}(\tilde{p}_{eq})$, where \tilde{p}_{eq} corresponds to the end of the radiation era (see later in Section 2.2.6). We notice also that, as $\tilde{p} \rightarrow +\infty$, $\alpha_{TS}(\tilde{p}) \rightarrow 0$. However, this fact alone does not imply that GR is an attractor to the corresponding cosmological solution, as explained in Section 2.2.1. We still have to check that $A(\tilde{p}) \rightarrow \text{cst} \neq 0$. According to the definition of the coupling constant (1.7), we integrate $\alpha_{TS}(\Sigma)$ to recover the exact conformal factor for any matter era:

$$A(\Sigma) = A_{eq} \frac{\cosh \left\{ -\frac{\Sigma(\tilde{p}) - \Sigma_{eq}}{\sqrt{3} \text{sg}(\Sigma'_{eq})} + \text{arcsinh}(\text{cst}_3) \right\}}{\cosh \{ \text{arcsinh}(\text{cst}_3) \}}, \quad (2.40)$$

or expressing it in terms of \tilde{p} ,

$$A(\tilde{p}) = A_{eq} \left(\frac{1 + \text{cst}_3^2 e^{-2\tilde{p}}}{1 + \text{cst}_3^2} \right)^{1/2} \quad \text{where } A_{eq} \equiv A(\tilde{p} = 0). \quad (2.41)$$

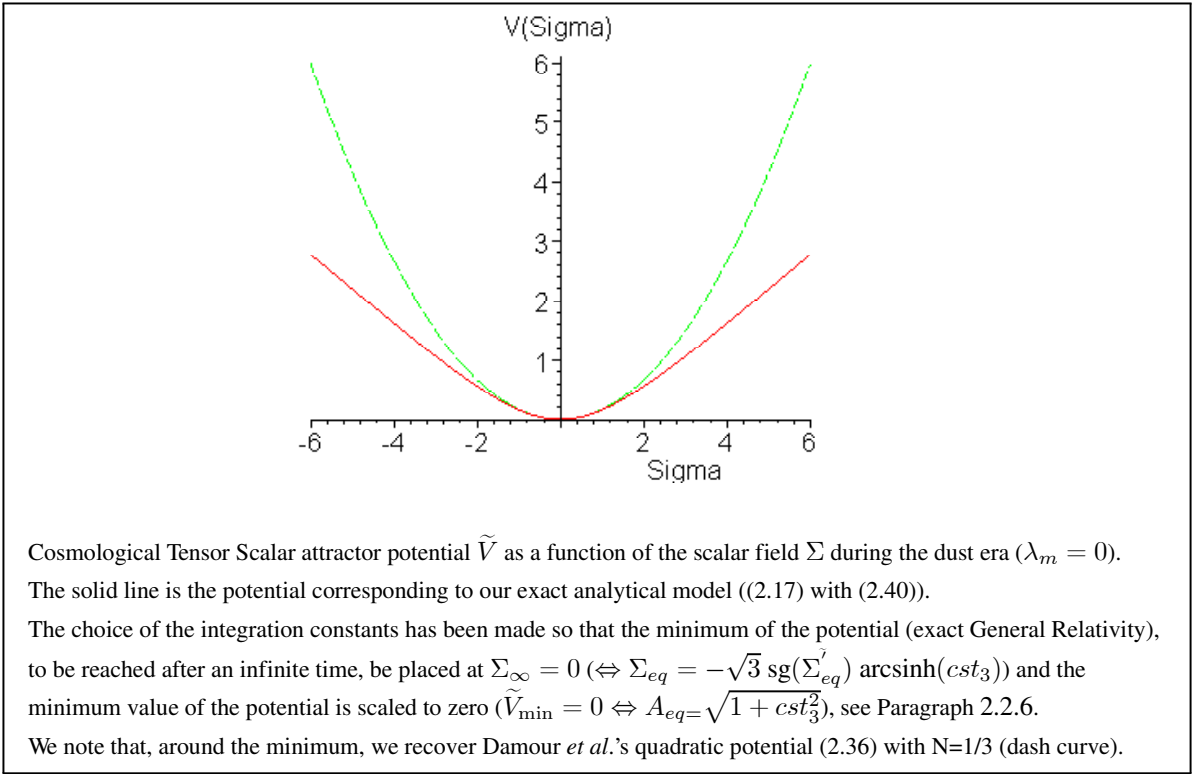
We can now verify that asymptotically the conformal factor tends towards a constant, $A_{eq}/\sqrt{1 + \text{cst}_3^2}$, which is nonzero if we reject the “trivial” solution $A(\tilde{p}) \equiv 0$ for all times. Consequently, we can conclude that a corresponding cosmological solution will asymptotically tend towards GR as demonstrated in Section 2.2.1. This means that the hypothesis we make of a smooth exit from the radiation era excludes at least all the solutions that do not hold GR as an attractor.

An additional interesting feature of this coupling is that, if we expand the forcing term of “the mechanical oscillator equation” (2.16) in Taylor series for small Σ using expression (2.39) for $\alpha_{TS}(\Sigma)$, we find

$$\begin{aligned}
\tilde{F}(\Sigma) &= -(1 - 3\lambda_m) \alpha_{TS}(\Sigma) \\
&\simeq + \frac{(1-3\lambda_m)}{\sqrt{3}} \text{sg}(\Sigma'_{eq}) \tanh \left[\frac{\Sigma_{eq}}{\sqrt{3} \text{sg}(\Sigma'_{eq})} + \text{arcsinh}(cst_3) \right] \\
&\quad - \frac{(1-3\lambda_m)}{3} \text{sg}(\Sigma'_{eq}) \cosh^{-2} \left[\frac{\Sigma_{eq}}{\sqrt{3} \text{sg}(\Sigma'_{eq})} + \text{arcsinh}(cst_3) \right] \Sigma(\tilde{p}).
\end{aligned}$$

So¹⁹ for $[\] = 0$, in the weak Σ limit and for any value of cst_3 , we naturally recover the damping force (2.36) proposed by Damour *et al.* (see Simulation (2.42)), with their arbitrary constant N set to $1/3$; namely,

$$\tilde{F}_{\text{Damour}}(\Sigma) \simeq -\frac{(1-3\lambda_m)}{3} \Sigma(\tilde{p}) \quad \text{for } N = 1/3.$$



Cosmological Tensor Scalar attractor potential \tilde{V} as a function of the scalar field Σ during the dust era ($\lambda_m = 0$).

The solid line is the potential corresponding to our exact analytical model ((2.17) with (2.40)).

The choice of the integration constants has been made so that the minimum of the potential (exact General Relativity), to be reached after an infinite time, be placed at $\Sigma_\infty = 0$ ($\Leftrightarrow \Sigma_{eq} = -\sqrt{3} \text{sg}(\Sigma'_{eq}) \text{arcsinh}(cst_3)$) and the minimum value of the potential is scaled to zero ($\tilde{V}_{\min} = 0 \Leftrightarrow A_{eq} = \sqrt{1 + cst_3^2}$, see Paragraph 2.2.6).

We note that, around the minimum, we recover Damour *et al.*'s quadratic potential (2.36) with $N=1/3$ (dash curve).

(2.42)

Let discuss the evolution of the scalar field with equations (2.31) and (2.29). We clearly see that the scalar field tends to a constant value as $\tilde{p} \rightarrow +\infty$, while its derivative with respect to \tilde{p} tends to zero: the scalar field falls into the potential well.

Another comment: we see that at the end of the radiation era, $\Sigma'_{eq} = \sqrt{3} \text{sg}(\Sigma'_{eq}) cst_3 \sqrt{1 + cst_3^2}$ is different from zero as long as cst_3 is nonzero (which means that we do not consider the solution of General Relativity). So the hypothesis suggested by Damour *et al.* (see Section 2.2.5.1), that $\Sigma'_{eq} = 0$, is inadequate for our cosmological model.

We now show that the cosmological equations for any λ_m can be solved exactly and analytically with the coupling constant given by (2.32) and the scalar field $\Sigma(\tilde{p}) \equiv \Sigma_r(\tilde{p})$ from (2.31). In the following, we use in fact (2.29).

¹⁹ We shall see in the next section that $[\] = 0 \Leftrightarrow \Sigma_{eq} = -\sqrt{3} \text{sg}(\Sigma'_{eq}) \text{arcsinh}(cst_3)$ corresponds to a particular but totally non significant choice of the integration constant Σ_{eq} .

We can rewrite the second equation of system (2.6) in terms of \tilde{p} and integrate it to find $\tilde{H}(\tilde{p})$:

$$\tilde{H}(\tilde{p}) = \tilde{H}_{eq} e^{-\frac{3}{2}(1+\lambda_m)\tilde{p}} \left(\frac{1 + cst_3^2 e^{-2\tilde{p}}}{1 + cst_3^2} \right)^{3\left(\frac{1-\lambda_m}{4}\right)} \quad \text{where } \tilde{H}_{eq} \equiv \tilde{H}(\tilde{p}_{eq} \equiv 0). \quad (2.43)$$

We see that the Hubble parameter tends asymptotically towards zero for $\tilde{p} \rightarrow +\infty$. This is also the case of $\tilde{\mathfrak{R}} = \tilde{H}(\tilde{p}) e^{\tilde{p}}$ and $\tilde{\mathfrak{R}} = \tilde{H}(\tilde{p}) e^{\tilde{p}} \left[\frac{d\tilde{H}(\tilde{p})}{d\tilde{p}} + \tilde{H}(\tilde{p}) \right]$.

Notice that we do recover the exact result of the radiation era just by substituting $\lambda_m = 1/3$ in this general expression for $\tilde{H}(\tilde{p})$.

To obtain $\tilde{\varrho}_m(\tilde{p})$, we need to express the third equation of system (2.6) in terms of \tilde{p} . This leads to

$$\tilde{\varrho}_m(\tilde{p}) = \tilde{\varrho}_{m\,eq} e^{-3(1+\lambda_m)\tilde{p}} \left(\frac{1 + cst_3^2 e^{-2\tilde{p}}}{1 + cst_3^2} \right)^{+\frac{1}{2}(1-3\lambda_m)} \quad \text{where } \tilde{\varrho}_{m\,eq} \equiv \tilde{\varrho}_m(\tilde{p}_{eq} \equiv 0) = \frac{3 \tilde{H}_{eq}^2}{\tilde{\kappa} c^4 (1 + cst_3^2)} \quad (2.44)$$

or, using (2.14),

$$\tilde{\varrho}_m(\tilde{\mathfrak{R}}) = \tilde{\varrho}_{m\,eq} \tilde{\mathfrak{R}}^{-3(1+\lambda_m)} \left(\frac{1 + cst_3^2 \tilde{\mathfrak{R}}^{-2}}{1 + cst_3^2} \right)^{+\frac{1}{2}(1-3\lambda_m)}. \quad (2.45)$$

From $\tilde{\varrho}_m(\tilde{p})$, we immediately get $\tilde{P}_m(\tilde{p})$ thanks to the definition of λ_m (2.3).

We see that the radiation dominated universe evolves as $\tilde{\mathfrak{R}}^{-4}$, whichever the value of the integration constant (cst_3) is. This allows to define the blackbody radiation of the primordial universe and the corresponding Cosmic Microwave Background (CMB) temperature (2.55), as already stated.

For $cst_3 = 0$, we recover the results of the Friedman-Robertson-Walker cosmology ($\tilde{\varrho}_m \sim \tilde{\mathfrak{R}}^{-3(1+\lambda_m)}$), that is to say, the matter density evolves respectively like $\tilde{\mathfrak{R}}_r^{-4}$ for the radiation era and $\tilde{\mathfrak{R}}_d^{-3}$ for the dust era.

Notice that, in the Einstein frame, the dust density does not evolve as $\tilde{\mathfrak{R}}_d^{-3}$ when $cst_3 \neq 0$, because of the presence of the scalar coupling in the last equation of system (2.6); unlike what is found in the Jordan frame, where the matter-density equation is simpler but the other cosmological equations are more intricate.

Finally, we see that the density asymptotically tends towards zero when $\tilde{p} \rightarrow +\infty$. This prediction is coherent with the fact that the universe expands and consequently the matter gets diluted.

B/ In terms of $(x(\tilde{t}), \vartheta(\tilde{t}))$: a coupling function independent of λ_m

One could argue that it is too restrictive a condition to impose that both the scalar field and the scalar coupling be the same functionals during the radiation and the dust era. We show here, in terms of the variables $x(\tilde{t})$ and $\vartheta(\tilde{t})$, that this condition is in fact equivalent to the assumption that the coupling α_{TS} is independent of λ_m .

In the differential equation for $x(\tilde{t})$ and $\vartheta(\tilde{t})$ (2.12), we can equal the coefficients of λ_m^1 and λ_m^0 respectively, thus using *ONLY the hypothesis that α_{TS} be independent of λ_m* . Doing so, we find a first equation for the coefficient of λ_m^1 ,

$$\begin{aligned} \alpha_{TS} &= -\frac{1}{\sqrt{3}} \frac{\tan \vartheta}{\sqrt{1+\tan^2 \vartheta}} \\ \Rightarrow |\alpha_{TS}| &< \frac{1}{\sqrt{3}} \quad \text{for all } \tilde{t}; \end{aligned} \quad (2.46)$$

and a second equation for the coefficient of λ_m^0 ,

$$\sqrt{3} \left[\frac{2}{3} \frac{\dot{\vartheta} x}{\cos \vartheta} + \sin \vartheta \right] = -\alpha_{TS}(\Sigma). \quad (2.47)$$

Replacing the expression for the scalar coupling from (2.46) into the above equation gives

$$\dot{\vartheta} x = -\frac{1}{2} \sin 2\vartheta. \quad (2.48)$$

Previously, with (2.12), (2.9) and the first equation of (2.10), we had three equations with four unknowns ($x = \tilde{H}^{-1}$, $\tilde{\varrho}_m$, α_{TS} , $\tilde{\Sigma}$). Now, with the requirement that the scalar coupling be independent of λ_m , we have four equations (2.10), (2.46), (2.47), and (2.9) with four unknowns and the system is determinate. Let us thus solve this system.

We can express equation (2.48) in terms of the variable \tilde{p} , to get rid of the variable x and be allowed to integrate:

$$\tan \vartheta = cst e^{-\tilde{p}}.$$

And if we take this expression at $\tilde{p}_{eq} \equiv 0$, using (2.9) and (2.8) with (2.30), we can rewrite

$$\Leftrightarrow \tan \vartheta = cst_3 e^{-\tilde{p}} \quad \text{with } cst_3 \equiv \tan \vartheta_{eq} \quad (2.49)$$

$$\Leftrightarrow \tan \vartheta = \frac{1}{e^{cst_1} cst_3 \tilde{\mathfrak{R}}}, \quad (2.50)$$

where in the last step we used the definition of the cosmological parameter \tilde{p} given by (2.14).

Replacing this result for $\vartheta(\tilde{p})$ in (2.46), we finally recover (2.39)... our “natural coupling function”!

If now we wish to derive an expression for $\tilde{\Sigma}(\tilde{p})$ and $\Sigma(\tilde{p})$ using (2.49) and the first equation in (2.9), we get

$$\tilde{\Sigma} = \sqrt{3} \frac{\tan \vartheta}{\sqrt{1 + \tan^2 \vartheta}},$$

that is, (2.29), from which (2.31) derives.

2.2.6 Values for the integration constants

It is now necessary to attribute a judicious value to the different integration constants Σ_{eq} , $\tilde{\Sigma}_{eq}$, $\alpha_{TS eq}$ and \tilde{H}_{eq} that we introduced in the preceding subsections.

As far as the constants $\tilde{\Sigma}_{eq}$ and $\alpha_{TS eq}$ are concerned, we can try to select a reasonable cosmological model in agreement with String theories which predict $|\alpha_{TS i}| = 1$ (the subscript “i” here stands for the value when exiting some primordial Planck era and entering the radiation era). We shall assume that the scalar coupling has not evolved much during the radiation era as it was decoupled in the cosmological equations, and so we impose $|\alpha_{TS eq}| \sim 1$. We then need to choose the value of the constant $\tilde{\Sigma}_{eq}$ (thus cst_3) accordingly. To do so, we first note that, owing to equations (2.33) and (2.30), the larger the absolute value of $\tilde{\Sigma}_{eq}$, the larger the absolute value of the scalar coupling will be. Nevertheless, since the absolute value of $\tilde{\Sigma}_{eq}$ is bounded from above by $\sqrt{3}$ (this value excluded), we find that the absolute value of $\alpha_{TS eq}$ is bounded from above by $1/\sqrt{3}$ (this value excluded) (see also (2.46)). So we shall choose as a value of our integration constant $\tilde{\Sigma}_{eq}^2$ the largest one possible in order to have $|\alpha_{TS eq}|$ as close to 1 as possible. Our choice will be a positive derivative of the scalar field at equilibrium time and the corresponding negative value for the scalar coupling, with respect to (2.32). Note that the sign of the scalar coupling α_{TS} is irrelevant, since only its square contributes to physical processes.

In the following section, we shall discuss how different choices of the integration constant $\tilde{\Sigma}_{eq}$ (or alternatively of cst_3) influence the predictions of our model on the Eddington-Robertson-Schiff parameter γ .

Now, let us determine the value of the integration constant Σ_{eq} .

For any value of λ_m , equation (2.17) tells us that the minimum of the potential is reached when the scalar coupling is zero, while equation (2.33) shows that $\alpha_{TS} \equiv \alpha_{TS r} \rightarrow 0$ when $\tilde{p} \rightarrow +\infty$. Thus, the minimum of the potential should be reached after an infinite time at least.

On the other side, expression (2.34) for $\alpha_{TS} \equiv \alpha_{TS} r$ provides the following equivalence:

$$\alpha_{TS \infty} = 0 \Leftrightarrow \Sigma_{\infty} - \Sigma_{eq} = \sqrt{3} \operatorname{sg}(\Sigma_{eq}^{\tilde{r}}) \operatorname{arcsinh}(cst_3) \quad \text{with } \Sigma_{\infty} \equiv \Sigma(\tilde{p} = \infty).$$

Since $\tilde{V} = \tilde{V}(\Sigma)$ is given up to a constant like any potential, we can freely fix the value of its minimum, $\tilde{V}_{\min} \equiv \tilde{V}(\Sigma_{\infty})$, by choosing

$$\Sigma_{\infty} \equiv \Sigma(\tilde{p} = \infty) = 0. \quad (2.51)$$

This choice, according to the previous equivalence, corresponds to fixing the value of the constant:

$$\Sigma_{eq} = -\sqrt{3} \operatorname{sg}(\Sigma_{eq}^{\tilde{r}}) \operatorname{arcsinh}(cst_3). \quad (2.52)$$

Finally, consider the last integration constant to choose, \tilde{H}_{eq} . To fix \tilde{H}_{eq} , we shall use the dust-era solution giving an explicit expression for $\tilde{H}_d(\tilde{p})$ and impose to recover the measured Hubble constant at the present time, \tilde{p}_0 :

$$\tilde{H}_d(\tilde{p} = \tilde{p}_0) = H_0|_{\text{exp}}.$$

2.2.7 Our model and the attractor mechanism

In Paragraph 2.2.5.2, we demonstrated that imposing a scalar coupling independent of λ_m leads to solutions that are identical to those of the radiation era concerning α_{TS} , A , Σ , and $\Sigma^{\tilde{r}}$. The solutions for different cosmological eras differ for \tilde{H} , $\tilde{\Omega}_m$, and $\tilde{\varrho}_m$ as those are functions of λ_m . In the case of $\lambda_m = 1/3$, we recover our previous radiation-era results.

We can say that even though the above hypothesis is restrictive, it gives rise to interesting types of solutions which all belong to the class of cosmological solutions admitting General Relativity as an attractor. Indeed,

$$\alpha_{TS}(\tilde{p}) \xrightarrow{\tilde{p} \rightarrow \infty} 0 \quad \text{while} \quad A(\tilde{p}) \xrightarrow{\tilde{p} \rightarrow \infty} \frac{A_{eq}}{\sqrt{1 + cst_3^2}} = cst \neq 0 \quad \text{if } A_{eq} \neq 0.$$

Let us now investigate the properties of the free parameter $\Sigma_{eq}^{\tilde{r}}$ (alternatively cst_3) of our class of exact solutions. We recall that **whichever of the types of universe (for any λ_m)** we adopt, the cosmological evolution is described by equation (2.16), which is analogous to the description of a particle motion with displacement Σ evolving in a potential. This equation is valid for all λ_m , at any time \tilde{t} (or \tilde{p}). The second equation from system (2.15) gives the constraint $\Sigma^{\tilde{r}2} < 3$, valid for all λ_m , and at any time \tilde{t} (or \tilde{p}).

Let us call **the beginning of the radiation era**, that is to say the early universe, $\tilde{p} = \tilde{p}_l$. At this time, the scalar field $\Sigma_l \equiv \Sigma(\tilde{p}_l)$ and its derivative $\Sigma_l^{\tilde{r}} \equiv \Sigma^{\tilde{r}}(\tilde{p}_l)$ do not necessarily vanish.

During the radiation era (for $\lambda_m = 1/3$), there is no external force in the mechanical oscillator equation (2.28), and so, only the viscous strength will gradually contribute to lower the speed $\Sigma^{\tilde{r}}$.

We call **the end of the radiation era** (thus the beginning of the matter dominated era) $\tilde{p} = \tilde{p}_{eq}$. Of course, the longer the radiation era will last, the smaller the speed will be at the end of the radiation era:

$$\Sigma_r^{\tilde{r}2}(\tilde{p}) \xrightarrow{\tilde{p} \rightarrow \tilde{p}_{eq}} \Sigma_{eq}^{\tilde{r}2} \quad \text{with } \Sigma_r^{\tilde{r}2} < 3.$$

However, at the end of the radiation era, $\Sigma_{eq}^{\tilde{r}}$ will not necessarily be zero, unlike the hypothesis made by Damour *et al.* Indeed, taking $\Sigma_{eq}^{\tilde{r}} = 0$ thus $cst_3 = 0$ corresponds to limiting ourselves to General Relativity, according to the exact analytical solutions we found for the radiation era. We can see with expressions (2.29), (2.31) and (2.33) that such a choice of the integration constant $\Sigma_{eq}^{\tilde{r}}$ leaves us with a constant scalar field $\Sigma(\tilde{p}) = \Sigma_{eq}$ for all \tilde{p} , and a null scalar coupling. This also means that the radiation density ($\varrho_{m \ r}$) and the dust density ($\varrho_{m \ d}$) evolve exactly like in the Standard Model (Friedman-Robertson-Walker cosmologies), that is to say respectively as \mathfrak{R}_r^{-4} and \mathfrak{R}_d^{-3} .

2.2.8 Evaluation of the observables

In the following paragraph, we study the predictions of our class of models regarding the present value of the PN Jordan frame parameter γ . First we recall its expression from Table (1.67)²⁰

$$1 - \gamma = \frac{2\alpha_{TS0}^2(\tilde{t}_0)}{1 + \alpha_{TS0}^2(\tilde{t}_0)}, \quad (2.53)$$

where $\alpha_{TS0}^2(\tilde{t}_0)$ is the cosmological background coupling at the present time \tilde{t}_0 .

2.2.8.1 Predicting γ and the present coupling α_{TS0}

A/ The elapsed time since the end of the radiation era

It is easy to see that an estimate of γ will be obtained simply by evaluating (2.39) and (2.53) at \tilde{p}_0 . Of course, we need first to estimate \tilde{p}_0 , the elapsed time since the end of the radiation era till now. This will be done thanks to the characteristic temperature of the Cosmic Microwave Background of photons resulting from the radiation era, and to the preserved blackbody spectrum as the matter particles decoupled from the photons.

Let us first define the cosmological redshift as

$$\tilde{Z}(\tilde{t}) \equiv \frac{1 + \tilde{z}(\tilde{t})}{1 + \tilde{z}_{eq}} = \frac{\tilde{\mathfrak{R}}_{eq}}{\tilde{\mathfrak{R}}(\tilde{t})} \quad \text{where } 1 + \tilde{z}(\tilde{t}) \equiv \frac{\tilde{\mathfrak{R}}_0}{\tilde{\mathfrak{R}}(\tilde{t})} \text{ is the usual redshift.} \quad (2.54)$$

The time elapsed since the end of the radiation era can then be expressed in terms of \tilde{Z} or of the cosmological observables²¹,

$$\begin{aligned} \tilde{p}(\tilde{t}) - \tilde{p}_{eq} &\stackrel{(2.14) \text{ and } (2.54)}{=} -\ln \tilde{Z}(\tilde{t}) \\ \stackrel{(2.45) \text{ and } (2.14)}{\Leftrightarrow} \tilde{p}(\tilde{t}) - \tilde{p}_{eq} &= +\ln \frac{\tilde{\varrho}_{dust}(\tilde{t})}{\tilde{\varrho}_{rad}(\tilde{t})} - \ln \left(\frac{1 + cst_3^2 e^{-2\tilde{p}(\tilde{t})}}{1 + cst_3^2} \right)^{1/2} \\ \stackrel{(2.41)}{\Leftrightarrow} \tilde{p}(\tilde{t}) - \tilde{p}_{eq} &= +\ln \frac{\tilde{\varrho}_{dust}(\tilde{t})}{\tilde{\varrho}_{rad}(\tilde{t})} - \ln \frac{A(\tilde{t})}{A_{eq}}, \end{aligned}$$

where $\tilde{\varrho}_{dust}(\tilde{t})$ is the dust-(only) density at time \tilde{t} in the Einstein frame²² given by $\tilde{\Omega}_{dust}(\tilde{t})$ in (2.19) and (1.17), while $\tilde{\varrho}_{rad}(\tilde{t})$ is the radiation-(only) density at time \tilde{t} .

We recall that the evolution of the radiation density is that of a black body. Assuming three generations of neutrinos, it is thus described by

$$\tilde{\varrho}_{rad}(\tilde{t}) = 1,68 \frac{a_B}{c^2} \tilde{T}_{CMB}^4(\tilde{t}), \quad (2.55)$$

with a_B , the Boltzmann-Stefan constant and $\tilde{T}_{CMB}^{\circ}(\tilde{t})$, the Cosmic Microwave Background temperature in the Einstein

²⁰ This may seem inconsistent, as we have been working in the Einstein frame for the derivation of our cosmological class of models (frame in which the cosmological equation system is simpler). By imposing a Robertson-Walker type of metric in the Einstein frame, we had implicitly chosen this frame to be the physical one, because by doing so we broke the conformal invariance. Indeed, the metric cannot be Robertson-Walker-like in both the Einstein and the Jordan frames simultaneously, as this would imply that the conformal factor $A(\Sigma)$ is equal to unity!

However, in the present subsection, we come back to the PN parameter γ in the Jordan frame (frame in which the relativistic calculations at a given cosmological time are simpler). There is no contradiction though. One has to be aware that predictions made consistently in each frame are the same. Indeed, for light deflection at first order for example, the PN parameters appear in the combination $(\alpha + \gamma) \frac{GM}{\rho_0 c^2}$. In the Jordan frame, α and γ are given by expressions in Table (1.67). These were inferred from the weak field limit of the Jordan frame equations, so to recover the Newtonian law of motion (1.58) with respect to $V_{TS}(\rho)$. We could have made the same reasoning in the Einstein frame with the weak field gravitational potential $\tilde{V}_{TS}(\tilde{\rho})$. This would have provided the corresponding PN parameters, $\tilde{\alpha} = \tilde{\gamma} = 1/(1 + \alpha_{TS0}(\tilde{t}_0))$. Remembering the relations between the gravitational ‘‘contant’’ in each frame ($G \leftrightarrow \tilde{G}$), and the mass in each frame ($M \leftrightarrow \tilde{M}$) given in respectively (1.15) and (1.18), we get $(\alpha + \gamma) \frac{GM}{\rho_0 c^2} = (\tilde{\alpha} + \tilde{\gamma}) \frac{\tilde{G}\tilde{M}}{\tilde{\rho}_0 c^2}$, whichever the frame that we use.

This is why we can consistently write expression (2.53) with the left-hand side estimated in the Jordan frame (because, in the literature, when the PN curvature parameter is estimated from VLBI light deflection measurements, it is $\alpha = 1$ which is assumed, meaning the Jordan frame), while the right-hand side is estimated in the Einstein frame.

²¹ Remember that we have $\tilde{\varrho}_{dust} = \tilde{\varrho}_{rad}$ at the so-called equilibrium time (t_{eq}).

²² $\tilde{\varrho}_m(\tilde{t}) \equiv \tilde{\varrho}_{dust}(\tilde{t}) + \tilde{\varrho}_{rad}(\tilde{t})$

frame at time \tilde{t} . Hence, using the definition of $\tilde{\Omega}_{dust}(\tilde{t})$, we write

$$\begin{aligned} \tilde{p}(\tilde{t}) - \tilde{p}_{eq} &= \ln \frac{3\tilde{H}^2(\tilde{t}) \tilde{\Omega}_{dust}(\tilde{t}) / (8\pi\tilde{G}(\tilde{t}))}{1,68 a_B \tilde{T}_{CMB}^4(\tilde{t})} - \ln \frac{A(\tilde{t})}{A_{eq}} \\ \stackrel{(2.41) \text{ and } (2.30)}{\Leftrightarrow} \tilde{p}(\tilde{t}) &= \frac{1}{2} \ln \left[\frac{3cst_{\text{cosmic}}^2(\tilde{t}) - \tilde{\Sigma}_{eq}^{\prime 2}}{3 - \tilde{\Sigma}_{eq}^{\prime 2}} \right], \end{aligned} \quad (2.56)$$

with $cst_{\text{cosmic}}(\tilde{t}) \equiv \frac{3\tilde{H}^2(\tilde{t}) \tilde{\Omega}_{dust}(\tilde{t}) / (8\pi\tilde{G}(\tilde{t}))}{1,68 a_B \tilde{T}_{CMB}^4(\tilde{t})}$,
 $\tilde{p}_{eq} \equiv 0$.

B/ Estimation of the elapsed time according to the cosmological observables

The experimental values for the present-time densities²³ given in Appendix A, together with the gravitational constant measured today (the Newtonian constant), the Hubble constant, and the experimental CMB temperature allow us to estimate \tilde{p}_0 , using (2.56) at the present time \tilde{t}_0 :

$$\tilde{p}_0 = \frac{1}{2} \ln \left[\frac{3 \left(\left\langle \begin{array}{c} 2175 \\ 6780 \end{array} \right\rangle \right)^2 - \tilde{\Sigma}_{eq}^{\prime 2}}{3 - \tilde{\Sigma}_{eq}^{\prime 2}} \right]. \quad (2.57)$$

Of course, this estimate²⁴ will depend the integration constant $cst_3 \in [0, \infty[$ or equivalently $|\tilde{\Sigma}_{eq}^{\prime}| \in [0, \sqrt{3}[$ according to (2.30). The minimum value of \tilde{p}_0 , which corresponds to General Relativity ($cst_3 \text{ GR} = \tilde{\Sigma}_{eq}^{\prime \text{ GR}} = 0$), is $\tilde{p}_0 \text{ min} \in [7.685, 8.822]$. The upper limit $cst_3 \rightarrow +\infty$ or equivalently $|\tilde{\Sigma}_{eq}^{\prime}| \rightarrow \sqrt{3}$ leads to an infinite value of \tilde{p}_0 .

C/ Estimation of $\alpha_{TS 0}$ and $1 - \gamma$ according to cosmological observables

We still need to substitute the expression for the cosmological parameter (2.56) evaluated at time \tilde{t}_0 , into expressions for the scalar coupling (2.39) and the curvature PN parameter (2.53). This leads to the following predictions according to the chosen value of constant $\tilde{\Sigma}_{eq}^{\prime}$:

$$\begin{aligned} \alpha_{TS 0} &\equiv \alpha_{TS}(\tilde{t}_0) = -\frac{1}{3} \frac{\tilde{\Sigma}_{eq}^{\prime}}{cst_{\text{cosmic } 0}} \\ \Rightarrow |\alpha_{TS 0 \text{ min}}| &= 0 \equiv \alpha_{TS 0 \text{ GR}} \\ \Rightarrow |\alpha_{TS 0 \text{ max}}| &\in [0.0000851; 0.0002654] \quad \text{and } \alpha_{TS 0 \text{ max}} \text{ is } < 0 (> 0) \text{ if } \tilde{\Sigma}_{eq}^{\prime} \text{ is } > 0 (< 0) \end{aligned}$$

and

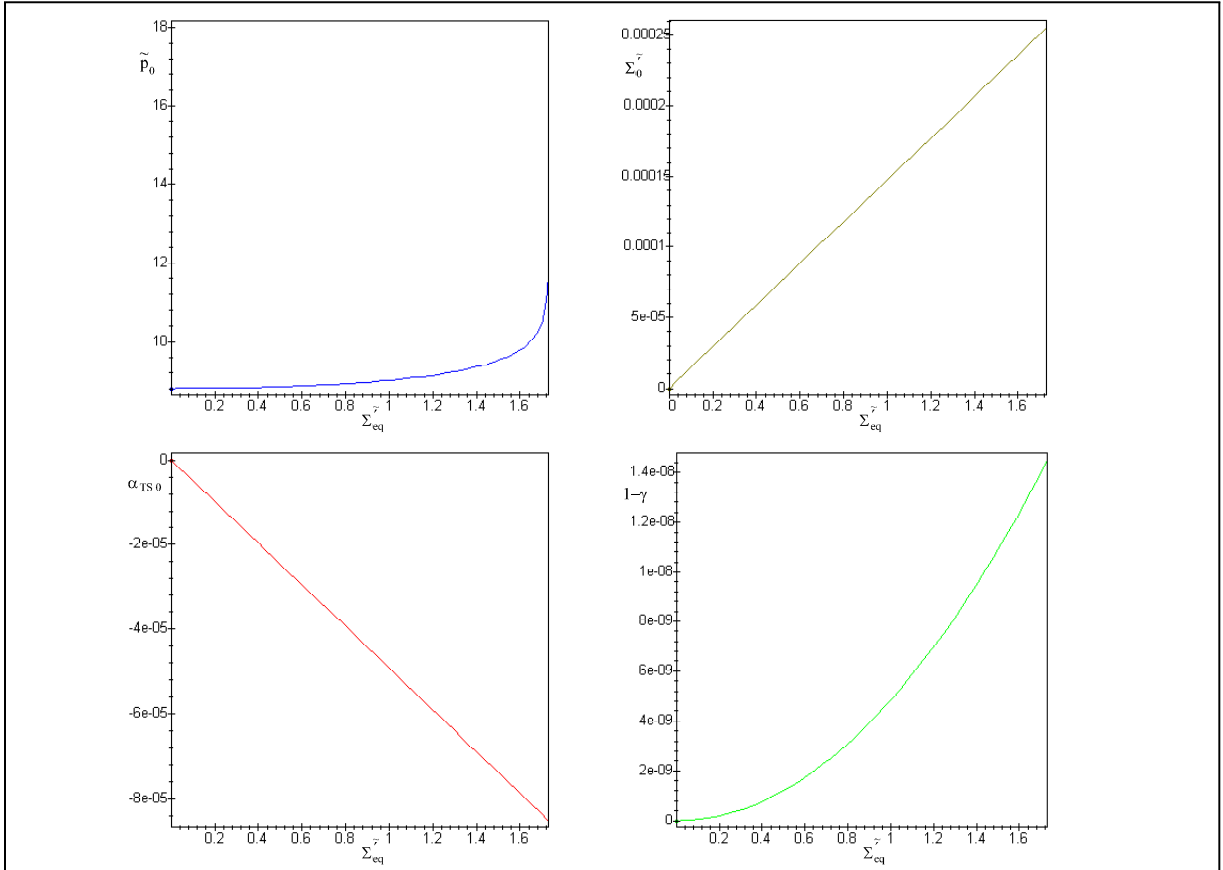
$$\begin{aligned} 1 - \gamma &= 2 \frac{\tilde{\Sigma}_{eq}^{\prime 2}}{9 cst_{\text{cosmic } 0}^2 + \tilde{\Sigma}_{eq}^{\prime 2}} \\ \Rightarrow (1 - \gamma)|_{\text{min}} &= 0 \equiv 1 - \gamma|_{\text{GR}} \\ \Rightarrow (1 - \gamma)|_{\text{max}} &\in [1.450 \cdot 10^{-8}; 1.409 \cdot 10^{-7}]. \end{aligned} \quad (2.58)$$

²³ $\Omega_{\Lambda 0 \text{ exp}}$ is different from $\Omega_{\Sigma 0}$. No cosmological constant is assumed in this section.

²⁴ The first value (2175) inside the $\langle \rangle$ brackets stands for the value calculated with the maximum Cosmic Microwave Background temperature, the minimum values of the matter density and of the Hubble constant (to get the minimum value of \tilde{p}_0). The second value (6780) corresponds to the minimum Cosmic Microwave Background temperature, the maximum values of the matter density and of the Hubble constant (to get the maximum value of \tilde{p}_0).

In the following graphs (2.59), we see how the predicted present values for the observables vary as we adopt different values for the integration constant cst_3 (or equivalently for $|\Sigma_{eq}^{\tilde{\gamma}}|$).

To conclude this paragraph, we might say that in the setting of our class of solutions, even if the upper limit of the deviation from General Relativity $(1 - \gamma)|_{\max}$ is reached, it will be hardly measurable with satellites like GAIA that should only reach a precision of $5 \cdot 10^{-7}$ on γ . However, the predictions of our class of solutions are in agreement with the present limits on the scalar coupling obtained from solar system experiments (see later Subsection 4.2.1): $\alpha_{TS0}^2 < 10^{-3}$.



The following graphs show how present values predicted for \tilde{p}_0 , $\Sigma_0^{\tilde{\gamma}}$, α_{TS0} , and $1 - \gamma$ (from left to right) vary as we adopt different values for the integration constant $\Sigma_{eq}^{\tilde{\gamma}} \geq 0$.

To realize those graphs, the exact dust-era solution under the hypothesis that the scalar coupling is independent of λ_m was used. The values taken for the observables (H_0 , T_{CMB0}° , Ω_{dust0} , G_0) in order to determine $cst_{cosmic0}$, are the ones that lead to the maximum value of \tilde{p}_0 (that is to say, $cst_{cosmic0} = 6780$). The graphs corresponding to the minimum value of \tilde{p}_0 (that is to say, $cst_{cosmic0} = 2175$) are analogous to those presented here.

Notice that all the integration constants at \tilde{p}_{eq} , except for cst_3 (or equivalently, $\Sigma_{eq}^{\tilde{\gamma}}$), present in the exact dust-era solution have been chosen according to the discussion made in Subsection 2.2.6.

(2.59)

2.2.8.2 Consistency check of our model

We will now come back to the remark made in Subsection 2.2.3 about our model being in conflict with SNIa results. It motivates us to study the consequences of adding a perturbing cosmological constant to our model, sufficiently large to account for the acceleration that is currently observed for SNIa.

But first, let us further develop our interpretation of SNIa observations in the framework of our model. The general relation for the apparent (m) versus absolute magnitude (of a SNIa) (M) is given by the following formula in terms of the luminosity distance (d_L)

$$m - M = 5 \log d_L + 25 \quad \text{with } d_L \text{ in [Mpc]}. \quad (2.60)$$

The luminosity distance, defined as $d_L \equiv \sqrt{L/(4\pi l)}$ with L the absolute luminosity and l the apparent flux of the source, can also be rewritten in terms of the metric distance \tilde{r} of emission:

$$d_L = \tilde{\mathfrak{R}}_0 (1 + \tilde{z}) \frac{\tilde{r}_e}{\tilde{\mathfrak{R}}_e} \quad (2.61)$$

where a subscript “ e ” stands for the point of emission in space-time.

This metric distance can be obtained by integrating a Robertson-Walker line element (2.1) along the photon path ($ds^2 = 0$), from the point of emission in space-time $(\tilde{t}_e, \tilde{r}_e/\tilde{\mathfrak{R}}_e)$ for the SNIa, to the observer at present time $(\tilde{t}_0, \tilde{r}_0/\tilde{\mathfrak{R}}_e = 0)$.

This leads to

$$\int_{\tilde{t}_0}^{\tilde{t}_e} \frac{1}{\tilde{\mathfrak{R}}_0} c d\tilde{t} = \int_0^{\tilde{r}_e/\tilde{\mathfrak{R}}_e} \frac{d\tilde{l}}{\sqrt{1 - \tilde{k} \tilde{r}/\tilde{\mathfrak{R}}}} \quad (2.62)$$

$$\Leftrightarrow \frac{1}{\tilde{\mathfrak{R}}_0} \int_0^{\tilde{z}} \frac{c}{H(\tilde{z})} d\tilde{z} = S(\tilde{k}, \tilde{r}_e/\tilde{\mathfrak{R}}_e),$$

$$\text{with } S(\tilde{k}, \tilde{r}_e/\tilde{\mathfrak{R}}_e) \equiv \begin{cases} \arcsin(\tilde{r}_e/\tilde{\mathfrak{R}}_e) & \text{if } \tilde{k} = +1, \\ \tilde{r}_e/\tilde{\mathfrak{R}}_e & \text{if } \tilde{k} = +0, \\ \operatorname{arctanh}(\tilde{r}_e/\tilde{\mathfrak{R}}_e) & \text{if } \tilde{k} = -1, \end{cases}$$

where $\tilde{H}(\tilde{z})$ depends on the cosmological model considered, while the redshift \tilde{z} is derived from (2.54) with $\tilde{z}_e \equiv \tilde{z}$ and $\tilde{z}_0 \equiv 0$.

With those definitions in hand, we can find the theoretical expression for the magnitude as a function of the redshift ((2.60), (2.61) and (2.62)) for our cosmological TS model with $\tilde{k} = 0$ and no cosmological constant. Thanks to our exact solution (2.43) for \tilde{H} particularized to the present dust universe, we get the following exact expression using (2.14) and (2.54),

$$m - \overline{M} = 5 \log \left[(1 + CST^2)^{3/4} c (1 + z) \mathfrak{S}(z, CST^2) \right]$$

$$\text{with } \begin{cases} \mathfrak{S}(z, CST^2) \equiv \int_0^z \frac{1}{(1+l)^{3/2}} \left(\frac{1}{1+CST^2(1+l)^2} \right)^{3/4} dt, \\ \overline{M} \equiv M + 5 \log \frac{1}{H_0} \quad \text{and } \tilde{H}_0 \text{ in } [\text{km s}^{-1} \text{Mpc}^{-1}], \\ CST^2 \equiv \frac{cst_3^2}{\mathfrak{R}_0^2} \stackrel{(2.14), (2.56), (2.30)}{=} \frac{cst_3^2}{cst_{\text{cosmic } 0}^2 - cst_{\text{cosmic } 0}^2 - cst_3^2}, \end{cases} \quad (2.63)$$

from which we recover the predictions of the Standard Cosmological Flat Model when $cst_3 = 0$.

As usual, relation (2.63) can be approximated at low redshifts, because $d_L \stackrel{(2.61) \text{ small } z}{\simeq} c \tilde{z} (1 + \tilde{z}) / \tilde{H}_0 + \dots$ Accordingly, from (2.60), we recover the Hubble law exactly like in the Standard Model, independently of cst_3 :

$$m - \overline{M} \stackrel{\text{small } z}{\simeq} 5 \log [c \tilde{z}]. \quad (2.64)$$

A fit to the previous equation of a number of n SNIa observed at low redshift $(z_i, m_i, \delta m_i)_{i=1\dots n}$ provides a value for \overline{M} and the corresponding error $\delta\overline{M}$. Thanks to the absolute magnitude M given by Cepheids, one can estimate \tilde{H}_0 . For example, the set of SNIa used by Perlmutter *et al.* [103] gives an estimate of the Hubble constant in agreement with reference [133]:

$$\begin{aligned}\overline{M} &= -3.318_{-0.393}^{+0.490}, \\ \delta\overline{M} &= 0.080, \\ M &\stackrel{[132]}{=} -17.5, \\ \Rightarrow \tilde{H}_0 &= 58 \text{ km s}^{-1} \text{ Mpc}^{-1}.\end{aligned}$$

Given our estimation of \overline{M} and \tilde{H}_0 from the low redshift supernovae, we might try to use relation (2.63) for the high redshift supernovae to test our model. However, if we remember the meaning of $cst_{\text{cosmic } 0}^2 \equiv cst_{\text{cosmic}}^2(\tilde{t}_0)$ from (2.56), we see that CST^2 (2.63) is very small. It is indeed a monotonous function of cst_3 that leads to

$$\begin{aligned}CST^2 &\rightarrow 0 && \text{when } cst_3 \rightarrow 0 \equiv GR, \\ CST^2 &\rightarrow \frac{1}{cst_{\text{cosmic } 0}^2 - 1} \lesssim 10^{-7} - 10^{-8} && \text{when } cst_3 \rightarrow +\infty.\end{aligned}$$

Hence, we need to check whether our model modifies significantly the prediction of the Standard Model (corresponding to $CST^2 = 0$) regarding the theoretical apparent magnitude. Unfortunately, we find from (2.63) that

$$\Delta m_{\text{theo}} \equiv m_{\text{theo}} \Big|_{CST_{\text{max}}^2} - m_{\text{theo}} \Big|_{CST^2=0} \sim 10^{-7} \ll \delta m_{\text{obs}} \sim 0.18 - 0.20,$$

which means that the error on the observed apparent magnitude is too large to allow SNIa experiments to distinguish between our cosmological model and the Standard Flat Cosmological Model with no cosmological constant. The attractor mechanism towards General Relativity proves to be very efficient! Moreover, knowing that the Standard model with no cosmological constant is falsified by SNIa observations, our model faces the very same problem with the same degree of importance! We might say that our exact analytical cosmological TS solution is not worse than the Standard Model with no cosmological constant!

2.3 The case of a *non* null cosmological constant

In the preceding section, we envisaged cosmological solutions for a flat universe with one scalar field and no cosmological constant. Even though the exact analytical class of solutions we found was promising, we have just seen that it does not agree with the SNIa results. Indeed, the SNIa light curves are in favor of an accelerating universe ($\tilde{q} < 0$). Two possible alternatives are available to rescue the TS model: either to add a cosmological constant, or to add an adequate scalar potential (extended quintessence). In this section, we will consider the first possibility.

2.3.1 Solutions that admit GR as an attractor

With a cosmological constant, the “mechanical oscillator equation” introduced in the preceding section becomes:

$$\frac{\frac{2}{3} \left[1 - \frac{3\tilde{\mathbf{k}}}{\tilde{\mathcal{R}}^2 \tilde{\kappa} \tilde{\varrho}_m c^2} + \frac{\tilde{\Lambda} c^4}{\tilde{\kappa} \tilde{\varrho}_m c^4} \right]}{\left[1 - \Sigma^{\tilde{r}^2}/3 \right]} \Sigma^{\tilde{r}} + \left[-\frac{4\tilde{\mathbf{k}}}{\tilde{\mathcal{R}}^2 \tilde{\kappa} \tilde{\varrho}_m c^2} + (1 - \lambda_m) + 2\frac{\tilde{\Lambda} c^4}{\tilde{\kappa} \tilde{\varrho}_m c^4} \right] \Sigma^{\tilde{r}} = -(1 - 3\lambda_m) \alpha_{TS}(\Sigma).$$

When comparing with equation (2.16), we see that the forcing coefficient and the external force are not affected by the presence of a cosmological constant. The cosmological constant only introduces additional terms in the mass and velocity coefficients. As a consequence of the presence of $\tilde{\Lambda}$, **even when $\tilde{\mathbf{k}} = \mathbf{0}$** , the coupling of $\Sigma^{\tilde{r}}$ to matter $\tilde{\varrho}_m$ does

not disappear from the velocity coefficient. Furthermore, **whichever the value of $\tilde{\mathbf{k}}$ is**, the mass term is complicated and prevents from finding exact analytical solutions except for some special values of λ_m .

2.3.2 A confrontation with SNIa results

A formulation of the cosmological equations in terms of densities helps to clarify the evolutionary tendency of the model, as well as to render more explicit the mass coefficient in the “mechanical oscillator equation”. If we recall the definition of the cosmological-constant density

$$\tilde{\Omega}_\Lambda \equiv \frac{\tilde{\Lambda}c^4}{3\tilde{H}^2} \equiv \frac{\tilde{\varrho}_\Lambda}{\tilde{\varrho}_c},$$

we can rewrite the cosmological field equations as

$$\begin{aligned} \tilde{q} &= \frac{1}{2}(1 + 3\lambda_m)\tilde{\Omega}_m + \frac{1}{2}(1 + 3\lambda_\Sigma)\tilde{\Omega}_\Sigma + \frac{1}{2}(1 + 3\lambda_\Lambda)\tilde{\Omega}_\Lambda, \\ 1 &= \tilde{\Omega}_\Sigma + \tilde{\Omega}_m + \tilde{\Omega}_\mathbf{k} + \tilde{\Omega}_\Lambda, \\ \tilde{\varrho}_\Sigma + 3(1 + \lambda_\Sigma)\tilde{\varrho}_\Sigma\tilde{H} &= -\alpha_{TS}(1 - 3\lambda_m)\tilde{\varrho}_m\dot{\tilde{\Sigma}}, \end{aligned} \quad (2.65)$$

$$\text{with } \lambda_\Lambda = -1.$$

We can still replace the third equation of this system by the additional redundant equation for the scalar field (last equation in (2.5)).

As far as the “mechanical oscillator equation” is concerned, it is rewritten in terms of densities with a positive mass term as

$$\frac{2}{3}\tilde{\Sigma}^{\ddot{r}} + \left[\frac{4}{3}\frac{\tilde{\Omega}_\mathbf{k}}{\tilde{\Omega}_m} + (1 - \lambda_m) + (1 - \lambda_\Lambda)\frac{\tilde{\Omega}_\Lambda}{\tilde{\Omega}_m} \right] \tilde{\Sigma}^{\dot{r}} = -(1 - 3\lambda_m)\alpha_{TS}(\Sigma).$$

The role played by the second term on the left-hand side depends on the relative value of the densities $\tilde{\Omega}_\Lambda$, $\tilde{\Omega}_m$ and $\tilde{\Omega}_\mathbf{k}$:

$$\begin{aligned} \text{if } \frac{\tilde{\Omega}_\mathbf{k}}{\tilde{\Omega}_m} + \frac{3}{4}(1 - \lambda_\Lambda)\frac{\tilde{\Omega}_\Lambda}{\tilde{\Omega}_m} &> -\frac{3}{4}(1 - \lambda_m) \text{ then the second term is a viscous coefficient,} \\ \text{if } \frac{\tilde{\Omega}_\mathbf{k}}{\tilde{\Omega}_m} + \frac{3}{4}(1 - \lambda_\Lambda)\frac{\tilde{\Omega}_\Lambda}{\tilde{\Omega}_m} &< -\frac{3}{4}(1 - \lambda_m) \text{ then the second term accelerates the motion.} \end{aligned}$$

According to (2.3), $-\frac{3}{4}(1 - \lambda_m)$ belongs to the interval $]-\frac{3}{2}, -\frac{1}{2}]$, while λ_Λ is always equal to -1 . Thus **when $\tilde{\mathbf{k}} = \mathbf{0}$** , we are forced to conclude that this contribution to the “mechanical oscillator equation” is always viscous if we impose $\tilde{q} < 0$ in system (2.65) to be in agreement with the SNIa results. This property, combined with the fact that the potential corresponding to the damping force in the “mechanical oscillator equation” is not modified by the presence of a cosmological constant, allows us to deduce that there still exists a special class of solutions admitting GR as an attractor.

2.3.3 Impact of the cosmological constant on γ -predictions

In Subsection 2.2.3, we have seen that our exact dust model solution was not compatible with the supernovae results. This led us to add a cosmological constant to remedy the problem. Anyway, we have argued in Paragraph 2.2.8.2 that our class of solutions would need the corrective contribution from a cosmological constant of the same importance as in General Relativity. Moreover, in a realistic cosmological model, the contribution of the cosmological constant is negligible during the radiation era. Hence, the exact radiation-era solutions found earlier without a cosmological constant for the scalar coupling (2.32) and the “velocity” of the scalar field (2.29) are still valid in a good approximation. Again, we can now invoke a smooth exit from the radiation to the dust era to keep the same solution for the scalar coupling during the dust era. We can then have a *rough* idea on how the values of the variables $\Sigma_d(\tilde{p})$, $\tilde{\Sigma}_d(\tilde{p})$, $\alpha_{TS}(\tilde{p})$, $1 - \gamma(\tilde{p})$ and $\tilde{H}(\tilde{p})$ evolve with the cosmological parameter during the dust era, when a cosmological constant is

present, thanks to numerical simulations.

For our numerical simulation ((2.68), (2.69)) we have adopted the following value for the integration constant, as advocated in Paragraph 2.2.6:

$$\tilde{\Sigma}_{eq}^{\sim} = +\sqrt{3} - 10^{-8}.$$

The chosen value of $cst_{\text{cosmic } 0}$ is different from what was taken in (2.57) because we reduce the matter-density contribution in order to include a cosmological-constant component. Indeed, we shall use this time

$$\begin{aligned} \Omega_{dust\ 0} &= 0.35, \\ \Omega_{\Lambda\ 0} &= 0.60, \\ \stackrel{(2.65)}{\Rightarrow} \Omega_{\Sigma\ 0} &= 0.05, \end{aligned}$$

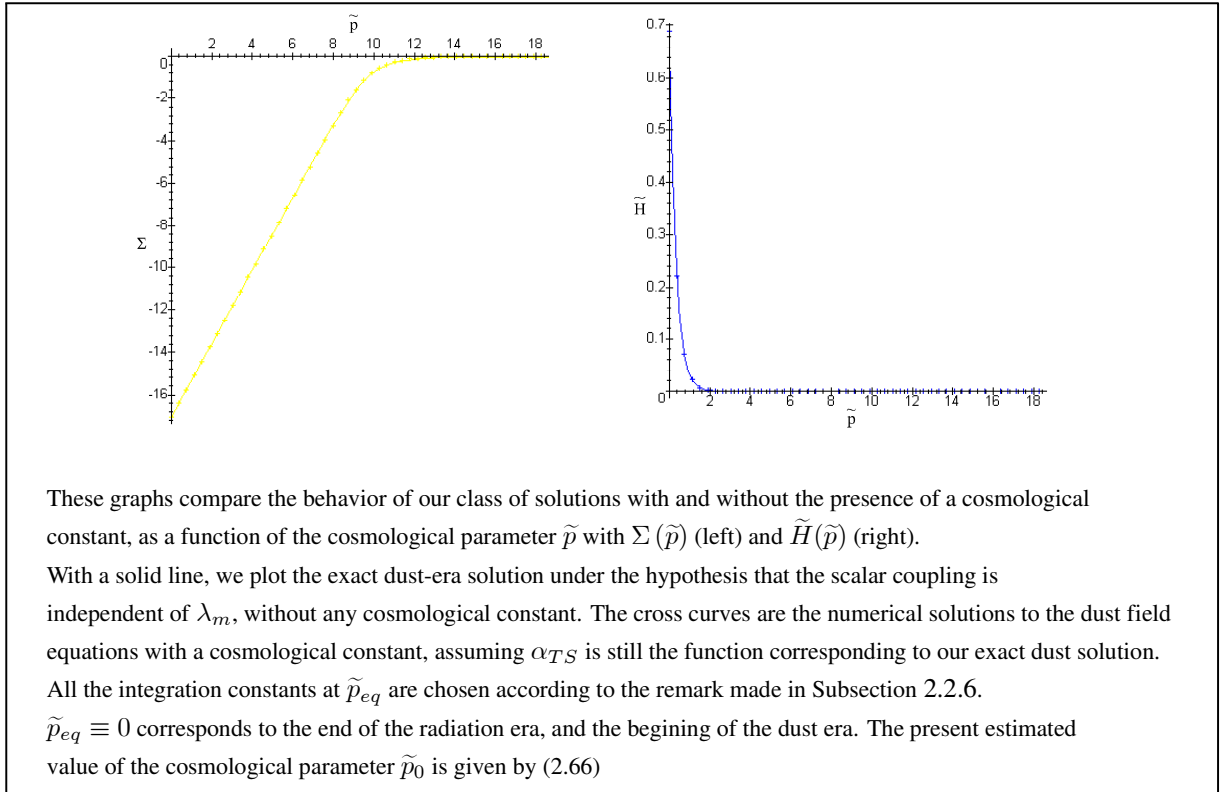
to estimate $cst_{\text{cosmic } 0}$ in (2.56).

Consequently, without changing the other present values for the observables, we estimate with equation (2.56)

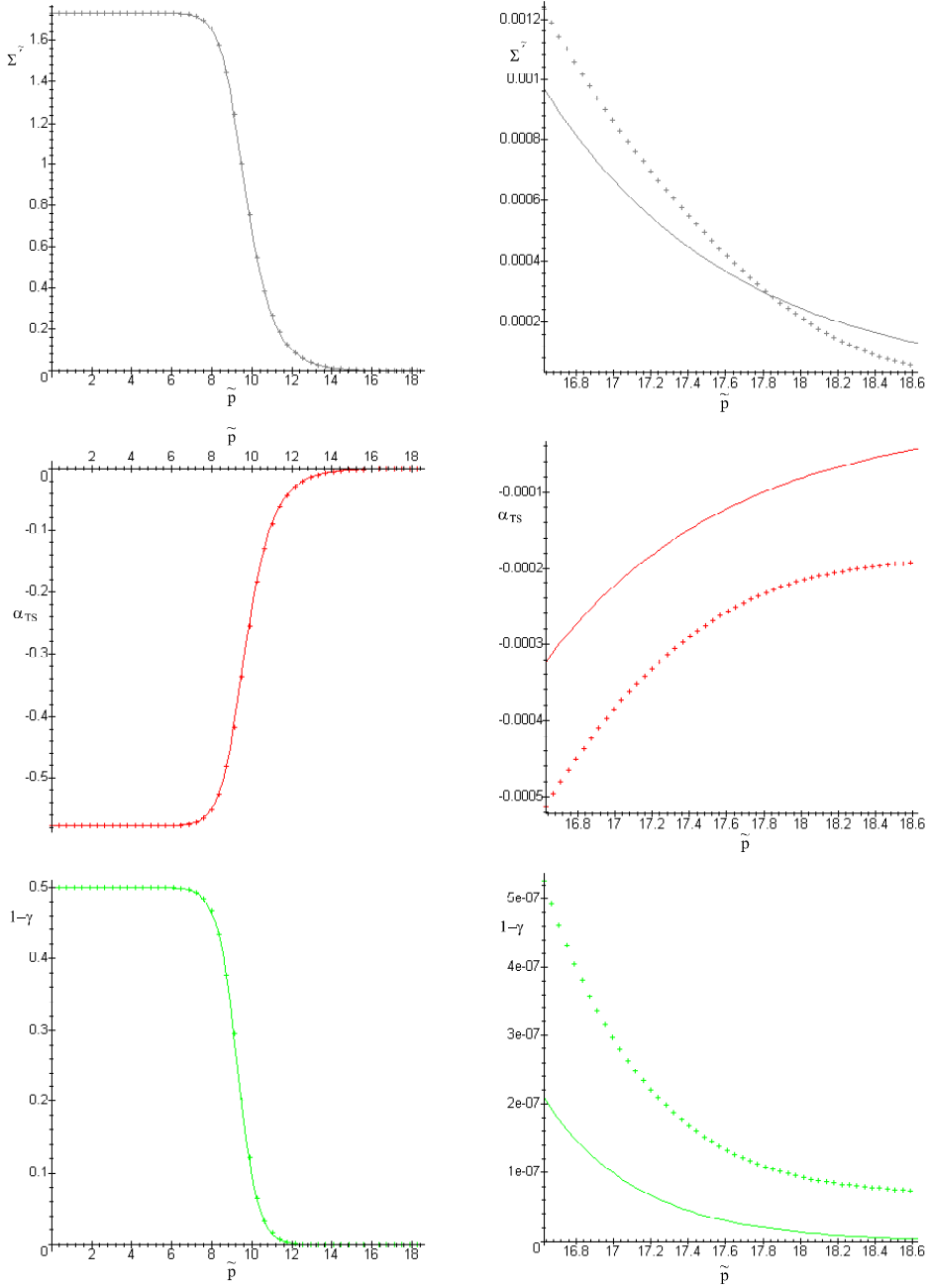
$$\tilde{p}_0 = 17.6278. \quad (2.66)$$

The simulations (2.67) and (2.68) allow us to compare the behavior of our class of solutions with and without the presence of a cosmological constant.

We can see how little the numerical curves including a cosmological-constant contribution depart from the exact solution without cosmological constant. The departure is only visible in the nearby vicinity of the present time \tilde{p}_0 . The differences are negligible in the past close to the radiation epoch due to our assumption. As a consequence, the order of magnitude for $1 - \gamma$ at the present time is the same with and without a cosmological constant... which means it is probably not measurable, even with the future satellites (GAIA, SIM...).



(2.67)



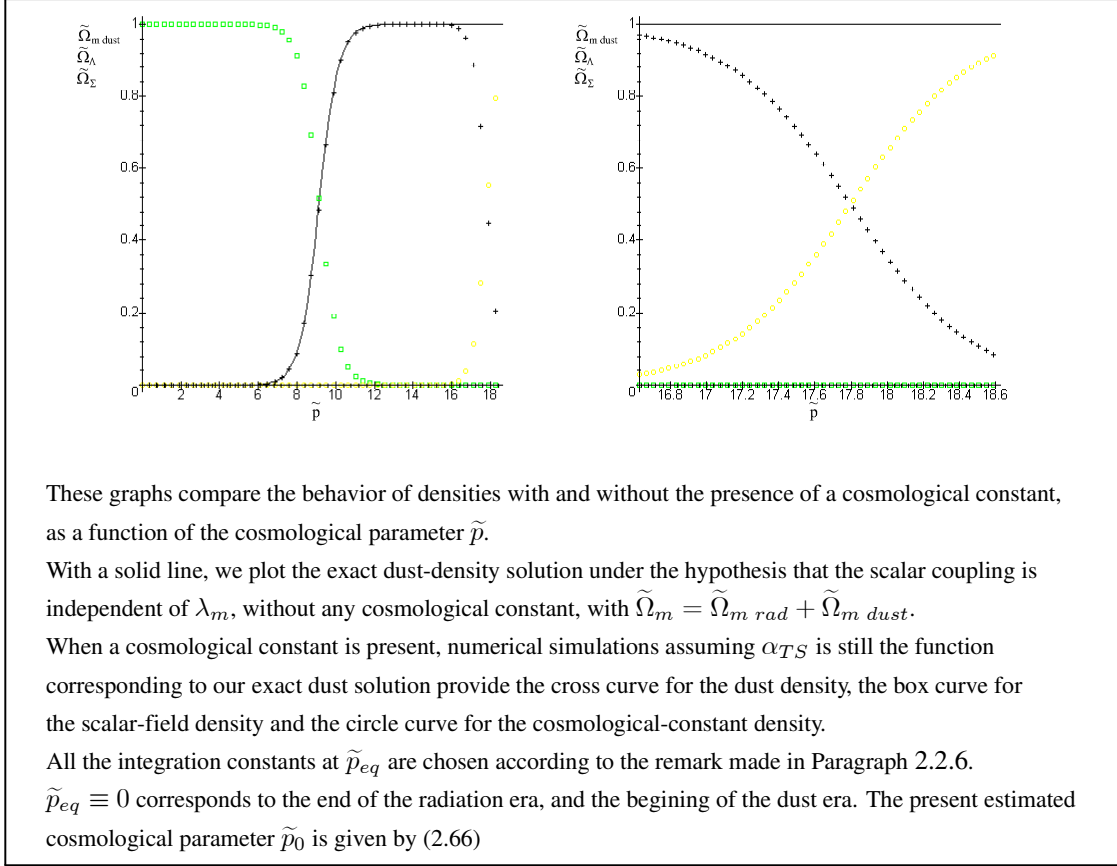
These graphs illustrate the behavior of our class of solutions with and without the presence of a cosmological constant, as a function of the cosmological parameter \tilde{p} . On the right-hand side is a zoom around the present estimated value of the cosmological parameter \tilde{p}_0 given by (2.66).

With a solid line, we plot the exact dust-era solution under the hypothesis that α_{TS} is independent of λ_m , still without any cosmological constant. The cross curves are the numerical solutions to the dust field equations with a cosmological constant, assuming α_{TS} is the function corresponding to our exact dust solution.

All the integration constants at \tilde{p}_{eq} are chosen according to the remark made in Subsection 2.2.6.

$\tilde{p}_{eq} \equiv 0$ corresponds to the end of the radiation era, and the beginning of the dust era.

If we have a look at the plots for densities as a function of the cosmological time \tilde{p} in simulation (2.69), we can clearly distinguish between the scalar-field era and the matter dominated era, while the cosmological-constant era is still coming.



2.4 Impact of the scalar potential and initial conditions on γ -predictions

Considering that the presence of a cosmological constant seems to have no interesting influence on the predicted value of the PN parameter γ (with $(1 - \gamma) \sim \alpha_{TS0}^2$ for a small present value of the scalar coupling, see (1.67)), we now illustrate the **strong dependence of the predictions on the arbitrary choice of the cosmological potential** thanks to some particular models listed in Table (2.71). The list is of course non-exhaustive. Those models concern a universe with no cosmological constant. They are based on the “mechanical oscillator equation” (2.16) and use the approximation that $\Sigma^{\tilde{\gamma}2}$ is negligible with respect to 3 in the mass term, since they assume to be sufficiently close to General Relativity set at the point $\Sigma_{GR}^{\tilde{\gamma}2} = \Sigma_{GR} \equiv 0$. This can be seen as an assumption on the initial conditions at the beginning of the dust era, when the scalar field starts to be coupled to the potential.

We remark that *the models with a scalar coupling which is a function of the absolute value of the scalar field* do not allow for a minimum of the corresponding cosmological potential $\tilde{V}(\Sigma)$. Indeed, $\tilde{V}(\Sigma)$ has an inflection point at $\Sigma_{GR} \equiv 0$. Consequently, GR is not necessarily an attractor for those potentials: some further constraints on the initial position Σ_{eq} and initial velocity $\Sigma_{eq}^{\tilde{\gamma}}$ of the scalar field at the beginning of the dust era, as well as on the constant N

(which has to be sufficiently small, meaning a sufficiently large viscous force in (2.16)) have to be verified²⁵. If not so, a scalar field with $\Sigma_{eq} > 0$ will roll down the potential but go beyond GR point, while a scalar field with $\Sigma_{eq} < 0$ will slide further away from GR point. This can be easily understood when looking at the potential curve in graph (2.70). On the contrary, *scalar couplings which are function of a positive even power of the scalar field* (like quadratic potential solutions given by the approximated solutions (2.37) or (2.38) discussed in Paragraph 2.2.5.1) necessarily admit GR as an attractor, as the corresponding cosmological potential is minimum at $\Sigma_{GR} \equiv 0$. Remember the examples in graph (2.42).

One thus understands why, naturally, the first type of cosmological model is much more “fine-tuned” to General Relativity. It thus provides much more stringent analytical constraints on the present value of the Tensor Scalar coupling (the strongest constraints are $\alpha_{TS0}^2 \lesssim 10^{-21}$), than the second type of models (the strongest constraints²⁶ are $\alpha_{TS0}^2 \lesssim 10^{-7}$) even when using the same observational data (Big Bang nucleosynthesis -BBN-). Moreover, as shown by Serna and his collaborators [128], such a discrepancy between the two types of model discussed above is not due to numerical instabilities unlike what was claimed by Damour *et al.* [43].

If one now considers another type of models in which the *scalar coupling is a function of a negative power of the scalar field*, thus leading to a minimum at infinity in the field space, this yields to a pretty large estimated value for $1 - \gamma \gtrsim 10^{-2}$, provided that we adopt the hypothesis that the coupling is of the order of 1 at the beginning of the radiation era. Such type of models must be consequently rejected according to observations like (3.2) or (3.3).

Concerning **the dependence on initial conditions** ($\Sigma_{eq}, \Sigma_{eq}^{\tilde{}}$), our class of exact analytical models (which in the weak scalar-field limit tends to a quadratic potential, meaning the second type of models discussed above) already illustrates this point. Indeed we have explained in Subsection 2.2.7 that to a specific choice of the integration constant cst_3 correspond specific initial conditions. Simulation (2.59) clearly shows the strong dependence of the predicted value of $1 - \gamma$ on cst_3 .

With those remarks in mind, regarding the $(1 - \gamma)$ predicted deviation of TS theories from General Relativity, we are now ready to proceed to the next chapter, where the role of the PN parameter γ in light deflection will be emphasized.

²⁵ When $\Sigma^{\tilde{}} \ll 3$, see reference [128] and solutions with $sg(\Sigma_d) = +1$ in (2.37):

$$\left. \begin{array}{l} \text{if } \delta = 1 : \\ N \leq 3/8 \\ \Sigma_{eq}^{\tilde{}} \geq -\left(\frac{3}{4} + \frac{3}{4}s_+\right) \Sigma_{eq} \end{array} \right\} \Leftrightarrow \text{GR is an attractor,}$$

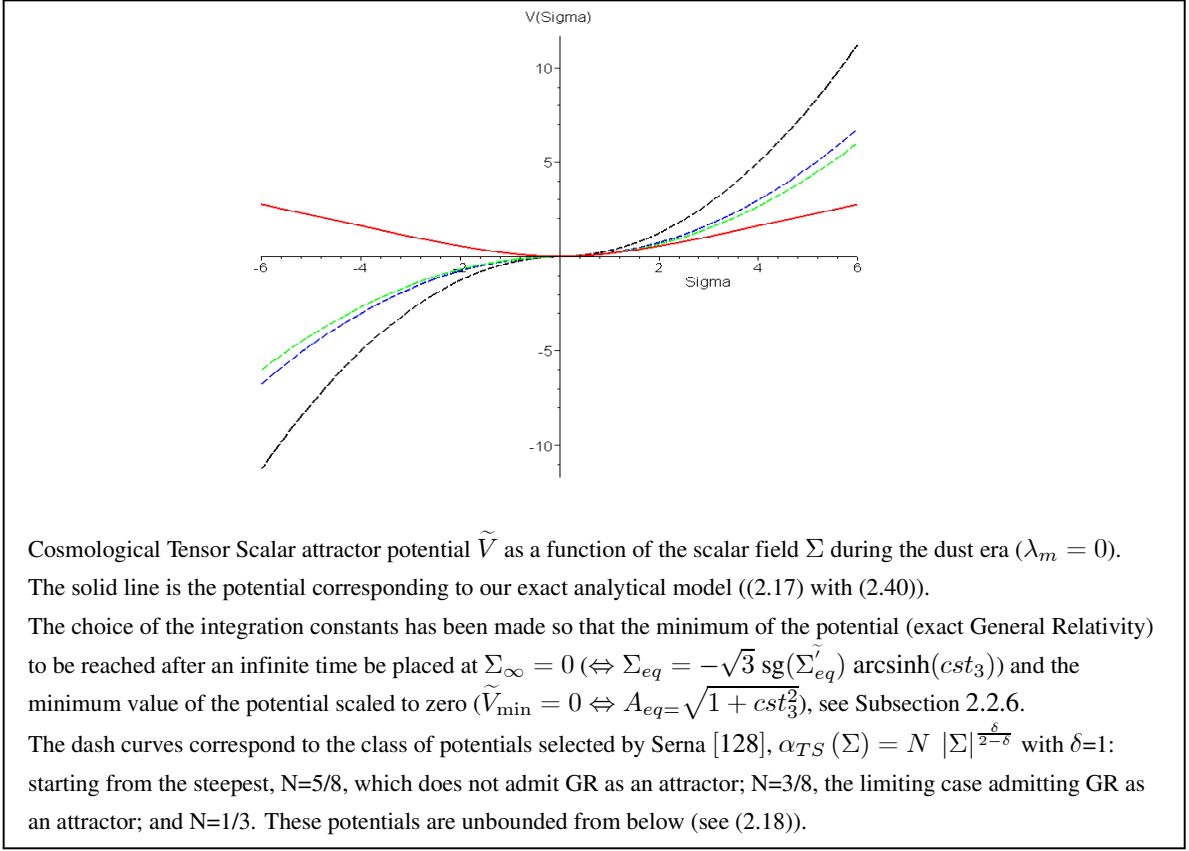
$$\text{if } \delta > 1 : \\ \Sigma_{eq}^{\tilde{}} \geq -\frac{3}{2}\Sigma_{eq} \Rightarrow \text{GR is an attractor,}$$

and if $1/2 < \delta < 1$:

\Rightarrow GR is NOT an attractor.

While in any case, GR is an attractor $\Rightarrow \Sigma_{eq}^{\tilde{}} > \sqrt{3} \frac{1 - e^{\sqrt{3}\Sigma_{eq}}}{1 + e^{\sqrt{3}\Sigma_{eq}}}$.

²⁶ Except for some very particular values of the cosmological potential curvature N in the oscillatory solution ($N > 3/8$), as can be seen in Figure 2.1.



(2.70)

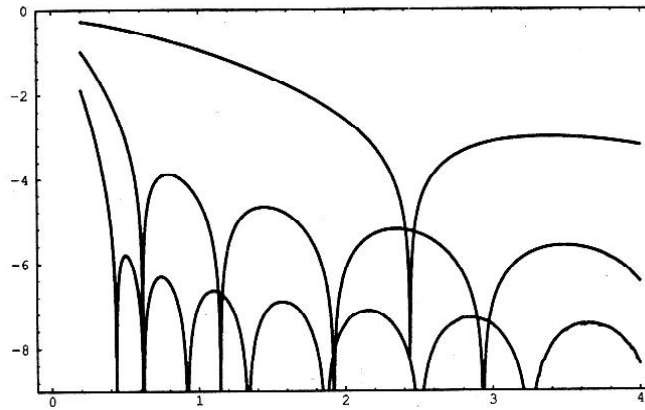


Fig. 2.1 Selected plots of $\log_{10}(1 - \gamma)$ as a function of the potential curvature N are shown, with the upper curve corresponding to $\tilde{\rho}_{m0}/(10^{-30} g cm^{-3}) = 0.1$, the intermediate one to 1, and the lower one to 10. The graph results from a direct numerical integration of the “mechanical oscillator equation” with $\alpha_{TS}(\Sigma) = N\Sigma$, $\tilde{\mathbf{k}} = -1$ and $\alpha_{TS eq} = 1$, for the oscillatory class of solutions ($N > 3/8$), taking into account the progressive change between radiation domination and dust domination. It can be seen that the analytical estimates given in the following table are slightly (except from a few particular values of N for which $1 - \gamma = 0$) larger than the estimates of this graph. This figure is extracted from reference [42].

Ref.	$\alpha_{TS}(\Sigma)$ \Downarrow (2.17) $\tilde{V}(\Sigma_d)$	remarks	predictions
[128]	$\alpha_{TS}(\Sigma) = N \Sigma ^{\frac{\delta}{2-\delta}}$ with $N = \text{constant} > 0$ $0 < \delta < 2$ \Downarrow $\tilde{V}(\Sigma_d) = \frac{2-\delta}{2} N \text{sg}(\Sigma_d) \Sigma_d^{\frac{2}{2-\delta}}$	constraints from Primordial Nucleosynthesis and assumes $\tilde{\Sigma}^i \sim 0$ $\tilde{p}_{BBN-eq} = 3$	if $\tilde{k} = 0$, and if $\delta = 1$, $N = 1/9$, α_{TS} monotonic: $\alpha_{TS 0}^2 \lesssim 10^{-19}$ or if $\delta = 1$, $N = 3/8$, α_{TS} monotonic: $\alpha_{TS 0}^2 \lesssim 10^{-21}$ or if α_{TS} non-monotonic: $\alpha_{TS 0}^2 \lesssim 0.02$
[43]	$\alpha_{TS}(\Sigma) = N \Sigma$ with $N = \text{constant} > 0$ \Downarrow $\tilde{V}(\Sigma_d) = \frac{N}{2} \Sigma_d^2$	constraints from Primordial Nucleosynthesis and assumes $\tilde{\Sigma}_{BBN} = 0$	if $\tilde{k} = 0$, then $\tilde{p}_0 = 10.09 + \ln(\tilde{\Omega}_{m 0} \tilde{h}_0) + \frac{e^{2N\tilde{p}_0} - 1}{2N} \alpha_{TS 0}^2$ and if $N < 0.2$: $\alpha_{TS 0}^2 < \frac{0.239 N}{e^{2N\tilde{p}_0} - 1 - N}$ $\Rightarrow \alpha_{TS 0}^2 \lesssim 0.015$ in the limit $N = 0$ or if $N \gtrsim 0.5$: $\alpha_{TS 0}^2 \lesssim 10^{-6.5} N^{-1} \left(\frac{\tilde{\Omega}_{m 0} h^2}{0.15}\right)^{-3/2}$
[41] [42]	$\alpha_{TS}(\Sigma) = N \Sigma$ with $N = \text{constant} > 0$ \Downarrow $\tilde{V}(\Sigma_d) = \frac{N}{2} \Sigma_d^2$	assumes $\tilde{\Sigma}_{eq} = 0$ $\alpha_{TS eq} \sim 1$ $N \sim 1$	if $\tilde{k} = 0$, then $\tilde{p}_0 \simeq 10$ and if $N < 3/8$: $1 - \gamma \simeq \begin{cases} 2\alpha_{TS eq}^2 \left(\frac{1+s_+}{2s_+}\right)^2 e^{-\frac{3}{2}(1-s_+)\tilde{p}_0} \\ \underset{N \ll 3/8}{\sim} 2\alpha_{TS eq}^2 e^{-2N\tilde{p}_0} \\ \gtrsim 4 \cdot 10^{-5} \end{cases}$ or if $N = 3/8$: $1 - \gamma \simeq \begin{cases} 2\alpha_{TS eq}^2 \left(1 + \frac{3}{4}\tilde{p}_0\right)^2 e^{-\frac{3}{2}\tilde{p}_0} \\ \sim 4 \cdot 10^{-5} \end{cases}$ or if $N > 3/8$: $1 - \gamma \simeq \begin{cases} \frac{2\alpha_{TS eq}^2}{1 - \frac{3}{8}N} \sin^2(\arctan(s_-)) e^{-\frac{3}{2}\tilde{p}_0} \\ \sim 3 \cdot 10^{-7} \end{cases}$ if $\tilde{k} = -1$, then $\tilde{p}_0 \simeq 10 + \ln\left(\frac{\tilde{\Omega}_{m 0}}{10^{-30} g \text{ cm}^{-3}}\right)$ and if $N > 3/8$, in the limit $\tilde{\Omega}_{k 0}/\tilde{\Omega}_{m 0} \gg 1$: $1 - \gamma \sim 2\alpha_{TS eq}^2 \left(\frac{\tilde{\Omega}_{m 0}}{10^{-30} g \text{ cm}^{-3}}\right)^{-3/2} 10^{-5}$
[42]	$\alpha_{TS}(\Sigma) = \alpha_{eq} \left(\frac{\Sigma}{\Sigma_{eq}}\right)^{-n-1}$ with $n = \text{constant} \geq 0$ \Downarrow $\tilde{V}(\Sigma_d) = -\alpha_{eq} \frac{\Sigma_{eq}}{n} \left(\frac{\Sigma_d}{\Sigma_{eq}}\right)^{-n}$	assumes $\tilde{\Sigma}_{eq} = 0$ $\alpha_{TS eq} \sim 1$	if $\tilde{k} = 0$, then $\tilde{p}_0 \simeq 10$: $1 - \gamma \sim \tilde{p}_0^{-\frac{2(n+1)}{n+2}} \sim 10^{-\frac{2(n+1)}{n+2}}$

2.5 Summary of the main results

2.5.1 Main properties of our model

In this chapter, we have presented a class of TS cosmological evolutionary models developed for a flat universe with no cosmological constant. We showed, using a mechanical oscillator analogy, that General Relativity is an attractor for each of those solutions. Even if our class of models does not contain all the possible solutions admitting GR as an attractor, it has several advantages, namely:

- its solutions are analytical;
- they are exact, unlike Damour and Nordtvedt's solution;
- the choice of the attractor potential is not arbitrary, unlike Damour and Nordtvedt's one. In our class of models, it stems from a natural transition from the radiation-era to the dust-era equations;
- if $\Sigma_{eq} = -\sqrt{3} \operatorname{sg}(\Sigma_{eq}^{\tilde{}}) \operatorname{arcsinh}(cst_3)$, in the limit of a weak scalar field Σ , we recover the same damping force term as in Damour *et al.*'s model with $N = 1/3$, that is to say a non-oscillatory solution. In Paragraph 2.2.6, we have shown that this value of Σ_{eq} corresponds to the choice of a null value of the scalar field at the minimum of the potential ($V_{\min} \Leftrightarrow$ exact GR theory). This means that we recover Damour *et al.*'s quadratic potential well, up to a constant term, when the scalar field is close to the minimum of our general potential. To recover exactly Damour *et al.*'s potential which is zero at the minimum, reached after an infinite time, one has further to impose $A_{eq} = \sqrt{1 + cst_3^2}$ according to (2.41) and (2.17). This means that $A(\tilde{p}) \rightarrow 1$ when $\tilde{p} \rightarrow +\infty$. Such a natural convergence towards Damour *et al.*'s model is independent of the value of cst_3 .
- the expressions for the scalar field ($\Sigma, \Sigma^{\tilde{}}$) and the scalar coupling (α_{TS}) do not depend on the type of matter (λ_m) dominating the universe. This means that we do not have to consider successive cosmological phases of different particles decoupling from the radiation to study, for example, the evolution of the scalar coupling. On the contrary, Damour and Nordtvedt's solution requires extensive discussions on the subject and the predictions of their model are sensitive to those;
- different values of the integration constant, cst_3 , define different cosmologies. Our solution is in fact a class of solutions that contain GR as a particular case ($cst_3_{GR} = 0$). In fact, the value of the integration constant, cst_3 , according to (2.52) and (2.30), fixes the initial conditions of the model at the beginning of the dust era ($\Sigma_{eq}, \Sigma_{eq}^{\tilde{}}$), when the scalar field starts to be coupled to matter (during the radiation era, it is totally decoupled) and starts to roll down the potential. That is to say, cst_3 fixes the dust-era starting point on the potential curve given in Simulation (2.42).

2.5.2 Predicted value of the PN parameter γ

The cosmological evolution of our class of models led us to a predicted value of today's scalar coupling, $\alpha_{TS 0}$. However, owing to the value of the integration constant, cst_3 , we only obtain an upper bound, namely, $|\alpha_{TS 0 \max}| \in [0.0000851; 0.0002654]$. The lower bound corresponds to General Relativity with $cst_3 = 0$ and a null scalar coupling. This prediction is in agreement with the present limits obtained from solar system experiments: $\alpha_{TS 0 \exp}^2 < 10^{-3}$. We remind the reader that physical processes are function of the square of the scalar coupling, and hence its sign is irrelevant.

The Post-Newtonian parameter γ is a function of $\alpha_{TS 0}$. Regarding γ , our class of models provided an upper bound on the PN deviation: $(1 - \gamma)_{\max} \in [1.450 \cdot 10^{-8}; 1.409 \cdot 10^{-7}]$. The lower bound is again the null value corresponding to GR. Such a result is less optimistic, from the point of view of measurements, than some earlier models of Damour *et al.* which led to a deviation around 10^{-5} .

We have shown that the above results are stable with regard to the addition of a cosmological constant. Indeed, the attractor mechanism towards General Relativity is very efficient. So this class of models is on an equal footing with GR from the point of view of the SNIa constraint of an accelerating universe: it needs the contribution of a cosmological constant in the same quantitative way as GR does.

However, we have seen through examples from the literature that the predictions on γ and α_{TS0} appear to be very dependent on the cosmological evolutionary potential adopted. Nevertheless, in our class of models, this cosmological potential seems to emerge naturally when considering a smooth transition from the radiation- to a dust-era universe, with a universal scalar coupling (independent of the type of matter dominating the universe).

To conclude, we recall the strong connection that exists between the PN parameter β and the curvature $N = \alpha'_{TS0}$ of this potential around its minimum: $1 - \beta = -N/8 \cdot (1 - \gamma) \cdot (1 + \gamma)$. Like Damour *et al.*'s model, our class of solutions is restricted to a negative $(1 - \beta)$ Post-Newtonian deviation.

Chapter 3:

Light deflection angle in the solar system: general considerations

In Chapter 2, we investigated a particular class of Tensor Scalar cosmological models and obtained a prediction concerning the Post-Newtonian deviation from General Relativity, namely, $1 - \gamma|_{theo} \lesssim 10^{-7}$. We will now focus on the achievable experimental limits regarding this PN parameter. As already stated in the introduction, among the solar system tests presently available, only light deflection and time-delay experiments provide a direct estimate of the deviation $1 - \gamma|_{exp}$.

The light ray propagation in the solar system corresponds to a case of weak gravitational lensing. There are no caustics, which means no multiple images of the same light source, only a change in the apparent position of the light source. Light bending in the gravitational field of the Sun constitutes the simplest and historically first investigated consequence of gravitational light deflection.

In this chapter, we shall emphasize the importance of solar system experiments as well as their limitations regarding this phenomenon, and throughout our discussion, we will emphasize the key role played by the PN parameter γ .

3.1 First order measurement

3.1.1 Why the solar system, and especially the Sun?

Presently, light deflection due to gravitational effects has been observed with various degrees of precision on distance scales ranging from 10^9 to 10^{21} m and on mass scales from 1 to $10^{14} M_{Sun}$, the upper ranges being determined by the extragalactic gravitational lensing of quasars and distant galaxies.

Changes in the apparent position of the stars (the light deflection angle) only probe the lowest ranges in mass and distance. In those lower scales, our sun is, of course, a “privileged” gravitational deflector, as its mass and distance to Earth are known with a fairly good precision. The solar gravitational field seems thus, so far, the best laboratory to test predictions for the light deflection angle. Notice that, as the precision shall increase dramatically with experiments like the astrometric measurements with GAIA satellite, other characteristics of the Sun such as its quadrupole moment and angular momentum may have to be taken into account. However, those parameters are not known with much accuracy so far. We shall consider this problem later in Section 3.2.3.

Note too that, in solar system experiments, the possible presence of a cosmological constant is irrelevant, as cosmological data indicate that the value of Λ is at most a cosmological effect ($\Lambda < 3 (H_0/c)^2$ with H_0 the present value of the Hubble constant). This small Λ value makes it unobservable in all non-cosmological gravitational experiments.

The deflection angle

$$\hat{\alpha}_{\text{weak field}}(b) = \frac{(\alpha + \gamma) 4G_N M}{2 c^2 b} + \mathcal{O}\left(\frac{V_N^2}{c^4}\right), \quad (3.1)$$

with M , the gravitational mass (for example, the Sun),
 G_N , the Newtonian gravitational constant,
 V_N , the Newtonian potential,
 b , the impact parameter of the light ray with respect to the deflector,

due to the Sun, in the setting of General Relativity ($\alpha = \gamma = 1$, see (1.67)), decreases rapidly when observing at non-grazing incidence. It is $\simeq 1.750$ arcsec at the solar limb, still $\simeq 4$ marcsec at 90° from the Sun center, $\simeq 0.2$ marcsec at 175° , and is of course null at 180° . So, measurements at small angles from the Sun are interesting as they increase the deflection and reduce the correlation with parallax. Nevertheless, all differential measurements at large angles allow a better randomization of the systematic errors (for a same experiment) and avoid additional plasma bending effects from the solar corona.

We can also, as precision increases, consider planets as gravitational deflectors. For example light bending by the Earth is at the level of $\simeq 40 \mu\text{arcsec}$, while at the Jovian limb, it is predicted to be $\simeq 17$ marcsec.

3.1.2 Present and future constraints on γ

Eddington and his British research group were the first to confirm GR prediction of light bending by the Sun, within 20 to 30% percent accuracy, thanks to a **solar eclipse** on the 29th May 1919. The scarcity of solar eclipses conjugated with unfavorable weather, instrumental... and political conditions did not help though, to improve the precision of these type of measurements during the last century.

The development of **Very Long Baseline Interferometry (VLBI)**, however, brought light deflection measurements to the status of precision tests, thanks to the capability of measuring angular separations and changes in angles as small as $100 \mu\text{arcsec}$. Indeed, early experiments specially designed to measure light deflection were monitoring the change in apparent angular separation of some strong quasi-stellar radio sources as they pass close to the Sun (as seen from the Earth), due to the Earth orbital motion. Using accurate ephemerides for the Earth and the initial position of the quasars, a least square fit of the angular separation then provided a determination of $(1 - \gamma)$. Measurements in 1995 using quasars 3C273 and 3C279 [78] lead to

$$\gamma = 0.9996 \pm 0.0017. \quad (3.2)$$

Now, VLBI type II experiments are in progress, no more dedicated to light deflection, but providing an indirect measurement of γ , while monitoring polar motion and Earth rotation. The project has grown into a network of more than 29 observatories and is sensitive to light deflection over almost the entire celestial sphere. A recent analysis of over 2 million observations quoted by Will [143] from reference [53] (still unpublished) lead to the value of

$$\frac{1 + \gamma}{2} = 0.99992 \pm 0.00014. \quad (3.3)$$

Those VLBI observations provide so far the best measurements of the light deflection effect and through the change in apparent position of light sources (time delay), they give today's most accurate determination of the Post-Newtonian parameter γ [143]. Note however that the accuracy reached for the light deflection by Jupiter is only of 50%.

Today is the blossoming of astrometric measurements (through dedicated satellite surveys or pointing spacecraft projects), as well as the dawn of the satellite experiment era for fundamental physics. Even though **Hipparcos**, a milli-astrometric satellite launched in 1989, only reached a precision of the order of 0.3% on $1 - \gamma$, it opened the way to microarcsecond astrometry which can improve the precision on γ by several orders of magnitude. Hipparcos determination of γ was an indirect one. Indeed, astrometric measurements necessitated the inclusion of stellar aberration up to

terms in $(v/c)^2$, and also a general relativistic treatment of light bending due to the gravitational field of the Sun and Earth, which was done in the setting of General Relativity.

The satellite **GAIA** [15], to be launched in 2011 (or at least no later than 2012) for a five-year mission as a cornerstone of ESA Space Science Program, will increase the domain of observations on light deflection by two orders of magnitude in length and six orders of magnitude in mass. Moreover, GAIA, improving Hipparcos performance, will reduce the avoidance angle towards the Sun²⁷, thus allowing to measure stronger light deflection effects with a reduced parallax correlation.

Notice that with such a precision, GAIA should be sensitive to light deflection due to the main planets. It will probably not be affected by the quadrupole moment of the Sun J_2 though, as this contribution to the light deflection will be negligible in the experiment, owing to the non null avoidance angle of GAIA²⁸.

This should all result into an estimated accuracy of $5 \cdot 10^{-7}$ on γ . This estimate (including only monopole and quadrupole first order terms in (3.32)) was obtained through a *rough* evaluation of GAIA's capabilities in the Study Report [15], assuming individual precision in individual position of stars of $10 \mu\text{arcsec}$. Nevertheless, scaling from Hipparcos results (accuracy, number of light sources) we can conclude to a possible improvement in the determination of γ of by two to three orders of magnitude.

In the meantime, other astrometric satellite experiments should measure the parameter γ (**FAME** 2004, **DIVA** 2004-2006, **SIM** 2009...) through the light deflection effect. On another side, fundamental space experiments of gravitational physics are planned, for example **Cassini**, **Gravity Probe B**, **BepiColombo**, **I.S.S.**, using light deflection or other methods like Doppler effect, geodetic precession, time-delay measurements, mostly with a precision around $10^{-5} - 10^{-6}$.

In Appendix B, we present a summary of various experiments measuring light deflection angles and more generally the PN parameter γ . For each experiment, a description is given and the start/end, advantages/drawbacks, concerning the attainable precision on the determination of γ , main causes of errors, are discussed. The reader might also check the included references for more exhaustive technical details.

3.2 Second order measurement

As VLBI II experimental precision is increasing and future space experiments aim at microarcsecond precision, should we consider the second order in light deflection, or even some other contributions?

3.2.1 Relevance of the impact parameter b

In most gravitational theories, the exact value of the predicted deflection angle requires some numerical integration. Indeed, elliptic functions of the first kind are already necessary in the simple case of General Relativity. Therefore, approximate analytical expressions are often used in the literature both in the weak and strong field limits.

In this paragraph, we would like to point out that when speaking about the asymptotic light deflection angle, $\hat{\alpha}$, at the second order, only expressions in terms of the impact parameter, b , are meaningful²⁹. Although this statement is rather academic in the case of General Relativity, we illustrate how it might have quantitative consequences once one wishes to compare GR predictions with extended theories of gravity.

The aim here is to provide an expression for the asymptotic light deflection angle which is invariant under coordinate transformations; for example shifting from the Schwarzschild coordinates (r, θ, φ) to the isotropic coordinates (ρ, θ, φ) .

²⁷ The GAIA project has been somewhat revised [91] and the avoidance angle is now larger, 40° , than in the previous design, 35° . Note that throughout this work, the original value of 35° is used.

²⁸ In the case of planets like Saturn or Jupiter being the deflector, the contribution of J_2 planet to the light deflection effect is non negligible, due to the important magnitude of J_2 planet and to the fact that grazing incidence is allowed.

²⁹ When the impact parameter is significant, that is to say in theories where the gravitational strength vanishes asymptotically as for example in MTS-SITS theories, but *not* in Weyl gravity.

3.2.1.1 In general

Let us consider a static and spherically symmetric space-time in spherical coordinates (q, θ, φ) , defined by the line element

$$ds^2 = A^2(q) c^2 dt^2 - B^2(q) dq^2 - D^2(q) q^2 (d\theta^2 + \sin^2 \theta d\varphi^2). \quad (3.4)$$

The geodesic equations in the $\theta = \frac{\pi}{2}$ plane lead to the following equation for trajectories:

$$\left(\frac{du}{d\varphi}\right)^2 + \frac{D^2}{B^2} u^2 = \frac{E^2}{J^2} \frac{D^4}{A^2 B^2} - \frac{F}{J^2} \frac{D^4}{B^2} \quad (3.5)$$

where E and J are integration constants for the total energy and the total angular momentum of the particle respectively, while we write

$$u \equiv \frac{1}{q}, \quad F \begin{cases} \equiv 0 & \text{for photons} \\ > 0 & \text{for massive particles} \end{cases}, \quad v \equiv c \quad \text{for photons.}$$

If space-time is asymptotically flat and the trajectory unbound, the impact parameter b can be expressed in terms of E , J , the radial coordinate of the point of closest approach³⁰ (q_0, φ_0) , and the asymptotic speed v of the particle:

$$b = \frac{c J}{v E} = \frac{c}{v} \sqrt{\frac{D^2(q_0)}{A^2(q_0)} - F} \quad q_0. \quad (3.6)$$

Particularizing expressions (3.5) and (3.6) to photons ($F \equiv 0$ and $v \equiv c$) gives the asymptotic light deflection angle $\hat{\alpha}$, usually defined as the angle between the inner and outer asymptotes to the photon trajectory (Figure 3.1),

$$\begin{aligned} \hat{\alpha}_{\text{exact}}(q_0) &\equiv 2 \int_0^{\varphi_0} d\varphi - \pi \\ &= 2 \int_{q_0}^{\infty} \frac{B(q)}{D(q)} \left\{ \left(\frac{q}{q_0}\right)^2 \frac{D^2(q)}{D^2(q_0)} \frac{A^2(q_0)}{A^2(q)} - 1 \right\}^{-\frac{1}{2}} \frac{dq}{q} - \pi. \end{aligned} \quad (3.7)$$

This exact expression requires in general a numerical integration.

When working in Schwarzschild coordinates ($q \equiv r$, $A^2 \equiv B^{-2} = 1 + 2V(r)/c^2 + \dots$ and $D \equiv 1$) **with a gravitational potential** $V(r)$, the exact expression reads

$$\hat{\alpha}_{\text{exact}}(r_0) = 2 |\varphi(r_0)| - \pi \quad (3.8)$$

$$\text{with } \varphi(r) = \int_0^{\sin \chi = r_0/r} \frac{\cos \chi}{\sqrt{A^2(r_0) - \sin^2 \chi A^2(r)}} d\chi. \quad (3.9)$$

In the weak field approximation at first order in $V(r)/c^2$, it is sufficient to write

$$\hat{\alpha}_{\text{weak field}}(r_0) = 2 \frac{V(r_0)}{c^2} \left| \int_0^{\pi/2} \left[-\sec^2 \chi + \frac{V(r)}{V(r_0)} (\sec^2 \chi - 1) \right] d\chi \right|. \quad (3.10)$$

When looking at second order contributions, it is usually more convenient to use the Eddington-Robertson-Schiff parametrization defined in the isotropic coordinates ($q \equiv \rho$ and $D \equiv B$), see Paragraph 1.6.1. In this

³⁰ In case of bound orbits, the point (q_0, φ_0) where $du/d\varphi = 0$ can be either the closest approach distance (perihelion) or the farthest approach distance (aphelion).

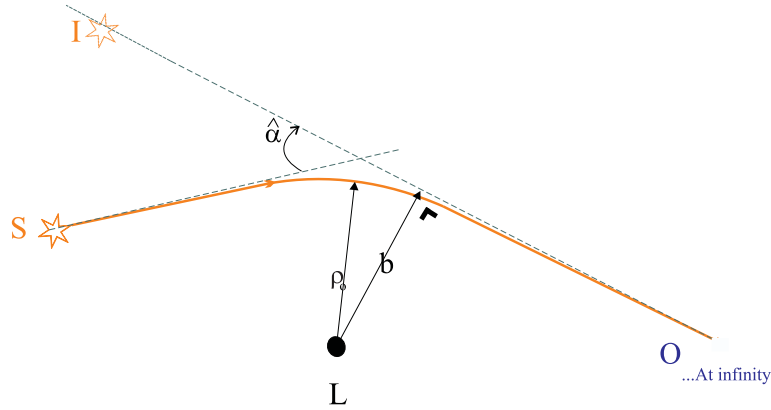


Fig. 3.1 Definition of the asymptotic light deflection angle. I= Image; S= Source; O= Observer; L= Lens (gravitational potential); $\hat{\alpha}$ = asymptotic light deflexion angle; ρ_0 = closest approach distance, written here in the isotropic coordinates (ρ, θ, φ) ; b = impact parameter. The solid line shows the light path while the dash line shows the inner and outer asymptotes to the geodesics.

approximation, the deflection angle as a function of the closest approach distance reads

$$\hat{\alpha}_{\text{weak field}}(\rho_0) = \frac{4GM}{c^2\rho_0} \left\{ \left(\frac{\alpha + \gamma}{2} \right) + \left[-\frac{(\alpha + \gamma)^2}{2} + \frac{(8\alpha^2 + 8\alpha\gamma - 4\beta + 3\delta)}{16} \pi \right] \frac{GM}{c^2\rho_0} \right\} + O\left(\frac{V^3}{c^6}\right). \quad (3.11)$$

Notice that thanks to this formalism, one easily checks the absence of light deflection in a space-time endowed with a conformally flat metric

$$g_{\mu\nu} = \left(1 + \frac{V}{c^2}\right)^2 \eta_{\mu\nu},$$

a theory which thus must be rejected according to observations.

However, we could also think of writing the deflection angle in the weak field limit in terms of the impact parameter, using expression (3.6) in isotropic coordinates. This leads to

$$\hat{\alpha}_{\text{weak field}}(b) = \frac{4GM}{c^2b} \left\{ \left(\frac{\alpha + \gamma}{2} \right) + \left[0 + \frac{(8\alpha^2 + 8\alpha\gamma - 4\beta + 3\delta)}{16} \pi \right] \frac{GM}{c^2b} \right\} + O\left(\frac{V^3}{c^6}\right). \quad (3.12)$$

We already notice the difference in the second order term between $\hat{\alpha}_{\text{weak field}}(\rho_0)$, equation (3.11) and $\hat{\alpha}_{\text{weak field}}(b)$, equation (3.12).

3.2.1.2 GR

In the case of General Relativity, **the Schwarzschild coordinates** ($q \equiv r$ and $B \equiv A^{-1}$) correspond to the choice

$$\begin{aligned} A^2(r) &= B^{-2}(r) = 1 - \frac{2GM}{c^2r}, \\ D^2(r) &= 1, \end{aligned} \quad (3.13)$$

for the well-known Schwarzschild metric.

Assuming that the closest approach distance (r_0) verifies (4.17) with (4.16) and $\Upsilon_{GR} \equiv 0$ to ensure deflection (these conditions will be explained when we will comment on the effective geodesic potential for photons, in Section 4.3.1.2), we obtain from equations (3.7) and (3.13) the asymptotic angle as an *exact* function of the closest approach distance [93]:

$$\hat{\alpha}(r_0) = 4 \left(\frac{r_0}{w} \right)^{\frac{1}{2}} \left[F\left(\frac{\pi}{2}, k\right) - F(\sigma_0, k) \right] - \pi. \quad (3.14)$$

Here, the elliptic integral of the first kind

$$F(\sigma, k) \equiv \int_0^\sigma \frac{dx}{\{1 - k^2 \sin^2 x\}^{\frac{1}{2}}} \quad (3.15)$$

is characterized by the amplitude σ with

$$\sigma_0 = \arcsin \left\{ \frac{w - r_0 + 2\frac{GM}{c^2}}{w - r_0 + 6\frac{GM}{c^2}} \right\}^{\frac{1}{2}} \quad (3.16)$$

and the modulus

$$k = \left\{ \frac{w - r_0 + 6\frac{GM}{c^2}}{2w} \right\}^{\frac{1}{2}} \quad (3.17)$$

where

$$w \equiv \left\{ \left(1 - \frac{2\frac{GM}{c^2}}{r_0} \right) \left(1 + \frac{6\frac{GM}{c^2}}{r_0} \right)^{\frac{1}{2}} \right\} r_0.$$

From this exact expression, we can obtain a **weak field approximation**, considering that

$$\epsilon \equiv \frac{GM}{c^2 r_0} \ll 1$$

and the modulus is small

$$k^2 = 4\epsilon(1 - 3\epsilon) + O(\epsilon^3).$$

Hence, expanding the elliptic integrals

$$\begin{aligned} F\left(\frac{\pi}{2}, k\right) &\simeq \frac{\pi}{2} \left(1 + \epsilon - \frac{3}{4}\epsilon^2 \right), \\ F(\sigma_0, k) &\simeq \frac{\pi}{4} \left(1 + \epsilon - \frac{3}{4}\epsilon^2 \right) - \epsilon, \end{aligned}$$

we obtain

$$\hat{\alpha}_{\text{weak field}}(r_0) \simeq \frac{4GM}{c^2 r_0} \left\{ 1 + \left[-1 + \frac{15}{16}\pi \right] \frac{GM}{c^2 r_0} \right\}. \quad (3.18)$$

Alternatively, using the expression (3.14), we could obtain a **strong field approximation**, noting that in this latter case

$$\epsilon \equiv 1 - \frac{3GM}{c^2 r_0} \ll 1,$$

and the modulus is close to 1 :

$$k^2 = 1 - \frac{4}{3}\epsilon + O(\epsilon^2).$$

Thus, expanding again the elliptic integrals

$$\begin{aligned} F\left(\frac{\pi}{2}, k\right) &\simeq \ln \frac{4}{\sqrt{1 - k^2}}, \\ F\left(\arcsin \frac{1}{\sqrt{3}}, 1\right) &\simeq 0.65848, \end{aligned}$$

a simple analytical expression for the deflection angle of a light ray grazing a black hole [93] is found:

$$\hat{\alpha}_{\text{strong field}}(b) \simeq \ln \left(\frac{3.482GM}{c^2 b - 3\sqrt{3}GM} \right). \quad (3.19)$$

The impact parameter here appears naturally... but how does one measure it?

If we are working **in the isotropic coordinates**, using the Eddington-Robertson-Schiff parameters given in Section 1.6.5 and expression (3.6), we find the following weak field angle

$$\hat{\alpha}_{\text{weak field}}(\rho_0) \simeq \frac{4GM}{c^2\rho_0} \left\{ 1 + \left[-2 + \frac{15}{16}\pi \right] \frac{GM}{c^2\rho_0} \right\}. \quad (3.20)$$

The apparent second order discrepancy between equations (3.18) and (3.20) can be understood in the following way. The asymptotic deflection angle should be an observable by definition; it has to be fully expressed in terms of measurable, *i.e.* coordinate independent, quantities. Here, the closest distance of approach (r_0 in Schwarzschild coordinates, ρ_0 in isotropic coordinates) is obviously not such a measurable quantity. Its corresponding substitution by the impact parameter b according to the identity (3.6) taken respectively in the Schwarzschild and in the isotropic coordinates,

$$\begin{aligned} b &\simeq r_0 + \frac{GM}{c^2} \\ &\simeq \rho_0 + 2\frac{GM}{c^2}, \end{aligned} \quad (3.21)$$

reconciliates our results of calculations performed with two physically equivalent forms of the metric. In General Relativity, the asymptotic deflection angle is correctly given by

$$\hat{\alpha}_{\text{weak field}}(b) = \frac{4GM}{c^2b} \left\{ 1 + \left[0 + \frac{15\pi}{16} \right] \frac{GM}{c^2b} \right\} + O\left(\frac{G^3M^3}{b^3c^6}\right). \quad (3.22)$$

This is analogous to what has been noted by Roos and Schiff [117] for the radar-echo experiment where the observable transit time has to be expressed in terms of the measurable orbital parameters (periods and eccentricities).

Equations (3.22) and (3.19) provide us with useful (weak and strong field, respectively) approximations to study lensing effects in terms of the asymptotic deflection angle $\hat{\alpha}(b)$ in the framework of GR. They readily replace the unpractical exact expression obtained from equation (3.14) after substitution of r_0 by b according to equations (3.21). However, the second order contribution to the deflection angle in equation (3.22) only improves the weak field approximation in a narrow domain of the impact parameter (Figure 3.2). In that sense, our comment on the ambiguous coordinate dependence of $\hat{\alpha}(r_0)$ defined in equation (3.18) is rather academic as far as General Relativity is concerned.

3.2.1.3 MTS/SITS

In the Schwarzschild coordinates, equation (3.7) and the MTS metric (1.29) imply

$$\hat{\alpha}_{\text{weak field}}(r_0) \simeq \frac{4GM}{c^2r_0} \left\{ 1 + \left[-2 + \frac{1}{\Upsilon} + \left(1 - \frac{1}{16\Upsilon^2}\right)\pi \right] \frac{GM}{c^2r_0} \right\}, \quad (3.23)$$

in the weak field approximation, if the condition on the closest approach distance, (4.17) with (4.16), to insure light deflection is fulfilled (see comments on the effective geodesic potential for photons in Section 4.3.1.2).

On the other hand, **in isotropic coordinates**, the MTS Eddington-Robertson-Schiff parameters in equation (3.11) lead to

$$\hat{\alpha}_{\text{weak field}}(\rho_0) \simeq \frac{4GM}{c^2\rho_0} \left\{ 1 + \left[-2 + \left(1 - \frac{1}{16\Upsilon^2}\right)\pi \right] \frac{GM}{c^2\rho_0} \right\}. \quad (3.24)$$

Since a deviation from GR arises only at the second order, the use of the physical impact parameter b according to identity (3.6) taken respectively in the Schwarzschild and in the isotropic coordinates,

$$b \simeq r_0 + \left(2 - \frac{1}{\Upsilon}\right) \frac{GM}{c^2} \simeq \rho_0 + 2\frac{GM}{c^2},$$

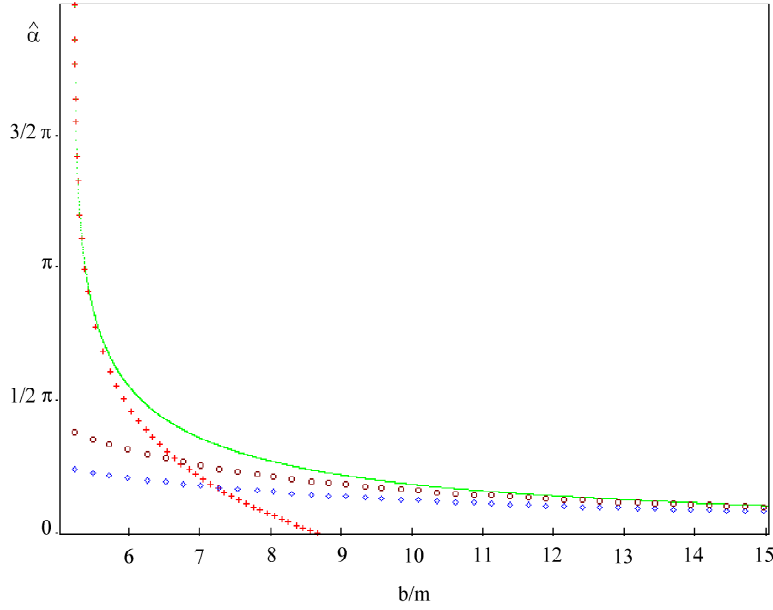


Fig. 3.2 The asymptotic light deflection angle $\hat{\alpha}$ predicted by GR as a function of the impact parameter b/m with $m \equiv GM/c^2$. The smooth curve corresponds to the exact expression after substitution of the closest distance of approach r_0 by b . Crosses (+) stand for the strong field approximation. Diamonds (\diamond) and circles (\circ) represent respectively the first and second order approximations in the weak field limit.

is now crucial to obtain the asymptotic deflection angle:

$$\hat{\alpha}_{\text{weak field}}(b) = \frac{4GM}{c^2 b} \left\{ 1 + \left(1 - \frac{1}{16\Upsilon^2} \right) \pi \frac{GM}{c^2 b} \right\} + O\left(\frac{G^3 M^3}{b^3 c^6}\right). \quad (3.25)$$

The same result for $\hat{\alpha}_{\text{weak field}}(b)$ would be obtained if working with the SITS theory whose Eddington-Robertson-Schiff parameters are given in Section 1.6.5.

Notice that the authors of reference [136] only gave the coordinate dependent equation (3.7) to analyze the quantitative modifications of lensing characteristics in the presence of the massless scalar field $\tilde{\Phi}$. We have just argued that equations (3.7) and (3.6) should always be carefully handled to get rid of the closest distance of approach dependence. The asymptotic deflection angle $\hat{\alpha}$ is then correctly expressed in terms of the physical impact parameter and does not depend on the arbitrary choice of a coordinate system.

3.2.2 Measurability of the impact parameter b and asymptotic deflection angle $\hat{\alpha}$

Unfortunately, the impact parameter is not a measurable quantity in the framework of the change in the apparent position of light sources. Indeed, to be able to measure the impact parameter, the observer should lie on the outer asymptote of the trajectory of the photon (see Figure 3.1). *In that case only*, the impact parameter is given exactly by

$$b = \rho_{obs} \cdot \sin \vartheta_I,$$

where ρ_{obs} is the radial distance from the gravitational deflector, say the Sun, to the observer; and ϑ_I is the angular position of the image with respect to the lens-observer axis. Both ρ_{obs} and ϑ_I are measurable quantities. We can now understand why, when considering changes in the apparent position of objects (when the gravitational source is not sufficiently far so to consider that the observer lies on the asymptote of the trajectory of the photon), the quantity $\hat{\alpha}$, **the asymptotic light deflection angle, defined as the angle between the inner and outer asymptotes of the**

trajectory of the photon, is not an appropriate observable quantity (see Figure 3.1). Instead, one should prefer the quantity $\Delta\vartheta$, the **finite distance light deflection angle**, defined as the angle between the position of the object in the sky when the gravitational deflector is absent (ϑ) and the position of its image when the gravitational source is present (ϑ_I), still with respect to the lens-observer axis (see Figure 3.3). That is

$$\begin{aligned}\Delta\vartheta &= \vartheta_I - \vartheta \\ &= \vartheta_I - (\pi - \varphi_{obs}),\end{aligned}\quad (3.26)$$

where ϑ_I is defined by the tangent to the light trajectory at the observer (see Figure 3.4),

$$\tan \vartheta_I = \frac{e_\varphi}{e_\rho} \Big|_{obs} = \left(\sqrt{\frac{g_{\varphi\varphi}}{g_{\rho\rho}}} \frac{d\varphi}{d\rho} \right) \Big|_{obs}, \quad (3.27)$$

and $\Delta\vartheta$ is indeed the true displacement in the apparent position of the object. Thus, when observing at infinity, we recover the asymptotic light deflection angle:

$$\begin{aligned}\Delta\vartheta &\xrightarrow{\rho_{obs} \rightarrow \infty} \hat{\alpha}, \\ \varphi_{obs} &\xrightarrow{\rho_{obs} \rightarrow \infty} \pi, \\ \vartheta_I &\xrightarrow{\rho_{obs} \rightarrow \infty} 0.\end{aligned}$$

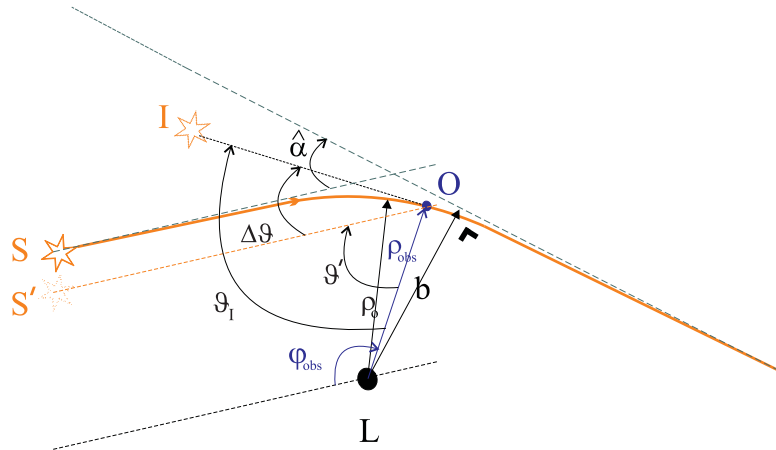


Fig. 3.3 Definition of the finite distance light deflection angle. I= Image; S= Source in presence of the gravitational potential; S' = Source when the gravitational potential is absent and the light goes straight to the observer; O= Observer; L= Lens (gravitational potential); $\hat{\alpha}$ = asymptotic light deflection angle; $\Delta\vartheta$ = finite distance light deflection angle; $(\rho_{obs}, \theta_{obs} \equiv \frac{\pi}{2}, \varphi_{obs})$ = the position of O written in isotropic coordinates; b = impact parameter; ρ_0 = closest approach distance; ϑ' , ϑ_I = angular positions of S' and I with respect to the O-L axis. The solid line shows the light path. Notice that ρ_0 is defined from the lens to the trajectory of the photon, while b is defined from the lens to the asymptote.

The distinction between $\hat{\alpha}$ and $\Delta\vartheta$ is irrelevant when considering only the first order contribution to light deflection, as it is irrelevant to distinguish between r_0 , ρ_0 and b at that level of precision. However, it may become crucial when looking at the second order: see for example light deflection due to the Sun (compare the B - and the E -contributions in Table (3.36)). Indeed the finite distance light deflection angle contains a term (B in (3.34)) that scales as the inverse of ρ_{obs}^2 , so that we recover the asymptotic light deflection angle only at a sufficiently large distance with respect to the square of the lens radius R (see expressions (3.32) and (3.34)). Notice finally that in the case of gravitational mirages, where distances between the source, the lens and the observer are large with respect to the radius of the lens, $\hat{\alpha} \simeq \Delta\vartheta$ with a sufficient accuracy.

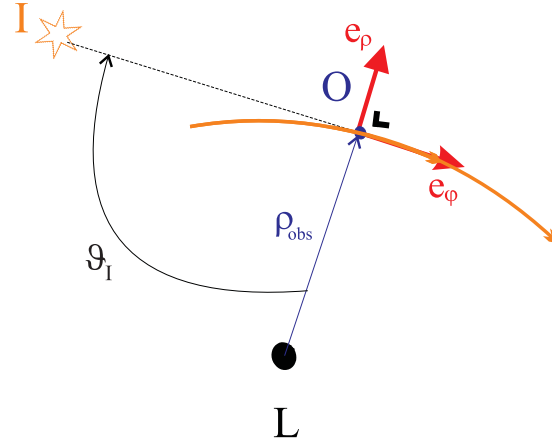


Fig. 3.4 Tangent to the light path at the observer.

3.2.3 Other effects: non sphericity of the gravitational source, angular momentum

In this section, we will calculate the finite distance light deflection angle, incorporating several effects like the deflector quadrupole moment and angular momentum. We will consider Fully Conservative, Purely Dynamical theories of gravity (in terms of PN parameters, $\alpha_3 = \zeta_1 = \zeta_2 = \zeta_3 = \zeta_4 = \xi = 0$).

Let us assume a quasi-spherically symmetric space-time **in isotropic coordinates**, defined by the line element

$$ds^2 = A^2(\rho) c^2 dt^2 - B^2(\rho) (d\rho^2 + \rho^2 d\theta^2 + \rho^2 \sin^2 \theta d\varphi^2) + 2H^2(\rho) dt (d\rho + \rho d\theta + \rho \sin \theta d\varphi) \quad (3.28)$$

and consider that the gravitational lens shows some oblateness (a quadrupole moment J_2 contributes to the potential expansion $U = U(\rho)$) and is in rigid homogeneous rotation (angular momentum \vec{J}) (see Figure 3.5).

It is sufficient when treating light deflection in the solar system to express the metric coefficients as [113, 130]:

$$\begin{aligned} A^2(\rho) &\simeq 1 + 2\alpha \left(\frac{U}{c^2}\right) + 2\beta \left(\frac{U}{c^2}\right)^2 + \mathcal{O}\left(\frac{1}{c^5}\right), \\ B^2(\rho) &\simeq 1 - 2\gamma \left(\frac{U}{c^2}\right) + \frac{3}{2}\delta \left(\frac{U}{c^2}\right)^2 + \mathcal{O}\left(\frac{1}{c^5}\right), \\ H^2(\rho) &\simeq 2(1 + \gamma) G_N \frac{\vec{J} \times \vec{\rho}}{2\rho^3 c^3} + \mathcal{O}\left(\frac{1}{c^5}\right), \end{aligned} \quad (3.29)$$

with the potential (at this order, the quadrupole contribution is sufficient)

$$\begin{aligned} U(\rho, \theta) &= -\frac{GM}{\rho} \left[1 - \sum_{n \text{ even}} \left(\frac{R}{\rho}\right)^n J_n P_n(\cos \theta) \right] \\ &\simeq -\frac{GM}{\rho} \left[1 - \left(\frac{R}{\rho}\right)^2 J_2 P_2(\cos \theta) \right] \\ &= -\frac{GM}{\rho} \left[1 - \left(\frac{R}{\rho}\right)^2 J_2 \left(1 - \frac{3}{2} \sin^2 \theta\right) \right], \end{aligned}$$

where α, β, γ , are the usual PN parameters, and δ is a Post-PN parameter.

Notice that owing to the smallness of J_2 among solar system bodies, we can neglect the quadrupole contribution in the β - and δ -terms.

The corresponding metric being independent of the coordinate φ , the angular momentum of the photon is thus conserved and θ is fixed on the photon path. *Let us consider the null geodesic equations in the equatorial plane of the gravitational*

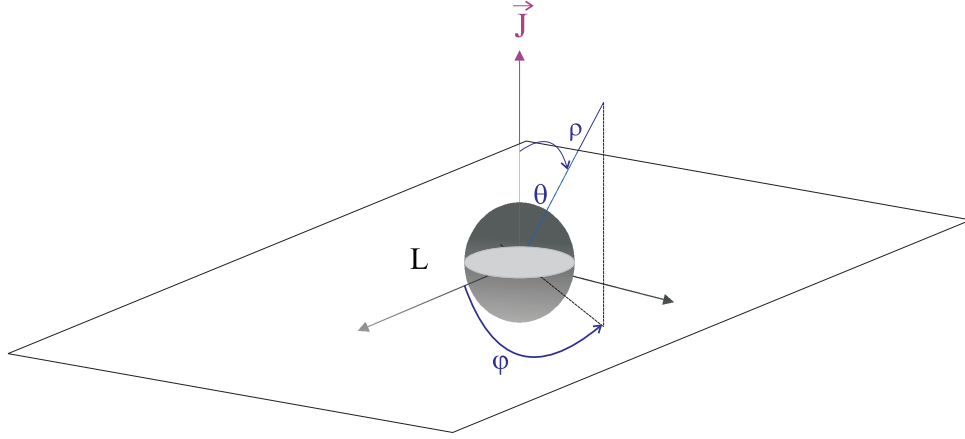


Fig. 3.5 Isotropic coordinates system (ρ, θ, φ) centered on the Lens (L) with angular momentum \vec{J} . The equatorial plane corresponds to $\theta = \pi/2$.

deflector ($\theta = \frac{\pi}{2}$). They lead to the following equation for the photon trajectory, with $u \equiv 1/\rho$:

$$H^4 \left(u - \frac{du}{d\varphi} \right)^2 + A^2 B^2 \left(u^2 + \left(\frac{du}{d\varphi} \right)^2 \right) = \frac{\left[\frac{H^4}{A^2} \left(u - \frac{du}{d\varphi} \right) + B^2 \right]^2}{\left[\frac{H^2}{A^2} - b u \right]^2} u^2.$$

Collecting terms up to $\mathcal{O}\left(\frac{1}{c^5}\right)$ gives

$$\begin{aligned} \left(\frac{du}{d\varphi} \right)^2 + \left\{ 1 - 2 \left(2\alpha^2 + 2\alpha\gamma - \beta + \frac{3}{4}\delta \right) \left(\frac{G_N M}{c^2} \right)^2 \frac{1}{b^2} \right\} u^2 - (\alpha + \gamma) J_2 \frac{R^2}{b^4} \frac{G_N M}{c^2} u^3 \\ \simeq \frac{1}{b^2} + 2 (\alpha + \gamma) \frac{1}{b^2} \frac{G_N M}{c^2} u + (\pm) 4 (1 + \gamma) \frac{1}{b^3} \frac{G_N |\vec{J}|}{c^3} u. \end{aligned}$$

The trajectory can be integrated:

$$\begin{aligned} \varphi &\simeq \pm \int_0^u \frac{du}{\left(\frac{du}{d\varphi} \right)} \\ &\simeq \pm \arcsin(b u) \\ &\mp (\alpha + \gamma) \frac{1}{b^2} \left(\frac{G_N M}{c^2} \right) \left[\frac{1}{\left(\frac{1}{b^2} - u^2 \right)^{1/2}} - b \right] \\ &\mp (\alpha + \gamma) \frac{J_2}{2} \frac{R^2}{b^2} \left(\frac{G_N M}{c^2} \right) \left[\frac{-u^2}{\left(\frac{1}{b^2} - u^2 \right)^{1/2}} + \frac{2}{b^2 \left(\frac{1}{b^2} - u^2 \right)^{1/2}} - \frac{2}{b} \right] \\ &\mp 2 (1 + \gamma) \frac{1}{b^3} \frac{(\pm) G_N |\vec{J}|}{c^3} \left[\frac{1}{\left(\frac{1}{b^2} - u^2 \right)^{1/2}} - b \right] \\ &\mp \left(2\alpha^2 + 2\alpha\gamma - \beta + \frac{3}{4}\delta \right) \frac{1}{b^2} \left(\frac{G_N M}{c^2} \right)^2 \left[\frac{u}{\left(\frac{1}{b^2} - u^2 \right)^{1/2}} - \arctan \left(\frac{u}{\left(\frac{1}{b^2} - u^2 \right)^{1/2}} \right) \right] \\ &\pm \frac{(\alpha + \gamma)^2}{2} \frac{1}{b^2} \left(\frac{G_N M}{c^2} \right)^2 \left[\frac{u^3}{\left(\frac{1}{b^2} - u^2 \right)^{3/2}} \right] \\ &+ cst, \end{aligned}$$

or, knowing that at $\varphi = 0$, we have $\rho_{\varphi=0} = \infty$, in other words $u_{\varphi=0} = 0$, and

$$\begin{aligned}
b u &\simeq + \sin(\pm\varphi) \\
&+ (1 - \cos \varphi) (\alpha + \gamma) \frac{1}{b} \left(\frac{G_{NM}}{c^2} \right) \\
&+ (1 - \cos \varphi)^2 (\alpha + \gamma) \frac{J_2}{2} \frac{R^2}{b^2} \frac{1}{b} \left(\frac{G_{NM}}{c^2} \right) \\
&+ (1 - \cos \varphi) \frac{1}{b^2} 2 (1 + \gamma) \frac{(\pm) G_N |\vec{J}|}{2 c^3} \\
&+ \cos \varphi (\tan \varphi - \varphi) \left(2\alpha^2 + 2\alpha\gamma - \beta + \frac{3}{4}\delta \right) \frac{1}{b^2} \left(\frac{G_{NM}}{c^2} \right)^2. \tag{3.30}
\end{aligned}$$

We can expand expression (3.27) using identity (3.26) for its left-hand side and the expansion of the metric (3.28), (3.29) for its right-hand side:

$$-\tan \varphi_{obs} + \frac{1}{\cos^2 \varphi_{obs}} \Delta\vartheta - \tan \varphi_{obs} \frac{1}{\cos^2 \varphi_{obs}} \Delta\vartheta^2 \simeq - \left[b/\rho \frac{d\varphi}{d(b/\rho)} \right] \Big|_{obs}.$$

Replacing the trajectory solution (3.30) in this last result, we find

$$\begin{aligned}
\Delta\vartheta(b) &\simeq + (1 + \cos \vartheta_I) (\alpha + \gamma) \left(\frac{G_{NM}}{b c^2} \right) \\
&+ (1 + \cos \vartheta_I) (2 + \cos \vartheta_I - \cos^2 \vartheta_I) (\alpha + \gamma) \frac{J_2}{2} \frac{R^2}{b^2} \left(\frac{G_{NM}}{b c^2} \right) \\
&+ (1 + \cos \vartheta_I) 2 (1 + \gamma) \frac{(\pm) G_N |\vec{J}|}{2 b^2 c^3} \\
&+ (\pi - \vartheta_I + \sin \vartheta_I \cos \vartheta_I) \left(2\alpha^2 + 2\alpha\gamma - \beta + \frac{3}{4}\delta \right) \left(\frac{G_{NM}}{b c^2} \right)^2 \\
&+ \mathcal{O} \left(\frac{1}{c^5} \right).
\end{aligned}$$

However, we still need to get rid of the impact parameter b , which is not measurable, and rephrase this expression using the observables ρ_{obs} and ϑ_I . The trajectory solution (3.30) taken at the observation point $(\rho_{obs}, \varphi_{obs})$ together with identity (3.26) provide an approximation for the impact parameter in terms of the observables at the required order:

$$\frac{1}{b} \simeq \frac{1}{\rho_{obs} \sin \vartheta_I} - (\alpha + \gamma) \frac{1}{\rho_{obs}^2 \sin \vartheta_I} \left(\frac{G_{NM}}{c^2} \right) + \mathcal{O} \left(\frac{1}{c^3} \right). \tag{3.31}$$

This allows us to rewrite the change in the apparent position of the light source as

$$\Delta\vartheta(\rho_{obs}, \vartheta_I) \simeq + \left[\begin{aligned} &+ \underbrace{\sqrt{\frac{1 + \cos \vartheta_I}{1 - \cos \vartheta_I}} (\alpha + \gamma)}_{A+B} \\ &+ \underbrace{\frac{(2 + 3 \cos \vartheta_I - \cos^3 \vartheta_I)}{\sin^3 \vartheta_I}}_C (\alpha + \gamma) \frac{J_2}{2} \frac{R^2}{\rho_{obs}^2} \end{aligned} \right] \left(\frac{G_{NM}}{\rho_{obs} c^2} \right)$$

$$\begin{aligned}
& + \left[\underbrace{\frac{1}{1 - \cos \vartheta_I} 2 (1 + \gamma)}_D \right] \frac{(\pm) G_N |\vec{J}|}{2 \rho_{obs}^2 c^3} \\
& + \left[\underbrace{\begin{aligned} & + \frac{\pi - \vartheta_I + \sin \vartheta_I \cos \vartheta_I}{\sin^2 \vartheta_I} (2\alpha^2 + 2\alpha\gamma - \beta + \frac{3}{4}\delta) \\ & - \sqrt{\frac{1 + \cos \vartheta_I}{1 - \cos \vartheta_I}} (\alpha + \gamma)^2 \end{aligned}}_E \right] \left(\frac{G_N M}{\rho_{obs} c^2} \right)^2 \\
& + \mathcal{O} \left(\frac{1}{c^5} \right). \tag{3.32}
\end{aligned}$$

Note the appearance of the $(\alpha + \gamma)^2$ -term when we substitute the impact parameter. Similarly to our earlier observation for $\hat{\alpha}$ in Paragraph 3.2.1, the expression of $\Delta\vartheta$ in terms of the isotropic radial coordinate of the observer (ρ_{obs}) is not coordinate invariant, unlike the expression in terms of the impact parameter (b). We conclusively realize the importance of having a coherent full PPN astrometric reference frame system in order to analyze the data to test for light deflection at the second order. Presently, as mentioned by Klioner and Soffel [75], there is a contradiction between the recommendation of the International Astronomical Union (IAU) concerning the relativistic reference system to be used for data reduction - like in VLBI measurements - which are only valid in the framework of GR, and the common practice to estimate the PN parameters (at least γ and β) from observations.

To obtain an estimation of the PN parameter γ from satellite measurements or VLBI data, expression (3.32) must be considered as the deflection angle $\Delta\vartheta_i$ due to the gravitational field of the i -th deflector characterized by R_i , M_i , J_{2i} and \vec{J}_i , when the light source is observed at an angle ϑ_{Ii} from this i -th body. $\Delta\vartheta_i$ is then summed over all the i -th bodies (Sun, Moon and planets) and is part of a multiparameter model that will be fitted to the observations. Although all the planets might be included in the model, mostly the Sun and Jupiter are important for the determination at present. For VLBI measurements, for example, it is very rare for other planets to pass sufficiently close to suitable radio sources. As far as the Earth contribution is concerned, in the case of VLBI, this contribution is static as seen from each antenna, for Earth-based networks used at present, and it cannot be separated, in the solution, from the station position and axis offset parameters. But this effect should be observable given future space-based observations, future optical interferometers in space or astrometric satellites... (see Appendix B).

In order to compare the order of magnitude of the different contributions to the light deflection angle at a finite distance, it is usually useful to consider its maximum value. To do so, we need to replace the value of ϑ_I that maximizes $\Delta\vartheta(\rho_{obs}, \vartheta_I)$ in expression (3.32), to obtain the grazing incidence. Using (3.30) taken once at the grazing incidence ($\rho = 1/u = R$, $\varphi \simeq \pi/2$) and once at the observation point ($\rho = 1/u = \rho_{obs}$, $\varphi = \varphi_{obs}$), we get

$$\sin \vartheta_{I \text{ grazing}} \simeq \frac{R}{\rho_{obs}} \left\{ 1 + (\alpha + \gamma) \frac{G_N M}{R c^2} \left[1 - \frac{R}{\rho_{obs}} \right] \right\}, \tag{3.33}$$

when equating the impact parameter in both expressions at the required order. Note that $\vartheta_{I \text{ grazing}}$ is always nonvanishing. We then replace this latter expression in (3.32), expand up to $\mathcal{O}(\frac{1}{c^5})$, and ignore terms such as $(J_2)^2$ since $J_2 \sim 10^{-7}$.

The light deflection angle at grazing incidence in the weak field limit due to a gravitational deflector of mass M , radius R , quadrupole moment J_2 , and angular momentum \vec{J} is thus, for an observer at a radial distance ρ_{obs} (in isotropic coordinates),

$$\begin{aligned}
\Delta\vartheta_{\text{grazing}}(\rho_{\text{obs}}) \simeq & + \left[\underbrace{2(\alpha + \gamma)}_A - \underbrace{\frac{1}{2}(\alpha + \gamma) \frac{R^2}{\rho_{\text{obs}}^2}}_B + \underbrace{2(\alpha + \gamma) J_2}_C \right] \left(\frac{G_N M}{R c^2} \right) \\
& + \left[\underbrace{(\pm) 2(1 + \gamma)}_D \right] \left(\frac{G_N |\vec{J}|}{R^2 c^3} \right) \\
& + \left[\underbrace{(8\alpha^2 + 8\alpha\gamma - 4\beta + 3\delta) \frac{\pi}{4} - 2(\alpha + \gamma)^2}_E \right] \left(\frac{G_N M}{R c^2} \right)^2 + \dots \quad (3.34)
\end{aligned}$$

Of course, we recover the maximum grazing asymptotic angle when sending the observer at infinity ($B \rightarrow 0$).

3.2.4 Orders of magnitude of the different contributions

A/ When the angle between the observed image and the deflector varies

The graphs in Figure 3.6 and Table (3.35) will help us to discuss the different contributions to the light deflection angle as obtained from formula (3.32). We present here the particular case of an observer located on Earth, in the setting of GR ($\alpha = \beta = \gamma = \delta = 1$), and for light deflection taking place in the equatorial plane of a rigidly rotating deflector (perpendicular to \vec{J}). The characteristics of different deflectors, namely M , R , J_2 , \vec{J} and $\rho_{\text{obs}} =$ maximum/minimum Earth-deflector distances are taken from the factsheets in reference [16].

In Figure 3.6, the plots give the order of magnitude of the different contributions to the gravitational light deflection angle due to the Sun and Jupiter.

We can see that at large angles (ϑ_I) from the gravitational deflector, the different contributions to the light deflection angle decrease rapidly; and that corrections to the usual first order contribution with spherical symmetry ($J_2 = 0$) are soon negligible at the microarcsecond level. We also easily understand from these graphs and Table (3.36) why the Sun is our best solar system laboratory.

Table (3.35) provides the maximum observation angle from the deflector ($\vartheta_{I \text{ max}}$) at which the terms $A+B$, C , D or E in the light deflection angle (3.32) become negligible for microarcsecond astrometry; *i.e.* when the corresponding term is inferior to $1 \mu\text{arcsec}$ for $\vartheta_{I \text{ max } 1}$ or to $10 \mu\text{arcsec}$ for $\vartheta_{I \text{ max } 10}$. In this table, a “–” sign means that the corresponding term (C , D or E) is negligible (inferior to $1 \mu\text{arcsec}$ or $10 \mu\text{arcsec}$ respectively) at any angle from the deflector. The elements in the table are given in decreasing first order contribution.

Remark that the influence of the distance between the gravitational deflector and the observer might be non negligible; the largest distance from the observer to the deflector leads to the smallest maximum observation angle from the image to the deflector (first value given), while the smallest distance leads to the largest maximum angle (second value given). We also note that if satellites like Titania, Oberon... must be considered in microarcsecond astrometry (at least at the $1 \mu\text{arcsec}$ level), it is only within one arcsecond from those bodies.

One can alternatively consider an observer on a geostationary satellite on orbit at about 36 000 kilometers, or a satellite like the future GAIA on its L2 orbit at about 1.5 million kilometers from the Earth. It is then only the maximum observation angles to the Earth and to the Moon which are sensibly modified, owing to the accordingly non negligible change in the observer-deflector distance. Indeed, we find for a geostationary satellite

$$\begin{aligned}
\text{for the Earth: } & \begin{cases} \vartheta_{I \text{ max } 1} \simeq 177.4^\circ, \\ \vartheta_{I \text{ max } 10} \simeq 154.0^\circ, \end{cases} \\
\text{for the Moon: } & \begin{cases} \vartheta_{I \text{ max } 1} \simeq 5.9^\circ - 7.9^\circ, \\ \vartheta_{I \text{ max } 10} \simeq 35.1' - 47.1'; \end{cases}
\end{aligned}$$

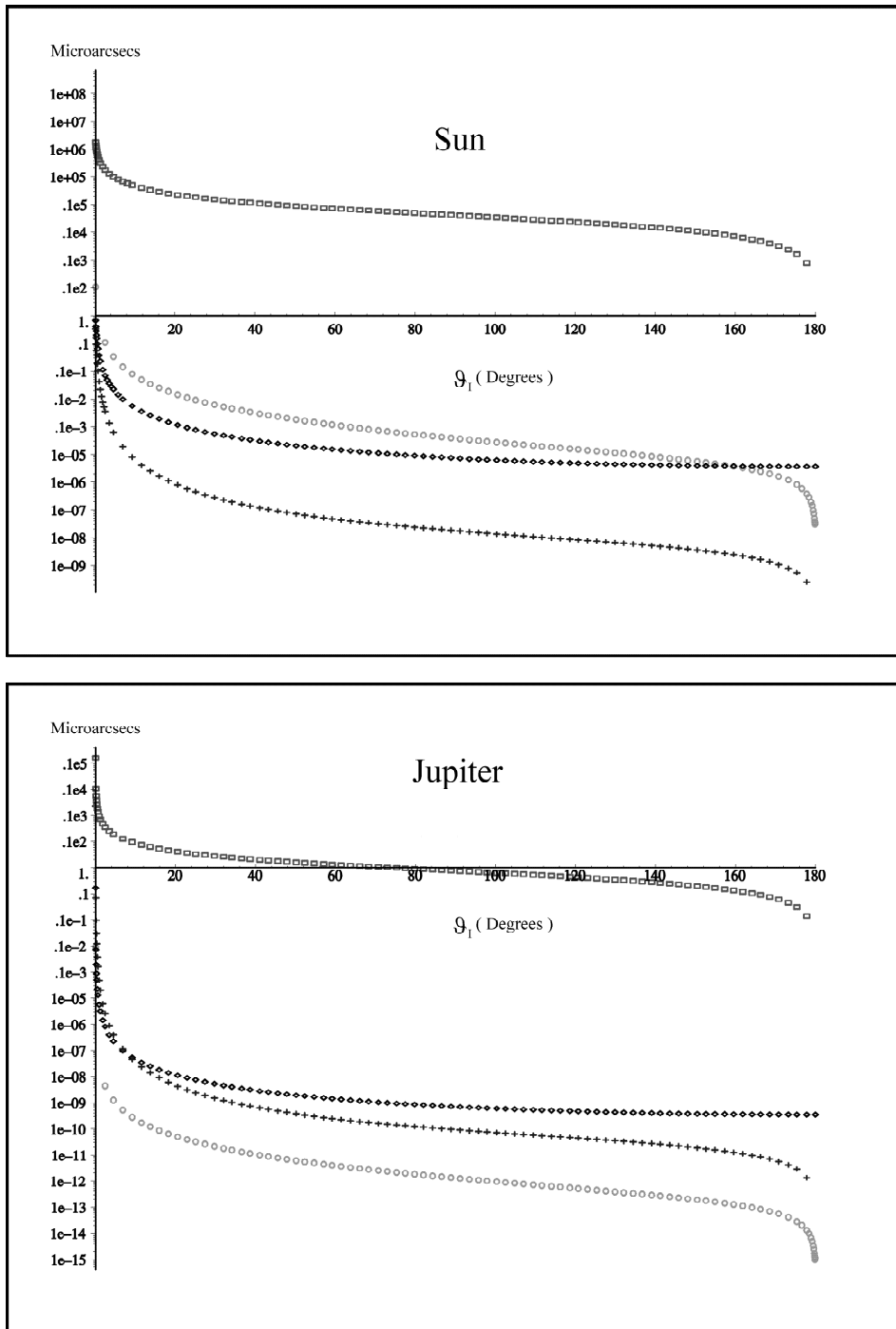


Fig. 3.6 Order of magnitude of the different contributions to the gravitational light deflection angle due to the Sun and Jupiter, as a function of the observation angle relative to the deflector, in the framework of General Relativity. The particular case of an observer located on Earth and for light deflection taking place in the equatorial plane of a rigidly rotating deflector (perpendicular to the angular momentum) is considered. The square curve is for the first order contribution with J_2 set to zero; the cross curve is for the first order contribution of J_2 alone; the diamond curve is for the 3/2 order contribution of the angular momentum; and the circle curve is for the second order term. The range for ϑ_I is from the corresponding nonzero grazing incidence (see expression (3.33)) to 180° .

while the values for the GAIA orbit shift to³¹

$$\begin{cases} \text{for the Earth: } \begin{cases} \vartheta_{I \max 1} \simeq 99.5 - 103.3^\circ, \\ \vartheta_{I \max 10} \simeq 13.5 - 14.4^\circ, \end{cases} \\ \text{for the Moon: } \begin{cases} \vartheta_{I \max 1} \simeq 81.5' - 147.4', \\ \vartheta_{I \max 10} \simeq 8.2' - 14.8'. \end{cases} \end{cases}$$

GR Earth observer maximum observable angle at 1 or 10 μ arcsec precision $\vartheta_{I \max 1} / \vartheta_{I \max 10}$	(A+B) * 1^{st} order	C * 1^{st} order	D * 3/2 order	E * 2^{nd} order
Sun	$180^\circ / 180^\circ$	—/—	—/—	$51.8' - 53.6' / -$
Jupiter	$62.0^\circ - 89.3^\circ / 7^\circ - 11^\circ$	$1.6' - 2.6' / 0.8' - 1.3'$	—/—	—/—
Saturn	$12.0^\circ - 16.6^\circ / 1.2^\circ - 1.7^\circ$	$34.1'' - 47.4'' / 15.9'' - 23.0''$	—/—	—/—
Neptune	$46.0' - 50.1' / 4.6' - 5.0'$	$2.4'' - 2.5'' / -$		—/—
Uranus	$58.0' - 70.8' / 5.8' - 7.1'$	$3.2'' - 3.9'' / -$	—/—	—/—
Earth	$179.6^\circ / 176.0^\circ$	—/—	—/—	—/—
Venus	$0.7^\circ - 4.5^\circ / 4' - 27'$	—/—	—/—	—/—
Mars	$3.4' - 24.8' / 0.4' - 2.5'$	—/—	—/—	—/—
Mercury	$3.2' - 9.0' / 18.8'' - 54.0''$	—/—	—/—	—/—
Moon	$6.4^\circ - 7.1^\circ / 38.2' - 42.6'$	—/—	—/—	—/—
Ganymede	$19.4'' - 31.8'' / 2.0'' - 3.2''$			—/—
Titan	$10.3'' - 14.3'' / 1.1'' - 1.5''$			—/—
Io	$11.7'' - 19.2'' / 1.2'' - 1.9''$			—/—
Titania	$0.2'' / -$			—/—
Oberon	$0.2'' / -$			—/—
Charon	$0.03'' - 0.06'' / -$			—/—
Rhea	$0.2'' - 0.3'' / -$			—/—
Iapetus	$0.2'' / -$			—/—
Ariel	$0.06'' / -$			—/—
Dione	$0.1'' - 0.2'' / -$			—/—
Umbriel	$0.05'' - 0.06'' / -$			—/—
Ceres	$0.3'' / -$			—/—

(3.35)

B/ Grazing incidence

For grazing incidence, in the particular conditions described above, we obtain the following magnitudes for the maximum light deflection angle (3.34):

³¹ The maximum angles we give here are smaller than the values given in reference [73].

GR Earth observer grazing magnitude (μarcsec)	A	B	C	D	E
	*	*	*	*	*
	1^{st} order	1^{st} order	1^{st} order	$3/2$ order	2^{nd} order
Sun	$1.75 \cdot 10^6$	$-(9.2 - 9.8) \cdot 10^0$	$0.28 - 0.42$	± 0.69	3.5
Jupiter	$1.627 \cdot 10^4$	$-(2.2 - 6.0) \cdot 10^{-5}$	$43.9 - 239.7$	± 0.17	$3.0 \cdot 10^{-4}$
Saturn	$5.78 \cdot 10^3$	$-(1.9 - 3.7) \cdot 10^{-6}$	94.2	± 0.04	$3.8 \cdot 10^{-5}$
Neptune	2533.6	$-(1.8 - 2.1) \cdot 10^{-8}$	8.6		$7.3 \cdot 10^{-6}$
Uranus	2081.0	$-(3.4 - 5.0) \cdot 10^{-8}$	7.0	$\pm 4.0 \cdot 10^{-3}$	$5.0 \cdot 10^{-6}$
Earth	$5.74 \cdot 10^2$	$-1.43 \cdot 10^2$	$6.2 \cdot 10^{-1}$	$\pm 2.9 \cdot 10^{-4}$	$3.8 \cdot 10^{-7}$
Venus	$4.93 \cdot 10^2$	$-6.6 \cdot 10^{-8} \rightarrow -3.1 \cdot 10^{-6}$	$2.2 \cdot 10^{-3}$	$\mp 9.8 \cdot 10^{-7}$	$2.8 \cdot 10^{-7}$
Mars	115.7	$-0.2 \cdot 10^{-8} \rightarrow -0.1 \cdot 10^{-6}$	0.23	$\pm 3.4 \cdot 10^{-5}$	$2 \cdot 10^{-8}$
Mercury	83.0	$-2.1 \cdot 10^{-7} \rightarrow -2.5 \cdot 10^{-8}$	$5.0 \cdot 10^{-3}$	$\pm 1.0 \cdot 10^{-7}$	$1 \cdot 10^{-8}$
Moon	25.9	$-1.2 \cdot 10^{-4} \rightarrow -1.4 \cdot 10^{-4}$	$5.2 \cdot 10^{-3}$	$\pm 1.5 \cdot 10^{-6}$	$1 \cdot 10^{-9}$

The list of deflecting bodies to be considered at least at **the first order monopole term (A)**, in case of maximum grazing incidence for an astrometric precision of $1 \mu\text{arcsec}$, is of course not exhaustive in Table (3.36). For example, the first order monopole term is larger than $x \mu\text{arcsec}$ if

$$\frac{R_i}{1 \text{ km}} \sqrt{\frac{\rho_i}{1 \text{ g/cm}^3}} \geq 624 \sqrt{\frac{x}{1 \mu\text{arcsec}}}$$

for a lens of radius R_i and mean density ρ_i . This means that when aiming at microarcsecond astrometry (even for a $10 \mu\text{arcsec}$ precision), smaller planets and several satellites of giant planets should be taken into account [73]. Table (3.35) illustrates this point: the first order monopole term at grazing incidence decreases from 35 to $1.1 \mu\text{arcsec}$ for minor planets and satellites, those being the contributions respectively of Ganymede, the satellite of Jupiter, and of the asteroid Ceres.

We clearly see that **the quadrupole term (C)** tends to increase the first order contribution to the light deflection. At the microarcsecond level of precision, this contribution is non negligible in the case of Jupiter, Saturn, Neptune and Uranus, while it is on the edge of this detection level for the Sun.

Note that for Jupiter, the first value of the C-term contribution is obtained with $J_2 \simeq 2.7 \cdot 10^{-3}$ based on a theoretical gaseous model [63], and the second estimation with $J_2 \simeq 14.736 \cdot 10^{-3}$ provided by [16].

For the Sun, $J_2 = (2.0 \pm 0.4) \cdot 10^{-7}$ is assumed (according to reference [109]). The evaluation of the solar quadrupole moment from solar properties still faces some controversy: on the one hand, the theoretical values strongly depend on the solar model used; whereas on the other hand, accurate measurements are very difficult to obtain from solar observations. Concerning this last point, let us recall some of the problems: the real differences of brightness of the solar limb dependence on the latitude; the influence of faculae, sunspots and magnetic fields; correlatively, real effects due to latitudinal variation of the solar limb darkening function. There is also the issue of the solar activity (solar cycle) dependence of the solar oblateness [77, 120, 121, 119]. In addition, it is difficult to calibrate ground data with regard to atmospheric disturbances and this is why space experiments have been suggested, like SoHO or the future Picard mission to the Sun (expected precision of 10^{-8} on $J_2 \text{ Sun}$). In reference [109], Table 2 illustrates those difficulties: it gives a critical compilation of the main determinations of the solar angular momentum, based on observations or solar theory.

In the preceding reference, the importance of confronting a dynamical determination of the solar angular momentum, independent of the solar model, to other solar model dependent values was thus emphasized. We have just seen that the corresponding solar angular-momentum contribution to the relativistic light deflection is unfortunately too small

to allow for a measurement of J_2_{Sun} when General Relativity is assumed. However, relativistic perihelion advances, precession of the orbital planes, or motion of spacecrafts are very promising. Presently, these dynamical determination methods are still dependent on the gravitational theory. Indeed J_2_{Sun} is too strongly correlated with the PN perihelion precession combination ($2\alpha^2 + 2\alpha\gamma - \beta$). The future GAIA or BepiColombo missions should be able to separate those two effects though, and so obtain a determination of the solar angular momentum that is independent of the gravitational theory (with a precision respectively better than 10^{-7} and of $2 \cdot 10^{-9}$ on J_2_{Sun}). A detailed discussion of the subject and a complete list of references can be found in [109].

On the contrary, **the finite distance term (B)** $\propto \frac{R^2}{\rho_{obs}^2}$ decreases the first order contribution, and must be considered at the microarcsecond level, when looking at second order contributions due to the Sun for an observer on Earth. The same order of magnitude (B^* 1st order $\simeq 9.3 \mu\text{arcsec}$) is reached when the observer is not on Earth, but for example, the astrometric satellite GAIA, located on a L2 orbit at $1.5 \cdot 10^9$ m from Earth. However, in the case of GAIA, grazing incidence is not allowed for the Sun and the Earth (avoidance angle of 35°) -see the corresponding graph in Figure 3.6 for the order of magnitude of the different contributions to the light deflection angle in the case of non-grazing incidence for the Sun-.

At the microarcsecond level, the B -term is also important for the gravitational field of the Earth in Earth-based observations, but it is totally negligible when observing with GAIA.

The contribution due to the gravitational deflector angular momentum (D) is differential (it is here estimated from a rough rigid rotation model, $\vec{J} = I \vec{\omega}$, with I , the inertia and ω , the rotation rate obtained from the sidereal rotation period). Indeed, this term either increases or decreases the first order contribution, whether the light passes on one side or on the other side of the gravitational deflector (see Figure 3.7). Thanks to this characteristic, this contribution could be easily identified. One could think of an experiment that could be carried out when a satellite (the light source) in conjunction with a gravitational source and the Earth (or another satellite playing the role of observer) would send a laser signal to the observer, simultaneously from the left or from the right of the gravitational body.

Unfortunately, the contribution from the angular momentum of the gravitational source shall not be helpful in providing interesting constraints on the parameter γ of alternative theories. This is due to the already so small deviation of γ from GR value of 1, for acceptable theories (see present VLBI experimental constraints on γ given in (3.2) or (3.3); and note that in our chosen cosmological evolutionary model for TS theories, presented in Chapter 2, the predicted deviation $1 - \gamma$ (2.58) is even weaker). Hence, the angular-momentum term is more likely to give only interesting constraints on the angular momentum of the gravitational source. This is an important fact because, in the case of the Sun, it would provide a *dynamical* estimation of the absolute value of the angular momentum, to confront with the somehow controversial solar model estimations which depend on the density and rotational velocity models adopted.

However, the dynamical determination of the angular momentum might be easier for Jupiter, because the contribution of the angular momentum (D) represents $1 \cdot 10^{-3} \%$ of the corresponding first order term (A) in this case; whereas it represents only $4 \cdot 10^{-5} \%$ of the corresponding first order term in the case of the Sun.

As far as the second order contribution is concerned (E), we see that it is crucial when considering grazing incidence for the Sun (Table (3.36)). However, it is negligible at any incidence for planets, and for non-grazing incidence in the case of the Sun, even when looking at microarcsecond detection (see the graphs in Figure 3.6).

Knowing the non null avoidance angle of GAIA for the Sun (while grazing incidence is allowed for planets), we see that the second order term is totally undetectable with such an experiment, although an incredible precision on the individual positions of light sources ($\sim 5 \cdot 10^{-1} \mu\text{arcsec}$). The situation is analogous for all present and future astrometric satellites like Hipparcos (Sun avoidance angle of 45° and \sim milliarcsecond precision), FAME (previously 45° , now changed to $35 \pm 5^\circ$, and precision better than $\sim 50 - 500 \mu\text{arcsec}$), DIVA (45° and precision 5 times better than Hipparcos), or SIM (45° and $\sim 4 \mu\text{arcsec}$ precision). To reach the second order in light deflection, one needs dedicated space experiments. Some have been proposed but are not yet financed, like TIPO, SORT, or ASTROD. See Appendix B for references and further details on light deflection measurements.

We also remark that **the gravitational field of the Earth is important at the microarcsecond precision level, for an observer located on Earth and thus subject to the Earth gravitational field**. Earth's A , B and C -terms are non negligible. However, when the observing instruments are located for example on the GAIA satellite on a L2 orbit, the B -term (B^* 1st order $\sim 10^{-3} \mu\text{arcsec}$) becomes negligible at grazing incidence.

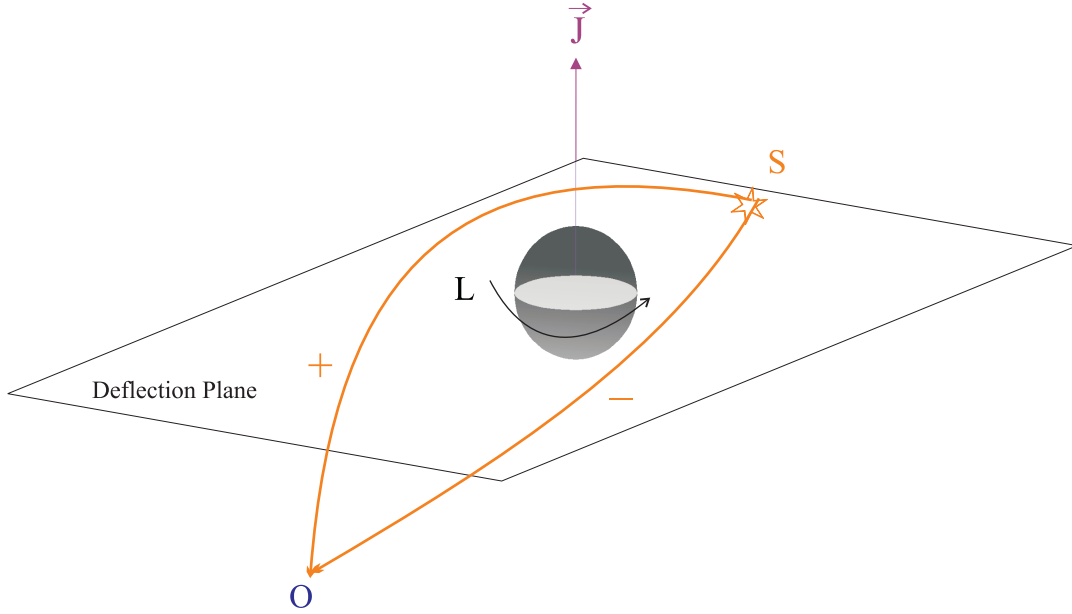


Fig. 3.7 The contribution of the gravitational deflector angular momentum to the light deflection angle is differential.

3.2.5 Further remarks on “corrective” effects

Our calculation, to provide the orders of magnitude of the quadrupole- and angular-momentum contributions to light deflection, is done for deflection taking place in the equatorial plane of the gravitational body, where the effect of those contributions is maximal. The reader can find a **generalization to deflection in any plane (not necessarily perpendicular to the angular momentum) and to any multipole momentum** in references [114] and [76] respectively.

The first generalization should be useful when studying light deflection in the gravitational field of Jupiter for the GAIA mission.

In this section, we considered a light source asymptotically far, whereas the observer could be at a finite distance from the deflector. However, in astrometric measurements, this assumption might not always be appropriate. A first example is the observation of solar system objects: the distance to the light source is finite. This remark is especially pertinent for the GAIA experiment which should lead to high quality astrometric measurements of small planets. A second example is the case of binaries, where the companion of the observed star plays the role of the lens. The observer is, on the contrary, very far from the gravitational source. The change in the apparent position of the observed star can reach $200 \mu\text{arcsec}$ for well separated binaries [92].

To be rigorous, let us notice that γ should be replaced by

$$\gamma^* = \gamma - \eta (1 + \gamma) \frac{E_{grav}}{Mc^2} + \mathcal{O}\left(\frac{1}{c^4}\right)$$

in expressions (3.32) and (3.34), where η is the Nordtvedt parameter (presently constrained to $2 \cdot 10^{-4} \pm 9 \cdot 10^{-4}$ [109]), E_{grav} is the gravitational bending energy of the gravitational source and M is its mass. This change would take into account the **sensitivity of the gravitational deflector** for theories where the Strong Equivalence Principle (SEP) is violated [38]. However, this correction is negligible in the case of solar system tests: $\frac{E_{grav}}{Mc^2}$ is only $\sim 2 \cdot 10^{-6}$ for the Sun, which means a correction smaller than 10^{-9} on γ .

Finally, we remark that, in addition to the gravitational effects (A , B , C and D -terms), some **parasitic non-gravitational effects** might have to be taken into account.

First of all, there is some refraction caused by the solar corona (if the Sun is the gravitational deflector), and by the

Earth ionosphere (if observations are made from the ground). To illustrate the order of magnitude of these non negligible effects, one should note that the refraction due to the solar corona at 3° from the Sun is $2-7$ marcsec in the X-band, depending on the level of solar activity. In the gravitational field of the Sun, its largest value is about 5% of the gravitational deflection. However, this coronal contribution decreases rapidly at large Sun angles ($\delta\vartheta_{\text{coronal refraction}} \propto 1/\vartheta_I^2$) while the gravitational deflection decreases nearly linearly [61]. Thus, only experiments at very small angles to the Sun, or at grazing incidence are subject to this effect.

Moreover, the Earth ionosphere and coronal deflections are dispersive ($\delta\vartheta_{\text{coronal diffraction}} \propto 1/\nu_{\text{obs}}^2$). So one can avoid using ionosphere and solar coronal models entangled with their own systematic errors to correct for coronal/ionospheric diffraction, if making simultaneous observations at widely separated frequencies. This alternative is presently used in VLBI measurements made in the X and S bands [115].

Secondly, even though parallactic displacements ($\delta\vartheta_{\text{parallactic displacement}} \propto \sin \vartheta_I$) and light deflection effects ($\delta\vartheta_{\text{gravitational first order term}} \propto \sin \vartheta_I / (1 - \cos \vartheta_I)$) differ in direction and in their dependence on ϑ_I , and despite a good coverage in the observation angle ϑ_I , the separation is not perfect and the parallactic displacements remain largely correlated with the estimation of γ from Hipparcos data. A careful simulation in the case of GAIA, which might do better owing to its extended capabilities in comparison with Hipparcos, still has to be done to confirm the rough estimation of γ on the accuracy achievable with GAIA given in Paragraph 3.1.2.

Thirdly, if parallactic displacements result from the motion of the observer, we should not forget the aberration too. And a comprehensive modelling of astrometric measurements taking into account light deflection must also include the motion of the source (proper motion), as well as the motion of the lens (microlensing event) according to the timescales and distance scales of the experiment.

3.2.6 Current state of the art

The astrometric satellite GAIA is the most precise and already financed project presently available on the market. An incredible precision on individual positions is expected for this mission: close to $2 \mu\text{arcsec}$ on the bright stars ($V < 12$). However, GAIA might not be able to measure the second order of light deflection (thus not enabling us to reach the PPN parameter δ) *using individual measurements*, because grazing incidence is not allowed for the Sun. To reach the second order, we might probably need to wait for dedicated projects like SORT or ASTROD (see Appendix B). For the same reason, GAIA might not be able to provide useful information on the solar values of J_2 and \vec{J} , but this should not be the case for Jupiter and Saturn.

Note that such conclusions concerning GAIA are not definitive. A thorough and careful simulation of the data analysis for GAIA is still needed to conclude whether it is possible to provide even some weak constraints on the parameters intervening in the additional contributions to the first order monopole term in light deflection. Such a simulation must include astrometric models complete to within $0.1 \mu\text{arcsec}$ to reach the announced accuracy of the mission. Presently, the analytical perturbation model of Klioner [73] is only complete to $1 \mu\text{arcsec}$. Nevertheless, it already nicely incorporates the motion of the observer, source and lens, and uses fully PPN astrometric reference frames (while previous work [74] only developed this formalism in the setting of GR).

An alternative global modelling has been proposed (now implemented for terms up to (v/c^2)) by the Padova-Torino group in the “GAIA Relativity and Space-Time Working Group”.

The efficiency and the ways to implement those two different models need yet to be compared and the models themselves refined.

Chapter 4: Testing alternative theories in the solar system using the light deflection angle?

In the previous chapter, we gave a general overview of what were, are and will be the experimental limits of light deflection tests in the solar system. We now would like to confront them with our chosen set of alternative theories.

4.1 Relevant (P)PN parameters at first and second order in light deflection

According to the various expressions for the light deflection angle (asymptotic (3.1), (5.1), (3.12) or finite distance (3.26), (3.32)), we can calculate the relevant combinations of (P)PN parameters for light deflection. Using Table (1.67), we find

	PN: $(\alpha + \gamma)$	Post-PN: $(8\alpha^2 + 8\alpha\gamma - 4\beta + 3\delta)$
<i>MTS/SITS</i> : $a = 2\Upsilon \in]0; 2]$ $G = G_N$	2	$15 + \frac{a^2 - 4}{a^2}$
<i>TS Jordan frame</i> : $a = 2/\sqrt{1 + \alpha_{TS0}^2}$ G	$\frac{2}{1 + \alpha_{TS0}^2}$	$15 - \frac{\alpha_{TS0}^2 (15\alpha_{TS0}^2 + 31 - 4\alpha'_{TS0})}{(1 + \alpha_{TS0}^2)^2}$
<i>STRINGS</i> <i>Jordan frame</i> : $a = \sqrt{2}$ \Downarrow $\alpha_{TS} = 1$ G	1	$\frac{7}{2}$
<i>GR</i> : $a = 2\Upsilon = 1$ \Downarrow $\alpha_{TS} = 0$ $G = G_N$	2	15

(4.1)

4.2 Theories leading to first order corrections

Let us first consider the predictions of some alternative theories of gravitation like Brans-Dicke theory (BD), Strings, modified Brans-Dicke with $\varpi(\Phi)$ (TS) and Large Extra-Dimension theories (LED), which already deviate from the GR ones at the leading order.

4.2.1 TS theories

Using the expression for the weak field light deflection angle (3.12) and the Tensor Scalar PN parameters (4.1), one recovers the predicted deflection angle for TS theories:

$$\begin{aligned} \widehat{\alpha}_{\text{weak field}}(b) &= \frac{1}{1+\alpha'_{TS0}} \frac{4G_N M}{bc^2} + \mathcal{O}\left(\frac{V^2}{c^4}\right) \\ &\stackrel{(1.7)}{=} \frac{2\varpi_0+3}{2\varpi_0+4} \frac{4G_N M}{bc^2} + \mathcal{O}\left(\frac{V^2}{c^4}\right), \end{aligned} \quad (4.2)$$

with ϖ_0 , the present value of $\varpi(\Sigma)$. TS theories thus already deviate from GR at first order.

The light deflection experiments in the vicinity of the Sun (VLBI) and the fact that $1 - \gamma$ is always positive for TS theories (Table (1.67)) constrain the present value of the TS parameter:

$$\begin{aligned} \varpi_0 \text{ exp} &\gtrsim 463 \quad \text{according to (3.2),} \\ \varpi_0 \text{ exp} &\gtrsim 2215 \quad \text{according to (3.3).} \end{aligned} \quad (4.3)$$

This minimum value corresponds to the measured maximum deviation of $1 - \gamma$ from zero. Such constraints of course exclude String theory with $\varpi_0 \text{ STRINGS} = -1$ (which is a high energy theory, not adapted for present physics) and the original BD theory. But we see that those present limits are still very far away from the predicted values of up-to-date cosmological models as discussed in Chapter 2, with some value of $\varpi_0 \text{ theo} \sim 10^5 - 10^7$ given by Damour *et al.* (see Table (2.71) with expression (1.7)), while the lower bound of our model is $\varpi_0 \text{ theo} \sim 10^7$. For this reason, space experiments *dedicated to* the measurement of γ with such a precision have been proposed (see Appendix B), in order for observations to fill the gap. Of course, getting information on the (P)PN parameters as a by-product of astrometric missions like GAIA is also interesting, but we already know from Chapter 3 that GAIA will probably not even reach the lower bound of our model.

To conclude this section, we would like to put the first order predictions from light deflection into perspective. Figure 4.1 shows the present best constraints on the Tensor Scalar parameter space $(\alpha_{TS0}, \alpha'_{TS0})$ (1.66) from binary pulsar experiments and solar system experiments. We remind the reader that, if a non constant scalar coupling is considered, α'_{TS0} contains a pertinent information for the cosmological models, because it is associated to the curvature of the cosmological evolutionary potential around its minimum, N (equal to $1/3$ in our particular model). Indeed, we showed in Paragraph 2.2.5.1 that $1 - \beta = -N/8 \cdot (1 - \gamma) \cdot (1 + \gamma)$; and presently β is constrained to $[0.9993; 1.0006]$ or $[0.9997; 1.0003]$. Those limits are obtained when combining the bounds on γ from VLBI, (3.2) or (3.3) respectively, with those on the Nordtvedt parameter $\eta \equiv 4\beta - \gamma - 3 = +0.0002 \pm 0.0009$ [144] (assuming $\alpha = 1$).

Let us come back to Figure 4.1. We can see that VLBI data (light deflection and time delay) provide the crucial information for the α_{TS0} -dimension. Light deflection measurements would only provide constraints on the α'_{TS0} -dimension if the second order was accessible to some dedicated experiments (see the PPN combination at second order in Table (4.1)). This dimension in the parameter space is now taken care of by Lunar Laser Ranging experiments and by pulsar data for negative values of the scalar coupling derivative.

Note that in the particular case of Damour *et al.*'s cosmological model given by (2.35), Chiba and his collaborators translated the Cosmic Microwave Background data provided by the space mission COBE into constraints on the tensor scalar theory parameters [31]. This method seems to be very efficient to shrink the allowed parameter space along its α'_{TS0} -dimension (see Figure 4.2). We think that it would be very interesting to apply it to our exact analytical cosmological solution in order to analyze its imprint on the density perturbations in inflationary cosmology, and to see whether CMB constraints strongly depend on the cosmological model. Indeed, we have shown that the attractor mechanism can be very efficient, so that the departure from General Relativity in present solar system tests is really weak. The Cosmic Microwave Background data might be able to probe the cosmological models at a time at which

they were very different from GR and from one another. Nevertheless, even if CMB constraints are considered in the picture, VLBI solar system data still constitute the most efficient test in the α_{TS0} -dimension presently available.

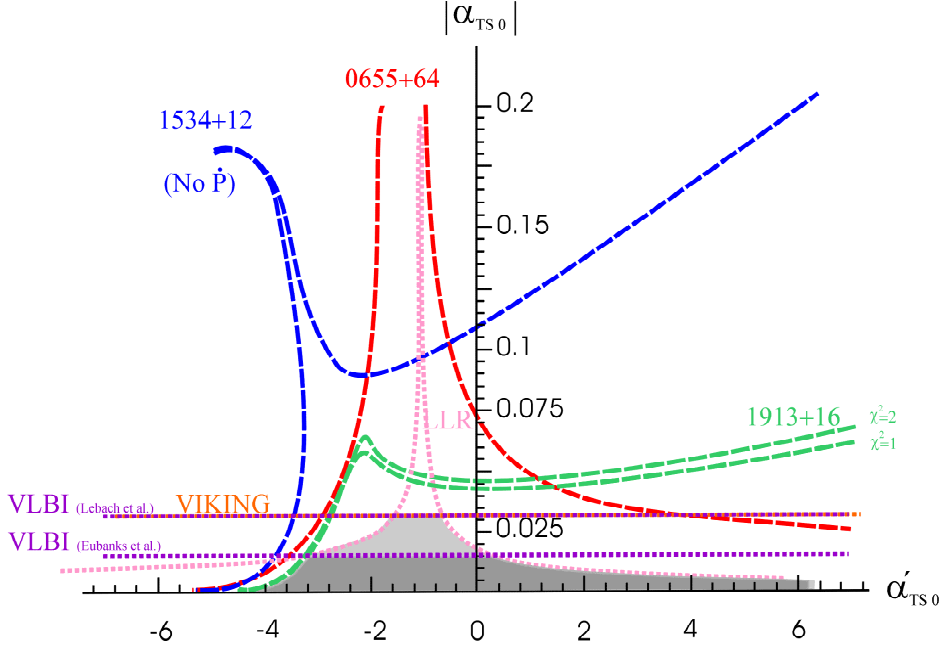


Fig. 4.1 Constraints on the Tensor Scalar models from experiments. In fact, only the square of α_{TS0} is physically measured. The regions allowed by solar system tests, respectively time-delay measurements to the Viking lander [110] (VIKING $\propto (\gamma + 1)$), Lunar Laser Ranging (LLR $\propto \eta = (4\beta - \gamma - 3)$) [144], Mercury perihelion shift ($\propto (2 + 2\gamma - \beta)$, not apparent on this graph) and Very Large Baseline Interferometry light deflection or time-delay measurements (VLBI $\propto (\gamma + 1)$) [53, 78] are beneath the corresponding dotted line. The region allowed by binary pulsar tests, given by the dash lines [37, 38, 39], are respectively to the right of the corresponding curves for PSR 1913+16 and PSR 1534+12, while it is in between the corresponding dash line for PSR 0655+64. The parameter space allowed by pulsars strongly depends upon the equation of state adopted. Softer equations of state for nuclear matter lead to stronger constraints on the theory parameters. In this graph, a polytropic equation of state for the neutron stars was assumed. It can be seen through the plots presented in reference [39], how the constraints vary with the equation of state (Note that solar system tests in those graphs are a bit outdated). The shaded region represents the parameter space $(\alpha_{TS0}, \alpha'_{TS0})$ allowed by solar system tests and binary pulsars simultaneously. Nevertheless, VLBI data so far dominates constraints on α_{TS0} and, for positive values of α'_{TS0} , solar system tests are still more efficient than pulsar data.

4.2.2 LED theories

4.2.2.1 Prediction using the result found for BD theory

At first order, we have seen that the effective action for the propagation and interaction of gravitational fields with matter is the same as in BD theories (1.38) with the corresponding scalar coupling given by (1.37) and BD parameter ϖ , (1.39). It is then straightforward to extrapolate the result we just obtained for TS theories (4.2), to Large Extra-Dimension theories. Accordingly, the light deflection angle due to a massive object is, at first order,

$$\hat{\alpha}_{\text{weak field}}(b) = \frac{d+2}{2(d+1)} \frac{4G_N M}{bc^2}. \quad (4.4)$$

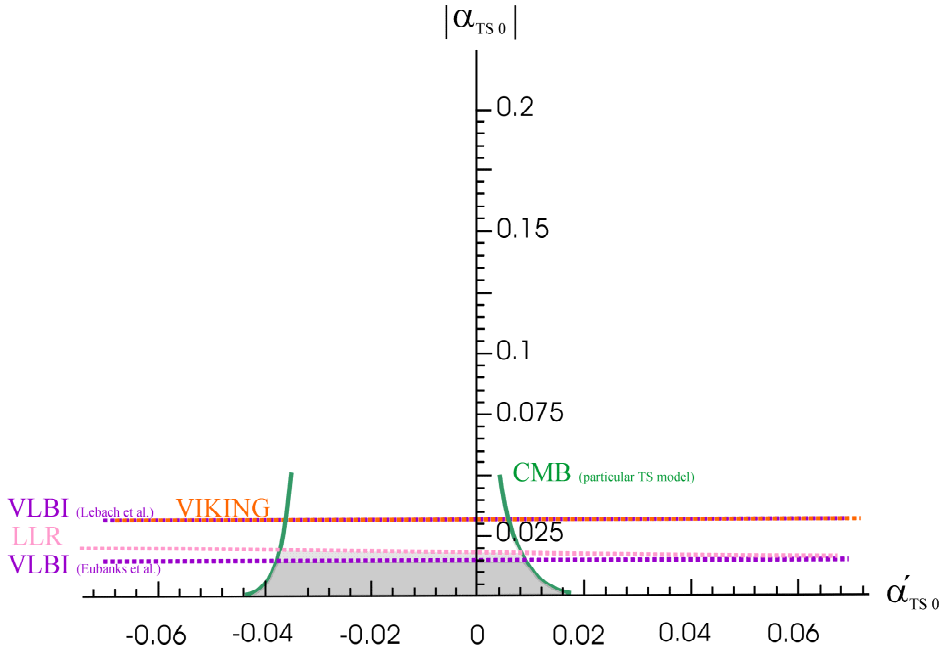


Fig. 4.2 This graph is to be compared with the previous figure. It shows how the constraints obtained by Chiba and his collaborators [31] on the Tensor Scalar parameter space from the Cosmic Microwave Background (CMB) with spectral index $n > 0.7$ further shrunk drastically the α'_{TS0} -dimension. However, this CMB analysis was made solely for Damour *et al.*'s model given by (2.35). The shaded region represents the parameter space $(\alpha_{TS0}, \alpha'_{TS0})$ allowed simultaneously by solar system tests and CMB data for this particular class of Tensor Scalar models. CMB constraints are about two orders of magnitude stronger than the pulsar or solar system limits on α'_{TS0} . But most recent VLBI data still provide the crucial information for the α_{TS0} -dimension. (Or alternatively the LLR data if the unpublished results in reference [53] are not confirmed).

This means that the PN parameter γ , when $\alpha = 1$, would be

$$1 - \gamma = \frac{d}{1 + d},$$

in terms of the number d of extra-dimensions; even though strictly speaking one cannot define a PN expansion of LED theories. The above expression makes it easy to compare with solar system experiments.

4.2.2.2 Prediction using a photon - scalar-field scattering process

Alternatively, we can compute the light bending by a massive object in the framework of field theory. This requires to calculate the classical limit of the scattering amplitude of a photon and a massive scalar (the presence of which will mimic the Sun as a deflector) through the gravitational interaction. Such a calculation is somewhat lengthy (see Appendix C), but **at first order** we just need the ratio of this scattering amplitude in LED theories, $\mathcal{M}_{LED}^{phot.-scal.}$, to the same amplitude for General Relativity, $\mathcal{M}_{GR}^{phot.-scal.}$.

For LED, we have

$$\begin{aligned} \mathcal{M}_{LED}^{phot.-scal.} &\sim \mathcal{M}_{(\vec{n}=0)}^{phot.-scal.} + \sum_{\vec{n}} \mathcal{M}_{(\vec{n} \neq 0)}^{phot.-scal.} \\ &\sim G T_m^{(phot.)} \cdot \left(\eta^{\mu\alpha} \eta^{\nu\beta} + \eta^{\mu\beta} \eta^{\nu\alpha} - \frac{2}{2+d} \eta^{\mu\nu} \eta^{\alpha\beta} \right) \left[\frac{1}{q^2} + \sum_{\vec{n}} \frac{1}{q^2 - m_n^2 c^2} \right] \cdot T_m^{(scal.)} \alpha\beta. \end{aligned}$$

As was explained in Subsection 1.4.3, the massive modes contributions to the propagator can be dropped. Using (1.37)

and (1.45), we find

$$\mathcal{M}_{LED}^{phot.-scal.} \sim G T_m^{(phot.)} \cdot (\eta^{\mu\alpha} \eta^{\nu\beta} + \eta^{\mu\beta} \eta^{\nu\alpha} - \eta^{\mu\nu} \eta^{\alpha\beta} + \alpha_{LED}^2 \eta^{\mu\nu} \eta^{\alpha\beta}) \frac{1}{q^2} \cdot T_{m\ \alpha\beta}^{(scal.)}.$$

However, the tracelessness of the photon stress tensor prevents any coupling to gravitational scalars (see the effective action for nonmassive modes (1.38)), which allows us to drop the α_{LED}^2 -term in this amplitude.

On the other hand, the general relativistic amplitude is

$$\mathcal{M}_{GR}^{phot.-scal.} \sim G_N T_m^{(phot.)} \cdot (\eta^{\mu\alpha} \eta^{\nu\beta} + \eta^{\mu\beta} \eta^{\nu\alpha} - \eta^{\mu\nu} \eta^{\alpha\beta}) \frac{1}{q^2} \cdot T_{m\ \alpha\beta}^{(scal.)}.$$

The ratio of the scattering amplitudes simply corresponds to the ratio of the coupling constants. The ratio of deflection angles ($\hat{\alpha}_{LED \text{ weak field}}$ and $\hat{\alpha}_{GR \text{ weak field}}$) by a massive object is consequently

$$\frac{\hat{\alpha}_{LED \text{ weak field}}}{\hat{\alpha}_{GR \text{ weak field}}} = \frac{\mathcal{M}_{LED}^\gamma}{\mathcal{M}_{GR}^\gamma} = \frac{G}{G_N}. \quad (4.5)$$

This ratio may be rewritten in terms of the number of extra-dimensions using (1.37) and (1.48) to recover our previous result (4.4).

4.2.2.3 The zero-mode scalar field getting a mass

When the zero-mode scalar field is nonmassive (which is the case in the original theory), we see immediately with expressions (4.4) or (4.5) that LED theories totally disagree with experiments. Indeed, they predict

$$\begin{aligned} \hat{\alpha}_{LED \ d=0 \text{ weak field}} &= \hat{\alpha}_{GR \text{ weak field}}, \\ \hat{\alpha}_{LED \ d=1 \text{ weak field}} &= \frac{3}{4} \hat{\alpha}_{GR \text{ weak field}}, \\ \hat{\alpha}_{LED \ d=2 \text{ weak field}} &= \frac{2}{3} \hat{\alpha}_{GR \text{ weak field}}, \\ \hat{\alpha}_{LED \text{ weak field}} &\xrightarrow{d \rightarrow \infty} \frac{1}{2} \hat{\alpha}_{GR \text{ weak field}}, \end{aligned} \quad (4.6)$$

while VLBI experiments have confirmed GR prediction at the level 1/10000 (3.3). The LED coupling for a massless scalar field ($G \neq G_N$) is too strong. Indeed, the weak equivalence principle as well is strongly violated, in complete contradiction with experiments. Hence, it is useless at this point to discuss a possible tiny contribution at next order from the massive Kaluza-Klein states.

This problem concerning light deflection experiments was mentioned in reference [19].

The solution found in order to rescue the LED theories was to **provide a mass to the zero-mode scalar field by some mechanism (at or after the supersymmetry breaking)**³². The argument is exactly the same as for Kaluza-Klein massive modes: the mass has to be sufficiently large in order to avoid observing any modification to the Newtonian law in laboratory experiments above one millimeter (see (1.47) in Subsection 1.4.3). If such a condition is fulfilled, the now massive scalar zero-mode contributes in principle in the same way to gravitational observation as the massive Kaluza-Klein states and

$$G = G_N$$

above millimeter scales.

Notice that in the case of light deflection, the now massive zero-mode scalar field does not contribute at all. Indeed, its only effect in the effective interaction term (1.36) would be to couple to the trace of the energy-momentum tensor of the matter particles in the process. However, since we are considering light deflection by a massive object, the energy-momentum tensor of the photon is traceless, so that only the massive spin-2 Kaluza-Klein states will contribute to modify GR prediction. Of course, the massive zero-mode scalar field would contribute to the deflection of a massive particle (orbital motion).

³² See references [17, 19, 35] about some mechanisms generating a mass. In the last reference, it is emphasized that such mechanisms often face many cosmological problems which are generally countered with *ad hoc* solutions (see comments on page 7 of [35] as well as the mentioned references).

But let us come back to the case of photons. The following expression obtained from the scattering amplitude (long) calculation **at the third order** (see Appendix C),

$$\hat{\alpha}_{LED \text{ weak field}} = \frac{4G_N M}{bc^2} \left\{ \frac{G}{G_N} + 2 (\hbar\omega)^2 \Delta_d(q^2) \left(\frac{G}{G_N} \right)^3 \left(\frac{4G_N M}{bc^2} \right)^2 \ln \left(\frac{G}{G_N} \frac{4G_N M}{bc^2} \right) \right\},$$

where $\Delta_d(q^2) \equiv \frac{1}{c^2} \sum_{n \neq 0} \frac{1}{q^2 - m_n^2 c^2} \stackrel{\text{small momentum transfer}}{\simeq} \begin{cases} 0 & \text{for } d = 0 \\ -\frac{\pi^2 \hbar^2 c^2}{3 (GM_s^3)^2 c^4} & \text{for } d = 1 \\ -\frac{\hbar c}{GM_s^4 c^4} \ln \frac{M_s^2 c^2}{m_{\min}^2 c^2 - q^2} & \text{for } d = 2 \\ -\frac{\hbar c}{GM_s^4 c^4} \frac{2}{d-2} & \text{for } d > 2 \end{cases}$,

$\hbar\omega \equiv$ energy of the incident photon,
 $M_s \equiv$ mass scale of the theory $\sim \text{TeV}/c^2$,
 $m_{\min} \equiv$ minimum mass among the massive gravitational modes
(in the following simulations, we took $m_{\min} \sim 10^{-3} \text{ eV}/c^2$),
 $q^2 c^2 \stackrel{\text{small momentum transfer}}{\simeq} -(\hbar\omega)^2 \theta^2 \simeq -(\hbar\omega)^2 \left(\frac{G}{G_N} \right)^2 \left(\frac{4G_N M}{bc^2} \right)^2$,

(4.7)

now with $G = G_N$, of course leads to a reasonable deviation from GR predictions. It can be formally written as

$$1 - \gamma = -4 (\hbar\omega)^2 \Delta_d(q^2) \left(\frac{4G_N M}{bc^2} \right)^2 \ln \left(\frac{4G_N M}{bc^2} \right), \quad (4.8)$$

and was discussed in reference [66] where the authors assumed a minimal coupling (thus some implicit not specified mechanism giving a mass to the zero-mode scalar field)³³.

Hence, the massive states increase the light deflection angle in comparison with GR (indeed, we are working here in the approximation $4G_N M / (bc^2) < 1$ and Δ_d is negative); this means that they could constitute an alternative to too large an amount of dark matter in gravitational mirages.

We see that this deviation from GR (formally, $|1 - \gamma|$) depends on the observation angle with respect to the deflector (unlike in TS theories or MST-SIST theories as we shall see in the next sections). It reaches its maximum at grazing incidence, but vanishes as ϑ_I increases faster than solar coronal diffraction. Moreover, for a given deflector, massive modes have a signature which is not only dependent on the number of extra-dimensions ($d \geq 2$), decreasing with d ; but which also exhibits a strong quadratic dependence on the energy of the incident photon, *i.e.* on the frequency at which the observation is made³⁴ (conversely to coronal deflection effects which are proportional to the inverse of the squared frequency). According to those characteristics of LED predictions, to test LED theories coherently with respect to light deflection observations, we should not use experimental data obtained at various or too large observation angles relative to the deflector and then extrapolated at grazing incidence. Likewise, we should not use experimental estimations of $1 - \gamma$ that are averaged over very different observation frequencies.

Another important characteristic of LED light deflection predictions is that the predicted deviation from GR is a function of the deflector mass and distance. In our solar system, the Sun is the best laboratory, leading to the largest $(1 - \gamma)$ -deviation. We will now briefly discuss its contribution to light deflection in LED theories, knowing that just one extra-dimension ($d = 1$) must be rejected since the corresponding compactification radius is too large, above the millimeter scale.

From the point of view of solar grazing incidence predictions ($b \simeq R_{Sun}$), LED theories are safe in the radio-waveband, predicting for example with two extra-dimensions $1 - \gamma|_{radio}^{d=2, M_s=3 \text{ TeV}/c^2} \simeq -7 \cdot 10^{-9}$. This latter estimate is made with the lowest frequency of VLBI (see the corresponding table for VLBI type I in Appendix B, and compare with the constraint (3.2)), for a mass scale $M_s \simeq 3 \text{ TeV}/c^2$ as favored by collider physics. However, already in the

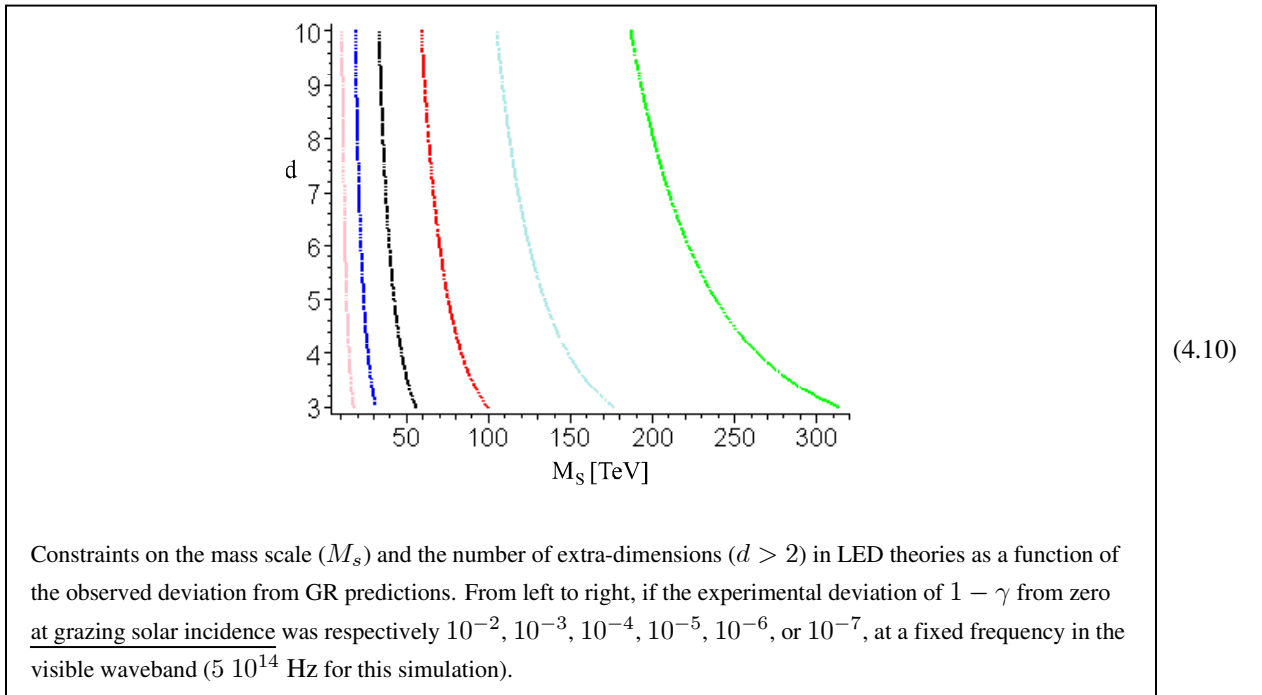
³³ Notice that there is a sign error propagating from equation (6) to (11) in the work of He *et al.* [66] which means they obtain the opposite sign for $1 - \gamma$ to the one we give in (4.8). See also Appendix C.

³⁴ As already stated in article [66], radiative corrections in GR would also lead to a dependence in the frequency [46]. However, this correction is much smaller ($\sim 0.1 (\hat{\alpha}_{GR \text{ grazing } Sun})^2 \sim 10^{-11}$) than the one introduced by massive modes.

visible-band, those theories disagree with observations at $d = 2$ for such a low mass scale. Indeed, they predict for example $1 - \gamma|_{\text{visible}}^{d=2, M_s=3 \text{ TeV}/c^2} \simeq -427$ at a frequency of $5 \cdot 10^{14}$ Hz. To agree with the observations in the visible at grazing incidence, the following lower bound has to be satisfied

$$\text{to verify } 1 - \gamma|_{\text{exp}} = 0.5 \pm 0.11 \text{ [71] in the visible at } 5 \cdot 10^{14} \text{ Hz: } \begin{cases} M_s \gtrsim 28 \text{ TeV}/c^2 & \text{for } d = 2, \\ M_s \gtrsim 9.5 \left(\frac{2}{d-2}\right)^{1/4} \text{ TeV}/c^2 & \text{for } d > 2. \end{cases} \quad (4.9)$$

Notice that there exist more precise estimations of $1 - \gamma$ in the visible from, for example, the Hipparcos satellite (see Appendix B), but these are an average over different observation angles (relative to the deflector) and frequencies. Increasing the precision of solar grazing experiments in the visible *at a fixed frequency* would push further the constraint on the mass scale of the theory or on the allowed number of extra-dimensions, as shown in simulation (4.10).



In a similar way, solar grazing observations at a fixed frequency in higher energy wavebands would help to constrain LED theories. For example, in the ultra-violet,

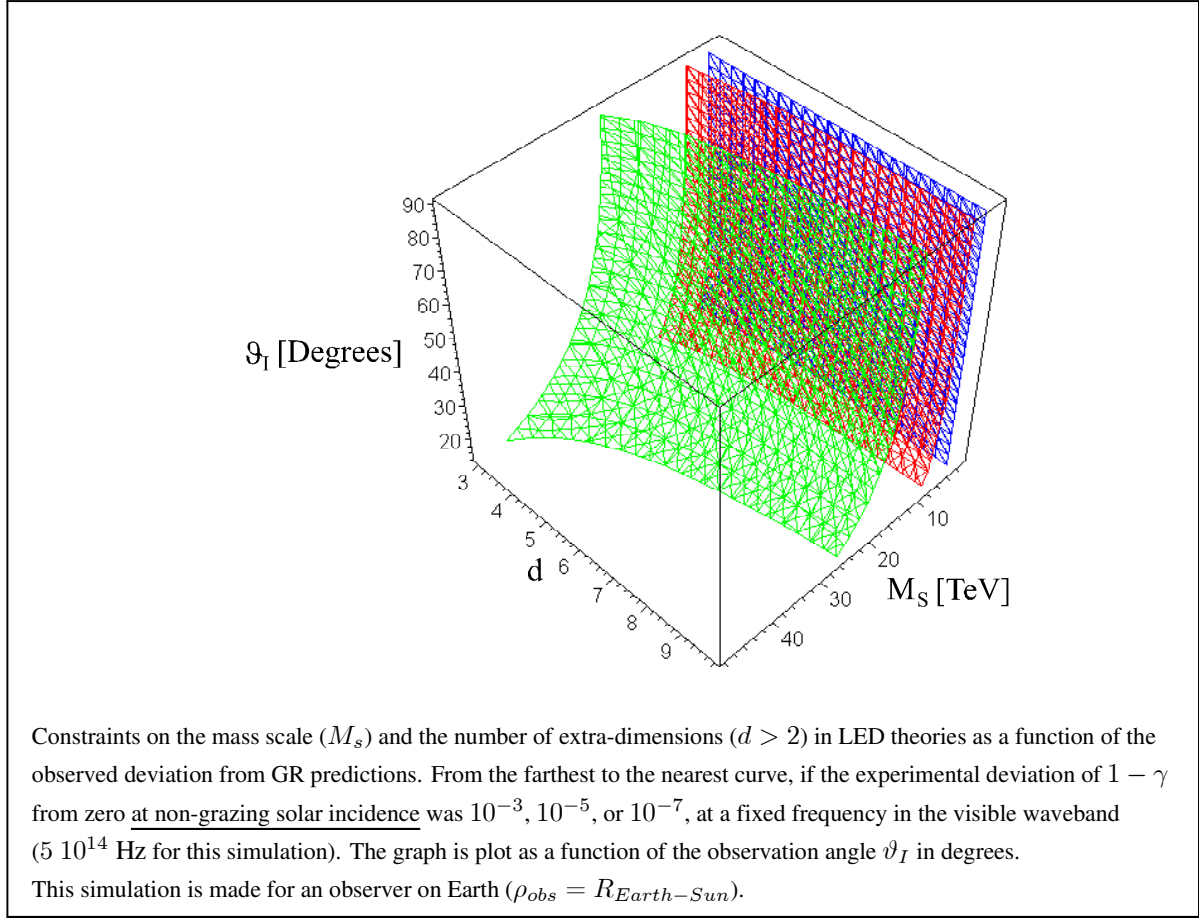
$$\text{if } 1 - \gamma|_{\text{exp}} = 0 \text{ within 10\% in the UV-band at } 5 \cdot 10^{15} \text{ Hz: } \begin{cases} M_s \gtrsim 78 \text{ TeV}/c^2 & \text{for } d = 2, \\ M_s \gtrsim 30 \left(\frac{2}{d-2}\right)^{1/4} \text{ TeV}/c^2 & \text{for } d > 2. \end{cases}$$

These constraints are even more stringent for gamma rays at grazing incidence, but, in such a frequency range, we are beyond the limit of the approximation used to obtain (4.8).

Nevertheless, the constraints on LED theories and the predicted deviation quickly weaken if we consider *solar non-grazing incidence* predictions, as can already be seen in (4.8) (with $b \sim \rho_{\text{obs}} \sin \vartheta_I$) when ϑ_I increases. Indeed, for the limiting mass scales verifying the observations in the visible (4.9), the predicted deviation at 35° for an observer on Earth would be:

$$\text{to verify (4.9) } \begin{cases} \text{in the visible at } 5 \cdot 10^{14} \text{ Hz: } & 1 - \gamma \simeq -6 \cdot 10^{-6}, \\ \text{in the UV-band at } 5 \cdot 10^{15} \text{ Hz: } & 1 - \gamma \simeq -6 \cdot 10^{-4}. \end{cases} \quad (4.11)$$

Simulation (4.12) shows the constraints (M_s , d) on LED theories in the visible waveband IF a given observed deviation $1 - \gamma|_{\text{exp}}$ is achieved.



(4.12)

Concerning future experiments, we see that dedicated precision experiments measuring the light deflection angle at frequencies in the optical waveband and above would be welcome. Of course, to avoid the absorption by the atmosphere at such frequencies, those have to be satellite missions. We know that (non-dedicated) astrometric satellites like GAIA will only observe at large angles from the Sun ($\vartheta_I \geq 35^\circ$ for GAIA) where the LED corrections to GR are weaker. However, the GAIA survey will be made from UV blue to far red (close to one micron) in order to allow the classification of stars. The upper energy range might be useful to test LED theories. Indeed, at 35° , the predicted deviation from GR in the visible and UV range (4.11)³⁵ is still within the reach of the precision of GAIA aiming at $5 \cdot 10^{-7}$ on $1 - \gamma$.

An alternative to giving a mass to the scalar zero-mode is to introduce quantum corrections to the coupling (String loops), so that the effective coupling of the scalar field to matter fields be weak and compatible with present experiments. References [35, 33] give a general overview of the idea, while articles [44, 45] provide a detailed model and motivate an improvement of the WEP experiments.

³⁵ These values were estimated for an observer on Earth, but the order of magnitude does not change when observations are made from GAIA.

4.3 Theories leading to second order corrections

We now consider two alternative theories, MTS and SITS, with a minimal scalar coupling contribution, that lead to a correction in the light deflection angle only at the second order; the first order term is exactly the same as the GR one.

4.3.1 Effective geodesic potential for light

4.3.1.1 General case

In the case of a general diagonal, spherically symmetric metric, the geodesic expression (3.5) with $u \equiv 1/q$ (either in Schwarzschild coordinates, $q \equiv r$; or in isotropic coordinates, $q \equiv \rho$), leads to an effective geodesic potential

$$\begin{aligned} \frac{1}{q^4} \left(\frac{dq}{d\varphi} \right)^2 \frac{A^2 B^2}{D^4} + \frac{1}{q^2} \frac{A^2}{D^2} + F \frac{A^2}{J^2} &= \frac{E^2}{J^2} \\ \Leftrightarrow \underbrace{\left(\frac{dq}{d\lambda} \right)^2}_{\text{"Kinetic Energy"}} + \underbrace{\left\{ \frac{1}{q^2} \frac{A^2}{D^2} + F \frac{A^2}{J^2} \right\}}_{V_{\text{geodesic}} = \text{"Effective geodesic potential"}} &= \underbrace{\frac{E^2}{J^2}}_{\text{"Total Energy"}}. \end{aligned} \quad (4.13)$$

This mechanical analogy turns out to be quite useful to discuss the trajectories of photons ($F \equiv 0$) and of massive particles ($F > 0$) in MTS/SITS and Weyl theories.

4.3.1.2 MTS/SITS theories

In the MTS or SITS theory, there is a transition value for the parameter, $\Upsilon_{\text{transition}} \equiv 0.5$, under which no black-hole can exist. This can be seen when plotting the effective geodesic potential for light ($F \equiv 0$) in Schwarzschild coordinates.

According to (4.13) and (3.6), we have indeed

$$\underbrace{\left(\frac{dr}{d\lambda} \right)^2}_{\text{"Kinetic Energy"}} + \underbrace{\frac{1}{r^2} \left(1 - \frac{\bar{r}}{r} \right)^{2\Upsilon-1}}_{V_{\text{geodesic light}} = \text{"Effective light potential"}} = \underbrace{\frac{1}{b^2}}_{\text{"Total Energy"}} \quad (4.14)$$

for the MTS as well as for the SITS theories, because expression (4.14) is invariant under conformal transformations when the coupling of matter to gravity is unchanged.

A/ For $\Upsilon \in]\Upsilon_{\text{transition}} \equiv 0.5; 1 \equiv \Upsilon_{GR}]$

The exponent in the effective geodesic light potential is positive and we can calculate the different characteristics of the potential curve, namely:

$$r_{\text{max}} = \frac{2\Upsilon+1}{2} \bar{r} \Leftrightarrow \left. \frac{dV_{\text{geodesic light}}}{dr} \right|_{r_{\text{max}}} = 0 \text{ and } V_{\text{geodesic light}}(r_{\text{max}}) = \frac{4}{\bar{r}^2} \frac{(2\Upsilon-1)^{2\Upsilon-1}}{(2\Upsilon+1)^{2\Upsilon+1}},$$

$$r_{\text{inflection point}} = \frac{6(2\Upsilon+1) \pm \sqrt{36(2\Upsilon+1)^2 - 24(2\Upsilon+1)(2\Upsilon+2)}}{12} \bar{r} \Leftrightarrow \left. \frac{d^2 V_{\text{geodesic light}}}{d^2 r} \right|_{r_{\text{max}}} = 0,$$

$$r = 0 \Leftrightarrow V_{\text{geodesic light}}(0) = -\infty,$$

$$\bar{r} \Leftrightarrow V_{\text{geodesic light}}(\bar{r}) = 0.$$

The shape of the potential is analogous to the usual Schwarzschild black-hole with a generalized Schwarzschild radius called

$$\bar{r} \equiv \frac{2GM}{\Upsilon c^2}. \quad (4.15)$$

Remember that the Schwarzschild solution is recovered for $\Upsilon_{GR} \equiv 1$, and that \bar{r} is then the usual horizon or Schwarzschild radius.

The instable orbit for photons is given by r_{\max} . It represents a critical value for closest approach distance,

$$r_{0c} \equiv r_{\max} = \frac{2\Upsilon + 1}{2} \bar{r}, \quad (4.16)$$

under which no light deflection can take place, since the light ray is captured by the black-hole. Equivalently, we can define the corresponding critical impact parameter:

$$b_c \equiv \frac{1}{2} \sqrt{\frac{(2\Upsilon + 1)^{2\Upsilon+1}}{(2\Upsilon - 1)^{2\Upsilon-1}}} \bar{r}.$$

Consequently, the condition for light deflection on the radial coordinate, r , is

$$\boxed{r \geq r_0 > r_{0c} > \bar{r}}. \quad (4.17)$$

Finally, we note that there is no minimum in this curve, unlike for the Weyl theory as we shall see later.

B/ For $\Upsilon = \Upsilon_{transition} \equiv 0.5$

The effective potential is here simply $V_{\text{geodesic light}} = \frac{1}{r^2}$. Its behavior is totally different from the potentials previously considered: the curve is monotonous, there exists no critical impact parameter, and thus no black-hole. Light rays are always scattered, never captured by the gravitational mass. The effective potential behaves like a wall ($r = 0 \Leftrightarrow V_{\text{eff}} = +\infty$) that prevents light rays to come too close to the massive body.

However, solutions to the MTS and SITS theories do not allow $r < \bar{r}$, as can be seen from expressions (1.30) and (1.63) for their respective scalar field. The condition on the radial coordinate, r , is hence

$$\boxed{r \geq r_0 > \bar{r} = r_{0c}}.$$

C/ For $\Upsilon \in]0; 0.5 \equiv \Upsilon_{transition}[$

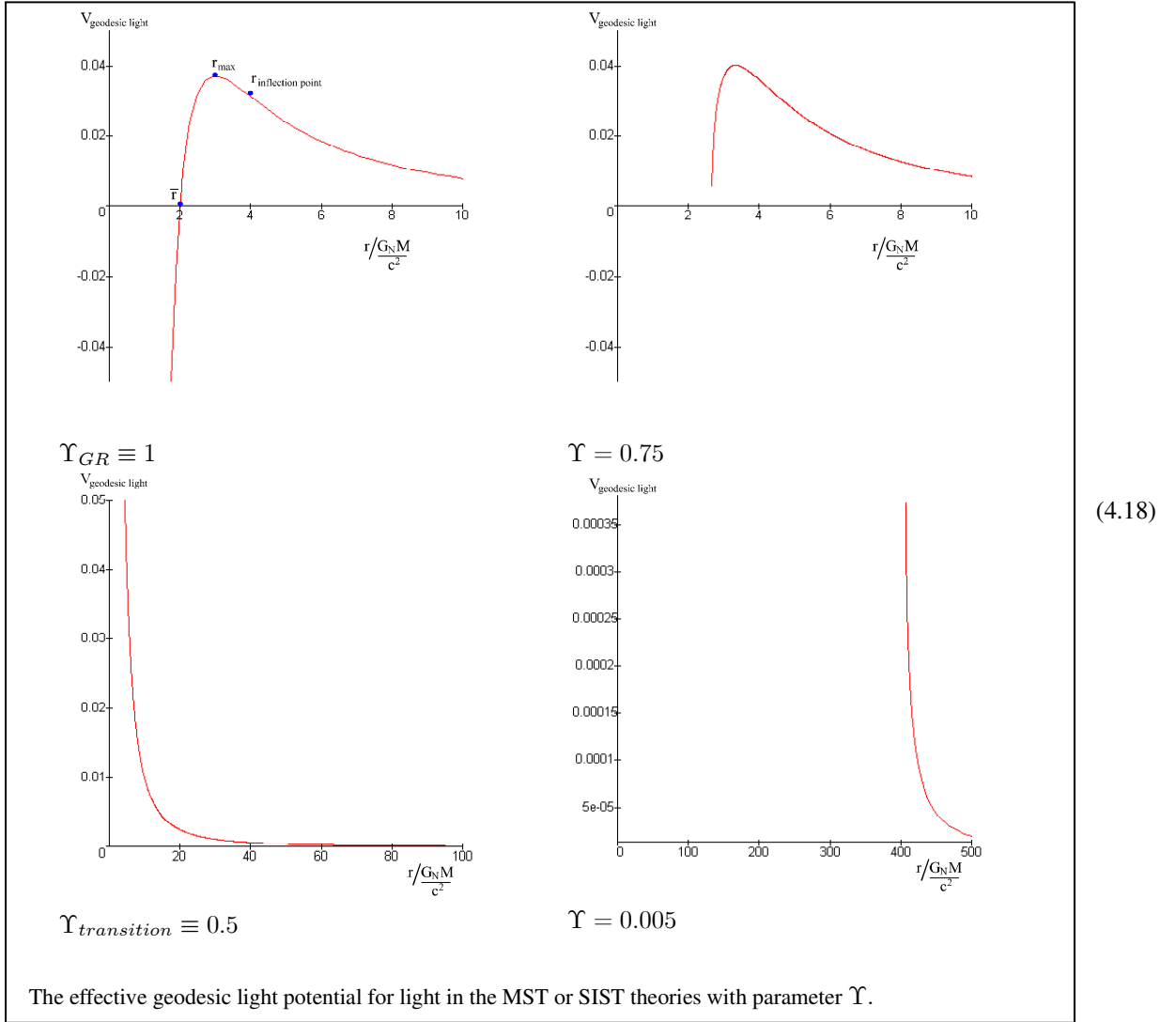
For those values of the theory parameter Υ , the potential exponent is negative and thus the properties of the effective potential are fundamentally different from those of the first category. Like for $\Upsilon = 0.5$, there exists no critical impact parameter, and thus no black-hole. Light ray are hence always scattered, never captured by the gravitational lens. The effective geodesic light potential behaves as a wall ($r = \bar{r} \Leftrightarrow V_{\text{geodesic light}} = +\infty$), exactly like in the $\Upsilon_{transition}$ case. Decreasing values of the Υ parameter lead to a shift of that wall towards increasing values of r (\bar{r} increases). The condition on the radial coordinate, r , for light deflection to take place is then analogous to the one for $\Upsilon = 0.5$:

$$\boxed{r \geq r_0 > \bar{r} > r_{0c}}.$$

We also note that there exists a local maximum for this potential:

$$r_{\max} = \frac{2\Upsilon + 1}{2} \bar{r} \Leftrightarrow V_{\text{geodesic light}}(r_{\max}) = \frac{4}{(2\Upsilon + 1)^2 \bar{r}^2} \left(\frac{2\Upsilon + 1}{2\Upsilon - 1} \right)^{1-2\Upsilon}.$$

The associated energy is negative though. Hence, like for the whole region $r < \bar{r}$, it corresponds to bound orbits.



4.3.2 Asymptotic weak field second order and finite distance deflection angle for MTS/SITS theories

Expressions (3.22) and (3.25) of the asymptotic light deflection angle, calculated to illustrate the importance of the impact parameter in a coordinate invariant formulation, showed us that the change in the apparent position of a light source only differs from GR predictions (when $\Upsilon \neq 1$) at the second order. This can also be seen immediately when looking at the relevant (PPN) combinations for light deflection in Table (4.1).

From expressions (3.23) and (3.25), one can easily see that there exists a closest approach distance, r_{00} , or alternatively a value of the impact parameter, b_{00} , under which the light deflection is divergent, if $\Upsilon < 1/4$:

$$\begin{aligned}
 r_{00} &\equiv - \left(1 + \frac{2}{\pi} - \frac{1}{\Upsilon\pi} - \frac{1}{16\Upsilon^2} \right) \pi \frac{GM}{c^2}, \\
 b_{00} &\equiv - \left(1 - \frac{1}{16\Upsilon^2} \right) \pi \frac{GM}{c^2}.
 \end{aligned}
 \tag{4.19}$$

For any solar system body acting as a deflector though, to have a *physical* distance r_{00} (or b_0) (in other words, r_{00} larger than the radius of the gravitational body) requires very small values of Υ , far from the general relativistic value $\Upsilon_{GR} \equiv 1$. For example, in the case of the Sun, it would imply $\Upsilon \lesssim 6.5 \cdot 10^{-4}$, and even smaller values of the MTS/SITS parameter for other solar system bodies. Consequently, light deflection as predicted by those theories is always convergent in the solar system, for not too small values of Υ . Also, with such a condition on Υ , light deflection always takes place in the case of solar system bodies, because the critical closest approach distance (4.16) is unphysical too.

The conclusion is that solar system light deflection experiments offer only a quantitative test of MTS/SITS theories with not too small values of Υ (there are no qualitative deviations from GR in the solar system) *if* the second order is measured. But as was discussed in Section 3.2.4 with regard to Tables (3.35) and (3.36), the only body whose second order contribution is non negligible at the level of the microarcsecond is the Sun, for an incidence angle inferior or equal to $51.8' - 53.6'$. However, we recall that astrometric satellites will not allow for observations at such a small angle from the Sun. Dedicated experiments are thus needed to investigate near grazing incidence. Moreover, a predicted deviation from GR in the second order contribution will be hard to distinguish from the angular-momentum, quadrupole-moment and other corrective effects. As an example, a deviation larger than one microarcsecond in the second order contribution at grazing incidence for the Sun, would require Υ to be smaller than about 0.65 as estimated in the isotropic coordinates in agreement with Table (3.36).

Let us recall that the parameter of the MTS and SITS theories, Υ belongs to the interval $]0, 1 \equiv \Upsilon_{GR}]$. The light deflection angle for MTS and SITS theories is hence always smaller (when $\Upsilon < 1$) than the GR one. This particular case confirms Bekenstein's statement: without dark matter, the light deflection angle predicted in Tensor Scalar theories is always smaller than that of General Relativity.

4.4 Theories leading to a modification of the Newtonian potential

4.4.1 Effective geodesic potential for the Weyl theory

In the Weyl theory, the shape of the effective geodesic potential for light crucially changes according to the sign chosen for the parameter γ_W , and to whether the contribution of some parameters (γ_W, β_W, k_W) is considered as negligible or not. There might exist no black-hole solution. Moreover, the effective geodesic potential for photons versus that for massive particles presents different features that might enlighten us on the role of the effective sign of the parameter γ_W , measured through light deflection or galactic rotation curves. We can check those statements by comparing the Weyl effective geodesic potential for light ($F \equiv 0$) with that for matter ($F > 0$) in Schwarzschild coordinates using (4.13) and the metric given in (1.51) with (1.52):

$$\underbrace{\left(\frac{dr}{d\lambda}\right)^2}_{\text{"Kinetic Energy"}} + \underbrace{\left\{\frac{1}{r^2} + F \frac{\chi^2(r)}{J^2}\right\} \left\{1 + 2 \frac{V_W(r)}{c^2}\right\}}_{V_{\text{geodesic}} = \text{"Effective potential"}} = \underbrace{\frac{E^2}{J^2}}_{\text{"Total Energy"}}. \quad (4.20)$$

First note that, as stated earlier, photon geodesics are independent of the conformal factor $\chi^2(r)$, to be specified by the symmetry breaking mechanism; this is not the case for massive geodesics.

To illustrate further the different behavior of massive versus massless geodesics, let us fix arbitrarily $\chi^2(r)$ to 1 and

consider the effective gravitational force. The derivative of the effective geodesic potential is given by [51]

$$\begin{aligned}
 -F_{\text{geodesic}}(r) \propto \frac{dV_{\text{geodesic}}}{dr} = & -\frac{2}{r^3} \\
 & +\beta_W(2-3\beta_W\gamma_W)\left\{\frac{3}{r^4} + \frac{F}{J^2 r^2}\right\} \\
 & +3\beta_W\gamma_W\left\{\frac{2}{r^3}\right\} \\
 & +\gamma_W\left\{-\frac{1}{r^2} + \frac{F}{J^2}\right\} \\
 & +k_W\left\{0 - 2\frac{Fr}{J^2}\right\}.
 \end{aligned} \tag{4.21}$$

The interpretation of the first three terms contributing to the ‘‘geodesic force’’ is unambiguous: the first term is asymptotically convergent with respect to the variable r and negative (repulsive) for any type of particle. Whereas the factor corresponding to the Newtonian term (multiplying $\beta_W(2-3\beta_W\gamma_W)$) is always positive (attractive), regardless of the type of particle. The same conclusion holds for the factor in front of the $(\beta_W\gamma_W)$ -term, which is always positive (thus attractive) if γ_W is positive, or alternatively negative (thus repulsive) for a negative γ_W . Both the Newtonian term and this last term are asymptotically convergent.

On the contrary, the fifth term clearly distinguishes between massive and nonmassive particles. The k_W -term has a null contribution for photons, unlike for massive particles; and for nonrelativistic particles, it is repulsive (negative) for a positive k_W or conversely for a negative k_W . Moreover, the corresponding term in the potential, $V_{\text{geodesic}}(r)$, is asymptotically divergent for massive particles at large r . However, in any case, we can neglect the k_W -contribution (set $k_W = 0$) on non-cosmological distances.

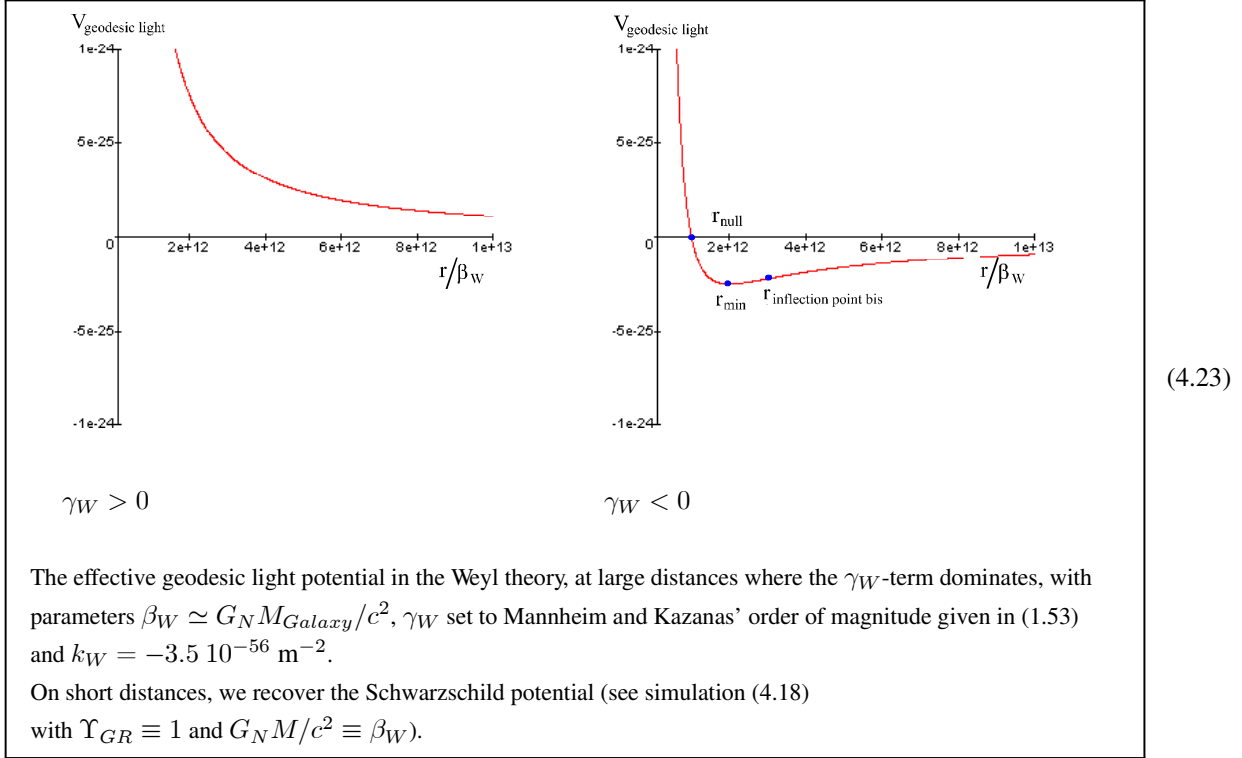
Let us therefore focus on the original feature of the Weyl gravity, the fourth term, which cannot be neglected at intermediate distances. We realize that the sign of the factor in front of the parameter γ_W depends on the type of particle: it is always negative for photons ($F = 0$) and for sufficiently relativistic particles, *i.e.* for particles verifying

$$\left\{-\frac{1}{r^2} + \frac{F}{J^2}\right\} < 0 \stackrel{\text{if } dr/d\lambda \sim 0 \text{ in (4.20) and (3.6)}}{\Leftrightarrow} J^2/E^2 \gtrsim r_0^2/2 \left\{1 - 2\frac{V_W(r)}{c^2}\right\} \quad \text{for } V_W(r)/c^2 \text{ small.}$$

In contrast, it is positive for massive, not too relativistic particles. For photons, moreover, the contribution of the γ_W -term in the potential $V_{\text{geodesic}}(r)$ is convergent on large radial distances; whereas it diverges linearly for massive, not too relativistic particles. Again, for photons, this term is attractive for $\gamma_W < 0$ or repulsive for $\gamma_W > 0$; while it is just the opposite for nonrelativistic particles.

We now analyze thoroughly the case of null geodesics ($F \equiv 0$ and we set k_W to zero), that is, the trajectory of photons and ultra relativistic particles. We find the following characteristics for the effective geodesic light potential, which we approximate (Simulation (4.23)), assuming that $\beta_W\gamma_W$ is small in comparison with β_W and γ_W alone:

$$\begin{aligned}
 r_{\min} = \frac{3\beta_W\gamma_W - 2}{\gamma_W} & \sim -\frac{2}{\gamma_W} \Leftrightarrow \left.\frac{dV_{\text{geodesic light}}}{dr}\right|_{r_{\max}} = 0 \text{ and } V_{\text{geodesic light}}(r_{\min}) = \frac{\gamma_W^2(\beta_W\gamma_W - 1)}{(3\beta_W\gamma_W - 2)^2}, \\
 r_{\max} = 3\beta_W & \Leftrightarrow \left.\frac{dV_{\text{geodesic light}}}{dr}\right|_{r_{\max}} = 0 \text{ and } V_{\text{geodesic light}}(r_{\min}) = \frac{3\beta_W\gamma_W + 1}{27\beta_W}, \\
 r_{\text{inflection point bis}} & = \frac{-3 + 9\beta_W\gamma_W - \sqrt{9 - 54\beta_W\gamma_W + 81(\beta_W\gamma_W)^2 + 48\gamma_W - 72\beta_W\gamma_W^2}}{2\gamma_W} \sim -\frac{3}{\gamma_W}, \\
 \Leftrightarrow \left.\frac{d^2V_{\text{geodesic light}}}{d^2r}\right|_{r_{\max}} & = 0 \text{ and } V_{\text{geodesic light}}(r_{\text{inflection point bis}}) \Big|_{\beta_W=0} = -\frac{2\gamma_W^2}{9}, \\
 r = 0 & \Leftrightarrow V_{\text{geodesic light}}(0) = \pm\infty, \\
 r_{\text{null}} = \frac{-1 + 3\beta_W\gamma_W - \sqrt{1 + 2\beta_W\gamma_W - 3(\beta_W\gamma_W)^2}}{2\gamma_W} & \sim -\frac{1}{\gamma_W} \Leftrightarrow V_{\text{geodesic light}}(r_{\text{null}}) = 0.
 \end{aligned} \tag{4.22}$$



A/ For $\gamma_W = 0$ ($F = k_W = 0$)

When γ_W is null, we essentially recover General Relativity: the effective geodesic light potential is that of a Schwarzschild black hole. There thus exists a critical value of the closest approach distance ($r_{0c} = r_{max}$) under which no deflection can take place:

$$r \geq r_0 > r_{0c} > \bar{r} \quad \text{with } \beta = G_N M/c^2 \text{ and } \Upsilon_{GR} \equiv 1 \text{ in (4.16) and (4.15).} \quad (4.24)$$

B/ For $\beta_W = 0$ ($F = k_W = 0$)

When β_W is assumed to be zero, the shape of the potential for light depends crucially on the sign of γ_W .

1/ $\gamma_W > 0$

For positive values of γ_W , the effective geodesic potential for light is a wall, and thus there exists no critical value of the closest approach distance. Indeed, the characteristic points of the curve (minimum, inflection point) are at negative radius and thus are non physical. Light deflection can occur at any radial distance:

$$\text{for } \gamma_W > 0: \quad r \geq r_0. \quad (4.25)$$

2/ $\gamma_W < 0$

In case of a negative γ_W , we have, again, a potential wall with no critical value of the closest approach distance, but it admits a minimum (r_{min}) and negative energies. This r_{min} constitutes the radius of a stable circular orbit for photons, and together with other orbits of negative effective total energy ($\left. \frac{E^2}{J^2} \right|_{photon} < 0$) it belongs to the class of bound states. There thus exists a maximum closest approach distance, r_{null} , allowed for asymptotically free trajectories, meaning

for light deflection to take place:

$$\boxed{\text{for } \gamma_W < 0: \quad r \geq r_0 \quad \text{and} \quad r_0 \leq r_{null}.} \quad (4.26)$$

The role of r_{null} will be clarified in the next paragraph, particularly with expression (4.35).

C/ For nonzero values of γ_W and β_W ($F = \mathbf{k}_W = 0$)

On short distance scales ($r \ll 1/|\gamma_W|$), the potential is Schwarzschild-like and analogous to case **A/** discussed above. The corresponding graph is given in simulation (4.18) with $\Upsilon_{GR} \equiv 1$ and $\beta_W \equiv G_N M/c^2$.

On intermediate distances ($r \sim 1/|\gamma_W|$), if $\gamma_W < 0$, the effective geodesic potential for light presents a minimum as described in case **B2/**. Otherwise, for $\gamma_W > 0$, the comments given in Paragraph **B1/** above apply.

Corresponding graphs at intermediate distances are given in (4.23).

4.4.2 Asymptotic deflection angle for the Weyl theory

Let us now consider more specifically trajectories for photons in the Weyl theory, and in particular, light deflection. The following analysis will be carried out with regards to the characteristic radius r_{\min} and r_{null} that we have just introduced.

4.4.2.1 Deflection angle and conditions for unbound photon orbits

A/ Weak field, first order deflection angle

We give here a first expression for the asymptotic light deflection angle due to a spherically symmetric gravitational potential in the Weyl theory. This result is based on the weak field approximation ($2V_W/c^2 \ll 1$), and hence is valid only on the distance scales mentioned in (1.54). It is obtained when using the first order expression (3.10) given in Schwarzschild coordinates, together with (1.52):

$$\hat{\alpha}_{\text{weak field}}(r_0) \simeq + \frac{2\beta_W (2 - 3\beta_W \gamma_W)}{r_0} + \frac{3}{2} \beta_W \gamma_W \pi - \gamma_W r_0, \quad (4.27)$$

$$\text{where } r_0 \text{ verifies (1.54) with (4.24) and (4.25), if } \gamma_W > 0: \quad r_0 \in]r_0 c, +\infty[, \\ (4.24) \text{ and (4.26), if } \gamma_W < 0: \quad r_0 \in]r_0 c, r_{null}[,$$

$$b \simeq r_0 .$$

We see that the $(\beta_W \gamma_W)$ -term contributes to a small constant deflection, independent of the radial distance, while the linear term tends to decrease or increase the usual Newtonian contribution (first term in (4.27)), according to the sign of the parameter γ_W .

If γ_W is negative, the asymptotic deflection angle is always convergent (positive); whereas if γ_W is positive, the deflection angle cancels at $r_{00}(M)$, which is a function of the deflector mass, and becomes divergent (negative) beyond that distance:

$$r_{00} \equiv \frac{3\pi \beta_W \gamma_W + \sqrt{9(\beta_W \gamma_W)^2 \pi^2 + 32\beta_W \gamma_W(2 - 3\beta_W \gamma_W)}}{4\gamma_W} \quad (4.28)$$

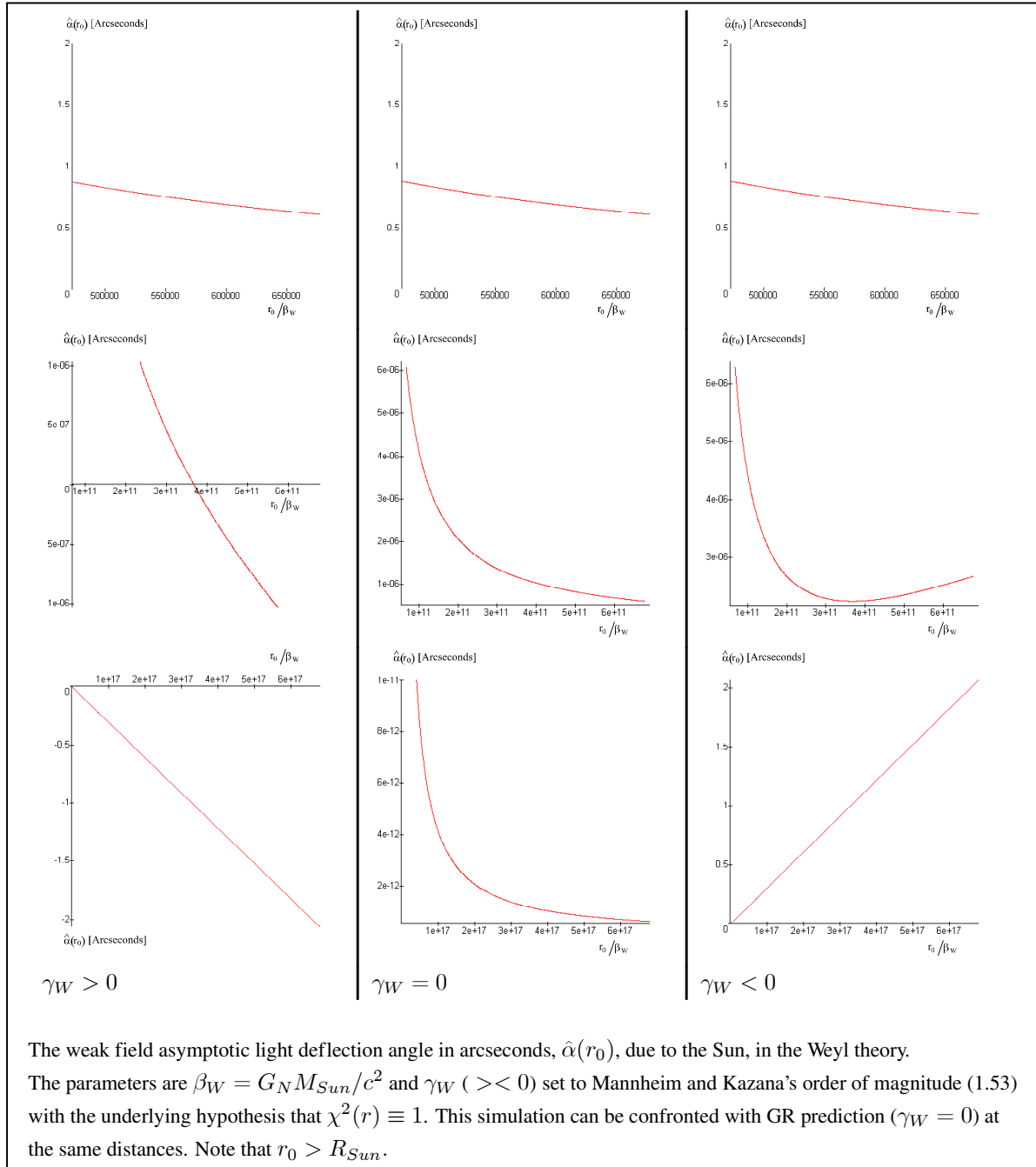
$$\sim 2\sqrt{\frac{\beta_W}{\gamma_W}}$$

$$\sim \sqrt{6} 10^{\frac{x+3}{2}} \frac{1}{\sqrt{|\gamma_W|}} \text{ m for } M = 10^x M_{Sun} \text{ and } \gamma_W \text{ in } [\text{m}^{-1}]$$

$$\stackrel{(1.53)}{\sim} \left\{ \begin{array}{l} 8 \cdot 10^{14} \text{ m for } M = M_{Sun} , \\ 2 \cdot 10^{20} \text{ m for } M = 10^{11} M_{Sun} , \\ 2 \cdot 10^{21} \text{ m for } M = 10^{13} M_{Sun} , \\ 8 \cdot 10^{21} \text{ m for } M = 10^{14} M_{Sun} , \\ 2 \cdot 10^{22} \text{ m for } M = 10^{15} M_{Sun} , \end{array} \right\} \begin{array}{l} \text{a galaxy} \\ \text{a cluster} \end{array} \quad \text{if } \chi^2(r) = 1 .$$

We also note that, whichever distance scales are, the cosmological k_W -term of the Weyl potential naturally cancels out in expression (3.7). Consequently, it does not contribute to the asymptotic light deflection angle. This agrees with the fact that for photons, the derivative of the effective geodesic light potential is blind to k_W , as stated in the preceding subsection.

The following simulation (4.29) illustrates the behavior of the asymptotic deflection angle for the Weyl theory in the gravitational field of the Sun, as a function of the closest approach distance.



(4.29)

The weak field asymptotic light deflection angle in arcseconds, $\hat{\alpha}(r_0)$, due to the Sun, in the Weyl theory. The parameters are $\beta_W = G_N M_{Sun}/c^2$ and $\gamma_W (>< 0)$ set to Mannheim and Kazana's order of magnitude (1.53) with the underlying hypothesis that $\chi^2(r) \equiv 1$. This simulation can be confronted with GR prediction ($\gamma_W = 0$) at the same distances. Note that $r_0 > R_{Sun}$.

B/ Strong field deflection angle

On larger radial distances, the weak field approximation is no longer valid. However, *if* distances are sufficiently large with respect to the order of magnitude of $1/|\gamma_W|$ and of the deflector mass M , that is to say,

$$\begin{aligned}
 r_{strong\ field} &\ggg \sqrt{\frac{2\beta_W}{|\gamma_W|}} \\
 &\ggg \sqrt{3} 10^{\frac{x+3}{2}} \frac{1}{\sqrt{|\gamma_W|}} \text{ m for } M = 10^x M_{Sun} \text{ and } \gamma_W \text{ in } [\text{m}^{-1}] \\
 &\stackrel{(1.53)}{\ggg} \left\{ \begin{array}{l} 2 \cdot 10^{20} \text{ m for } M = 10^{11} M_{Sun} \\ 2 \cdot 10^{21} \text{ m for } M = 10^{13} M_{Sun} \\ 6 \cdot 10^{21} \text{ m for } M = 10^{14} M_{Sun} \\ 2 \cdot 10^{22} \text{ m for } M = 10^{15} M_{Sun} \end{array} \right\} \begin{array}{l} \text{a galaxy} \\ \\ \\ \text{a cluster} \end{array} \quad \text{if } \chi^2(r) = 1,
 \end{aligned} \tag{4.30}$$

the gravitational Weyl potential can be approximated to its linear and quadratic contributions only:

$$V_W(r)_{\beta_W \equiv 0} = +\frac{\gamma_W}{2} r c^2 - \frac{k_W}{2} r^2 c^2. \tag{4.31}$$

Note that the radial variable r must belong to the following allowed ranges, to insure a proper definition of the line element in Schwarzschild coordinates, (1.51), when $\beta_W \equiv 0$:

proper definition of line element (1.51)

$$\Leftrightarrow A_{\beta_W \equiv 0}^2(r) = B_{\beta_W \equiv 0}^{-2}(r) > 0:$$

Let $K \equiv -k_W - \frac{\gamma_W^2}{4}$,

if $K > 0 \Leftrightarrow k_W < -\frac{\gamma_W^2}{4} < 0$: $r \in [0, +\infty[$

if $K = 0 \Leftrightarrow k_W = -\frac{\gamma_W^2}{4}$: $\begin{cases} \gamma_W > 0 \Rightarrow r_{\min} < 0: & r \in [0, +\infty[\\ \gamma_W < 0 \Rightarrow r_{\min} > 0: & r \in [0, r_{\min}[\end{cases}$

if $K < 0$: $\begin{cases} k_W > 0 \Rightarrow r_- < 0 \text{ and } r_+ > 0: & r \in [0, r_+[\\ k_W = 0: \begin{cases} \gamma_W > 0 \Rightarrow r_{null} < 0: & r \in [0, +\infty[\\ \gamma_W < 0 \Rightarrow r_{null} > 0: & r \in [0, r_{null}[\end{cases} \\ k_W < 0: \begin{cases} \gamma_W > 0 \Rightarrow r_- < 0 \text{ and } r_+ < 0: & r \in [0, +\infty[\\ \gamma_W < 0 \Rightarrow r_- > r_+ > 0: & r \in [0, r_+[\cup]r_-, +\infty[\end{cases} \end{cases}$

where r_{\min} is the root of $A_{\beta_W \equiv 0}^2(r)$ when $K = 0$
 $r_{\pm} \equiv \frac{\gamma_W \pm \sqrt{-4K}}{2k_W}$ are the roots of $A_{\beta_W \equiv 0}^2(r)$ when $K < 0$
 r_{null} is the root of $A_{\beta_W \equiv 0}^2(r)$ when $k_W = 0$
 \dots \nexists roots of $A_{\beta_W \equiv 0}^2(r)$ when $K > 0$.

(4.32)

Moreover, we need to add certain conditions on the distances r and r_0 , so that the square-root of the integrand be positive³⁶:

conditions for $\Delta(r) \equiv (1 + \gamma_W r_0) r^2 - \gamma_W r_0^2 r - r_0^2 \geq 0$ in (3.9) when $\beta_W \equiv 0$:

if $\gamma_W > 0$: $r \in [r_0, +\infty[$

if $\gamma_W < 0$: $\begin{cases} 0 < r_0 < r_{null} \Rightarrow r_* < 0: & r \in [r_0, +\infty[\\ r_0 = r_{null}: & r \in [r_0, +\infty[\\ r_{null} < r_0 < r_{min} \Rightarrow 0 < r_0 < r_*: & r \in [r_0, r_*] \\ r_0 = r_{min} \Rightarrow r_* = r_0 \\ r_0 > r_{min} \Rightarrow 0 < r_* < r_0: & r \in [r_*, r_0] \end{cases}$ (4.33)

where $r_* \equiv \frac{-r_0}{1+\gamma_W r_0}$ and r_0 are the roots of $\Delta(r)$ when $r_0 < r_{min}$ and $r_0 \neq r_{null}$
 r_{null} is the root of $\Delta(r)$ when $r_0 = r_{null}$
 \nexists roots of $\Delta(r)$ when $r_0 > r_{min}$ and $\gamma_W < 0$.

The above conditions already provide a distinction between bound and unbound orbits.

Bearing discussions (4.32) and (4.33) in mind, the potential (4.31) permits an exact integration of the photon trajectory (3.9) given by

$$\varphi(r)_{\beta_W \equiv 0} = \left[\pm \arctan \left(\frac{r_0 (\gamma_W r + 2)}{2\sqrt{\Delta(r)}} \right) \right]_{r_{initial}}^r$$

with $\begin{cases} r_{initial} = +\infty & \text{for an unbound orbit} \\ r_{initial} = r_0 & \text{for a bound orbit} \end{cases}$

$$\Rightarrow \pm \varphi(r)_{\beta_W \equiv 0} \pm \varphi_{initial} = \arcsin \left(\frac{2 r_0 / r + \gamma_W r_0}{2 + \gamma_W r_0} \right)$$

$$\Leftrightarrow r_{\beta_W \equiv 0} = \frac{-2/\gamma_W}{1 - \frac{2+\gamma_W r_0}{\gamma_W r_0} \cdot \sin(\pm\varphi \pm \varphi_{initial})} \quad (4.34)$$

where $\begin{cases} \varphi_{initial} \equiv \begin{cases} + \arcsin \left(\frac{\gamma_W r_0}{2+\gamma_W r_0} \right) & \forall r_0 \text{ if } \gamma_W > 0; \text{ or for } r_0 < r_{null} \text{ if } \gamma_W > 0 \\ \mp \frac{\pi}{2} & \text{for } r_0 = r_{null} \text{ or } r_0 > r_{min} \text{ if } \gamma_W < 0 \\ \pm \frac{\pi}{2} & \text{for } r_{null} < r_0 < r_{min} \text{ if } \gamma_W < 0 \end{cases} \\ e \equiv \left| \frac{2+\gamma_W r_0}{\gamma_W r_0} \right| \text{ eccentricity.} \end{cases}$

The types of allowed orbits can thus be classified [51] according to (4.35), with respect to r_{null} , r_{min} and r_* given in (4.22) and (4.33). Figures 4.3 and 4.4 illustrate this point.

³⁶ It should be further restricted to a strict inequality for the integration variable r in (3.9).

types of orbits in Schwarzschild coordinates :

for r verifying (4.33) and (4.32):

a/ if $\gamma_W > 0$: $\forall r_0$, hyperbolic

b/ if $\gamma_W < 0$: 1/ $r_0 < r_{null}$, hyperbolic ($e > 1$)

2/ $r_0 = r_{null}$, parabolic ($e = 1$)

3/ $r_0 > r_{null}$, elliptic ($e < 1$)

... with perihelion/aphelion alternatively given by r_0 and r_*

... particular case if $r_0 = r_{min}$, circular ($e = 0$).

(4.35)

Note that, strictly speaking, expression (4.34) cannot be used for the circular orbit. Instead, one needs to come back to the geodesic equation for photons ($F = 0$) (4.20) and to its derivative with respect to r . Then, constant radius orbits are found when imposing $\partial r / \partial \lambda = \partial^2 r / \partial \lambda^2 = 0$. The circular orbit radii obtained correspond to r_{min} and r_{max} given in (4.22), of which r_{max} is unstable.

Consequently, the light deflection angle (3.8) which requires asymptotically free orbits (hyperbolic or parabolic as described by (4.35) and summarized in conditions (4.25) or (4.26)) is given exactly by

$$\hat{\alpha}_{\beta_W \equiv 0}(r_0) = -2 \arcsin \left(\frac{\gamma_W r_0}{2 + \gamma_W r_0} \right), \quad (4.36)$$

where r_0 verifies (4.30) and (4.25), if $\gamma_W > 0$: $r_0 < +\infty$

(4.26), if $\gamma_W < 0$: $r_0 \leq r_{null}$

$b \neq r_0$

$= \frac{r_0}{\sqrt{A_{\beta_W \equiv 0}^2(r_0)}}$ from (3.6) particularized to photons, $q_0 = r_0$ and $V_W(r)_{\beta_W \equiv 0}$

is meaningless because gravity does not vanish asymptotically.

We thus recover the linear contribution of (4.27)³⁷ for small enough values of $\gamma_W r_0$.

We now understand thoroughly the role of the radius r_{null} , at which the effective geodesic potential for light is zero. It truly defines an influence region and is the borderline between unbound and bound orbits. If we consider the order of magnitude given to γ_W by Mannheim and Kazanas (1.53) which rests on the (arbitrary) choice $\chi^2(r) \equiv 1$, then $r_{null} \sim 10^{26}$ m is a cosmological distance. On the other hand, if we consider the more conservative estimate of γ_W , to be derived in Paragraph 4.4.2.3 from light deflection measurements and which does not imply any restriction on $\chi^2(r)$, then $r_{null} \gtrsim 10^{18}$ m might be within galactic distances.

It is also interesting to notice that the strong field limit radius given in (4.30) is of the same order of magnitude as the particular closest approach distance r_{00} (4.28). This means that each time we are allowed to work in the strong field limit, we necessarily work in the divergent regime for $\gamma_W > 0$. This is why all the photon orbits given in (4.35) for a positive parameter, or shown in Figure 4.3 are divergent.

³⁷ Note that expressions (4.27) and (4.36) have been previously calculated and discussed in our work [107] in 1997, but were recovered in Edery *et al.*'s articles [51, 50] in 1998.

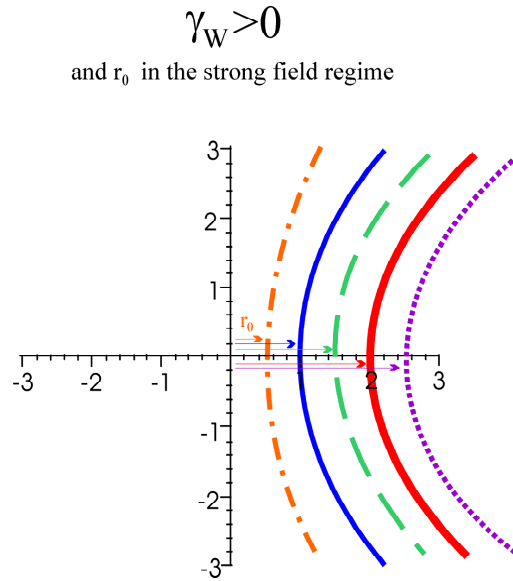


Fig. 4.3 Asymptotic photon trajectories for a positive value of the Weyl parameter γ_W and the deflector located at the origin of the coordinate system. All the orbits are hyperbolic and divergent. In this simulation, $r_0 = \frac{1}{2\gamma_W}$, $r_0 = \frac{1}{\gamma_W}$, $r_0 = \frac{3}{2\gamma_W}$, $r_0 = \frac{2}{\gamma_W}$, and $r_0 = \frac{5}{2\gamma_W}$ respectively for the dash-dot curve, solid line, dash curve, bold curve and dotted line.

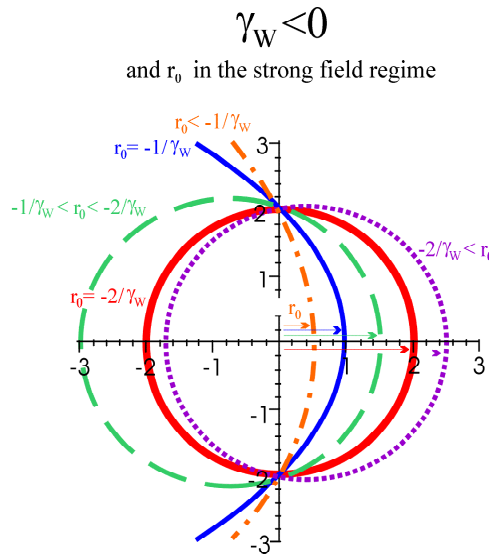


Fig. 4.4 Asymptotic photon trajectories for a negative value of the Weyl parameter γ_W and the deflector located at the origin of the coordinate system. With respect to the characteristic distances $r_{null} \equiv -1/\gamma_W$ and $r_{min} \equiv -2/\gamma_W$, the orbits are convergent and elliptic for $r_0 > r_{null}$ (in particular, circular for $r_0 = r_{min}$), parabolic for $r_0 = r_{null}$ and hyperbolic for $r_0 < r_{null}$. Hence, light deflection is only possible when $r_0 \leq r_{null}$. Note that all the orbits have the same semi-lattice rectum (position located at an angle $\pi/2$ from the closest approach distance position) value of $2/|\gamma_W|$. In this simulation, $r_0 = \frac{-1}{2\gamma_W}$, $r_0 = \frac{-1}{\gamma_W}$, $r_0 = \frac{-3}{2\gamma_W}$, $r_0 = \frac{-2}{\gamma_W}$, and $r_0 = \frac{-5}{2\gamma_W}$ respectively for the dash-dot curve, solid line, dash curve, bold curve and dotted line.

4.4.2.2 Link to the asymptotic conformally flat space

In the following, we assume that conditions (4.25) or (4.26) allowing unbound states are fulfilled.

Before proceeding to the confrontation of the Weyl theory with light deflection experiments, it is important to investigate further the typical asymptotic behavior of Weyl gravity.

The careful reader must have noticed, when using formula (3.7) or (3.8) to obtain expressions for the light deflection angle in asymptotically flat space-times ((4.27), (4.36)), that the spherically symmetric solution (1.51) for the Weyl theory is not asymptotically flat. Indeed, $V_W(r)$ diverges when r goes to infinity. However, this apparent contradiction is solved once we realize that, at large radial distances, the Weyl metric is conformal to a Robertson-Walker metric with spatial curvature $K \equiv \frac{k}{\mathfrak{R}^2} = -k_W - \gamma_W^2/4$. Indeed, when applying the following coordinate transformation [87] with appropriate conditions for the new radius ρ to be positive,

$$\begin{array}{l}
 \text{Weyl Schwarzschild : } (t, r) \mapsto \text{conformal to RW : } (\tau, \rho) \\
 \\
 \text{if } K \leq 0 : \left\{ \begin{array}{l} ct = \int \frac{cd\tau}{\mathfrak{R}(\tau)} \\ \rho = \frac{2 + \gamma_W r - 2\sqrt{A_{\beta_W=0}^2(r)}}{-Kr} \end{array} \right. \quad \begin{array}{l} \text{with condition } r \in [0, r_{\min}[\text{ if } \gamma_W < 0 \text{ and } K < 0 \\ \text{where } A_{\beta_W=0}^2(r) \equiv 1 + \gamma_W r - k_W r^2 \end{array} \\
 \\
 \text{if } K = 0 : \left\{ \begin{array}{l} ct = \int \frac{cd\tau}{\mathfrak{R}(\tau)} \\ \rho = \frac{2r}{2 + \gamma_W r} \end{array} \right. \quad \begin{array}{l} \text{with condition } r \in [0, r_{\min}[\text{ if } \gamma_W < 0 \end{array} \\
 \\
 \Rightarrow r = \frac{\rho}{(1 - \frac{\gamma_W}{4}\rho)^2 + \frac{k_W}{4}\rho^2};
 \end{array} \quad (4.37)$$

and respecting the allowed range (4.32) for the radial variable so that the Weyl metric is properly defined (in which case, the polynomial $A_{\beta_W=0}^2(r)$ under the square root in (4.37) is of course positive), we obtain a Robertson-Walker metric in isotropic coordinates multiplied by a conformal factor:

$$\begin{aligned}
 ds^2 &= \frac{\Omega(\tau, \rho)}{W_{\text{eyl}\beta_W=0} \rightarrow \text{RW}} * \left\{ d\tau^2 - \frac{\mathfrak{R}^2(\tau)}{[1 + \rho^2 K/4]^2} (d\rho^2 + \rho^2 d\Omega^2) \right\}, \\
 \text{where } \frac{\Omega(\tau, \rho)}{W_{\text{eyl}\beta_W=0} \rightarrow \text{RW}} &\equiv \frac{1}{\mathfrak{R}^2(\tau)} \frac{[1 + \rho^2 K/4]^2}{[(1 - \gamma_W \rho/4)^2 + k_W \rho^2/4]^2} \\
 &= \frac{1}{\mathfrak{R}^2(\tau)} \frac{r^2}{\rho^2} [1 + \rho^2 K/4]^2.
 \end{aligned}$$

This Robertson-Walker metric can be recast in Schwarzschild-like coordinates (2.1) multiplied by the same conformal factor. The corresponding radial coordinate is then given by $r_s = \mathfrak{R} \rho / (1 \mp K \rho^2/4)$ for $K \leq 0$. The Robertson-Walker metric constitutes the asymptotic background metric in which the photon moves on a straight line, as $\frac{d\varphi}{d\rho} \Big|_W \xrightarrow{\rho \rightarrow \infty} 0$ in (3.7). A hint to this is that the derivative of the effective geodesic potential for light ((4.21) with $F = 0$) vanishes asymptotically. Or another way to understand the link to asymptotic conformal flat space is to realize that, as the radial distance tends towards infinity, the Weyl tensor goes to zero because all its components are null or proportional to

$$W_{rttr} = \frac{\beta_W}{r^2} \left[\frac{2 - 3\beta_W \gamma_W}{r} + \gamma_W \right] \xrightarrow{r \rightarrow \infty} 0.$$

Consequently, the asymptotic Weyl space-time is conformally related to a flat space.

The coordinate transformations to be performed in order to recover a conformally flat metric are given by the following:

$$\begin{array}{l}
\text{conformal to RW : } (\tau, \rho) \mapsto \text{conformal to Minkowski : } (\iota, \varkappa) \\
\text{if } K > 0: \begin{cases} c\eta = \frac{1}{\sqrt{|K|}} \int \frac{cd\tau}{\mathfrak{R}(\tau)} \\ ct = \sin c\eta \left[\sqrt{|K|} \sqrt{1 - \frac{\rho^2}{(1+\rho^2 K/4)^2}} + \cos c\eta \right]^{-1} \\ \varkappa = \frac{\rho}{1+\rho^2 K/4} \sqrt{|K|} \left[\sqrt{|K|} \sqrt{1 - \frac{\rho^2}{(1+\rho^2 K/4)^2}} + \cos c\eta \right]^{-1} \end{cases} \\
\text{if } K = 0: \begin{cases} c\eta = \int \frac{cd\tau}{\mathfrak{R}(\tau)} \\ ct = c\eta \\ \varkappa = \rho \end{cases} \\
\text{if } K < 0: \begin{cases} c\eta = \frac{1}{\sqrt{|K|}} \int \frac{cd\tau}{\mathfrak{R}(\tau)} \\ ct = e^{c\eta} \sqrt{1 + \frac{\rho^2}{(1-\rho^2 K/4)^2}} \\ \varkappa = e^{c\eta} \frac{\rho}{1-\rho^2 K/4} \end{cases} .
\end{array}$$

These lead to

$$\begin{aligned}
ds^2 &= \underset{Weyl_{\beta_W=0} \rightarrow Minkowski}{\Omega(\tau, \rho)} * \{d\tau^2 - (d\varkappa^2 + \varkappa^2 d\Omega^2)\}, \\
\text{where } \underset{Weyl_{\beta_W=0} \rightarrow Minkowski}{\Omega(\tau, \rho)} &\equiv \underset{Weyl_{\beta_W=0} \rightarrow RW}{\Omega(\tau, \rho)} * \underset{RW \rightarrow Minkowski}{\Omega(\tau, \rho)}, \\
\text{and } \underset{RW \rightarrow Minkowski}{\Omega(\tau, \rho)} &\equiv \mathfrak{R}^2(\tau) * \begin{cases} \left[\sqrt{1 - \frac{\rho^2}{(1+\rho^2 K/4)^2}} + \frac{\cos c\eta}{\sqrt{|K|}} \right]^2 & \text{if } K > 0 \\ 1 & \text{if } K = 0 \\ e^{-2c\eta} & \text{if } K < 0. \end{cases} \quad (4.38)
\end{aligned}$$

The conditions for the global conformal transformation $Weyl_{\beta_W=0} \mapsto Minkowski$ to exist are essentially the conditions necessary for the radial variable transformation $\rho(r)$ (4.37) to be defined together with (4.32). An additional condition, $\rho < 2/\sqrt{3K}$, must however be given for $K > 0$ with $\gamma_W < 0$. It is fulfilled automatically for $K > 0$ with $\gamma_W > 0$, as $\rho(r = \infty) < 2/\sqrt{3K}$.

Because we wish to consider a metric which is properly defined at any radial distance $r \in]0, +\infty[$, with regard to the conditions summarized in (4.32), we shall from now on restrict ourselves to the cases ($\gamma_W > 0, K \geq 0$), ($\gamma_W > 0, K < 0, k_W \leq 0$) and ($\gamma_W < 0, K > 0$). Consequently, the conditions cited in (4.37) are verified and hence, a global conformal transformation of the asymptotic Weyl metric into a conformally flat space is always possible for unbound orbits.

Our demonstration, that the Weyl metric can be recast (at large radial distances) into a conformally flat metric for which no deflection occurs, must sound like a new contradiction: we clearly see in expression (4.36) that the asymptotic light deflection angle is nonzero when $r_0 \rightarrow \infty$. Indeed, if we recall that, for a negative γ_W , the radius r_{null} is the maximum value allowed for the closest approach distance in order to have scattering states, the limit of the light deflection angle is

$$\begin{aligned}
&\text{if } \gamma_W > 0, \quad \hat{\alpha}_{\beta_W=0}(r_0) \xrightarrow{r_0 \rightarrow \infty} -\pi \quad \text{is divergent,} \\
&\text{if } \gamma_W < 0, \quad \hat{\alpha}_{\beta_W=0}(r_0) \xrightarrow{r_0 \rightarrow r_{null}} +\pi \quad \text{is convergent.}
\end{aligned}$$

This agrees with the fact that, in terms of the conformally flat coordinates (ι, \varkappa) , the photon moves on a straight line. And infinity cannot be reached in those coordinates because the corresponding values of (ι, \varkappa) on the inner and outer asymptotes to the trajectory ($r \rightarrow +\infty$ when $t \rightarrow \pm\infty$) are finite. The deflection angle is thus nonzero: $\hat{\alpha}_{\beta_W=0} = \pi - \hat{A}$, where \hat{A} is the angle between the gravitational mass, the point $(\iota_{-\infty}, \varkappa_{-\infty})$ in the asymptotically flat

coordinates corresponding to the inner asymptote, and the point $(\iota_{+\infty}, \varkappa_{+\infty})$ corresponding to the outer asymptote. We now understand why the light deflection angle can be nonzero in a conformally flat space!

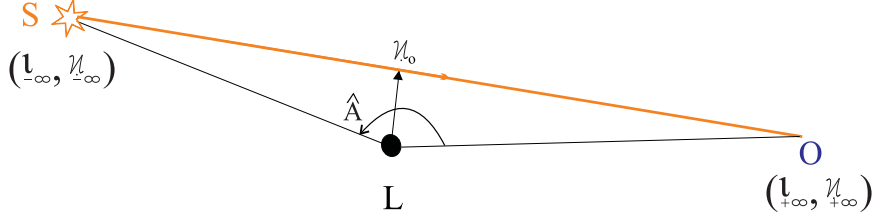


Fig. 4.5 The deflection angle is nonzero: $\hat{\alpha}_{\beta_W \equiv 0} = \pi - \hat{A}$, where \hat{A} is the angle between the gravitational mass (L), the point $(\iota_{-\infty}, \varkappa_{-\infty})$ in the asymptotically flat coordinates corresponding to the inner asymptote ($t = -\infty$, $r = +\infty$), and the point $(\iota_{+\infty}, \varkappa_{+\infty})$ corresponding to the outer asymptote ($t = +\infty$, $r = +\infty$).

4.4.2.3 Estimation of γ_W from VLBI data

In the previous paragraphs, we have analyzed the conditions for light deflection to take place in the Weyl theory and obtained the expression for the asymptotic light deflection angle. The present paragraph aims at a confrontation with solar system experiments.

We will now assume that the $(\beta_W \gamma_W)$ -contribution in the Weyl gravitational potential (1.52) is negligible when compared with that of β_W and γ_W alone. This leads to the following expression for the asymptotic light deflection angle:

$$\hat{\alpha}_{\text{weak field}}(r_0) \simeq +\frac{4\beta_W}{r_0} - \gamma_W r_0. \quad (4.39)$$

We see that the prediction about the weak field first order deflection angle already differs from the GR one as soon as γ_W is nonzero.

Now, one can use the first order light deflection measurements (VLBI) to provide the following constraints on the Weyl parameter γ_W . Let us assume that the parameter β_W is given by $\frac{G_N M_{Sun}}{c^2}$, in order to recover the Newtonian potential in the solar system's weak field limit, and let us extrapolate the VLBI results for light deflection at the solar limb:

$$\gamma_W = \frac{(1-\gamma)}{2} \frac{4G_N M_{Sun}}{R_{Sun} c^2} \frac{1}{R_{Sun}} \Rightarrow \begin{cases} -7.9 \cdot 10^{-18} \text{ m}^{-1} \leq \gamma_W \leq 1.3 \cdot 10^{-17} \text{ m}^{-1} & \text{for (3.2),} \\ -3.7 \cdot 10^{-19} \text{ m}^{-1} \leq \gamma_W \leq 1.4 \cdot 10^{-18} \text{ m}^{-1} & \text{for (3.3).} \end{cases} \quad (4.40)$$

This estimation with most recent VLBI data provides a range of values for γ_W which contains the particular order of magnitude needed by Mannheim and his collaborators to fit the galactic rotation curves. Notice that the range is narrower than that given by Ederly *et al.* [50], based on an article of 1976.

Although higher precision tests on light deflection (like with the future GAIA mission) could reduce the allowed range of values for γ_W , the test of light deflection in the neighborhood of the Sun cannot help us to decide on the sign of the parameter γ_W .

Considering that the light deflection angle calculated in the setting of GR for the visible gravitational mass in galaxies or clusters at galactic distance scales is often inferior to the observed deflection, the presence of gravitational dark matter is inferred. This phenomenon is even sometimes presented as evidence for the presence of gravitational dark matter in the halo of galaxies. So, if one wishes the linear γ_W -term of the Weyl potential to be an alternative to (a too large amount of) dark matter contributing to light deflection, then $-\gamma_W r_0$ must be positive. This means that γ_W is negative. However, this sign is just the opposite of the sign argued by Mannheim and Kazanas in their parametrization (1.53). Two types of arguments might be given in order to solve this apparent contradiction and prevent from ruling out the Weyl theory.

A first possibility is to consider γ_W to be positive ($\gamma_W \in [0 \equiv GR; 1.3 \cdot 10^{-17} \text{ m}^{-1} \text{ or } 1.4 \cdot 10^{-18} \text{ m}^{-1}]$), so that

the theory would still need the “magic” contribution of dark matter to explain light deflection due to galaxies and clusters, just like General Relativity does. This possibility leads to divergent deflection (4.39) on radial closest approach distances from the deflector larger than $r_{00}(M, \gamma_W)$ given by (4.28), where the linear divergent contribution becomes dominant! This positive sign was considered in our graduate thesis work [107], without dark matter.

An alternative argument would be to claim that tests of the Weyl theory taking into account massive particles or bodies are more ambiguous, in comparison with those based on nonmassive particles like photons, or ultra relativistic particles. Indeed, the presence of matter breaks the conformal symmetry of the theory, and this symmetry breaking mechanism is not well understood. In order to fit galactic rotation curves, we need to fix the arbitrary conformal factor of the line element (1.51) because massive geodesics are not conformally invariant. Mannheim and Kazanas (arbitrarily) chose $\chi^2(r) \equiv 1$ and obtained $\gamma_W > 0$ through those fits. Their work corresponds to a particular theory:

$$\boxed{\text{Mannheim-Kazanas theory} \equiv \text{Weyl theory} + \begin{cases} \chi^2(r) \equiv 1 \\ \text{parametrization of galactic rotation curves (1.53)} \end{cases}} \quad (4.41)$$

However, the physical conformal factor in the spherically symmetric metric (1.51), specified by the symmetry breaking mechanism, could be different from a constant. Hence, the physical parameter γ_W present in the metric would be different from the estimate of these authors. For example, Edery *et al.* [49] have shown that, in the weak field limit (which applies to the galactic rotation-curve parametrization and to light deflection in the solar system), it is possible to find an appropriate conformal factor $\chi^2(r)$ and a radial coordinate transformation $r'(r)$, so as to change the sign of the γ_W -term in the Weyl gravitational potential when the $(\beta_W \gamma_W)$ -term is set to zero. One indeed can easily check that,

$$\begin{aligned} ds^2(r, t, \gamma_W)_{\text{given by (1.51)}} &\simeq + \left[1 - \beta_W \frac{(2 - 3\beta_W \gamma'_W)}{r'} - 3\beta_W \gamma'_W + \gamma'_W r' - k_W r'^2 \right] c^2 dt^2 \\ &\quad - \left[1 - \beta_W \frac{(2 - 3\beta_W \gamma'_W)}{r'} - 3\beta_W \gamma'_W + \gamma'_W r' - k_W r'^2 \right]^{-1} dr'^2 - r'^2 d\Omega^2 \\ &\equiv ds^2(r', t, \gamma'_W)_{\text{Mann-Kaz}} \\ &\quad \text{with } \begin{cases} \beta_W \gamma_W \text{ neglected,} \\ \chi^2(r) \stackrel{\text{weak field}}{\simeq} 1 - 2\gamma_W r, \\ \gamma'_W \equiv -\gamma_W. \end{cases} \end{aligned} \quad (4.42)$$

In conclusion, until a conformal factor is specified by a coherent study of the coupling of Weyl gravity to matter fields, the conservative bounds deduced from solar system light deflection experiments (4.40) are preferable.

And if a negative sign is taken for γ_W for photons, then light deflection is always convergent.

4.5 Summary of the main results

4.5.1 TS theories

In TS theories, the predicted angle is smaller than its counterpart in GR. Hence, TS theories offer no alternative to dark matter.

Solar system experiments so far provide the best constraints on the scalar coupling, with VLBI measurements providing the upper bound (Figure 4.1): $\alpha_{TS0}^2 \lesssim 0.0011$ (or 0.0002). The lower bound of the TS parameter ϖ_0 is accordingly constrained to 463 (or 2215 but the corresponding reference is unpublished).

However, these experimental limits are still far from the theoretical ones, since, in our model, the lower bound on $|\alpha_{TS0}|$ is $\sim 10^{-7} - 10^{-8}$. Dedicated experiments are needed to fill the gap. The (undedicated) astrometric satellite mission GAIA will probably not even reach the theoretical lower bound.

We also recall that improved constraints on the PN parameter β would be welcome, as they correspond to constraints on the curvature of the theoretical cosmological potential around its minimum.

4.5.2 LED theories

Originally, in Large Extra-Dimension theories, the coupling to matter is much too strong. It is in conflict with light deflection experiments and the Weak Equivalence Principle is strongly violated, unless a mass is given to the zero-mode scalar field.

In this latter case, the deviation from GR predictions regarding light deflection is at the third order. It is a function of the mass of the lens, of the incidence angle, and more important, it depends quadratically on the frequency of the observed photons. This allows to constrain the mass scale M_s of the theory and the number of extra-dimensions d .

To agree with observations [71] in the visible at grazing incidence, the lower bound on the mass scale must be of the order of 28 TeV/ c^2 for $d = 2$ and of the order of 9.5 $(2/(d-2))^{1/4}$ TeV/ c^2 for $d > 2$.

Increasing the precision of solar grazing experiments in the visible at a fixed frequency would improve the constraints, as shown in simulation (4.10). Also, solar grazing observations at a fixed frequency in higher energy wavebands would be useful. For example, a measurement showing no deviation from GR within ten percent at an ultra-violet frequency would lead to a lower bound like $M_s \sim 78$ TeV/ c^2 for $d = 2$ and like $\sim 30 (2/(d-2))^{1/4}$ TeV/ c^2 for $d > 2$.

Contrary to TS theories, LED theories increase the light deflection angle with respect to GR.

4.5.3 MTS/SITS theories

In MTS/SITS theories, there exists a critical value of the MTS/SITS parameter ($\Upsilon = 0.5$) under which there exists no black hole solution.

Also, we noticed that light deflection becomes divergent for closest approach distances smaller than r_{00} (4.19). This radius is unphysical for solar system bodies with not too small values of Υ . Consequently, for such Υ , light deflection is always convergent in the solar system. Furthermore, MTS/SITS theories only differ from GR at the second order. Hence, solar system experiments offer only a quantitative test of those theories with not too small a Υ , *if* the second order can be measured. As explained in Chapter 3, dedicated experiments would be welcome for such a task... which should not be simple, because of various corrective effects and of angular-momentum or quadrupole-moment contributions.

We note also that MTS/SITS theories decrease the light deflection angle with respect to GR.

4.5.4 The Weyl theory

The Weyl gravity appears to be a very peculiar theory.

First of all, the contribution of the Weyl linear parameter (γ_W) to the effective geodesic potential is opposite for massive and nonmassive geodesics. We note also that photon geodesics do not depend on the unknown conformal factor, unlike massive geodesics. Hence light deflection offers an interesting test of the Weyl theory.

Secondly, the effective geodesic potential for light showed us that, if γ_W is negative, there exists a maximum closest approach distance, r_{null} (4.22), for light deflection to take place. Beyond that distance, photon trajectories are bound. There does not exist such a condition when γ_W is positive. Nevertheless, light deflection can then be divergent beyond some closest approach distance $r_{0,0}$ (4.28).

Also, we needed to distinguish between a weak field (1.54) and a strong field (4.30) approximation to compute the asymptotic light deflection angle, because the Weyl gravity does not turn off asymptotically, and becomes even stronger at larger distances.

The weak field regime applied to the VLBI data gave us an upper bound on the linear parameter: $|\gamma_W| \sim 10^{-18} \text{ m}^{-1}$ (4.40). However, it did not settle its sign.

The asymptotic behavior of the Weyl space was also analyzed thanks to the strong field approximation.

Finally, we saw that a positive γ_W decreases the light deflection angle, while a negative one increases it with respect to GR.

Chapter 5:

Gravitational lensing/microlensing

Previously, we argued for considering the Sun and other solar system bodies in the light deflection test, because these constitute the most well-known deflectors. However, the preceding chapter showed us that measurements of the change in apparent position of light sources due to solar system bodies were only able to test quantitatively our chosen set of alternative theories (with the exception of Large Extra-Dimension theories endowed with a massive scalar field which predict a dependence in the frequency of the deflected photon). But we have seen that MTS/SITS theories and the Weyl gravity present a characteristic divergent to convergent, and convergent to divergent respectively, transition in their predicted light deflection angle. Unfortunately, this feature is irrelevant for solar system mass and distance scales. We have seen also that the linear contribution to the gravitational potential in the Weyl theory might be dominant beyond extragalactic distances. This is why the idea that will now guide us throughout this chapter is to seek qualitative deviations from General Relativity on large mass and/or distance scales, using microlensing events and gravitational mirages.

5.1 Present and future of microlensing/gravitational lensing

Gravitational mirages [111, 139] are due to a mass concentration in galaxies or clusters of galaxies. They give rise to the formation of (partial) Einstein rings, giant arcs and arclets, the characteristic Einstein cross consisting of five images, clubs (four images), etc.

Historically, the possibility of forming multiple images was first considered by Eddington, as early as in 1920. Nevertheless, despite a proposal in 1923 by Frost (Yerkes Observatory), no observational campaign took place to verify this speculation. In 1924, Chwolson developed further the gravitational mirage theory: formation of rings, amplification, specific intensity preserved... These characteristics were independently rediscovered by Einstein in 1936, who lent his name to the ring mirages. Einstein himself was skeptical though about observing a star by star lensing case, since alignment is very rare and angular separation of images was too weak to be resolved by telescopes. However, in 1937, Zwicky revived the interest in gravitational lensing by calculating the probability for a light source to be lensed by a galaxy. He also proposed to use galaxies as natural cosmic telescopes that amplify the light of otherwise too faint objects. Moreover, Zwicky already spoke about testing GR or weighing galaxy-lenses.

Despite Zwicky's enthusiastic predictions, twenty years later, no mirage had been found. The discovery of quasars, quasi stellar objects (QSO) that are very bright, at extragalactic distance (large lensing probability), brought back the whole story onto the front stage. Finally, it is in 1979 that the first gravitational mirage of a QSO (0957+561A B) lensed by a foreground galaxy was discovered by Walsh, Carswell and Weymann [138].

Since then, more than three thousand papers have been published on the subject, nearly one hundred mirage candidates are recorded, and telescope time as well as systematic searches are devoted to mirages. For example, the Liquid Mirror Telescope (LMT) project [7, 27] will contribute to increase the number of gravitational lens candidates.

Today, gravitational mirages are used to provide the most accurate mass determination of the central regions of galaxy-lenses, gravitational mirages of a variable source (quasar) are used to constrain cosmological GR models (Λ , H_0) as first suggested by Refsdal in 1964, and natural galaxy lenses allow us to observe objects too faint to be seen otherwise.

On the opposite, **microlensing** consist of lensing events due to a small lensing object (or a small number of objects) with a mass characteristic of a planet or a star ($10^{-6} - 10^2 M_{Sun}$) [95, 96]. Those events have a timescale between two hours and two years. First thought to be unobservable by Einstein as we just recalled, they are now used to

estimate the amount and the nature of the dark matter in the galaxy (for example the search for MAssive Compact Halo Objects, MACHOs). Following Paczynski's suggestion in 1986 that compact objects in the Galactic Halo may be detected by the monitoring of the light curves of stars in the Large Magellanic Cloud, many groups are searching for microlensing events: MACHO, EROS, OGLE, DUO... Several hundreds of microlensing events have been observed so far. Moreover, the Space Interferometry Mission (SIM) will be able to exploit astrometric signatures created in a microlensing event to reconstruct the mass and the kinematic properties of the lens, something that is not currently possible with a vast majority of photometric-only detections.

5.2 Brief summary of the phenomenon

Before studying the prediction of our set of alternative theories regarding gravitational mirages and microlensing events, we will recall the general characteristics of these phenomena.

5.2.1 Asymptotic first and second order light deflection angle

The expression of the asymptotic light deflection angle ($\hat{\alpha}$) as a function of the angular position (ϑ_I) and the position of the observer ($\rho_{obs} = D_{ol}$) can be easily obtained at the **second order** by replacing expression (3.31) for the impact parameter into the invariant expression for the asymptotic light deflection angle (3.12):

$$\hat{\alpha}(\vartheta_I, D_{ol}) = \frac{4GM}{c^2 D_{ol} \sin \vartheta_I} \left\{ \begin{array}{l} + \left(\frac{\alpha + \gamma}{2} \right) \\ + \left[-\frac{(\alpha + \gamma)^2}{2} \sin \vartheta_I + \frac{(8\alpha^2 + 8\alpha\gamma - 4\beta + 3\delta)}{16} \pi \right] \frac{GM}{c^2 D_{ol} \sin \vartheta_I} \end{array} \right\} + \mathcal{O}\left(\frac{V^3}{c^6}\right). \quad (5.1)$$

We note that while it is not appropriate at second order, at **first order** in $1/c^2$, we can use $b \simeq D_{ol} \sin \vartheta_I$.

5.2.2 Lens equation

The light deflection by a gravitational mass, called the lens (L), allows an observer (O) to detect one or several images (I_i with $i=1, 2, 3, \dots$) of the same light source (S) (see Figure 5.1). When there are only two images, those are noted as + and - respectively.

Knowing the observer-lens (D_{ol}) and observer-source (D_{os}) distance scales necessary for this lensing phenomenon to occur, it is reasonable to adopt the thin lens approximation as well as the asymptotic light deflection angle approximation (weak field limit). Accordingly, we can consider the lens as localized in a plane called the "deflector plane".

Similarly, we can in good approximation reduce the photon path to its asymptotes and suppose that all the deflection takes place in the deflector plane. Doing so, we obtain a modelling of the O-L-S system for which O-L plays the role of a reference axis to measure angular positions [111] (see Figure 5.2).

The *exact* expression for the angle α , formed by S-O-I (not to be confused with the asymptotic light deflection angle $\hat{\alpha}$) can be obtained for either a converging lens ($\hat{\alpha}$ is positive and the "+" sign should be taken in the following formula) or a diverging lens ($\hat{\alpha}$ is negative and the "-" sign should be taken in the following formula):

$$\left\{ \begin{array}{l} \alpha = \text{sg}(\vec{\vartheta}_I) \text{sg}(\vec{\hat{\alpha}}) \left(\vec{\vartheta}_I - \vec{\vartheta}_S \right), \\ \alpha = \arcsin \left[\frac{D_{ls} \tan \hat{\alpha}}{D_{os} \cos \vartheta_I \{1 \pm \tan \vartheta_I \tan \hat{\alpha}\}} \right], \end{array} \right.$$

where all the angles are taken as positive unless the possibility of considering positive and negative values is noted by an arrow sign \rightarrow ; and "sg()" means the sign of "()".

The positions of the images can be written equally for a converging or a diverging lens as the crossing points of two curves: F_1 , a straight line encoding the alignment/non-alignment conditions, and F_2 , a curve function of the

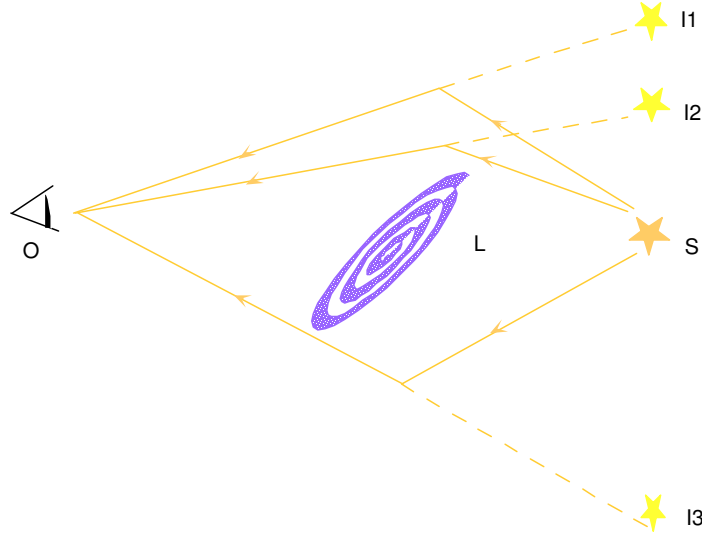


Fig. 5.1 Gravitational mirages: a massive object (L) placed between an observer (O) and a light source (S) can produce multiple images (I_1, I_2, I_3, \dots).

gravitational theory and the lens model. This leads to **the exact lensing equation**:

$$\begin{cases} F_1 = \vec{\vartheta}_I - \vec{\vartheta}_S, \\ F_2 = \text{sg}(\vec{\vartheta}_I) \arcsin \left[\frac{D_{ls} \tan \vec{\hat{\alpha}}(\vartheta_I, D_{ol})}{D_{os} \cos \vartheta_I \{1 + \text{sg}(\vec{\vartheta}_I) \tan \vartheta_I \tan \vec{\hat{\alpha}}(\vartheta_I, D_{ol})\}} \right], \end{cases} \quad (5.2)$$

with the following conditions for a diverging lens ($\vec{\hat{\alpha}} < 0$),

$$\begin{cases} \text{sg}(\vec{\vartheta}_I) = \text{sg}(\vec{\vartheta}_S), \\ \vartheta_S \neq 0, \\ \vartheta_S > \vartheta_I. \end{cases}$$

Indeed in the case of a diverging lens, these conditions must all be fulfilled in order to provide an image. The first condition accounts for the fact that there only exists the possibility for diverging image(s), on the same side of the lens as the source. The second condition is expressing the impossibility of forming any diverging image in the alignment configuration; thus no diverging ring can exist. Finally, the last condition expresses the fact that the divergent image will be located at a smaller angle from the deflector than the source: the divergent image is in between the lens and the source when projected onto the sky (see Figure 5.2).

Unless all three conditions above are verified, the F_2 curve is not defined for a diverging lens, since the image (ϑ_I) does not exist.

In the small angle approximation (ϑ_I, ϑ_S and $\hat{\alpha} \ll \sqrt{3}$ [rad]), from the equation of the crossing points of F_1 and F_2 , we recover the usual lens equation:

$$\vec{\vartheta}_I - \vec{\vartheta}_S \simeq \text{sg}(\vec{\vartheta}_I) \frac{D_{ls}}{D_{os}} \vec{\hat{\alpha}}(\vartheta_I, D_{ol}). \quad (5.3)$$

The three essential conditions for a diverging lens ($\vec{\hat{\alpha}} < 0$) still apply.

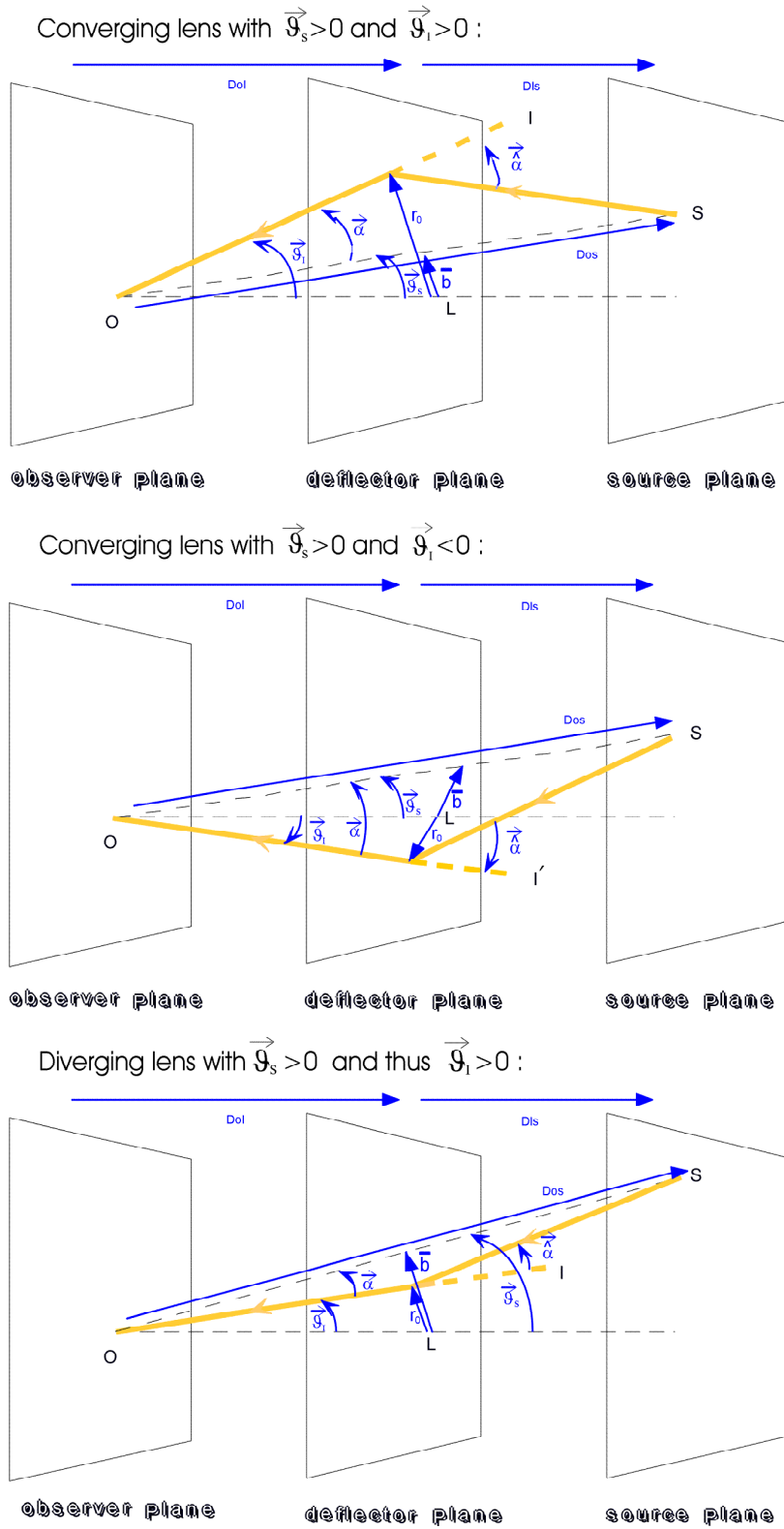


Fig. 5.2 Usual thin lens model of a gravitational mirage. Notice that in the case of a diverging lens, there is no image formed on the opposite side of the source.

In the small angle approximation, **at first order in light deflection**, one can even use

$$\begin{aligned} \vec{b} &\stackrel{1^{st} \text{ order}}{\simeq} Dol \sin \vartheta_I \simeq Dol \vec{\vartheta}_I, \\ \vec{b} &= Dol \tan \vartheta_S \simeq Dol \vec{\vartheta}_S, \end{aligned} \quad (5.4)$$

where \vec{b} is the impact parameter of the lens onto the O-S direction, to rewrite the weak angle lens equation (5.3) in the following way:

$$\vec{b} - \vec{b} \simeq \text{sg}(\vartheta_I) \frac{Dls}{Dos} Dol \vec{\alpha}(\vartheta_I, Dol). \quad (5.5)$$

Finally, note that the distances (Dol , Dos and Dls) appearing in the lens equations (5.2), (5.3), (5.4) or (5.5) should be taken as angular diameter distances.

The value of the asymptotic deflection angle should depend on the gravitational lens model and on the relativistic theory of gravitation chosen.

5.2.3 Amplifications

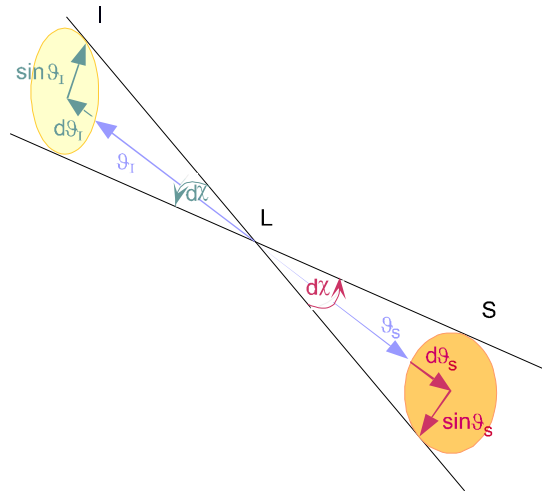


Fig. 5.3 Projection of the image and the light source on the sky.

Amplification curves can also be useful to determine whether a given image should be observable or not, or to deduce the microlensing light curve.

As the specific intensity is conserved during light deflection, if only gravitational lensing effects are considered [111], the amplification (μ) is defined as the quotient of the solid angle of the images relatively to the source one (see Figure 5.3):

$$\begin{aligned} \mu &\equiv \frac{d\Omega_I}{d\Omega_S} = \frac{\sin \vartheta_I d\vartheta_I d\mathcal{A}}{\sin \vartheta_S d\vartheta_S d\mathcal{A}} = \left(\frac{\sin \vartheta_I}{\sin \vartheta_S} \right) \left(\frac{d\vartheta_I}{d\vartheta_S} \right) \equiv (\mu_t) (\mu_r) \\ &\stackrel{\text{small angles}}{\simeq} \frac{\vartheta_I}{\vartheta_S} \frac{d\vartheta_I}{d\vartheta_S} \stackrel{1^{st} \text{ order}}{\simeq} \frac{b}{b} \frac{db}{db} \end{aligned} \quad (5.6)$$

$$\text{where } \begin{cases} \mu_r = \text{radial amplification,} \\ \mu_t = \text{tangential amplification.} \end{cases}$$

A singularity in the tangential amplification curve (i.e. at ϑ_I^* so that $\mu_t(\vartheta_I^*) = \infty$) signifies the presence of a ring, which corresponds to the tangential fusion of two images in one single image.

On the contrary, **a singularity in the radial amplification curve** (i.e. at ϑ_I^* so that $\mu_r(\vartheta_I^*) = \infty$) denotes the presence of a caustic. In other words, there is a radial fusion of the images.

If several images are present (consider for example the case of two images), the total amplification can be calculated as the sum of the absolute amplification for each image. It is this total amplification which is to be considered as soon as the observer cannot resolve the two (or several) images:

$$\mu_{tot} = |\mu_+| + |\mu_-|. \quad (5.7)$$

5.2.4 Microlensing

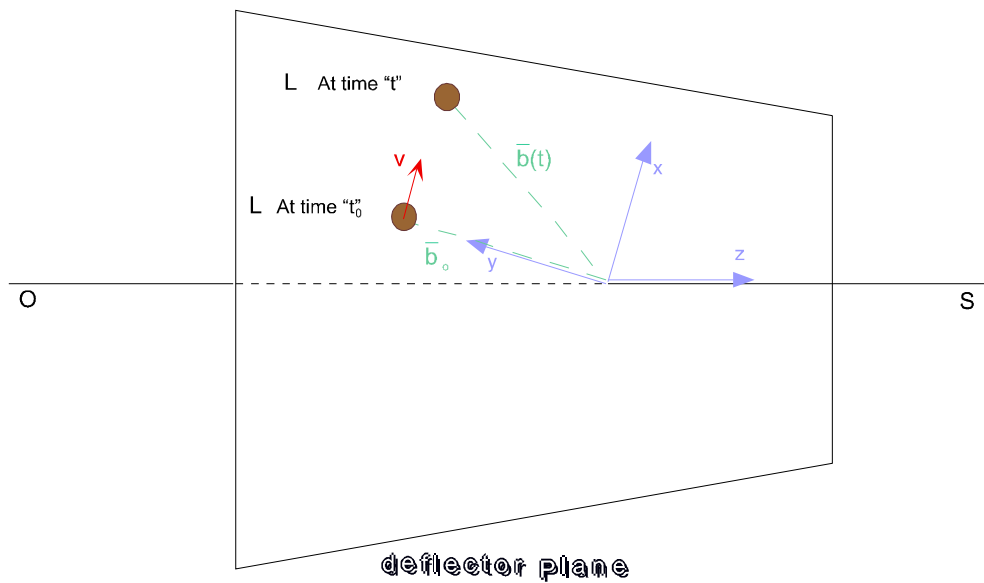


Fig. 5.4 The microlensing effect: the lens (L) possesses a speed (v) in the deflector plane (say, a constant speed along the x -axis). \bar{b}_0 represents the minimal impact parameter of the deflector, and $\bar{b}(t)$ is the impact parameter as a function of time. The total amplification of the images will be now a function of time: $\mu_{tot}(t)$.

When the lens is moving in the deflector plane (suppose a speed v along the x -axis), the impact parameter of the lens onto the O-S direction, \bar{b} (not to be confused with the impact parameter of the photon onto the lens, b), is a function of time (see Figure 5.4). Its expression is given by:

$$\bar{b}^2(t) \simeq \bar{b}_0^2 \left[1 + \frac{t^2}{T_0^2} \right]$$

or

$$\bar{B}^2(t) \simeq \bar{B}_0^2 \left[1 + \frac{t^2}{T_0^2} \right]$$

$$\begin{aligned}
\text{with } T_0 &\equiv \text{time corresponding to the minimal impact parameter} & (5.8) \\
&= \bar{b}_0/v, \\
v &= \text{speed of the lens in the deflector plane along the x-axis,} \\
\bar{b} &= \text{impact parameter of the deflector on the O-S direction,} \\
\bar{b}_0 &= \text{minimal impact parameter of the deflector on the O-S direction,} \\
\bar{B} &\equiv \bar{b}/r_E = \text{dimensionless impact parameter of the deflector,} \\
\bar{B}_0 &\equiv \bar{b}_0/r_E = \text{dimensionless minimal impact parameter of the deflector,} \\
B &\equiv b/r_E = \text{dimensionless impact parameter of the photon,} \\
r_E &\equiv \text{radius of the Einstein ring given by GR} \\
&\simeq \vartheta_E D_{ol}, \\
\vartheta_E &\equiv \text{angular radius of the Einstein ring given by GR} \\
&= \sqrt{4 \frac{GM}{c^2} \frac{D_{ls}}{D_{ol} D_{os}}}.
\end{aligned}$$

When replacing these equations in the expression found for the amplification (5.6), we obtain a time-dependent total amplification: $\mu_{tot}(t)$. This quantity is relevant to microlensing events, as those have a measurable timescale.

5.3 Testing alternative theories of gravitation with microlensing/gravitational lensing?

We are now ready to investigate the predictions of TS, MTS/SITS and Weyl theories. Throughout this section, several simulations were realized for some typical values of the O-L-S parameters.

5.3.1 Parameters of the simulations

5.3.1.1 For microlensing events

The numerical example for a microlens is realized for a point-like lens (L) of one solar mass placed in the galactic cloud, and a stellar source (S) present in the Large Magellanic Cloud. That is to say that when looking towards the halo of our Galaxy, an O-L-S microlensing system characterized for example by

$$\begin{aligned}
D_{os} &= 2 \cdot 10^{21} \text{ m}, \\
D_{ol} &= 5 \cdot 10^{20} \text{ m}.
\end{aligned} \tag{5.9}$$

This corresponds to an Einstein ring of radius

$$r_E = 1.5 \cdot 10^{12} \text{ m} \tag{5.10}$$

and a typical angular separation between the images of the order of the milliarcsecond. Alternatively, if one was considering microlensing towards the Galactic Bulge, the characteristic distances would be instead $D_{os} \sim 8 \text{ kpc} = 2.5 \cdot 10^{20} \text{ m}$ and $D_{ol} = D_{os}/2$. For a lens of one solar mass, this means an Einstein radius of $6.1 \cdot 10^{11} \text{ m}$.

Microlensing by a point mass model is a good approximation of reality if we consider the simple limiting case in which the lensing probability along the line of sight is small. A microlensing event in the massive halo of the Milky Way is a good example of this. On the contrary, if the line of sight passes through the center of the galaxy, the lensing optical depth (lensing probability) may approach 1, requiring a more complex lensing model with intricate mass contributions.

In the case of microlenses in the dark halo, the lens speed is negligible with respect to the speed of light. This allows us to ignore the frequency shift of the light due to the changing of path length along the different lines of sight for the different images. Hence, the surface brightness is the same for all the images, and the flux density is proportional

to the solid angle of the images as described by formula (5.6), which can be used in expression (5.7) together with (5.8).

5.3.1.2 For mirages

In the case of mirages, we shall use a point-like lens model representing either a galaxy ($M \sim 10^{11} M_{Sun}$) or a cluster of galaxies ($M \sim 10^{13} - 10^{14} - 10^{15} M_{Sun}$), with the following distance scales:

$$\begin{aligned} Dol &= 10^{10} \frac{GM}{c^2}, \\ Dos &= 2 Dol. \end{aligned} \quad (5.11)$$

Such a choice for the O-L-S parameters, inspired by reference [136] and our graduate work, agrees with the Taylor expansion of expression (5.18) in $\frac{GM}{c^2 Dol \sin \vartheta_I}$, as long as ϑ_I is not too small. That is to say that values of ϑ_I as small as 10^{-3} arcsec are acceptable because they lead to $\frac{GM}{c^2 Dol \sin \vartheta_I} \sim 10^{-2}$ in the expression for the asymptotic weak field deflection angle (5.1).

The angular separation between the lensed images in a gravitational mirage is of the order of the arcsecond in General Relativity. The radius of the corresponding Einstein ring³⁸ is given by

$$r_E = 14 \cdot 10^4 \frac{GM}{c^2} \simeq \begin{cases} 2 \cdot 10^{19} \text{ m} & \text{for } M = 10^{11} M_{Sun}, \\ 2 \cdot 10^{21} \text{ m} & \text{for } M = 10^{13} M_{Sun}, \\ 2 \cdot 10^{22} \text{ m} & \text{for } M = 10^{14} M_{Sun}, \\ 2 \cdot 10^{23} \text{ m} & \text{for } M = 10^{15} M_{Sun}. \end{cases} \quad (5.12)$$

Note that, in the following, the F_1 curves will be plotted for position of the source ($\vec{\vartheta}_S$) of respectively 0 and +10 arcsec. Also, when a black hole potential is created, we need to consider closest approach distances, or alternatively impact parameters, which are larger than the critical value (4.16), so that the photon does not fall into the black hole and that light deflection is possible. Finally, recall that we work here in the weak field limit for $\hat{\alpha}$.

We are now ready to investigate the predictions of our chosen set of alternative theories.

5.3.2 TS theories

5.3.2.1 Asymptotic first order light deflection angle

At first order, the asymptotic light deflection angle in TS theories can be rewritten, according to Table (1.67), constraints (4.3) and formula (3.1), as

$$\hat{\alpha}_{TS}(b) = \frac{4GM}{b c^2} g(\varpi) \quad (5.13)$$

$$\text{with } g(\varpi) = \frac{1}{2} \frac{2\varpi + 3}{\varpi + 2} \stackrel{(1.7)}{=} \frac{1}{1 + \alpha_{TS0}^2} \in \begin{cases} [3/2; 1] & \text{for } \varpi \in [0, +\infty], \\ [\sim 0.9989; 1] & \text{for } \varpi \in [463, +\infty], \\ [\sim 0.99978; 1] & \text{for } \varpi \in [2215, +\infty]. \end{cases}$$

It is important to emphasize that, at first order, the TS deflection angle is only modified by a scale factor in comparison with GR prediction. This multiplicative factor, $g(\varpi)$, corresponds to a redefinition of the gravitational ‘‘constant’’, as can be seen in equation (1.14). This function is strictly increasing and positive with respect to the allowed parameter space for ϖ . Hence, we can already state here that, when looking at TS predictions for light deflection at the first order, they are always qualitatively analogous to the GR ones. Furthermore, at the first order, the predicted deflection angle

³⁸ estimated for an Euclidean space-time: $Dls = Dos - Dol$.

is always smaller for TS theories than for GR ($\varpi_{GR} = \infty$), according to the limit

$$g(\varpi) \xrightarrow{\varpi \rightarrow \infty} 1.$$

This result illustrates what was demonstrated by Benkenstein and Sanders [23], namely that in a scalar tensor theory, the light deflection angle can never exceed the value predicted by GR.

We can thus immediately understand that TS theories cannot offer an alternative to the great amount of dark matter needed and looked for, since without the assumption of dark matter, these theories already predict light deflection angles which are smaller than those predicted by GR.

5.3.2.2 Lens equation

As an example, let us derive the predictions of TS theories relative to gravitational mirages. In the following, the mass of the lens does not need to be mentioned for distances scales given by (5.11).

The lens equation in the small angle limit, at first order, is given by expressions (5.3) and (5.5):

$$\begin{aligned} \vec{\vartheta}_I^2 - \vec{\vartheta}_S \vec{\vartheta}_I - g(\varpi) \vartheta_E^2 &\simeq 0 \quad \text{with } \vartheta_E \text{ given in (5.8),} \\ \vec{b}^2 - \vec{b} \vec{b} - g(\varpi) r_E^2 &\simeq 0 \quad \text{with } r_E \text{ given in (5.8).} \end{aligned} \quad (5.14)$$

Alternatively, in terms of the dimensionless quantities defined in (5.8), we find

$$\vec{B}^2 - \vec{B} \vec{B} - g(\varpi) \simeq 0. \quad (5.15)$$

The lens equation for a point-like lens is analogous in TS theories and in GR theory. It provides a second order equation giving either two separate or degenerate roots for the respective image(s) position.

An image-position diagram is given in (5.21) for $\varpi = \varpi_{GR} \equiv +\infty$ which corresponds to $\Upsilon = \Upsilon_{GR} \equiv 1$ in the MTS/SITS parametrization (last graph).

A/ Perfect alignment O-L-S: $\vartheta_S = 0$ (i.e. $\vec{b} = 0$)

We easily obtain that the image ($\vartheta_I = g(\varpi) \vartheta_E$) is a ring of radius r_{TS} given by the following formula, modulated by the function $g(\varpi)$ which reaches its maximum value in the setting of GR:

$$\begin{aligned} \vartheta_I &= g(\varpi) \vartheta_E, \\ r_{TS} &\simeq g(\varpi) r_E \propto \sqrt{\frac{GM}{c^2}}. \end{aligned}$$

The width of the ring ($2 d\vartheta_I$) given as a function of the angular diameter of the light source ($d\vartheta_S$) will be identical in TS theory, for any value of ϖ , to the value predicted by GR:

$$d\vartheta_I = \frac{1}{2} d\vartheta_S. \quad (5.16)$$

B/ Non-alignment O-L-S: $\vartheta_S \neq 0$ (i.e. $\vec{b} \neq 0$)

In the case of non-alignment, the ring breaks up into two arcs whose positions, ϑ_{I+} and ϑ_{I-} , are given by:

$$\vec{\vartheta}_{I+/-} = \frac{\vec{\vartheta}_S \pm \sqrt{\vec{\vartheta}_S^2 + 4g(\varpi) \vartheta_E^2}}{2}.$$

In the small angle approximation, at first order, we can alternatively write

$$\vec{b}_{+/-} \simeq \frac{\vec{b} \pm \sqrt{\vec{b}^2 + 4g(\varpi) r_E^2}}{2},$$

or

$$\vec{B}_{+/-} \simeq \frac{\vec{B} \pm \sqrt{\vec{B}^2 + 4g(\varpi)}}{2}.$$

The image ϑ_{I+} is on the same side of the lens as the source, while ϑ_{I-} is on the opposite side. The angular separation between the two images,

$$\Delta\vartheta_I \equiv \vartheta_{I+} - \vartheta_{I-} = \sqrt{\vartheta_S^2 + 4g(\varpi) \vartheta_E^2},$$

shows us that, in the case of a quasi-alignment ($\vartheta_S \sim 0$), both images lie very close to the ring position: one being outside the ring, ϑ_{I+} , while the other one is inside. Of course, the angular separation between the two images is an increasing function of ϖ .

The width of the arcs, $2 d\vartheta_{I+}$ or $2 d\vartheta_{I-}$, is

$$d\vartheta_{I+/-} = \frac{1}{2} \left[1 \pm \frac{1}{\sqrt{1 + 4g(\varpi) (\vartheta_E/\vartheta_S)^2}} \right] d\vartheta_S,$$

so that the image on the opposite side of the source (ϑ_{I-}) tends to disappear, becoming too thin to be seen in case of too strong an unalignment ($\vartheta_S \gg g(\varpi) \vartheta_E$).

5.3.2.3 Amplifications

Let us now study the amplification of the images. If we consider the amplification as a function of the image position, the amplification curves (using (5.14) to eliminate ϑ_S in (5.6), in the small angle approximation) are given by

$$\mu = \mu_t \cdot \mu_r$$

$$\text{with } \mu_t \left(\vec{\vartheta}_I \right) \simeq \frac{-\left(\vec{\vartheta}_I / \vartheta_E \right)^2}{g(\varpi) - \left(\vec{\vartheta}_I / \vartheta_E \right)^2},$$

$$\mu_r \left(\vec{\vartheta}_I \right) \simeq \frac{\left(\vec{\vartheta}_I / \vartheta_E \right)^2}{g(\varpi) + \left(\vec{\vartheta}_I / \vartheta_E \right)^2}.$$

We can observe the presence of a pair of singularities for $\vartheta_I = \sqrt{g(\varpi)} \vartheta_E$ in μ_t , which locates the position of the ring corresponding to the perfect alignment ($\vartheta_S = 0$). In μ_r , we can remark the absence of singularities for any value of the parameter ϖ , which shows that in TS theories, like in GR, there are no caustics for a point mass lens.

Graphs of the amplifications in TS theories as a function of the image position are given in (5.29) and (5.31) for $\varpi = \varpi_{GR} \equiv +\infty$ which corresponds to $\Upsilon = \Upsilon_{GR} \equiv 1$ in the MTS/SITS parametrization discussed in Paragraph 5.3.3.3.

If we now consider the amplification as a function of the source position, we get,

A/ Perfect alignment O-L-S

for a perfect alignment,

$$\mu \simeq \frac{2 \sqrt{g(\varpi)} \vartheta_E}{d\vartheta_S} = \frac{2 \sqrt{g(\varpi)} r_E}{d\bar{b}}.$$

Hence, if there is an alignment of the light source (S) along the observer-deflector (O-L) direction, the amplification is infinite in the case of a point-like source ($d\vartheta_S = 0$), like in GR.

B/ Non-alignment O-L-S

When the alignment is broken, the amplification of each image as a function of the source position (ϑ_S or \bar{b}) is

$$\begin{aligned} \mu_{+/-} &\simeq \frac{1}{4} \left[2 \pm \left(\frac{\Delta\vartheta_I}{\vartheta_S} + \frac{\vartheta_S}{\Delta\vartheta_I} \right) \right] \\ &\pm \frac{\left(\bar{b} \pm \sqrt{\bar{b}^2 + 4g(\varpi) r_E^2} \right)^2}{4\bar{b}\sqrt{\bar{b}^2 + 4g(\varpi) r_E^2}} = \pm \frac{\left(\bar{B} \pm \sqrt{\bar{B}^2 + 4g(\varpi)} \right)^2}{4\bar{B}\sqrt{\bar{B}^2 + 4g(\varpi)}}. \end{aligned}$$

Suppose now that the observer can resolve the two images that are formed. We remark that in the limit of strong non-alignment $\vartheta_S \gg \sqrt{g(\varpi)} \vartheta_E$, the image positions are given by $\vartheta_{I+} \rightarrow \sqrt{g(\varpi)} \vartheta_E$ and $\vartheta_{I-} \rightarrow 0$ respectively. So, $\Delta\vartheta_I \rightarrow \sqrt{g(\varpi)} \vartheta_E$. This gives the respective amplification of the two separate images, $\mu_+ \rightarrow 1$ and $\mu_- \rightarrow 0$. Hence, the image on the opposite side of the source (ϑ_{I-} , for $\vartheta_S > 0$) disappears in this limit.

If on the contrary the observer does not resolve the two images, the total amplification is given by

$$\mu_{tot} \simeq \frac{\bar{b}^2 + 2g(\varpi) r_E^2}{\bar{b}\sqrt{\bar{b}^2 + 4g(\varpi) r_E^2}} = \frac{\bar{B}^2 + 2g(\varpi)}{\bar{B}\sqrt{\bar{B}^2 + 4g(\varpi)}}.$$

Note that the total amplification is always weaker in the case of non-alignment than in the case of a perfect alignment.

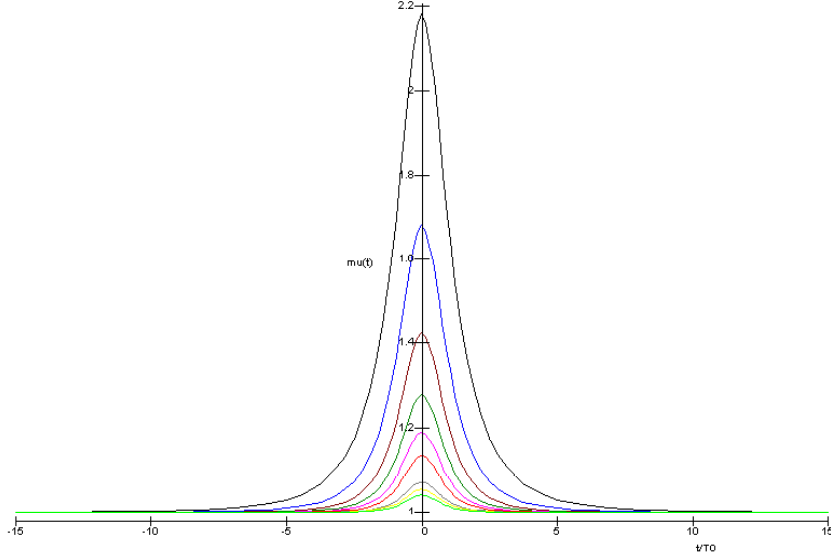
5.3.2.4 Microlens

When the images are not resolved and the distance scales allow to consider the motion of the lens, a point mass lens leads to

$$\begin{aligned} \mu_{tot}(t) &\simeq \frac{\bar{B}_0^2 \left[1 + \frac{t^2}{T_0^2} \right] + 2g(\varpi)}{\bar{B}_0 \sqrt{1 + \frac{t^2}{T_0^2}} \sqrt{\bar{B}_0^2 \left[1 + \frac{t^2}{T_0^2} \right] + 4g(\varpi)}} \\ &= \frac{\bar{B}_{TS0}^2 \left[1 + \frac{t^2}{T_0^2} \right] + 2}{\bar{B}_{TS0} \sqrt{1 + \frac{t^2}{T_0^2}} \sqrt{\bar{B}_{TS0}^2 \left[1 + \frac{t^2}{T_0^2} \right] + 4}}, \end{aligned}$$

where we have defined $\bar{B}_{TS0} \equiv \bar{b}_0/r_{TS}$ with $r_{TS} = \sqrt{g(\varpi)} r_E$, the tensor scalar radius.

For this lens model, the time-dependent total amplification provides the following simulation (5.17), plotted for different values of the normalized minimal impact parameter \bar{B}_{TS0} .



Total amplification (μ_{tot}) as a function of time (microlensing event) for a punctual mass in the setting of TS theories.

On this diagram, the angles are given in radians.

The curves are plotted for different values of the normalized minimal impact parameter:

$\overline{B}_{TS0} = 0.5, 0.7, 0.9, 1.1, 1.3, 1.5, 1.7, 1.9, 2.1$ and 2.3 .

Values of the variables in the simulation are given by (5.9) when considering lensing towards the Halo of the Galaxy.

(5.17)

Let us remark that the maximum of the total amplification curve, located at $\frac{t}{T_0} = 0$ (*i.e.* when the O-L-S system is in the closest configuration to alignment), is a decreasing function of \overline{B}_{TS0} . This is logical since if \overline{B}_{TS0} increases, the configuration moves away from the perfect alignment scenario where the amplification is maximal.

We see that the total amplification curve $\mu_{tot}(t)$ usually expressed with scales appropriate for General Relativity (\overline{B}_0 meaning the scale r_E) can be redefined in terms of scales appropriate to Tensor Scalar theories (\overline{B}_{TS0} that is to say, the scale $r_{TS} = \sqrt{g(\varpi)}r_E$). Consequently, the characteristic parameters of the light curve - its maximum $\mu_{tot\max}$, width-half-maximum $L_{1/2}$ and average surface $S_{average} = L_{1/2} \mu_{tot\max}$ - will be the same functionals, independently of the value of the parameter ϖ . In other words, the characteristics of the microlensing curve do not allow us to decide between GR and TS theories, as we cannot measure absolutely the light curve. We only measure it according to a chosen scale corresponding to the visible ring (r_E for GR, or r_{TS} for TS theories).

In fact, the mass of the deflector is not a quantity directly accessible to observations. Indeed, the microlensing event is used to infer the mass function, the total gravitational mass present (luminous or not), in the setting of GR. Even if some color photometric measurements are made, providing the spectra of the lensing star, the uncertainty on the estimated mass is in the best cases around ten percent, thus far from the precision needed to constrain $g(\varpi)$ (see (5.13)). Hence, we can say that the rescaling of the Einstein radius amounts to absorbing the TS factor $g(\varpi)$ into the mass:

$$\begin{aligned}
 M &\mapsto M g(\varpi) = M_{TS} \\
 &\Downarrow \\
 r_E &\mapsto \sqrt{g(\varpi)}r_E = r_{TS}
 \end{aligned}$$

We conclude this paragraph on TS theories by the characteristic expressions of the light curve:

$$\begin{aligned}\mu_{tot\ max} &\simeq \frac{\overline{B}_{TS\ 0}^2+2}{\overline{B}_{TS\ 0}\sqrt{\overline{B}_{TS\ 0}^2+4}}, \\ L_{1/2} &\simeq \frac{2}{\overline{B}_{TS\ 0}}\sqrt{\left(\overline{B}_{TS\ 0}^2+2\right)\frac{4\sqrt{F(\overline{B}_{TS\ 0})-F(\overline{B}_{TS\ 0})}}{F(\overline{B}_{TS\ 0})}}, \\ \text{with } F(\overline{B}_{TS\ 0}) &\equiv \left(\overline{B}_{TS\ 0}^2+2\right)^2-4\overline{B}_{TS\ 0}^2\left(\overline{B}_{TS\ 0}^2+4\right).\end{aligned}$$

5.3.3 MTS/SITS theories

Fortunately, a rescaling of the lens mass will not be possible for MTS/SITS theories. Simulations will enable us to see that MTS/SITS predictions regarding gravitational lensing can be qualitatively different from those of GR for some small values of the parameter Υ .

5.3.3.1 Asymptotic second order light deflection angle

To analyze how MTS/SITS theories differ from GR from the point of view of light deflection, we have seen that it is necessary to consider the second order contribution.

The asymptotic light deflection angle ($\hat{\alpha}$), as a function of the angular position of the image (ϑ_I) and the position of the observer ($\rho_{obs} = Dol$), is easily obtained from (3.12) using the corresponding PPN parameters for MTS/SITS (1.67) with (3.31):

$$\hat{\alpha}(\vartheta_I, Dol) = \frac{4GM}{c^2 Dol \sin \vartheta_I} \left\{ 1 + \left[-2 \sin \vartheta_I + \frac{(16 - 1/\Upsilon^2)}{16} \pi \right] \frac{GM}{c^2 Dol \sin \vartheta_I} \right\} + \mathcal{O}\left(\frac{V^3}{c^6}\right). \quad (5.18)$$

We can see that this angle can either be convergent ($\hat{\alpha} > 0$) or divergent ($\hat{\alpha} < 0$) (\leftrightarrow GR) according to the respective value of Υ and ϑ_I . Indeed, the angle ϑ_{I0} (which has to be positive, as it is not written as $\overrightarrow{\vartheta}_I$) at which the asymptotic light deflection angle cancels is

$$\vartheta_{I0} = \arcsin \left\{ \frac{\left(\frac{1}{16\Upsilon^2} - 1\right) \pi \frac{GM}{c^2 Dol}}{1 - 2 \frac{GM}{c^2 Dol}} \right\}. \quad (5.19)$$

Light deflection is divergent (convergent) for $\vartheta_I < \vartheta_{I0}$ ($\vartheta_I > \vartheta_{I0}$).

Seeing that the denominator $1 - 2 \frac{GM}{c^2 Dol}$ is positive for the mass and distance scales involved in microlensing events (5.9) or gravitational mirages (5.11), and that the image position ϑ_I in (5.18) is defined as positive, the condition on Υ for having a convergent to a divergent lens transition is

$$\left(\frac{1}{16\Upsilon^2} - 1\right) > 0 \Leftrightarrow \Upsilon < 1/4 \equiv \Upsilon_{critical}.$$

If it is true that the ray of light diverges for angles (relative to the deflector) smaller than ϑ_{I0} , the angle ϑ_{I0} is not on an equal footing for gravitational mirages and for microlensing. Indeed, for **gravitational mirages** described by (5.11), an angle ϑ_{I0} of the order of the arcsecond relevant to gravitational mirages requires $\Upsilon \sim 10^{-3} - 10^{-4}$ for $\vartheta_{I0} \sim 10^{-1} - 10^{+1}$ arcsec. While in a **microlensing** event described by (5.9), an angle ϑ_{I0} of the order of the milliarcsecond relevant to microlensing events would require a very strong scalar contribution to the MTS/SITS theories, far from $\Upsilon_{GR} = 1$: $\Upsilon \sim 10^{-5} - 10^{-6}$ for $\vartheta_{I0} \sim 10^{-4} - 10^{-2}$ arcsec.

As we shall see in the next paragraph, very small values of Υ ($< \Upsilon_{special}$ (5.22), with $\Upsilon_{special} \simeq 0.0019$ in our simulation (5.11) of gravitational mirages, and $\Upsilon_{special} \simeq 2.26 \cdot 10^{-5}$ in our microlensing simulation (5.9)) do not allow for the formation of images in case of alignment, *i.e.* ring(s) if the images could be resolved. The case $\Upsilon = 0.001$ in Simulation (5.21) for gravitational mirages illustrates this point.

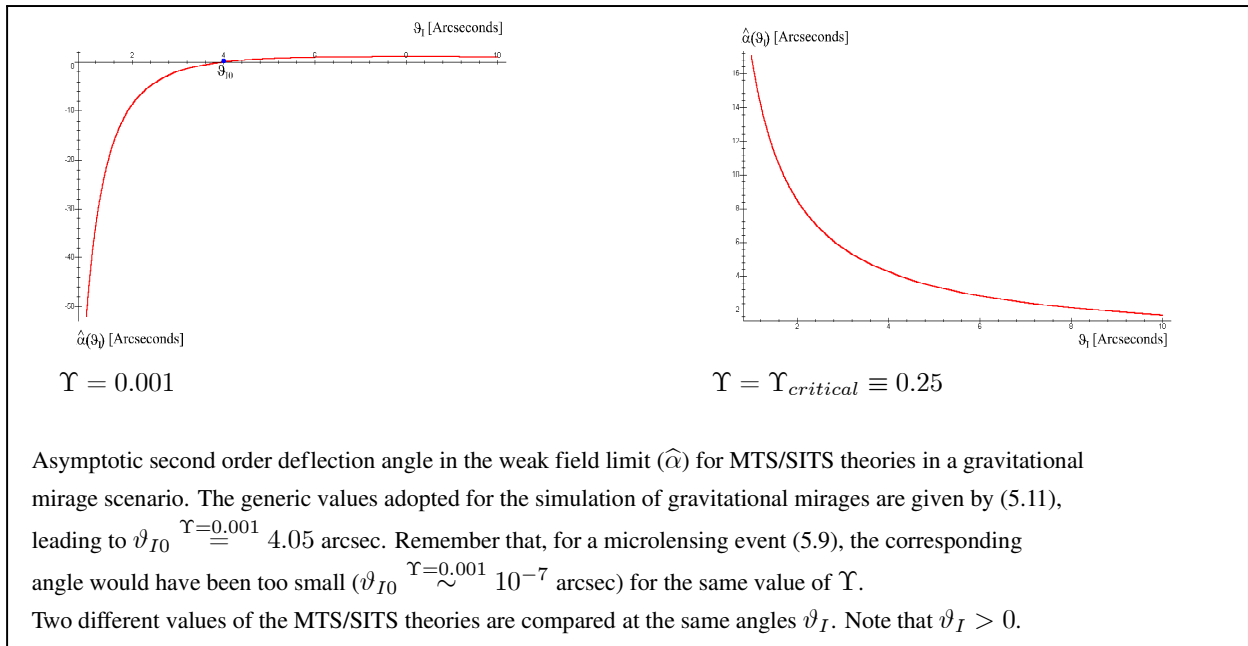
Such a prediction is based on our very simple model (point-like lenses and sources), but is also valid for a sufficiently small light source, with an angular radius smaller than the model dependant angle ϑ_{Sc} in Simulation (5.21). Likewise, no image of a point-like source shall form when the alignment is only slightly broken ($\vartheta < \vartheta_{Sc}$).

The possible absence of image for $\Upsilon < \Upsilon_{special}$ is of course directly related to the existence of a value ϑ_{I0} relevant for the microlensing event or the gravitational mirage scenario considered. In microlensing, $\Upsilon < \Upsilon_{special}$ could thus lead to an observed extinction of the light source if the source passes within the region centered on the lens and defined by ϑ_{Sc} (speaking in terms of projections onto the sky). This is a dramatic difference with the general relativistic prediction for the same microlensing model.

If we thus exclude very strong scalar contributions (*i.e.* for $\Upsilon > \Upsilon_{special}$), in microlensing events, the corresponding ϑ_{I0} is too small to be effective, and light deflection is always convergent. This means that microlensing events do not constitute in this case a qualitative test of MTS/SITS theories, as deviations from GR predictions will only be quantitative. Hence, knowing the numerous unknowns in the O-L-S system, plus the fact that the deviation from GR is only a second order effect already on the limit of detection in solar system light deflection experiments, microlenses are totally irrelevant to test MTS/SITS theories for $\Upsilon > \Upsilon_{special}$. Consequently, we will only consider gravitational mirages in the next paragraphs.

The following plots (5.20) of the asymptotic weak field second order deflection angle as a function of ϑ_I illustrate the above remarks, in the setting of our numerical simulation for gravitational mirages. We can see that the asymptotic deflection angle can become quite large for a diverging ray of light, and thus we have to be cautious with the small angle approximation on $\hat{\alpha}$. On the contrary, $\hat{\alpha}$ remains small for a converging ray.

Note that the angle ϑ_{I0} considered in this section corresponds, in terms of radial distances, to r_0 (or b_0) defined earlier in (4.19).



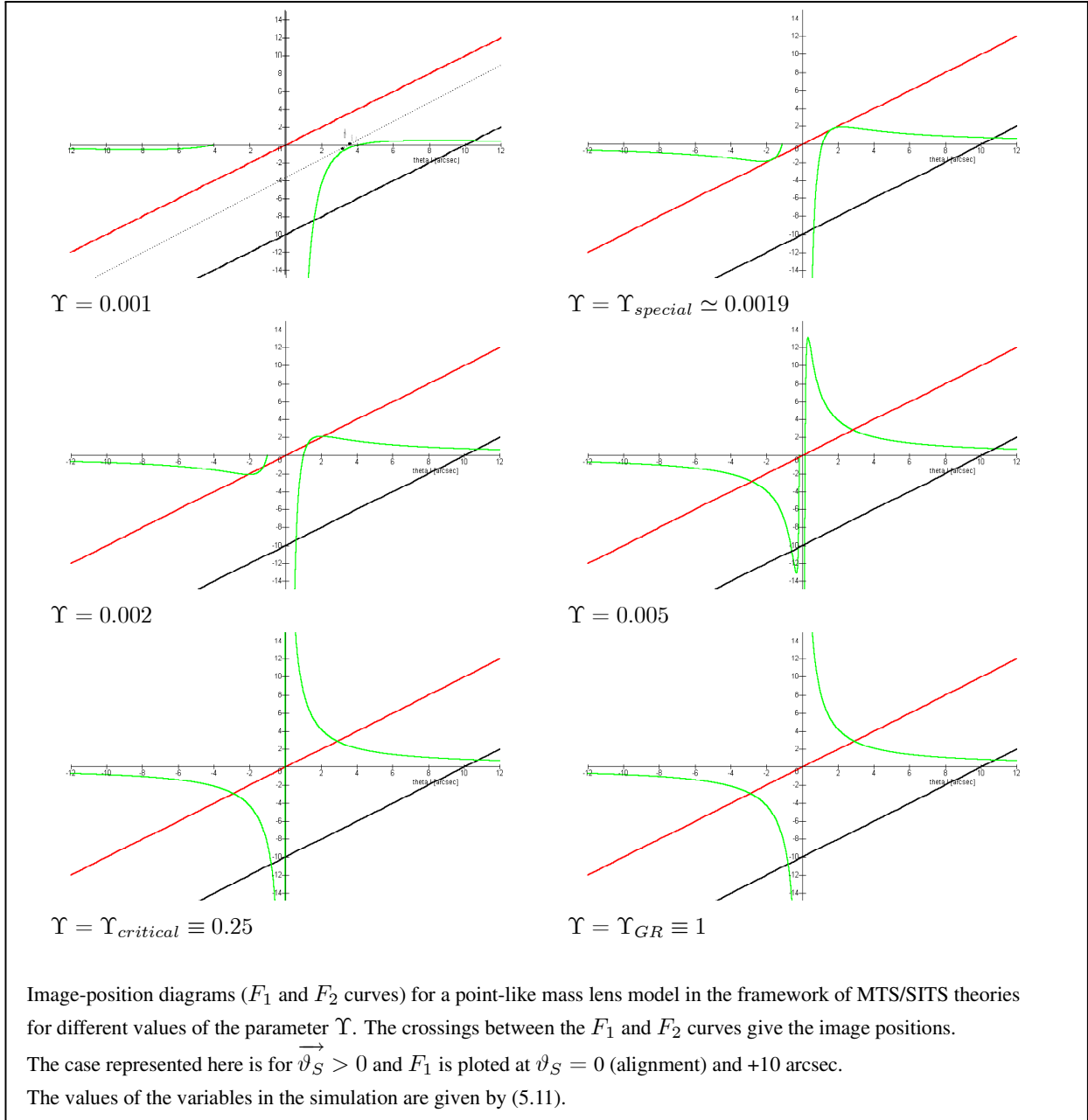
(5.20)

5.3.3.2 Lens equation

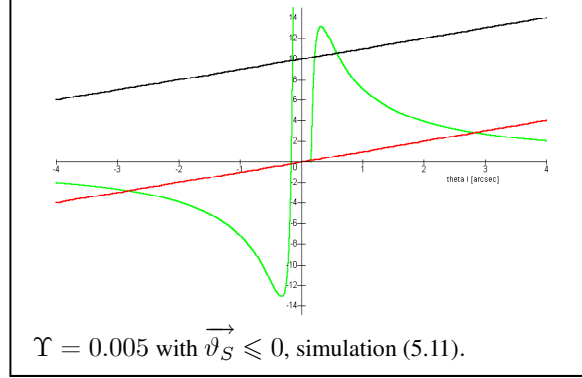
The exact lens equation (5.2) together with the light deflection angle in the weak field limit (5.18) provide the position of the images. In fact, the small angle lens equation (5.3) is sufficient most of the time for the simulations we have performed, unless explicitly stated otherwise.

A/ Different F_2 curves for different values of Υ

With the help of the image-position diagrams, we realize that according to the value of the parameter Υ , for any fixed position of the source (ϑ_S), the observer might see a very different mirage, whether $\Upsilon \in]0; \Upsilon_{special}[$, $\Upsilon = \Upsilon_{special}$, $\Upsilon \in]\Upsilon_{special}; 1/4[$ or $\Upsilon \in [1/4; 1 \equiv GR]$. The following graphs of the F_1 and F_2 curves given in (5.2) for MTS/SITS theories illustrate this claim.



Let us first notice how the F_2 curve should be plotted when $\vec{\vartheta}_S \leq 0$, according to the fact that there exists only one divergent image on the same side of the deflector as the source. The example is here given for $\Upsilon = 0.005$:



We can now explain analytically those different features...

For very small values of $\Upsilon \in]0; \Upsilon_{special}[$, the F_2 curve allows for a divergent contribution (when $\hat{\alpha} < 0$ which implies that F_2 is negative). The negative values of the deflection angle $\hat{\alpha}(\vartheta_I)$, for $\vartheta_I < \vartheta_{I0}$, are usually very large, so as to prevent us to use the small $\hat{\alpha}$ approximation.

For $\Upsilon = \Upsilon_{special}$, the F_2 curve will still allow for a value ϑ_{I0} separating the divergent from the convergent contributions. However, the set of intersections between F_1 and F_2 will dramatically change: the formation of one ring will become possible at $\vartheta_I = \vartheta_{Ic}$.

One can easily calculate this special minimal value of Υ using the small angle approximation which is consistent because $\vartheta_{Ic} > \vartheta_{I0}$, and in this region, $\hat{\alpha}$ is positive thus small.

For $\Upsilon_{special}$, the caustic position ϑ_{Ic} (the angular position of the image for which the slope of the F_2 and F_1 curves is the same - equal to 1-), given by the following equation

$$\frac{D_{os} D_{ol}}{D_{ls}} \frac{1}{\frac{4GM}{c^2}} \vartheta_{Ic}^3 + \left(1 - \frac{2GM}{D_{ol} c^2}\right) \vartheta_{Ic} - 2 \left(\frac{1}{16\Upsilon^2} - 1\right) \pi \frac{GM}{D_{ol} c^2} \simeq 0,$$

is tangent to the F_1 curve taken at $\vartheta_S = 0$. This provides another equation,

$$\frac{D_{os} D_{ol}}{D_{ls}} \frac{1}{\frac{4GM}{c^2}} \vartheta_{Ic}^3 - \left(1 - \frac{2GM}{D_{ol} c^2}\right) \vartheta_{Ic} + \left(\frac{1}{16\Upsilon^2} - 1\right) \pi \frac{GM}{D_{ol} c^2} \simeq 0,$$

which can be combined with the previous one to lead to the value of $\Upsilon_{special}$,

$$\Upsilon_{special} \simeq \frac{3}{4} \frac{1}{\sqrt{9 + \frac{4\sqrt{3}}{\pi} \frac{D_{ol} c^2}{GM} \sqrt{\frac{GM}{c^2} \frac{D_{ls}}{D_{os} D_{ol}} \left(1 - \frac{2GM}{D_{ol} c^2}\right)^3}}}. \quad (5.22)$$

In our simulation for gravitational mirages (5.11), we find $\Upsilon_{special} \simeq 0.0019$; while the simulation for microlensing events (5.9) would give $\Upsilon_{special} \simeq 2.26 \cdot 10^{-5}$ for a lens of one solar mass.

For small values of $\Upsilon \in]\Upsilon_{special}; 1/4 \equiv \Upsilon_{critical}[$, the F_2 -curve presents some foldings and allows for a divergent contribution. This shape of the F_2 -curve provides a richer variety of mirages for different angular positions of the source as described in details in the next paragraph.

For larger values of $\Upsilon \in [\Upsilon_{critical} \equiv 1/4; 1 \equiv GR]^{39}$, the shape of the F_2 -curve will be the same as for General Relativity, that is to say, two hyperbolas. No divergent contribution is allowed in this case (ϑ_{I0} does not exist when $\Upsilon > 1/4$). Indeed, extrema of F_2 are prevented, as their positions are given by $\vec{\vartheta}_{I \max/\min} \simeq \pm 2\vartheta_{I0}$.

**B/ Change in the angular position of the source (ϑ_S) for a fixed value of the parameter Υ :
the number and the type of images**

The lens being non transparent, the number of images observed for any position of the light source except on a caustic is always even, according to Burke's theorem [29]. The characteristics of the image configurations are summarized in the following tables.

For very small values of $\Upsilon \in]0; \Upsilon_{special}[$:

MTS/SITS $\Upsilon \in]0; \Upsilon_{special}[\Rightarrow \exists \vartheta_{I0}, \exists \vartheta_{Ic}, \exists \vec{\vartheta}_{I \max/min}$				
Position of S $\vec{\vartheta}_S \geq 0$	# of I	type of I: convergent (C) if $\hat{\alpha} > 0$ direct (O) if $\hat{\alpha} = 0$ divergent (D) if $\hat{\alpha} < 0$	parity of I: same side as S (+) if $\text{sg}(\vec{\vartheta}_S) = +\text{sg}(\vec{\vartheta}_I)$ opposite side of S (-) if $\text{sg}(\vec{\vartheta}_S) = -\text{sg}(\vec{\vartheta}_I)$	remarks
$= 0$	0			alignment
$\in]0; \vartheta_{Sc}[$	0			
$= \vartheta_{Sc}$	1	C	+	caustic
$\in]\vartheta_{Sc}; \vartheta_{I0}[$	2	C	+, +	
$= \vartheta_{I0}$	1	C	+	\ni null deflection
	1	O	+	
$> \vartheta_{I0}$	1	C	+	
	1	D	+	

(5.23)

An important feature of this range of values for Υ is that it will not allow for the formation of any ring. This last point can also be seen with the absence of a vertical asymptote in the tangential amplification curve (see next paragraph). Hence, only two images should be visible, both on the same side of the deflector as the source (\leftrightarrow GR) in case of non-alignment, and none in case of alignment.

For $\Upsilon = \Upsilon_{special}$:

MTS/SITS $\Upsilon = \Upsilon_{special} \Rightarrow \exists \vartheta_{I0}, \exists \vartheta_{Ic}, \exists \vec{\vartheta}_{I \max/min}$				
Position of S $\vec{\vartheta}_S \geq 0$	# of I	type of I: convergent (C) if $\hat{\alpha} > 0$ direct (O) if $\hat{\alpha} = 0$ divergent (D) if $\hat{\alpha} < 0$	parity of I: same side as S (+) if $\text{sg}(\vec{\vartheta}_S) = +\text{sg}(\vec{\vartheta}_I)$ opposite side of S (-) if $\text{sg}(\vec{\vartheta}_S) = -\text{sg}(\vec{\vartheta}_I)$	remarks
$= 0 = \vartheta_{Sc}$	1 ring	C	+, -	alignment
$\in]0; \vartheta_{I0}[$	2	C	+, +	
$= \vartheta_{I0}$	1	C	+	\ni null deflection
	1	O	+	
$> \vartheta_{I0}$	1	C	+	
	1	D	+	

(5.24)

This time, the F_2 -curve allows for one single ring in case of alignment, and again, two images on the same side of the source in case of misalignment.

For small values of $\Upsilon \in]\Upsilon_{special}; 1/4 \equiv \Upsilon_{critical}[$:

MTS/SITS $\Upsilon \in]\Upsilon_{special}; 1/4 \equiv \Upsilon_{critical}[\Rightarrow \exists \vartheta_{I0}, \exists \vartheta_{Ic}, \exists \vec{\vartheta}_{I \max/min}$				
Position of S: $\vec{\vartheta}_S \geq 0$	# of I	type of I: convergent (C) if $\hat{\alpha} > 0$ direct (O) if $\hat{\alpha} = 0$ divergent (D) if $\hat{\alpha} < 0$	parity of I: same side as S (+) if $\text{sg}(\vec{\vartheta}_S) = +\text{sg}(\vec{\vartheta}_I)$ opposite side of S (-) if $\text{sg}(\vec{\vartheta}_S) = -\text{sg}(\vec{\vartheta}_I)$	remarks
$= 0$	2 rings	C	+, +, -, -	alignment
$\in]0; \vartheta_{I0}[$	4	C	+, +, -, -	
$= \vartheta_{I0}$	3	C	+, -, -	\ni null deflection
	1	O	+	
$\in]\vartheta_{I0}; \vartheta_{Sc}[$	3	C	+, -, -	
	1	D	+	
$= \vartheta_{Sc}$	2	C	+, -	caustic
	1	D	+	
$> \vartheta_{Sc}$	1	C	+	
	1	D	+	

(5.25)

For this range of values of the parameter Υ , the alignment leads to two concentric rings, while only one ring is possible in the case of GR. The radii of the rings are given, for example for $\Upsilon = 0.005$, by

$$r_{E \text{ inner}} \simeq \tan \vartheta_{+/-\text{inner}} \text{Dol} \stackrel{\Upsilon=0.005}{=} 0.787 \cdot 10^4 \frac{GM}{c^2},$$

$$r_{E \text{ outer}} \simeq \vartheta_{+/-\text{outer}} \text{Dol} \stackrel{\Upsilon=0.005}{=} 13.732 \cdot 10^4 \frac{GM}{c^2}.$$

Those two rings break up into four colinear images when there is a slight misalignment. This again is very different from GR predictions which predicts a maximum of two images for the same lens model!

Moreover, for this simple lens model and $\Upsilon < \Upsilon_{critical}$, there exists a caustic (\leftrightarrow GR). For example, for $\Upsilon = 0.005$ and $\vec{\vartheta}_S \geq 0$, the caustic position is $\vec{\vartheta}_{Ic} = -0.3200$ arcsec which corresponds to $\vec{\vartheta}_{Sc} = +12.8146$ arcsec in F_1 .

On the caustic, the internal and external images located on the opposite side of the deflector with respect to the source position merge to form one single image. A total of three images are present in this case (\leftrightarrow GR).

Outside the caustic ($\vartheta_S > \vartheta_{Sc}$), there will be two images like in General Relativity for the same lens model, but their position relative to the lens (*i.e.* their parity) will be different: in MTS/SITS both images will be again on the same side of the deflector as the source, whereas in GR, there is one image on each side of the deflector (see Table (5.28) and simulations (5.21)).

Those characteristics of the mirages can also be described from the reading of the tangential and radial amplification curves, showing respectively two singularities (*i.e.* two rings: $\vartheta_{IE \text{ inner}}$ and $\vartheta_{IE \text{ outer}}$) plus one singularity (*i.e.* a caustic ϑ_{Ic}) located between the two first singularities.

Table (5.26) illustrates the positions of the images in arcseconds for a fixed value of $\Upsilon = 0.005$, as a function of the position of the source.

MTS/SITS $\Upsilon = 0.005$, simulation (5.11).				
Outside image position on the opposite side of the source $\vec{\vartheta}_{I-outer}$ (arcsec)	Inner image position on the opposite side of the source $\vec{\vartheta}_{I-inner}$ (arcsec)	Source position $\vec{\vartheta}_S$ (arcsec)	Inner image position on the same side as the source $\vec{\vartheta}_{I+inner}$ (arcsec)	Outer image position on the same side as the source $\vec{\vartheta}_{I+inner}$ (arcsec)
-2.8324	-0.1624	+0.0000	+0.1624	+2.8324
-2.5852	-0.1640	+0.5000	+0.1609	+3.1008
-2.3592	-0.1657	+1.0000	+0.1594	+3.3901
-1.8006	-0.1711	+2.5000	+0.1553	+4.3735
-1.1877	-0.1821	+5.0000	+0.1492	+6.3132
-0.8209	-0.1971	+7.5000	+0.1440	+8.4838
-0.5796	-0.2201	+10.0000	+0.1394	+10.7776
-0.3768	-0.2780	+12.5000	+0.1353	+13.1396
none	none	+15.0000	+0.1317	+15.5418
none	none	+17.5000	+0.1283	+17.9693
none	none	+20.0000	+0.1253	+20.4135
none	none	+22.5000	+0.1225	+22.8694
none	none	+25.0000	+0.1199	+25.3337
none	none	+27.5000	+0.1175	+27.8043
none	none	+30.0000	+0.1153	+30.2795

(5.26)

For larger values of $\Upsilon \in [1/4; 1 \equiv GR]$:

MST/SIST $\Upsilon \in [1/4; 1 \equiv GR] \Rightarrow \# \vartheta_{I0}, \# \vartheta_{Ic}, \# \vec{\vartheta}_{I \max / \min}$				
Position of S: $\vec{\vartheta}_S \geq 0$	# of I	type of I: convergent (C) if $\hat{\alpha} > 0$ direct (O) if $\hat{\alpha} = 0$ divergent (D) if $\hat{\alpha} < 0$	parity of I: same side as S (+) if $\text{sg}(\vec{\vartheta}_S) = +\text{sg}(\vec{\vartheta}_I)$ opposite side of S (-) if $\text{sg}(\vec{\vartheta}_S) = -\text{sg}(\vec{\vartheta}_I)$	remarks
= 0	1 ring	C	+, -	alignment
> 0	2	C	+, -	

(5.27)

For such values of the parameter Υ , the mirages are qualitatively the same as for GR. That is to say that the unique Einstein ring formed in case of alignment breaks up into two images when the alignment configuration is not respected; there is no caustic point.

Table (5.28) provides the image position according to the position of the source for GR.

GR or MTS/SITS with $\Upsilon = \Upsilon_{GR} \equiv 1$, simulation (5.11).		
Image position on the opposite side of the source $\vec{\vartheta}_{I-}$ (arcsec)	Source position $\vec{\vartheta}_S$ (arcsec)	Image position on the same side as the source $\vec{\vartheta}_{I+}$ (arcsec)
-2.9171	+0.000	+2.9171
-2.6778	+0.500	+3.1777
-2.4596	+1.000	+3.4596
-1.9236	+2.500	+4.4236
-1.3418	+5.000	+6.3418
-1.0010	+7.500	+8.5010
-0.7888	+10.000	+10.7887
-0.6473	+12.500	+13.1472
-0.5474	+15.000	+15.5473
-0.4735	+17.500	+17.9734
-0.4168	+20.000	+20.4168
-0.3721	+22.500	+22.8720
-0.3359	+25.000	+25.3359
-0.3061	+27.500	+27.8060
-0.2811	+30.000	+30.2810

(5.28)

5.3.3.3 Amplifications

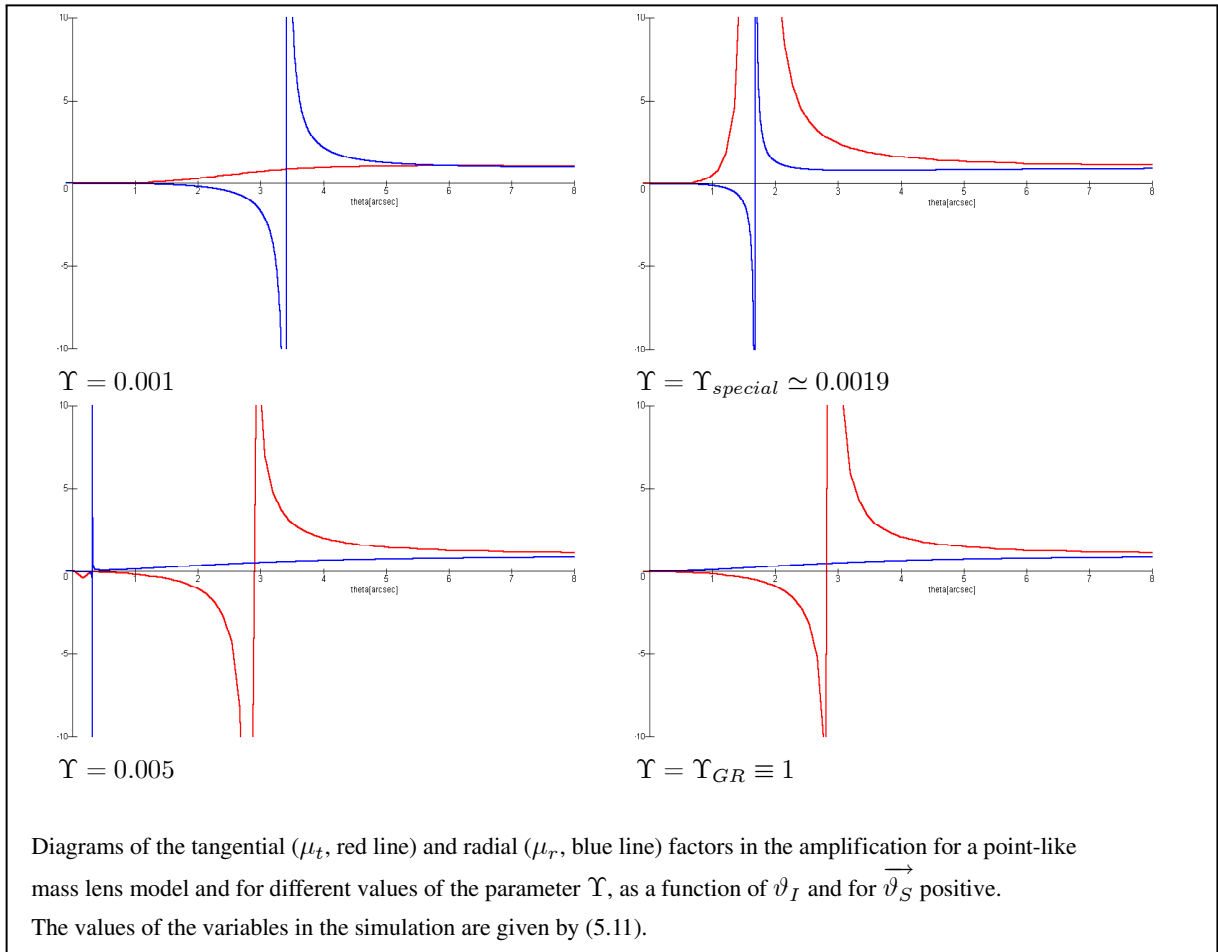
Regarding the amplification diagrams, we only plot them as a function of ϑ_I (not $\vec{\vartheta}_I$). We can see the confirmation of the characteristics of the gravitational mirages described earlier for different values of Υ : the presence of a singularity in the tangential amplification curve signals the presence of a ring, while in the radial amplification curve, it reveals a caustic.

However, the amplification curve complements the image-position diagram analysis, as it is crucial to predict the visibility of images. Indeed, let us first say that the alignment configuration, for any $\Upsilon > \Upsilon_{special}$, is the configuration of maximum amplification (when excluding caustic points). The amplification decreases as ϑ_S increases, but all the images are not amplified equally. Indeed, for $\Upsilon \in]\Upsilon_{special}; 1/4 \equiv \Upsilon_{critical}[$, $\vartheta_S \nearrow \Rightarrow$

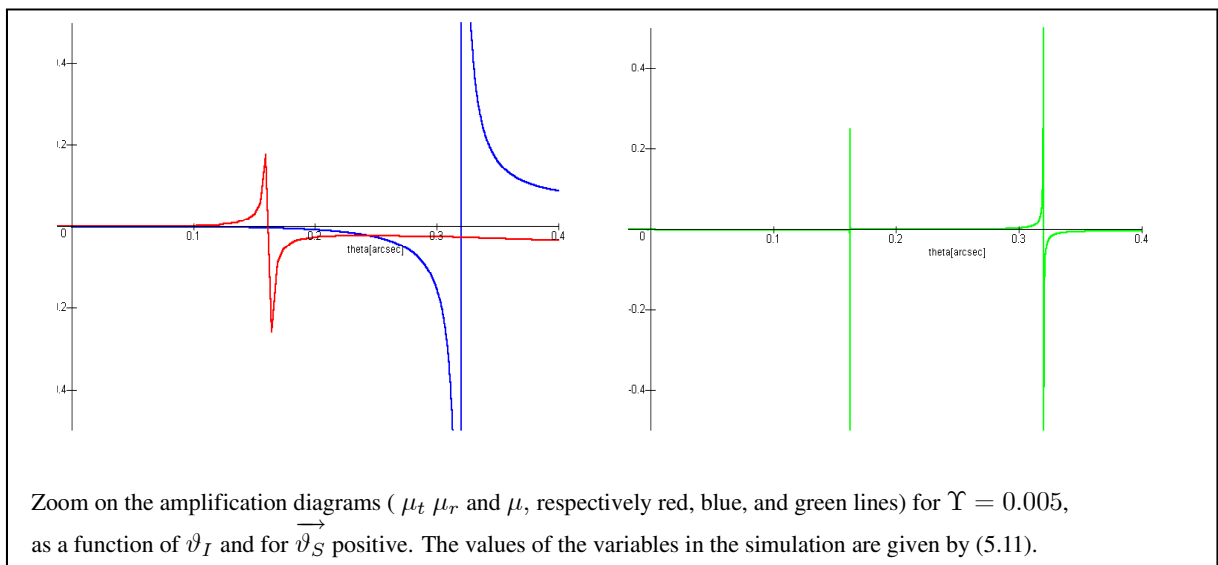
$(\vartheta_{I- outer} \searrow, \vartheta_{I- inner} \nearrow, \vartheta_{I+ inner} \searrow, \vartheta_{I- outer} \nearrow)$ as we see in Table (5.26). While correspondingly (simulations (5.31) for $\Upsilon = 0.005$, and (5.30)), outer-odd-parity (and respectively inner-even-parity) image becomes the faintest. Moreover, we see that the inner images are way less amplified than the outer images; and that the amplification decreases faster for the inner images than for the outer images, when moving away from the alignment position. The inner images are thus always fainter, which means intrinsically more difficult to observe than the outer images.

This difficulty adds up to the fact that the inner images lie close to the deflector for a given position of the source, and that the angle between them decreases as Υ increases (from a few tenth of arcseconds to a few milliarcseconds). On the contrary, the outer images are well separated (a few arcseconds), and are fairly close to the position of the sole images predicted by General Relativity (compare Table (5.26) with Table (5.28)). Thus if the instrument resolution is not too good, not knowing the mass properties of the lens, the observer might well conclude to observe GR predictions, even for $\Upsilon \neq 1$!

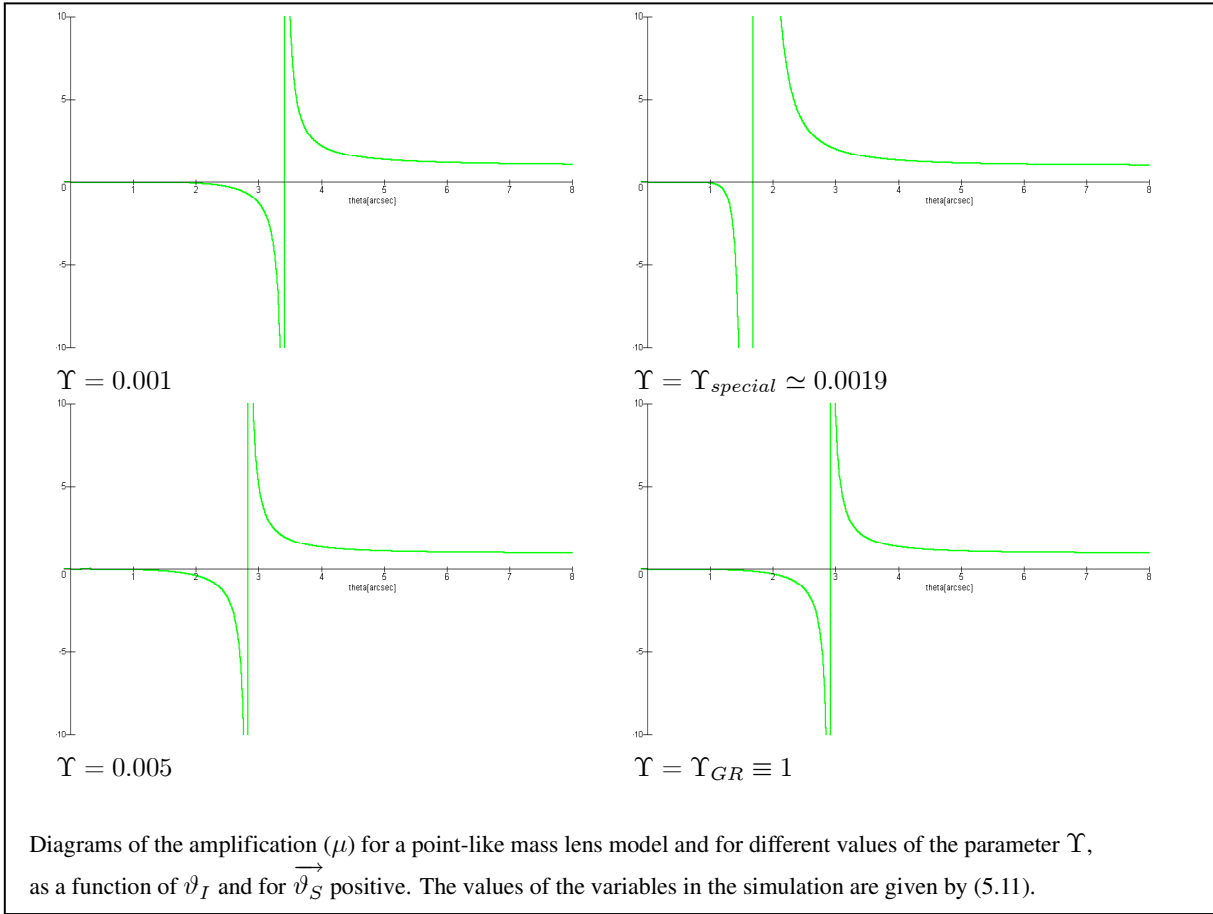
We note that the angular separation between the two rings increases with Υ ($\vartheta_{IE inner} \searrow$ while $\vartheta_{IE outer} \nearrow$ in Table (5.26)), that is, the singularities in the tangential amplification curve move apart. Hence, the two inner images become easier to separate from the outer images. However, we know that this advantage is balanced by a weaker amplification for the inner images.



(5.29)



(5.30)



(5.31)

MTS/SITS Υ $\vec{\vartheta}_S \geq 0$ simulation (5.11)	Singularity in the tangential amplification curve μ_t $\vartheta_{It \text{ inner}}$ (arcsec) $= \vartheta_{IE \text{ inner}}$	Singularity in the radial amplification curve μ_r ϑ_{Ir} (arcsec) $= \vartheta_{Ic}$	Singularity in the tangential amplification curve μ_t $\vartheta_{It \text{ outer}}$ (arcsec) $= \vartheta_{IE \text{ outer}}$
0.001	none	3.4159	none
$\Upsilon_{\text{special}} \simeq 0.0019$	none	1.6841	1.6841
0.002	1.2324	1.5700	2.0985
0.003	0.4615	0.8321	2.6588
0.004	0.2550	0.4921	2.7811
0.005	0.1624	0.3200	2.8324
0.01	0.0404	0.0808	2.8966
$\Upsilon_{\text{critical}} \equiv 0.25$	none	none	2.9170
0.1	none	none	2.9169
0.5	none	none	2.9170
$\Upsilon_{GR} \equiv 1$	none	none	2.9171

(5.32)

5.3.4 The Weyl theory

We will now consider the Weyl theory and the physical consequences of its linear correction to the Newtonian potential.

5.3.4.1 Constraints on a negative Weyl parameter from the existence of gravitational mirages

We have seen in the preceding chapter, in particular through discussion (4.35), that there exists no asymptotic state for photons if the closest approach distance is larger than r_{null} , when the Weyl linear parameter γ_W is **negative**. Hence no light deflection can take place. The existence of gravitational mirages with an Einstein angle (corresponding to the Einstein radius) of a few arcseconds puts a stronger upper bound on the absolute value of the Weyl linear parameter. Indeed,

$$\begin{aligned} \frac{r_0}{D_{ol}} &\sim \frac{r_E}{D_{ol}} \simeq \vartheta_E \lesssim \frac{r_{null}}{D_{ol}} \\ \stackrel{(4.22)}{\Leftrightarrow} |\gamma_W| &\lesssim \left[\frac{1}{\vartheta_E} h_0 \frac{0.3}{z_L} \right] 1.7 \cdot 10^{-31} \text{ m}^{-1} \quad \text{for } \gamma_W < 0 \end{aligned} \quad (5.33)$$

with $\begin{cases} \vartheta_E, \text{ the Einstein ring of the mirage (5.8) in [arcsec],} \\ h_0, \text{ the normalized Hubble parameter given in Appendix A,} \\ z_L, \text{ the redshift of the lens,} \end{cases}$

where a rough estimation of the distance as a function of the redshift was made,

$$D \simeq \frac{c}{H_0} z \quad \text{for } z < 1. \quad (5.34)$$

Consequently, it seems reasonable to admit the following conservative limit on γ_W :

$$|\gamma_W| < 10^{-31} \text{ m}^{-1} \quad \text{for } \gamma_W < 0. \quad (5.35)$$

When γ_W is **positive**, on the contrary, we cannot find a better upper bound than the conservative value (4.40) obtained from solar system experiments, unless we adopt the Mannheim-Kazanas parametrization (1.53) based on an arbitrary constant value of the conformal factor.

5.3.4.2 Relevance of the weak field versus the strong field limit

If we wish to infer some further constraints on the Weyl parameter from microlensing or gravitational lensing events, it is crucial to stick to the constraints so far available on the parameter, respectively (5.35) for a negative parameter, or (4.40) for a positive parameter, and to respect the limits of the approximations we introduced in the previous chapter.

In fact, the weak (or alternatively strong) field limit on the radial distance measured from the gravitational lens has to be verified on the photon path, all the way from the light source to the observer. That is to say that the limit not only applies to the distance from the lens to the observer (D_{ol}) and to the distance from the lens to the source (D_{ls}), but also to the closest approach distance of the photon onto the lens (r_0). The order of magnitude of this latter distance will be considered to be the same as the Einstein ring radius (r_E) associated with the O-L-S system.

Immediately, we see from expression (4.30) that **the strong field limit** is unfortunately of no use here, because we only have in hand an upper bound on $|\gamma_W|$. The lower bound is given by General relativity ($\gamma_W = 0$) and leads to a strong field limit only valid at infinity.

As far as the **weak field limit** is concerned, we see from expression (1.54) that we are again limited by our upper bound on $|\gamma_W|$. Indeed, owing to the distance scales involved in microlensing events, (5.9) and (5.10), the conservative estimate (4.40) of γ_W , from solar system experiments, will not allow us to improve our constraints on a positive parameter, because, strictly speaking, we are not allowed to use this weak field limit. On the contrary, the more stringent bound (5.35) that we have just obtained for a negative parameter makes it possible to discuss the predictions regarding microlensing when $\gamma_W < 0$.

From the point of view of gravitational mirages, the distance scales involved, see (5.11) and (5.12), prevent us from using the weak field approximation with our bounds on γ_W , either for a positive or a negative value of the parameter. One could argue that our parametrization of the distance to the lens in terms of its mass given in (5.11) is somewhat overestimated. Nevertheless, if we take the example of the distance to the closest galaxy (Andromeda) which is approximately of $2 \cdot 10^{22}$ m, or the distance to the closest cluster (Virgo) of about $4 \cdot 10^{23}$ m, we understand why the weak field approximation cannot be used to try to further constrain γ_W .

It is important to notice also that, *whichever type of lensing event (microlensing or gravitational mirages) we consider*, the conditions for light deflection to take place are fulfilled each time we work in the weak field limit, according to (1.54), (4.26), (4.25) with (4.22).

5.3.4.3 Constraints on a negative Weyl parameter from Microlensing events

With the above remarks in mind, we shall try to extract some information from the microlensing events for a negative value of the linear Weyl parameter.

A/ Asymptotic weak field light deflection angle

In the weak field limit, using (4.39) and the fact that the closest approach distance is given by $r_0 \simeq b \simeq Dol \sin \vartheta_I$ at zero order in $V_W(r)/c^2$, the asymptotic light deflection angle in the Weyl theory can be rewritten, at first order, as

$$\hat{\alpha}_{\text{weak field}}(\vartheta_I, Dol) \simeq + \frac{4\beta_W}{Dol \sin \vartheta_I} - \gamma_W Dol \sin \vartheta_I. \quad (5.36)$$

Looking at this equation, we insist on the following points. The deflection angle in the weak field limit for the Weyl theory cannot be rescaled to GR prediction by a redefinition of the mass, as it was the case in TS theories. So, we might expect the predictions of the Weyl gravity to be qualitatively different from the general relativistic ones.

We also remind the reader that the deflection angle (5.36) might even be larger than the GR one, unlike predictions for TS theories.

B/ Lens equation in the weak field limit

The lens equation in the small angle and weak field limit (5.3) associated with (5.36) is

$$\vec{\vartheta}_I^2 - \frac{\vec{\vartheta}_S}{1+n_W} \vec{\vartheta}_I - \vartheta_W^2 = 0, \quad (5.37)$$

where we have defined

$$\begin{aligned} \beta_W &= \frac{G_N M}{c^2}, \\ \vartheta_W &\equiv \text{angular radius of the Weyl ring} \\ &= \sqrt{\frac{4G_N M}{c^2} \frac{1}{1+n_W} \frac{Dls}{Dol Dos}}, \\ r_W &\equiv \text{radius of the Weyl ring} \\ &\simeq \vartheta_W Dol, \\ n_W &= \gamma_W \frac{Dls Dol}{Dos} \quad \text{dimensionless with } \text{sg}(n_W) = \text{sg}(\gamma_W). \end{aligned} \quad (5.38)$$

The lens equation is again quadratic, like for GR. It is important to note that, because this lens equation is only valid in the weak field limit (1.54), the parameter n_W is always smaller in norm than 1. Thus the corrective factor with respect to GR is

$$\frac{1}{1+n_W} > 1 \quad \text{for } \gamma_W < 0.$$

It of course reduces to 1 when $\gamma_W|_{GR} = 0$.

In case of alignment, we see from equation (5.37) that the image is a ring of angular radius $\vartheta_I = 1/\sqrt{1+n_W} \vartheta_E \equiv \vartheta_W$. The predicted width of the ring ($2 d\vartheta_I$) given as a function of the angular diameter of the light source ($d\vartheta_S$) will be different from the GR one, even if we refer to the natural size in the physical problem (ϑ_W):

$$d\vartheta_I = \frac{1}{2(1+n_W)} d\vartheta_S.$$

The Weyl ring will also be thicker than its general relativistic counterpart. Consequently, the amplification will be larger:

$$\mu \simeq \frac{2 \vartheta_W}{(1+n_W) d\vartheta_S} = \frac{2 r_W}{(1+n_W) d\bar{b}},$$

and again infinite in the limit of a point-like lens mass.

In case of misalignment ($\vartheta_S > 0$), the ring breaks up into two arcs located at

$$\vartheta_{+/-} = \frac{\vartheta_S \pm \sqrt{\vartheta_S^2 + 4 \vartheta_W^2 (1+n_W)^2}}{2(1+n_W)},$$

and separated by an angle

$$\Delta\vartheta_I \equiv \vartheta_{I+} - \vartheta_{I-} = \frac{\sqrt{\vartheta_S^2 + 4 \vartheta_W^2 (1+n_W)^2}}{(1+n_W)}.$$

We remark that, interestingly, those predictions not only depend on the parameter of the Weyl theory through n_W , but also on the physical properties of the O-L-S system via the relative size of Dls , Dol , and Dos .

The width of the arcs ($2d\vartheta_{I\pm}$) is given by

$$d\vartheta_{I\pm} = \frac{1}{2(1+n_W)} \left[1 \pm \frac{1}{\sqrt{1 + 4 (\vartheta_W/\vartheta_S)^2 (1+n_W)^2}} \right] d\vartheta_S.$$

Consequently, each image will be more amplified than in General Relativity according to (5.6), with

$$\begin{aligned} \mu_{+/-} &\simeq \frac{1}{4(1+n_W)^2} \left[2 \pm \left((1+n_W) \frac{\Delta\vartheta_I}{\vartheta_S} + \frac{1}{(1+n_W)} \frac{\vartheta_S}{\Delta\vartheta_I} \right) \right] \\ &= \frac{1}{(1+n_W)^2} \frac{\pm \left[\bar{B}_W \pm \sqrt{\bar{B}_W^2 + 4(1+n_W)^2} \right]^2}{4\bar{B}_W \sqrt{\bar{B}_W^2 + 4(1+n_W)^2}} \\ &= \frac{1}{(1+n_W)^2} \frac{\pm \left[\bar{B}_{\hat{W}} \pm \sqrt{\bar{B}_{\hat{W}}^2 + 4} \right]^2}{4\bar{B}_{\hat{W}} \sqrt{\bar{B}_{\hat{W}}^2 + 4}}, \end{aligned}$$

where we have defined the following dimensionless quantities:

$$\begin{aligned} \bar{B}_W &\equiv \bar{B}/r_W, \\ \bar{B}_{\hat{W}} &\equiv \bar{B}_W/(1+n_W). \end{aligned}$$

Hence, the total amplification, when the two images are not resolved, is again larger than the GR value:

$$\begin{aligned}\mu_{tot} &\simeq \frac{1}{(1+n_W)^2} \frac{\overline{B}_W^2 + 2(1+n_W)^2}{\overline{B}_W \sqrt{\overline{B}_W^2 + 4(1+n_W)^2}} \\ &= \frac{1}{(1+n_W)^2} \frac{\overline{B}_W^2 + 2}{\overline{B}_W \sqrt{\overline{B}_W^2 + 4}}.\end{aligned}$$

The above expression and (5.8) are the relevant equations to be used for microlensing amplification curves. We see that, strictly speaking, we cannot rescale the amplification curve to fit GR prediction because of the front factor. In view of the upper bound given in (5.35) and of our simulation⁴⁰, we find

$$GR \equiv 1 \leq \frac{1}{(1+n_W)} \Big|_{\text{microlens (5.9)}} \stackrel{(5.35)}{\lesssim} 1 + 10^{-11} \quad (5.39)$$

We see that this corrective factor might be very small for microlensing events if $|\gamma_W|$ happens to be much smaller than our present upper bound. Nevertheless, we think that there is a possibility to further constrain the Weyl parameter from a statistic on microlensing curves.

The optical depth of microlensing [95] is the probability, at a given time, that a light source be within the corresponding ring radius of a given star lens; hence, it is the probability for this light source to be lensed. If we estimate this optical depth in the setting of the Weyl theory, we must integrate over the surface included in the ring radius, thus, over $\pi\vartheta_W^2$ in this case. According to (5.38), this means that the corrective factor enters in the integral. Consequently, one might have hoped that the Weyl theory would substantially increase the optical depth, so maybe to account for the observations leading to a larger value than initially estimated with General Relativity. Unfortunately, even for the upper bound on $|\gamma_W|$ in (5.35), the correction is irrelevant with respect to the observational uncertainties.

5.3.4.4 The Mannheim-Kazanas parametrization ($\gamma_W > 0$)

We have argued, in Paragraph 5.3.4.2 that we could not so far use the weak field limit to further constrain a positive γ_W . However, we can investigate the possibility to invalidate the Mannheim-Kazanas theory (4.41), or try to extract useful predictions on microlensing or gravitational mirages from this theory where the weak field limit extends to cosmological distances (1.54). Accordingly, we can use the weak field lens equation (5.37) with the corresponding definition (5.38). Nevertheless, an additional condition is necessary, as the deflection angle might be divergent for positive values of the linear Weyl parameter:

$$\text{if } \gamma_W > 0 \text{ with } \vartheta_I > \vartheta_{I0} \text{ (diverging lens: } \vec{\alpha} < 0), \exists \text{ additional conditions to (5.37):} \quad (5.40)$$

$$\begin{cases} \text{sg}(\vec{\vartheta}_I) = \text{sg}(\vec{\vartheta}_S), \\ \vartheta_S \neq 0, \\ \vartheta_S > \vartheta_I, \end{cases}$$

$$\text{with } \vartheta_{I0} = \arcsin \left\{ \frac{r_0 a}{D_{ol}} \right\}, \\ r_0 \text{ from (4.28).}$$

This time, the corrective factor is

$$GR \equiv 1 \geq \frac{1}{(1+n_W)} > 0.$$

⁴⁰ Remember that the corrective factor depends upon the O-L-S distances, the mass of the lens and the parameter γ_W .

As far as **microlensing** is concerned, the interesting closest approach distance r_{00} (4.28), at which the light deflection becomes divergent, is larger than the microlensing Einstein radius (5.10) and hence is irrelevant. Thus, light deflection is always convergent on the microlensing scales, which means no qualitative deviations from General Relativity. Moreover, an estimation of the order of magnitude of the corrective factor,

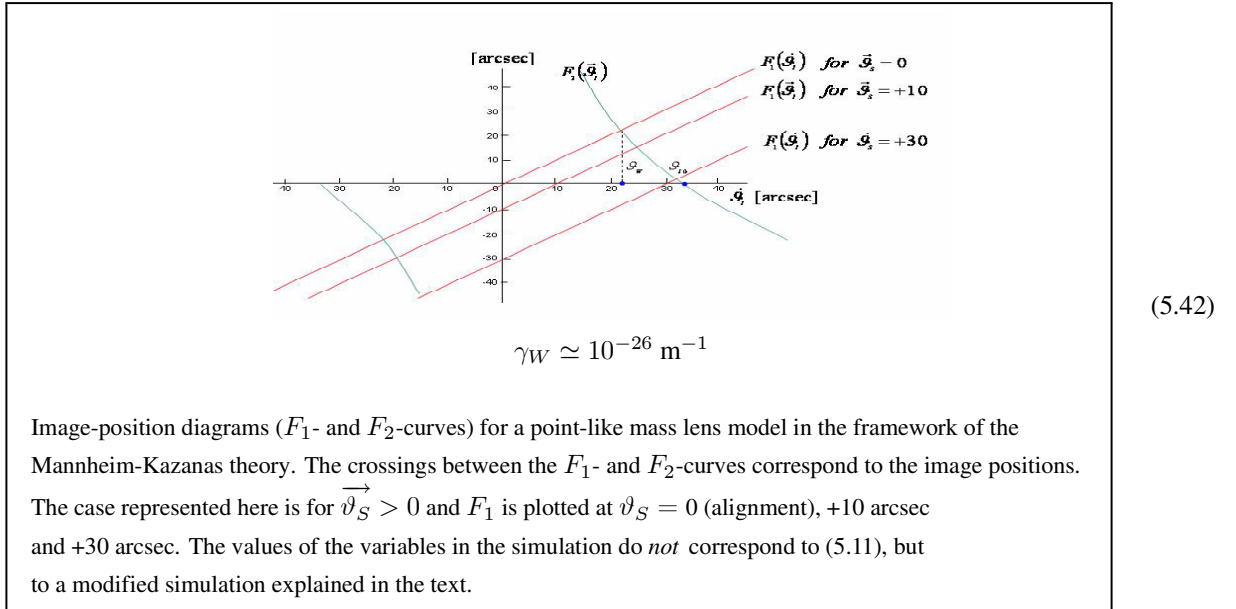
$$\frac{1}{1+n_W} \Big|_{\text{microlens (5.9)}} \stackrel{(1.53)}{\simeq} \frac{1}{1+6.25 \cdot 10^{-6}} \simeq 1, \quad (5.41)$$

shows us that microlenses are definitely not an appropriate tool to test the Mannheim-Kazanas theory.

Regarding **gravitational mirages**, the closest approach distance r_{00} (4.28) can be comparable or even smaller than the corresponding Einstein radius (5.12). This means that the divergent regime becomes significant. However, we can see that the O-L-S parameters chosen for our simulation (5.11) might not be appropriate for the weak field limit. Indeed, if for a typical galaxy of 10^{11} solar masses, the distance observer-lens is smaller than the inverse of the Weyl parameter ($D_{ol} \sim 10^{24} \text{ m} < 10^{26} \text{ m} \simeq 1/\gamma_W$), it is not the case for clusters of $10^{13} - 10^{15}$ solar masses ($D_{ol} \sim 10^{26} - 10^{28} \text{ m} \gtrsim 10^{26} \text{ m} \simeq 1/\gamma_W$).

We may consider an alternative simulation to (5.11), with this time $D_{ol} = 10^8 \text{ GM}/c^2$. This reflects better the O-L-S parameters of a lens like for example the Andromeda galaxy (approximately of $10^{11.5} M_{Sun}$, at a distance of about $2 \cdot 10^{22} \text{ m}$) or the Abell 370 cluster (around $10^{14} - 10^{15} M_{Sun}$, at an estimated redshift of 0.373 [24] leading with (5.34) to a rough estimate of $7 \cdot 10^{25} \text{ m}$ for its distance). With such a new simulation, the estimated Einstein radii (5.12) change to $2 \cdot 10^{18}$, $2 \cdot 10^{20}$, $2 \cdot 10^{21}$, and $2 \cdot 10^{22} \text{ m}$ respectively. The interesting closest approach distance r_{00} , the weak field and strong field limiting radii remain unchanged. We see that, in this latter simulation, r_{00} is relevant to the most massive clusters. But in this case, the O and L points of the photon trajectory lie about on the edge of the weak field limit, while $r_0 \sim r_E$ is still well within it.

Nevertheless, let us discuss the corresponding image-position diagrams.



We see from simulation (5.42) that the F_2 -curve (5.2) allows for a value ϑ_{I0} (5.40), at which the F_2 -curve crosses the ϑ_I -axis, separating the divergent from the convergent contributions. F_2 presents no foldings, unlike in MTS/SITS theories for $\Upsilon \in]\Upsilon_{special}; 1/4[$ (compare with simulation (5.21)). This means that the predictions of the Mannheim-Kazanas theory will be the same as the GR ones from the point of view of the number of images and their parity, which seems to prevent it to be tested using gravitational mirages. One can just say that the Mannheim-Kazanas gravity even needs more dark matter than General Relativity (the Weyl radius being smaller than the Einstein ring), because

the corrective factor is smaller than 1. To illustrate this, note that the modified simulation we discussed provides $1/(1 + n_W) \simeq 1/(1 + 0.75 \cdot 10^{-15+x})$ for the Mannheim-Kazanas parametrization (1.53) where $M = 10^x M_{Sun}$; and $10^{15} M_{Sun}$ is on the edge of the weak field approximation, as we just explained.

5.3.4.5 Attempts in the literature to deduce a negative value for γ_W

We would like now to make a few comments about reference [50]. In this article, Edery and Paranjape are interested in a negative value of the linear Weyl parameter in order to explain gravitational mirages without dark matter. They extract an order of magnitude for γ_W from the observations of giant arcs in clusters. It happens to be just the same order of magnitude (the inverse of the Hubble length) as needed in the Mannheim-Kazanas parametrization (1.53)... but with the opposite sign.

The idea behind this estimation is to equate the predicted Einstein radius based on an estimated value of the total gravitational mass (luminous plus an *ad hoc* amount of dark matter, to fit the observations in the framework of GR) with the Weyl radius for the same O-L-S system, but this time with only the luminous matter.

In the Cluster lenses used for this purpose, namely A 370, A 2390 and Cl 2244-02, the ratios of the luminous over the total mass were estimated respectively to be $M_L/M_{tot} \sim 1/200$, $\sim 1/120$ and $< 1/100$, thanks to a complete modeling of each lens in the setting of GR [24, 64, 97].

We first comment that **it is the general relativistic estimate of the luminous mass that the authors implicitly inserted into the Weyl radius** when using the above luminous to total mass ratios.

Also, in their estimation of the Weyl radii, the authors use the general relativistic **relation between the redshift and the distance**. In the framework of General Relativity, it is the Robertson-Walker metric, solution to the Einstein equations in presence of matter, which is used to infer the concept of cosmological distance as a function of the redshift, the matter density and the curvature of the universe. However, in the Weyl theory, the Robertson-Walker metric is *not* a solution of the Bach equations with matter! Indeed, the Weyl tensor ($\bar{W}_{\mu\nu\rho\sigma}$) associated with the Robertson-Walker metric is null, hence the Bach equations (1.50) *in presence of* matter,

$$B_{\mu\nu} = -1/4 \sqrt{\kappa} T_{m \mu\nu} ,$$

are not verified!

It is important to remember that the concept of distance in the Weyl theory (as well as the concept of time) requires the specification of the conformal factor. This conformal factor is crucial in cosmology to obtain the appropriate Weyl prescription relating the observed redshift to the cosmological distances. Otherwise, one can only work in terms of distance ratios (or time ratios, or the mixed time to distance ratios) and angles.

Note that, in the limit of small redshifts, the rough relation between the redshift and the distance given in (5.34) together with the approximation of an Euclidean space ($Dls = Dos - Dol$) are sufficient to recover the same order of magnitude for γ_W as the one calculated by Edery *et al.* [50]. We obtain as well the natural connection between γ_W and the inverse of the Hubble length:

$$|\gamma_W| = \left(1 - \frac{M_L}{M_{tot}}\right) \frac{Dos}{Dls - Dol} \stackrel{(5.34) \text{ and Euclidean approximation}}{\simeq} \left(1 - \frac{M_L}{M_{tot}}\right) \frac{z_s}{(z_s - z_l) z_l} \frac{H_0}{c} \quad (5.43)$$

A370, A2390 and Cl2244-02
 $\simeq 5 \cdot 10^{-26} - 6 \cdot 10^{-26} \text{ m}^{-1}$.

The approximation (5.34) can be obtained simply from the observational redshift which is related to the recession speed of galaxies (v_{recess}) by a simple Doppler effect, and from the empirical Hubble law based on observations:

$$\frac{v_{recess}}{cst D} \simeq 1 \quad \text{with } cst = H_0 |_{exp} .$$

Interestingly, the Hubble law cited above, and the measured redshift (which is a ratio of frequencies) do not require to specify the conformal factor in (1.51).

Another point concerns **the weak field approximation** that the authors use, through lens equation (5.37) and the corresponding definitions of the Weyl radius (5.38).

The gravitational mirages considered in their article,

lens	z_L	z_S
A 370	0.375	0.724
A 2390	0.231	0.913
CL 2244 – 02	0.331	0.83

correspond to observer-lens or to lens-source distances, as can be calculated using the rough estimation (5.34), that are dangerously close to the weak field limit associated with the derived value of γ_W . This leaves us dubious about the above result (5.43).

Finally, in another article [49], Edery *et al.* speak of the “theoretical arbitrariness” of the choice of the conformal factor in the Weyl spherically symmetric solution (1.51). They furthermore use the conformal transformation given in (4.42) to argue that the parameter γ_W might be measured as positive for matter particles with $ds^2_{matter} \equiv ds^2(r', t, \gamma'_W)_{Mann-Kaz}$ in (4.42); and on the contrary, as negative for photons with $ds^2_{photons} \equiv ds^2(r, t, \gamma_W)$ in (4.42). Their aim is to try to connect their estimate of γ_W to the Mannheim-Kazanas theory and explain the discrepancy in the sign of the linear Weyl parameter.

However, if the motion of ultra-relativistic particles and photons is independent of the conformal factor $\chi^2(r)$ and the choice of $\chi^2(r)$ is arbitrary when restricting to those types of particles, we have seen that on the contrary, the motion of matter as well as the definition of distance scales and timescales crucially depend on it. Because our world is made of matter, it is not conformally invariant (we indeed have clocks and rods to make measurements). Hence, **the conformal factor is not arbitrary, as long as we are looking for a theory to describe Nature! Nature has chosen a specific conformal factor**. We might even say that the Weyl theory should be called “Weyl theories”, because it in fact corresponds to a class of theories, with each theory being specified by a choice of $\chi^2(r)$ and (γ_W, k_W) ⁴¹. The Mannheim-Kazanas theory is a particular example.

Moreover, even though the linear γ_W -contribution to the effective potential might have an opposite effect on massless in comparison with massive particles (Subsection 4.4.1), it is of course necessary to use the same radial variable in order to have the same definition of γ_W when we compare the estimate of γ_W obtained from photon trajectories to the one obtained from massive particle motion.

5.3.4.6 Amazing features of the strong field limit for a negative value of γ_W

Before concluding about microlensing and gravitational mirages, we would like to illustrate some amazing features of this theory in the strong field regime, for a negative linear Weyl parameter.

To start with, we realize from the graph of photon trajectories (Figure 4.4) that the semi-lattice rectum, located at $r = -2/\gamma_W$ for any orbit in the strong field limit, is an **accumulation point**. Indeed, if we interpolate between the weak field regime, in which the description of light deflection is qualitatively analogous to the description in General Relativity, and the strong field regime, we might possibly find the following Figure 5.5. Consequently, the surface of a sphere of radius $r = -2/\gamma_W$, centered on a given lens, is a very particular region of space.

Another remark is the existence of a particular O-L-S alignment configuration in the strict strong field regime ($\beta_W = 0$), in which the observer and the source are located on the semi-lattice rectum points. There would then be an infinite number of photon trajectories coming from the source to the observer (see Figure 5.6)!

Of course, one needs to analyze further the intermediate regime between the weak field and strong field limits. However, we remark that the limiting radial distance from the lens defining the strong field regime (4.30) is inferior (in terms of orders of magnitude) to the limiting radial distance from the lens defining the weak field regime (1.54) when

$$x < y - 3 \quad \text{with} \quad \begin{cases} M = 10^x M_{Sun}, \\ \gamma_W = 10^{-y} \text{ m}^{-1}. \end{cases}$$

⁴¹ While $\beta_W \equiv \frac{G_N M}{c^2}$.

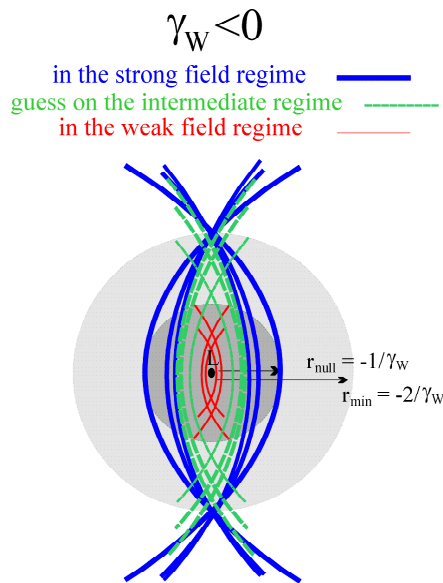


Fig. 5.5 The semi-lattice rectum, located at $r = -2/\gamma_W$ for any orbit in the strong field limit, is an accumulation point. In the weak field limit, light deflection for a point mass is similar to the general relativistic predictions: light converges on short distances when it passes close to the gravitational mass, while it converges on farther distances when it has a larger closest approach distance from the lens. We may guess the intermediate regime.

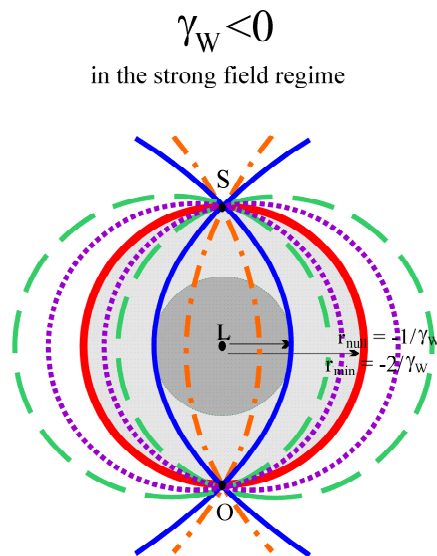


Fig. 5.6 In the strict strong field regime ($\beta_W = 0$), there exists a particular O-L-S alignment configuration in which the observer and the source aligned with the lens are located on the semi-lattice rectum points. There would then be an infinite number of photon trajectories coming from the source to the observer.

According to the constraint (5.35) that we derived for a negative γ_W from (5.33), we have $y \gtrsim 31$.

It would also be interesting to investigate further which regions of space are observable (connected by light geodesics) in the different regimes. For example, in the presence of one single lens (L), when we wish to understand if an observer, in the strict strong field limit ($\beta_W = 0$), will be able to see some given source, we realize that it depends on the position of the source with respect to the concentric spheres of radius r_{null} and r_{min} surrounding the lens. The equation of orbits described in (4.34) and (4.35) are useful for such a discussion, see Figure 5.7.

Indeed, if the light source (S_1) is inside the smallest sphere of radius r_{null} , then, the closest approach distance of any photon originating from the source is necessarily smaller than r_{null} . This means that all these photons have unbound orbits (hyperbolas centered on L).

Also, if the source (S_2) is on the sphere of radius r_{null} , the closest approach distance of its photons can be either smaller or equal to r_{null} , which means that all the orbits are again unbound (hyperbolas or a parabola). In those two cases (S_1 and S_2), the source can be seen from any region of space (except just behind the lens if it is not transparent). Whereas if the source (S_3) is located in between the two spheres, there are in addition photons originating from this source that have a closest approach distance to the lens larger than r_{null} . Accordingly, those photons are captured on elliptical orbits. Hence, in this case, there will be some regions of space that cannot be reached by any photon of S_3 .

We have already evoked the particular case of a source (S_4) situated on the sphere of radius r_{min} , which allows all four types of orbits: hyperbolic, parabolic, circular and elliptic.

For a source outside the larger sphere (S_5) there will also be some regions of space that cannot be reached by any photon originating from the source.

One could now complicate the game by considering many lenses and relax the strong field regime!

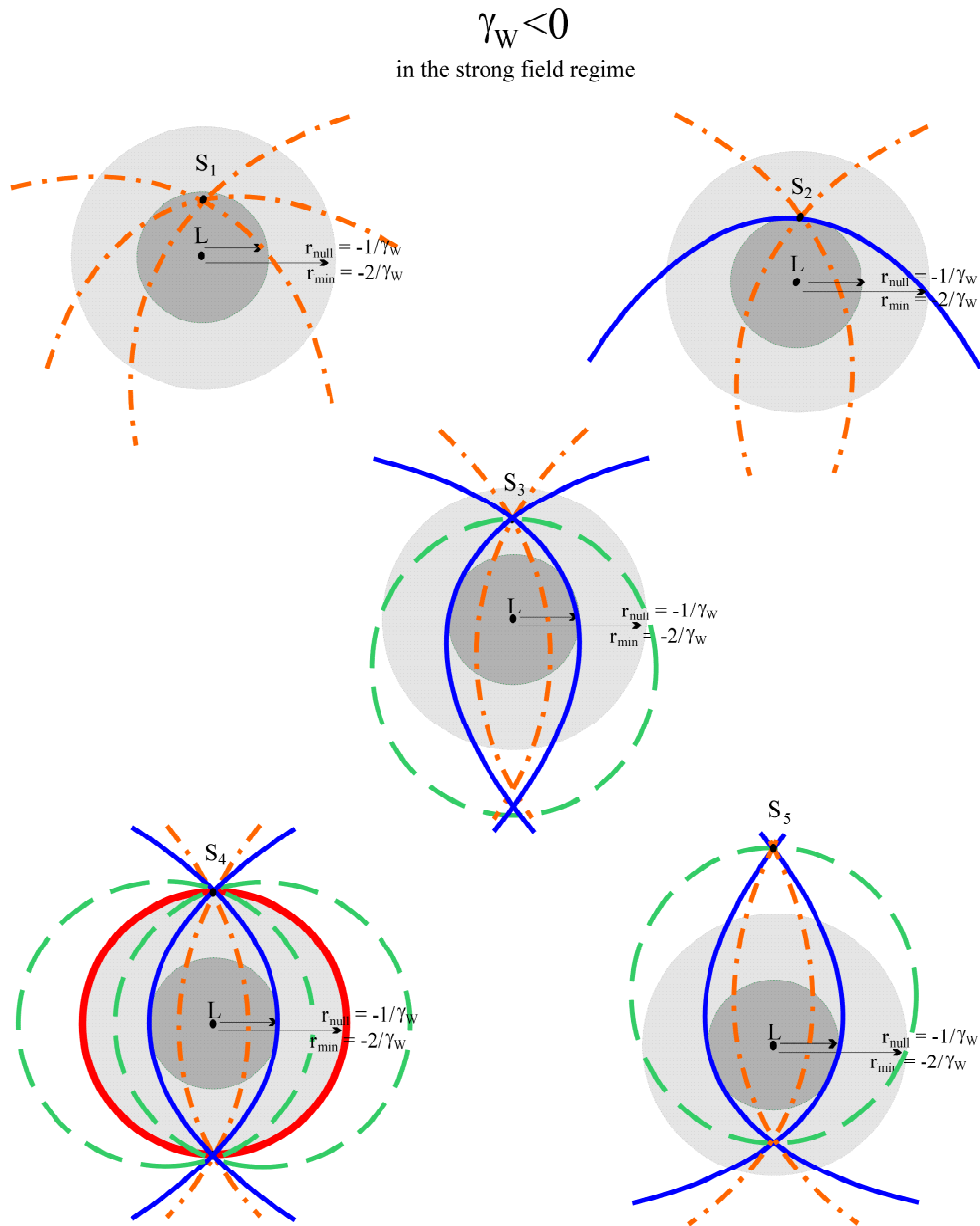


Fig. 5.7 In the strong field regime, for a light source, (S_1) located inside the sphere of radius r_{null} , the closest approach distance of any photon originating from the source is necessarily smaller than r_{null} . This means that all these photons have unbound orbits: hyperbolas centered on L.

When the source (S_2) is on the sphere of radius r_{null} , the closest approach distance of its photons can be either smaller or equal to r_{null} , which means that all the orbits are again unbound: hyperbolas or a parabola.

Whereas for a source (S_3) located in between the two spheres of radius r_{null} and r_{min} , there are additionally photons originating from this source that have a closest approach distance to the lens larger than r_{null} . Accordingly, those photons are captured on elliptic orbits. The particular case of a source (S_4) situated on the sphere of radius r_{min} allows all four types of orbits: hyperbolic, parabolic, circular and elliptic. The photon trajectories will be again hyperbolic, parabolic or elliptic for a source (S_5) outside the larger sphere of radius r_{min} .

5.4 Summary of the main results of this chapter

5.4.1 TS theories

Predictions of TS theories on microlensing and gravitational lensing only differ from GR by a scale factor, $g(\varpi) = 1/(1 + \alpha_{TS0}^2)$. This scale factor, already constrained to be very close to 1 (5.13), corresponds to a redefinition of the gravitational “constant” (1.14). However, seeing that only the quantity GM is meaningful for physical measurements, one can alternatively absorb this factor in a redefinition of the mass. Hence, TS theories are difficult to differentiate from GR, because this requires quantitative measurements, and usually the characteristics of the O-L-S system (M_{lens} , D_{ol} , D_{ls} ...) are not known with sufficient precision; those parameters are even inferred assuming GR.

5.4.2 MTS/SITS theories

Speaking in terms of projections onto the celestial sphere, we have seen that MTS/SITS theories can predict the extinction of a microlensed light source *if* the source passes within a certain region centered on the lens, *and if* Υ is smaller than the value $\Upsilon_{special}$ corresponding to the microlensing event.

Also, *some values of the parameter* Υ lead to predictions regarding gravitational mirages that are qualitatively different from the GR ones. Namely: no or two concentric rings, up to four colinear images for a point mass lens, etc. This is due to the fact that, for those specific values of Υ , the effective potential for photons has a totally different shape than the usual Schwarzschild black hole one. The second order contribution in MTS/SITS theories can lead to a negative deflection angle: the effective potential is not always attractive and can also be repulsive for small angles at a given value of Υ (see Section 4.3.1.2).

Nevertheless, as the alignment configuration is highly improbable, one should not hope to test those theories by counting the number of concentric rings seen (0, 1 or 2). Moreover, the detection of rings⁴² in the radio waveband, like 0218+357, MG 1131+0456, MG 1549+3047, MG 1654+1346, PKS 1830+211, or even in the optical waveband, like 0047-2808, does not allow us to exclude ranges of the parameter Υ smaller than $\Upsilon_{special}$ for this type of lens model. Indeed, those observed gravitational mirages correspond to extended light sources and lenses, leading to thick rings.

We have seen that, unless Υ is small (smaller than the critical value of 1/4, but yet larger than $\Upsilon_{special}$), it might also be difficult to test MTS/SITS theories according to the number of colinear images seen (2, 3 or 4). If we recall the present resolution of Earth-based instruments ($\sim 1/100$ arcsec in the optical and $\sim 1/1000$ in the radio waveband), we might say that the radio waveband seems more appropriate to detect the possible presence of inner images.

Being more optimistic, we have shown that the study of the image parity carries many promises if the lens position is known (not inferred from GR). Two images of even parities detected, aligned with the lens and the source, for a symmetric point-mass lens model, would rule out General Relativity, but would invite to consider theories like MTS or SITS.

In conclusion, unlike what was said for TS theories, gravitational mirages can be good qualitative tests of MTS/SITS theories for $\Upsilon < 1/4$, even if the mass and distances in the O-L-S system are not known independently with sufficient precision. However, for $\Upsilon > 1/4$, the gravitational mirages are not appropriate tests because they lead solely to slight quantitative deviations from GR. For the same reason, we argued in Paragraph 5.3.3.1 that microlensing events are not interesting either, for a value of the free parameter of the theory larger than $\Upsilon_{special}$.

5.4.3 The Weyl theory

In the Weyl theory, we considered, when applicable, the weak field approximation to study microlensing and gravitational mirages. The strong field limit was found to be useless for our purposes.

For a negative γ_W , the condition for unbound photon orbits derived in Chapter 4 and the existence of gravitational mirages were used to improve the constraints obtained from solar system data on the γ_W -parameter. The upper bound on the absolute value of γ_W was accordingly lowered to about 10^{-31} m^{-1} (see (5.33) and (5.35)).

Contrary to TS theories, the characteristics of the microlensing curve in the Weyl theory cannot, by a simple rescaling

⁴² See reference [4] for the properties of the O-L-S systems and a complete bibliography.

of the mass or the ring radius, be recast into GR predictions. However, the corrective factor, function of γ_W and the O-L-S distances, is small. Indeed, it is equal to 1 when γ_W is equal to zero (GR), and to $\sim 1 + 10^{-11}$ for our upper bound on $|\gamma_W|$ (5.39). This means that it might effectively be negligible. This point requires further study.

In the Mannheim-Kazanas theory ($\gamma_W \simeq 10^{-26} \text{ m}^{-1} > 0$), gravitational mirages do not seem to be an appropriate test. Indeed, the predictions will be the same as the general relativistic ones, from the point of view of the number of images and of their parity. One can just say that the Mannheim-Kazanas gravity needs even more dark matter than GR, because the Weyl radius is smaller than the Einstein ring.

In microlensing, the interesting closest approach distance separating the convergent from the divergent contributions (r_{00}) is cosmological in the Mannheim-Kazanas theory, and thus irrelevant. Moreover, the smallness of the corrective factor (5.41) showed that one cannot distinguish between General Relativity and the Mannheim-Kazanas theory from the point of view of microlensing, either.

In this chapter, we also commented on the concept of distance that needs to be defined coherently in the Weyl theory. We then concluded by a few amazing features of the strict strong field regime.

Conclusions and perspectives

The purpose of this work was to study the possibility of constraining typical alternative theories of gravitation using the light deflection tests. Throughout, we emphasized the key role played by the Post-Newtonian parameter γ , present at the first order in light deflection ($\propto (\alpha + \gamma)$ with $\alpha = 1$ in Metric theories). We also analyzed the contribution of Post-Post-Newtonian terms, the contributions due to the quadrupole moment and angular momentum of the gravitational deflector, or finite distance effects. In addition, we briefly cited corrections due to the refraction from the solar corona or the Earth ionosphere, parallactic displacements, aberration, and the motion of the source or the lens. We furthermore tried to add some perspective by referring to some past, present or future experiments. However, this work is not intended directly for measurements, as our simulations are very rough and based solely on a simple point-mass model for microlensing events or gravitational mirages. The aim here was to provide some insight about the peculiar features of some theories; hopefully, in some cases, orders of magnitude; or to motivate a systematic and self consistent analysis of light deflection in the setting of an alternative theory.

We have seen that the change in the apparent position of a light source, that allows to test a relativistic theory on solar system mass and distance scales; the microlensing events at galactic distances; or gravitational mirages requiring galactic to cluster masses on extra-galactic distances; are not all on an equal footing for our purposes. Certain light deflection events are more appropriate than some others to test a particular theory, or even a particular range of the free parameter of the theory.

We now summarize the main results obtained in this thesis, concerning the predictions of Tensor Scalar (TS), Minimal Tensor Scalar (MTS), Scale Invariant Tensor Scalar (SITS), Large Extra-Dimension (LED) theories and the Weyl (W) gravity respectively.

1 TS theories

In Tensor Scalar theories, the key parameter, when discussing light deflection, is the present value of the scalar coupling to matter, α_{TS0} , function of the Post-Newtonian parameter γ .

Brans-Dicke (BD) theories correspond to constant values of the scalar coupling, with the particular case of a null coupling for General Relativity and a coupling equal to one in String theories.

We noted that **the TS geodesic light potential, at first order**, is analogous to the GR one. The Newtonian constant G_N is replaced by $G = 1/(1 + \alpha_{TS0}^2) \cdot G_N$. So light deflection always takes place, provided a minimum closest approach distance (or impact parameter) is verified, so to avoid the capture by a black hole.

Let us first consider the change in apparent position of a light source. **Light deflection experiments in the vicinity of the Sun** (VLBI experiments) and the fact that $1 - \gamma$ is always positive for TS theories, allow to constrain the scalar coupling to a maximum value: $\alpha_{TS0}^2 \lesssim 0.0011$ or 0.0002 . It corresponds to the measured maximum deviation of $1 - \gamma$ from zero. In fact VLBI data so far dominate constraints on the scalar coupling, and for positive values of its derivative, solar system tests are still more efficient than pulsar data (see Figure 4.1). Remember that all the physical measurements are blind to the sign of α_{TS0} .

From a theoretical point of view, we have considered a cosmological evolutionary model for TS theories to provide an estimation of today's value of the parameter $\gamma(\alpha_{TS0})$.

The advantage of this proposed model, which admits General Relativity as an attractor, is that it is exact, analytical, simple and natural. In fact it constitutes a class of solutions with respect to a free parameter. The value of this integration constant fixes the initial conditions of the model at the beginning of the dust era, when the scalar field starts

to be coupled to matter (during the radiation era, it is totally decoupled) and to roll down the potential. Thus, it fixes the dust-era starting point on the potential curve. Moreover, in the weak scalar-field limit, we recover Damour *et al.*'s quadratic potential well. The corresponding curvature, which is independent of our integration constant, is that of a non-oscillatory solution. However, like Damour *et al.*'s model, our class of solutions is restricted to a negative Post-Newtonian deviation $1 - \beta$, because the derivative of the scalar coupling with respect to the scalar field is necessarily positive in such models.

An additional advantage of this exact model, is that the expressions for the scalar field and its coupling at a given time (α_{TS}) do not depend on the type of matter dominating the universe. This means that we do not have to consider successive cosmological phases of different particles decoupling from the radiation, to study the evolution of the coupling. On the contrary, Damour and Nordvedt's solution requires extensive discussions on the subject and the predictions of their model are sensitive to those. Furthermore, we have shown that this model is on an equal footing with General Relativity regarding the constraint of an accelerating universe (SNIa): it needs the contribution of a cosmological constant in the same quantitative way as General Relativity does. However, the addition of a cosmological-constant contribution to this model will not influence the order of magnitude of the $1 - \gamma$ deviation from zero. It is in the most optimistic case of our model very small ($\sim 10^{-7} - 10^{-8}$), and virtually not measurable by present and future satellite experiments like GAIA (with a rough estimated precision on γ of $5 \cdot 10^{-7}$), SIM, ect. On the contrary, we have seen that the predictions on γ appear to be very dependent on the cosmological evolutionary model adopted. Too optimistic estimations of $1 - \gamma \sim 10^{-5}$ have been reached with some of Damour *et al.*'s models. If Nature favors this last type of models, such a deviation could be measurable even in a near future with the Cassini mission, Gravity Probe B, etc. (see Appendix B).

Nevertheless, future experiments would constitute an astonishing improvement on the experimental value of $\alpha_{TS 0}$, and are in any way an interesting check of General Relativity corresponding to a null coupling. Moreover, any experiment improving the present limits on the Post-Newtonian parameter β , contributing to the second order in light deflection, would also help to constrain the curvature of the cosmological evolutionary potential (near its minimum) chosen for the model.

In a more general framework, we confirm Bekenstein's statement [23] that light deflection predictions for such theories can never exceed those given by General Relativity. The angular displacement will always be smaller, and the angular separation between two arclets as well as the radius of the "Einstein" ring are decreasing functions of the parameter $\alpha_{TS 0}^2$.

TS theories can thus never offer an alternative to dark matter.

As far as **lensing** is concerned, at first order, the number of images predicted by TS theories is the same as that predicted by General Relativity. Indeed, the weak field asymptotic deflection angle at first order is analogous to the GR one owing to a scale factor, $1/(1 + \alpha_{TS 0}^2)$. This factor corresponds to a rescaling of the Newtonian constant. When the mass distribution is unknown, the factor can be absorbed in a redefinition of the mass to fit the general relativistic predictions. Indeed, experiments are truly sensitive to the product GM , and not to those quantities taken separately! The various models of gravitational mirages (whichever the mass distribution of the deflector, be it a black hole, an SIS type of distribution, an infinite/truncated homogeneous plane, a spiral galaxy...) will not allow us to distinguish between General Relativity and Tensor Scalar theories for a scalar coupling $\alpha_{TS 0}^2 \leq \alpha_{TS 0 \text{ exp}}^2$. The only way out would be an O-L-S system for which the total gravitational mass could be determined independently (like for a binary system...) with an *extremely* good precision according to the present allowed range for $1/(1 + \alpha_{TS 0}^2)$.

This argument is valid also for **microlensing** events, in which crucial scales can be redefined to absorb the factor $1/(1 + \alpha_{TS 0}^2)$ characteristic of TS theories. This also means no longer referring all our distance scales to the radius of the Einstein ring (inherited from General Relativity) but to the radius of the TS ring, which is the Einstein ring radius multiplied by the factor $1/\sqrt{1 + \alpha_{TS 0}^2}$.

2 MTS/SITS theories

In MTS and SITS theories, which share the same predictions regarding photon trajectories, the key Post-Newtonian parameter γ , encoding light deflection predictions at first order, is equal to its general relativistic value of one. This means that one needs to look at the specific combination of the (Post-)Post-Newtonian parameters (γ , β , and δ), that appears in photon geodesics at the second order (see Table (4.1)). This latter expression can be rewritten in terms of the single parameter, Υ , of the MTS-SIST theories. Our study of light deflection, in those theories, was thus centered on Υ , in the allowed range $]0, 1 \equiv \Upsilon_{GR}]$. We have seen how the shape of **the effective geodesic light potential** depends on the value of this free parameter. Indeed, for $\Upsilon \in]0.5 \equiv \Upsilon_{transition}, 1 \equiv \Upsilon_{GR}]$, we could already see, when looking at this potential, that the predictions regarding light deflection would be qualitatively the same as those of GR: the potential is analogous to a Schwarzschild black hole with its corresponding critical closest approach distance (4.16). However, for $\Upsilon \in]0, 0.5 \equiv \Upsilon_{transition}]$, there is no black hole, but a potential wall.

Moreover, **in a more general framework**, for $\Upsilon < \Upsilon_{critical}$, with $\Upsilon_{critical} \equiv 1/4$ correctly identified, light deflection is allowed to be divergent if the incidence angle is below a specific value, ϑ_{I0} . This is a new feature in comparison with GR.

Whichever the value of the free parameter of the theory is, the bending angle in MTS/SITS theories will always be smaller than the general relativistic prediction, for a given value of the incidence angle. Hence those theories offer no alternative to dark matter.

From the point of view of **solar system light deflection experiments**, the free parameter Υ should be very easy to constrain *if* the second order could be measured. However, the second order effect in the solar system is maximal for the Sun at grazing incidence, and it is then only a contribution of the order of the microarcsecond; while it is negligible for any planet and for non-grazing solar incidence. In fact, it is still just above (equal to) one microarcsecond at an angle smaller than (equal to) about $51.8' - 53.6'$ from the Sun. Unfortunately, the future astrometric satellite experiments aiming at microarcsecond precision have a non null avoidance angle towards the Sun of the order of $35^\circ - 45^\circ$. One will thus have to wait for dedicated experiments allowing (near) grazing incidence.

As far as **microlensing** is concerned, an angle ϑ_{I0} of the order of the milliarcsecond relevant to microlensing events would require a very strong scalar contribution to the MTS/SITS theories ($\Upsilon \sim 10^{-5} - 10^{-6}$ for $\vartheta_{I0} \sim 10^{-4} - 10^{-2}$ arcsec), thus far from $\Upsilon_{GR} = 1$. We have seen that such very small values of the MTS/SITS parameter, $\Upsilon < \Upsilon_{special}$, do not allow for the formation of Einstein rings for a point-mass lens model. This may lead to an extinction of the microlensed light source.

When $\Upsilon > \Upsilon_{special}$, the corresponding ϑ_{I0} is too small to be effective for microlensing events, and light deflection is always convergent. This means that microlensing events do not constitute a qualitative test of MTS/SITS theories in this case, as deviations from GR predictions will only be quantitative. Hence, knowing the numerous unknown in the O-L-S system, plus the fact that the deviation from GR is only a second order effect, already on the edge of detection in solar system light deflection experiments, we conclude that microlenses are irrelevant to test MTS/SITS theories when Υ is larger than $\Upsilon_{special}$.

From the point of view of **gravitational mirages**, the range $]0, \Upsilon_{special}]$ (note that $\Upsilon_{special}$ is a function of the O-L-S mass and distance scales) does not allow for the formation of rings in the framework of our model (point-like sources and lenses leading to thin rings). However, the observation of rings in the radio and in the optical wavebands does not allow us to exclude the corresponding ranges of the parameter Υ . Indeed, those observed mirages correspond to extended light sources and lenses, leading to thick rings.

For $\Upsilon \in]\Upsilon_{special}, 1/4 \equiv \Upsilon_{critical}]$, MTS/SITS theories also offer a whole set of predictions which are qualitatively different from those of General Relativity. For a singular black hole lens model, they predict the formation of up to four colinear images (or two concentric Einstein rings in case of alignment); which if observed, could not be explained by General Relativity. Three images can even be formed, while General Relativity provides a maximum of two images for this same lens model.

Most interesting is the predicted parity of the images which differs from the general relativistic prediction. This should allow to test the whole range $]0, 1/4 \equiv \Upsilon_{critical}]$ if the lens position is known (see Tables (5.23), (5.24), and (5.25)). Indeed, MTS-SIST theories do predict two images on the same side of the light source. Interestingly, the discussion made in this thesis with a black hole lens can be easily extended to other lens models like a galaxy, a SIS or more complicated models, as it was sketched in some of our previous work [108].

Nevertheless, as we explained in Paragraph 5.3.3.3, the additional inner images lie close to the deflector for a given position of the source and are less amplified in comparison with the outer images (that lie close to the image positions predicted by General Relativity). This might render the observation of such qualitative original predictions a bit complicated... and one could erroneously conclude to observe the general relativistic predictions.

Finally, the range $]1/4 \equiv \Upsilon_{critical}, 1 \equiv \Upsilon_{GR}]$ allows only for predictions which are quantitatively different from General Relativity and those unfortunately can only be checked if the O-L-S configuration and mass of the deflector are known precisely.

3 LED theories

Large Extra-Dimension theories, with a number of extra-dimensions $d \geq 2$ and a mass scale M_s , do not admit a (Post-)Post-Newtonian expansion, because they originate from a $(4 + d)$ -metric. However, the linearized massless zero-mode action can be related to the Brans-Dicke one, with a scalar coupling to matter $\alpha_{LED}^2 = d/(d + 2)$. General Relativity thus corresponds to $d = 0$ and String theories to $d = +\infty$.

Light deflection experiments in the neighborhood of the Sun are hence sufficient to disqualify LED theories in their original formulation, as $1 - \gamma = d/(d + 1)$. Indeed, the predicted coupling, α_{LED} , is much too strong. Such a conclusion could also be obtained thanks to simple considerations on the 4-dimensional field content of the gravitational sector, through a decomposition of the $(4 + d)$ -graviton propagator.

Not only the light deflection angle, but also the Weak Equivalence Principle is strongly violated. Indeed, those theories are non-Metric. This problem has been solved in the literature by providing a mass to the zero-mode scalar field, through some (still obscure) mechanism, or by quantum corrections to produce an acceptable effective coupling.

When a mass is acquired by the zero-mode scalar field, the coupling is minimal ($G = G_N$) and only massive spin-2 states contribute, in addition to the usual graviton, in such a way to increase the light deflection angle. This means that LED theories could constitute an alternative to a too large amount of dark matter in gravitational mirages. The deviation from General Relativity (formally $|1 - \gamma|$) depends on the observation angle with respect to the deflector. It reaches its maximum at grazing incidence and vanishes faster, as we observe at larger angles from the deflector, than solar coronal diffraction. Moreover, for a given deflector, massive modes have a signature which is not only dependent on the number of extra-dimensions, decreasing with d ; but it also exhibits a strong quadratic dependence on the energy of the incident photon, *i.e.* on the frequency at which the observation is made. This, conversely to coronal deflection effects which are proportional to the inverse of the squared frequency. According to those characteristics, if we wish to coherently test LED theories with light deflection observations, we should not use experimental data obtained at various angles, or at too large angles from the deflector and then extrapolated at grazing incidence; nor should we use experimental estimates of $1 - \gamma$ that are averaged over very different frequencies.

Another important characteristic of LED light deflection predictions is that the deviation from General Relativity is a function of the deflector mass and distance.

We have seen that from the point of view of solar grazing incidence predictions, LED theories are safe in the radio-waveband, for the mass scale of about $3 \text{ TeV}/c^2$ favored by collider physics. However, already in the visible-band, for $d = 2$, those theories strongly disagree with observations for such a low mass scale. To agree with observations in the visible at grazing incidence, $1 - \gamma|_{\text{exp}} = 0.5 \pm 0.11$ [71], the lower bound on the mass scale must be of the order of $28 \text{ TeV}/c^2$ for $d = 2$ and of the order of $9.5 (2/(d - 2))^{1/4} \text{ TeV}/c^2$ for $d > 2$. Increasing the precision of solar grazing experiments in the visible *at a fixed frequency* would push further the constraints on the mass scale of the theory or on the allowed number of extra-dimensions, as shown in simulation (4.10).

Also, solar grazing observations at a fixed frequency in higher energy wavebands would help to constrain LED theories. For example, a measurement showing no deviation from General Relativity within ten percent, at a ultra-violet frequency of $5 \cdot 10^{15} \text{ Hz}$, would constrain the lower bound on the mass scale to about $78 \text{ TeV}/c^2$ for $d = 2$ and to about $30 (2/(d - 2))^{1/4} \text{ TeV}/c^2$ for $d > 2$. The constraints are even more stringent for gamma rays at grazing incidence, but at such frequency we are beyond the limit of the approximation used to obtain the weak field light deflection angle.

Nevertheless, the constraints on LED theories and the predicted deviation quickly weaken if we consider solar non-

grazing incidence. Simulation (4.12) shows the constraints on the mass scale and the number of extra-dimensions in the visible waveband *if* a given observed deviation $1 - \gamma|_{\text{exp}}$ is achieved.

Concerning future experiments, we see that dedicated precision experiments measuring the light deflection angle at and above the optical waveband frequency would be welcome. Of course, to avoid atmospheric absorption at such frequencies, those have to be satellite missions. We know that (non-dedicated) astrometric satellites like GAIA will only observe at large angles from the Sun (beyond 35° for GAIA) where the LED corrections to General Relativity are weaker. However, the GAIA survey will be made from UV blue to far red (close to one micron) in order to allow the classification of stars. The upper energy range might be useful to test LED theories, indeed, at 35° , the predicted deviation from General Relativity in the visible and UV range might be within the reach of GAIA's precision aiming at $5 \cdot 10^{-7}$ on $1 - \gamma$.

4 The Weyl theory

The Weyl gravity does not admit a Post-Newtonian parameterization, because the corresponding gravitational potential holds terms that are linear and quadratic in the radial distance. However, the quadratic term does not contribute to photon trajectories. Hence, the parameter γ_W , corresponding to the linear contribution, is the crucial parameter in our discussion. Of course, in General Relativity, $\gamma_W = 0$.

It is in the Weyl theory, that the study of **the effective geodesic light potential** leads to the most interesting informations. Indeed, it shows the richness of the case $\gamma_W < 0$ in comparison with the case $\gamma_W > 0$. The latter only allows unbound orbits (light deflection) for closest approach distances larger than the critical value imposed by the Schwarzschild black hole seen at short distances. On the contrary, for $\gamma_W < 0$, the light geodesic potential provides the key distance, r_{null} (4.26), to separate unbound from bound orbits permitted in this case; as well as the minimum radius corresponding to a circular orbit (4.22).

All our study of the Weyl theory was articulated coherently around those key distances.

In addition, a comparison between the geodesic potential for light and that of massive particles enlightened us as to the opposite effect of the linear term in the Weyl potential on massive particles in comparison with massless or sufficiently relativistic particles. We showed also that massive geodesics, unlike photon trajectories, need the conformal factor in the metric (1.51) to be specified. Only a coherent study of the conformal symmetry breaking mechanism, through the coupling of Weyl gravity to matter fields, would allow to specify the physical conformal factor. We reminded the reader that the Mannheim-Kazanas parametrization of the rotation curves rests on the (arbitrary) choice of a constant conformal factor (we called it the Mannheim-Kazanas theory).

The study of light deflection is interesting as it is free from such considerations.

In a general framework, analyzing the expression for the asymptotic deflection angle in the Weyl theory, it was found to allow for a diverging effect at closest approach distances larger than r_{00} (4.28), function of the mass of the lens, *if* γ_W is positive. However, the convergent to divergent transition is not explicitly relevant to solar system experiments.

The case of a *negative* γ_W is always convergent, whichever the distances and the mass of the deflector are. It also predicts a larger deflection than General Relativity. A negative parameter might thus be an alternative to a too large amount of dark matter.

After deriving the expression for the light deflection angle, we then investigated in details the asymptotic behavior of light geodesics. The conformal transformations to asymptotic flat space were provided.

We also distinguished between a weak field approximation (1.54), originally introduced for computing the light deflection angle, and a strong field approximation (4.30), later introduced to study the asymptotic behavior of the Weyl space-time.

We noticed that the limiting minimum strong field radius is of the same order of magnitude as r_{00} . Hence, in the strong field regime, light deflection is always divergent for a positive γ_W . Also, the limiting maximum weak field radius corresponds to r_{null} , and thus, light deflection is always possible for a negative γ_W , when working in the weak field regime. However, the maximum weak field radius unfortunately also corresponds to the distance at which the Weyl theory becomes essentially different from General Relativity.

We reminded the reader too that, to be coherent, the weak (or alternatively strong) field limit on the radial distance, measured from the gravitational deflector, has to be verified on the photon path, all the way from the light source to the observer. Thus, the limit does not only apply to the distance from the lens to the observer, to the distance from the lens to the source, but also to the closest approach distance of the photon onto the lens.

The strong field limit is unfortunately of no use to constrain γ_W , because we only have in hand an upper bound on $|\gamma_W|$. Remember that the lower bound is given by General Relativity ($\gamma_W = 0$) and it leads to a strong field limit only valid at infinity.

In the very last section of this work though, we illustrated a few amazing features of this strong field regime.

Yet at the end of the last chapter, we made a general, but crucial, comment about the concept of distance in the Weyl theory. We recalled that in the framework of General Relativity, it is the Robertson-Walker metric, solution to the Einstein equations in presence of matter, which is used to infer the concept of cosmological distance as a function of the redshift, the matter density and the curvature of the universe. However, in the Weyl theory, the Robertson-Walker metric is *not* a solution of the Bach equations with matter. Hence, the general relativistic expression for the distance cannot be used in the Weyl gravity!

Here, we would like to recall that the concept of distance in the Weyl theory (as well as that of time) requires the specification of the conformal factor: our universe contains matter and thus conformal invariance is broken. This conformal factor is crucial in cosmology in order to obtain the appropriate Weyl prescription relating the observed redshift to the cosmological distances. Otherwise, one can only work in terms of distance ratios (or time ratios, or the mixed time to distance ratios) and angles.

Coming back to the more specific tests of light deflection, we saw that, **in the neighborhood of the Sun**, they gave us strong constraints on the parameter of the theory as listed in (4.40), with an upper bound on $|\gamma_W|$ around 10^{-18} m^{-1} . Nevertheless, they did not help us to settle its sign. Even though the bounds so obtained on γ_W are conservative in comparison with Mannheim's estimated value of $\gamma_W \sim +10^{-26} \text{ m}^{-1}$, they are preferable because they are not biased by any arbitrary assumption on the conformal factor. We noted too that the particular value of Mannheim and Kazanas belongs to the allowed range that we derived.

For a negative γ_W , the existence of **gravitational mirages** with an Einstein angle of a few arcseconds allowed us to put a stronger upper bound on the absolute value of the Weyl parameter, around 10^{-31} m^{-1} . Indeed, the existence of gravitational mirages means the possibility for light deflection to take place, and hence a constraint on $r_{null}(\gamma_W)$. When we analyzed *The Mannheim-Kazanas theory* ($\gamma_W > 0$) regarding gravitational mirages, we saw that the divergent regime can become significative for massive lenses. Unfortunately, the predictions of the Mannheim-Kazanas theory will be the same as the general relativistic ones from the point of view of the number of images and of their parity. This seems to prevent this theory to be tested using gravitational mirages. Indeed, one can just say that the Mannheim-Kazanas gravity even needs more dark matter than General Relativity, because the Weyl radius is smaller than the Einstein ring. Furthermore, there is the problem of the unknown mass and distances involved, and the fact that one cannot observe the difference between a photon received from a divergent or a convergent path.

For $\gamma_W < 0$, we used the weak field limit to show that, contrary to Brans-Dicke and Tensor Scalar theories, the characteristics of the **microlensing curve** in the Weyl theory cannot, by a simple rescaling of the mass or the ring radius, be recast into the general relativistic predictions. There exists a corrective factor depending not only on the parameter γ_W of the theory, but also on the characteristic distances of the O-L-S system. Consequently, the width of the images (or the ring) will be larger in the Weyl theory than in General Relativity, and hence the total amplification too. This corrective factor, between 1 (GR) and around $1 + 10^{-11}$, might be very small (even irrelevant) for microlensing events if $|\gamma_W|$ happens to be much smaller than our present upper bound. Regarding the optical depth of microlensing events, unfortunately, even for the upper bound on $|\gamma_W|$, the correction is irrelevant with respect to the observational errors. We then investigated the possibility to test, in the weak field limit, *the Mannheim-Kazanas theory* ($\gamma_W > 0$). It appears that as far as microlensing is concerned, the interesting closest approach distance r_{00} is cosmological and thus irrelevant. Consequently, light deflection is always convergent on the microlensing scales, which means no qualitative deviations from General Relativity. Moreover, an estimation of the order of magnitude of the corrective factor showed us that one cannot distinguish between General Relativity and the Mannheim-Kazanas theory from the microlensing point of view.

5 General

We have seen that **the Sun is still a privileged laboratory for constraining the (Post-)Post-Newtonian parameters of a theory through angular deflection measurements. Indeed, it is the best-known and contributes to the largest deflection.**

Solar system tests are more appropriate for theories leading to a deviation from General Relativity at first order, like Tensor Scalar theories. However, remember that, if experimental precision is increasing, one has to consider additional gravitational effects (quadrupole, angular-momentum contributions) and many parasitic effects which complicates the determination of PN parameters (and especially of Post-PN parameters at the second order).

When considering microlensing or gravitational mirages, whichever of the theories we consider, we face the problem of the determination of masses and distances involved in the O-L-S system. Indeed, the lens position is not always detected, and most of the time, its redshift and mass are not known. In fact, lensing is presently used as a way to evaluate the total mass of the lens (luminous and non luminous, meaning detected and ad-hoc dark matter), assuming the theory of General Relativity is verified. This is why we say that **when looking at experiments outside our solar system, it is only predictions qualitatively different from the general relativistic ones which can help us exclude some range of the free parameter(s) of an alternative theory, according to some level of confidence (number of observations...); or theories leading to statistically different distributions of gravitational mirages or microlensing events, which should be tested.** From that point of view, we are lucky that the sample of microlensing/gravitational mirages is rapidly enlarging.

Remark that if, in a microlensing event, the lensing star is observed so that its spectral type can be measured, the estimate we get on the mass might not be precise enough (presently within 10% at the best) to fix the scale factor $1/(1 + \alpha_{TS}^2)$ in TS theories .

Additionally, if for microlensing events, the cosmological geometry can reasonably be assumed to be flat to evaluate the distances from the redshifts, for gravitational mirages, on the contrary, the angular diameter distances involved have to be evaluated consistently in the framework of the alternative theory (in terms of the Hubble constant, the cosmological deceleration parameter, the cosmological curvature, and the free parameter(s) of the theory). In this case, it might not be appropriate to assume an Euclidean geometry. In 1972, Weinberg [140] provided us with the corresponding formula valid only in the framework of General Relativity. Too often, in tests of alternative theories of gravitation, General Relativity is implicitly used to evaluate quantities indirectly observed. The corresponding **formula giving the angular diameter distance in terms of the redshift (plus the Hubble constant, the cosmological deceleration parameter and curvature, together with the free parameter(s)) appropriate for the alternative theory being tested has to be used.**

It also needs to be reminded that astrophysicists are confronted with the maximum resolution of their instruments, so that an additional image (remember the example of MTS/SITS theories) predicted by an alternative theory of gravitation might not be observed (because too faint or not resolved from the other images, from the lens), even if it is indeed present and even though gravitational mirages constitute in this case a qualitative deviation from General Relativity.

6 Perspectives

Some alternative theories of gravitation lead to lens equations or deflection angle functions that are analytically difficult to solve (see for example the exact expression for the light deflection angle in MTS/SITS theories). **It might be interesting to use topological arguments, Morse theory or critical points of the functional to extract some relevant information from the exact expression.** Consult references [90, 99, 100, 101, 102] for this formalism.

In this work, we looked at gravitational weak field deflection. **It might be interesting to consider, at least from a theoretical point of view, the strong field predictions.** For such a task, the PPN formalism is not appropriate (remember that it is not suited for describing the emission/detection of gravitational waves, either).

One could think of investigating strong field deflection in Tensor Scalar theories with a formalism similar to that used by Damour [34], who replace G by an effective body dependent gravitational “constant” G_{AB} , γ by γ_{AB} , etc. There is also an interesting remark to make at this point about TS theories. Weak field predictions are all proportional to

α_{TS0}^2 and thus deviations from General Relativity should be weak, as cosmological evolutionary models predict a weak present scalar coupling α_{TS0}^2 . However, it has been shown by Damour and Esposito-Farèse [37, 39] that, on the contrary, strong field deviations from General Relativity do not tend to zero with the scalar coupling *if* α'_{TS0} , the present value of the scalar coupling derivative with respect to the scalar field, is sufficiently negative. Unfortunately, the class of exact analytical cosmological solutions presented in this thesis is restricted to positive values of α'_{TS0} . This means that strong fields predictions for such models should be small too.

In the case of the Weyl theory, we know that the gravitational field can be strong at large distances, and we have already given the exact expression (4.36) for the asymptotic deflection angle in that case. It would be interesting though, to study the intermediate regime to the weak field and the strong field approximations that we introduced. Some numerical study of the image diagrams and of the light deflection angle might be useful. Concerning strong gravitational fields at short distances, like that due to a black hole, the metric can be considered to be that of Schwarzschild/GR, for which we have an analytical strong field approximation, (3.19).

Concerning the exact TS analytical attractor mechanism to General Relativity in a flat universe, the analysis could be pushed a bit further. One could study for example the influence of non flat geometry, or consider the addition of a scalar-field quintessence potential (2.7) as an alternative to the cosmological constant.

However, what seems the most promising is to apply Chiba's analysis to our model; namely to translate the Cosmic Microwave Background data provided by the space mission COBE into constraints on the TS parameters [31]. This method used by Chiba and his collaborator in the case of Damour *et al.*'s cosmological model seems to be very efficient to shrink the α_{TS0} -dimension in the allowed parameter space (compare Figure 4.1 with Figure 4.2). It would be interesting to analyze the imprint of Tensor Scalar cosmological evolution on the density perturbations in inflationary cosmology, and to see whether CMB constraints strongly depend on the cosmological model or not. Indeed, we have seen that the attractor mechanism can be very efficient, so that the departure from General Relativity in present solar system tests is really weak; but the Cosmic Microwave Background data might be able to probe the cosmological models at a time at which they were very different from General Relativity and from one another.

The work done with a rough point mass model could also be refined. A realistic statistical study of existing gravitational mirage observations to further constrain, for example, the upper bound of a negative Weyl parameter (see equations (5.33) and (5.35)), or the interesting MTS/SITS range $]\Upsilon_{special}, 1/4 \equiv \Upsilon_{critical}]$, with $\Upsilon_{special}$ depending on the lensing system, should be carried out.

In this work, we did not investigate the **weak lensing phenomenon**. Early measurements of the galaxy-galaxy lensing signal were limited by the small amount of lenses/sources. However, with the advent of panoramic cameras on 4 m telescopes, measurements of weak lensing by galaxies has become feasible. The simplest approach to this phenomenon is to measure the ensemble averaged tangential distortion as a function of the radius around the sample of lenses. This provides interesting constraints on the shape and size of dark matter halos, because it probes the gravitational potential on large scales. One can also think to use such measurements to test alternative theories of gravitation (without dark matter). According to a recent reference [67], the best constraint comes from the anisotropy of the lensing signal around lens galaxies, suggesting that the dark matter halos are flattened. The authors of reference [67] applied a maximum likelihood analysis, using point model lenses (because they assumed no dark matter), to the MOND theory (Modified Newtonian Dynamics). They were able to exclude it with 99% confidence. However, the MOND theory is not a relativistic theory of gravitation. One could recycle the idea though, to test interesting relativistic theories like for example the Weyl theory, which, we recall, introduces interesting corrections to General Relativity on galactic distances.

Finally, there are still **many other alternative** theories, the predictions of which, in the field of light deflection, could be investigated: like fractal universes, variable dimension universes [89], etc.

Bibliography

- [1] DIVA homepage. <http://www.ari.uni-heidelberg.de/diva>.
- [2] FAME homepage. <http://www.usno.navy.mil/FAME/>.
- [3] GAIA homepage. <http://astro.estec.esa.nl/SA-general/Projects/GAIA/gaia.html>.
- [4] Gravitational lensing: Bibliography and database homepage. <http://vela.astro.ulg.ac.be/themes/extragal/gravlens/bibdat/>, see candidates.
- [5] Gravity Probe B homepage. <http://einstein.stanford.edu>.
- [6] Hipparcos homepage. <http://astro.estec.esa.nl/SA-general/Projects/Hipparcos/hipparcos.html>.
- [7] LMT homepage. <http://astra.astro.ulg.ac.be/themes/telins/lmt/>.
- [8] Mercury Orbiter homepage. <http://www.estec.esa.nl/spdwww/future/html/meo2.htm>.
- [9] SIM homepage. <http://sim.jpl.nasa.gov>.
- [10] Space VLBI homepage. http://sgra.jpl.nasa.gov/mosaic_vo.o/svbli_old.html.
- [11] US Space VLBI homepage. <http://us-space-vlbi.jpl.nasa.gov/>.
- [12] VSOP homepage. <http://www.vsop.isas.ac.jp>.
- [13] The Space Interferometry Mission: taking the measure of the universe. Technical report, SIM. Final report of the Space Interferometry Science Working Group, April 1996. <http://www.ess.sunysb.edu/simswg/siswg/siswg.html>.
- [14] Review of particle physics. *European Journal of Physics C*, 54:1–4, 1998.
- [15] GAIA: Composition, formation and evolution of the galaxy. Results of the Concept and Technology Study. Technical report, GAIA Science Advisory Group, 2000. <http://astro.estec.esa.nl/SA-general/Projects/GAIA/march-report.pdf>, version 1.6.
- [16] Planetary fact sheets webpage, 2001. <http://nssdc.gsfc.nasa.gov/planetary/factsheet/>.
- [17] I. Antoniadis, S. Dimopoulos, and G. Dvali. Millimetre-range forces in superstring theories with weak-scale compactification. *Nuclear Physics B*, 516:70, 1998. hep-ph/9710204 v2.
- [18] N. Arkani-Hamed, S. Dimopoulos, and G. Dvali. Phenomenology, astrophysics, cosmology of theories with submillimeter dimensions and TeV scale quantum gravity. *Physical Review D*, 59(086004), 1999. hep-ph/9807344.
- [19] N. Arkani-Hamed, S. Dimopoulos, and J. March-Russel. Stabilization of sub-millimeter dimensions: the new guise of the hierarchy problem. *Physical Review D*, 63(064030), 2001. hep-th/9809124 v2.
- [20] N. Ashby. Relativity and the Global Positioning System. *Physics Today*, pages 41–47, May 2002.
- [21] A. Ashtekar. Quantum geometry and gravity: recent advances. *gr-qc/0112038*, December 2001. Report of the plenary talk at the 16th International Conference on General Relativity and Gravitation, Durban, South Africa, July 2002.
- [22] A. Bec-Borsenberger, J. Christensen-Dalgaard, M. Cruise, A. Di Virgilio, D. Gough, M. Keiser, A. Kosovichev, C. Laemmerzahl, J. Luo, W-T. Ni, A. Peters, E. Samain, P. H. Scherrer, J-T. Shy, P. Toboul, K. Tsubono, A-M. Wu, and H-C. Yeh. Astrodynamical space test of relativity using optical devices - ASTROD. A proposal submitted to ESA in response to "Call for mission proposals for two Flexi-Missions F2/F3". 2001. <http://gravity5.phys.nthu.edu.tw/webpage/proposals.html>.
- [23] J. D. Bekenstein and R. H. Sanders. Gravitational lenses and unconventional gravity theories. *Astrophysical Journal*, 429:480–490, July 1994.
- [24] A. G. Bergmann, V. Petrosian, and R. Lynds. Gravitational lens models of arcs in clusters. *Astrophysical Journal*, 350:23–35, February 1990.
- [25] B. Bertotti and G. Giampieri. Solar coronal plasma in Doppler measurements. *Solar Physics*, 178:85–107, 1998.
- [26] A. Boders, S. Unwin, and M. Shao. Space Interferometer Mission (SIM, NASA): Global astrometry with the

Space Interferometry Mission. <http://sim.jpl.nasa.gov/discussion/experiments>.

- [27] E. Borra, N. Ninane, and J. Surdej. The liquid mirror telescope (LMT) project. Technical report, Institut d'Astrophysique et de Geophysique, Université de Liège (ULg), 1997.
- [28] C. Brans and R. H. Dicke. Mach's principle and a relativistic theory of gravitation. *Physical Review*, 124:925–935, November 1961.
- [29] W. L. Burke. Multiple gravitational imaging by distributed masses. *Astrophysical Journal*, 244, February 1981.
- [30] C. G. Jr. Callan, S. Coleman, and R. Jackiw. A new improved energy-momentum tensor. *Annals of Physics*, 59:42–73, 1970.
- [31] T. Chiba, N. Sugiyama, and J. Yokoyama. Imprints of the metrically-coupled dilaton on density perturbations in inflationary cosmology. *Nuclear Physics B*, 530:304–324, 1998. gr-qc/9708030 v2 May 1998. Notice that the title changed from the preprint version.
- [32] B. Creyn. Private communication, January 2000. Haystack Observatory, MA, USA.
- [33] T. Damour. Was einstein 100 percent right? 1995. Invited talk given at the 7th Marcel Grossmann Meeting on General Relativity, Stanford, July 1994; gr-qc/9412064.
- [34] T. Damour. Gravitation, experiment and cosmology. 1996. Proceedings of the 5th Hellenic school of Elementary Particle Physics; based on lectures given at Les Houches 1992, SUSY 1995 and Corfu 1996; gr-qc/9606079.
- [35] T. Damour. Experimental tests of relativistic gravity. *Nuclear Physics Proceeding Supplements*, 80:41–50, 2000. gr-qc/9904057.
- [36] T. Damour and G. Esposito-Farèse. Non-perturbative strong field effects in tensor-scalar theories of gravitation. *Physical Review Letters*, 70(15):2220–2223, April 1993.
- [37] T. Damour and G. Esposito-Farèse. Tensor-scalar gravity and binary-pulsar experiments. *Physical Review D*, 54(12):1474–1491, 1996.
- [38] T. Damour and G. Esposito-Farèse. Testing gravity to second Post-Newtonian order: a field theory approach. *Physical Review D*, 53:5541–5578, 1996. gr-qc/9506063.
- [39] T. Damour and G. Esposito-Farèse. Gravitational waves versus binary-pulsar tests of strong field gravity. *Physical Review D*, 58:042001, 1998.
- [40] T. Damour and G. Esposito-Farèse. Tensor-multi-scalar theories of gravitation. *Classical Quantum Gravity*, 9:2093–2176, 1992.
- [41] T. Damour and K. Nordtvedt. General Relativity as a cosmological attractor of tensor scalar theories. *Physical Review Letters*, 70(15):2217–2223, April 1993.
- [42] T. Damour and K. Nordtvedt. Tensor-scalar cosmological models and their relaxation towards General Relativity. *Physical Review D*, 48(8):3446–3450, October 1993.
- [43] T. Damour and B. Pinchon. Big Bang nucleosynthesis and tensor-scalar gravity. *Physical Review D*, 59:123502–1–13, May 1999.
- [44] T. Damour and A. M. Polyakov. The string dilaton and a least coupling principle. *Nuclear Physics B*, 423:532–558, January 1994. hep-th/9401069.
- [45] T. Damour and A. M. Polyakov. String theory and gravity. *General Relativity and Gravitation*, 26(12):1171–1176, 1994. gr-qc/9411069.
- [46] R. Delbourgo and P. Phocas-Cosmetatos. Radiative corrections to the photon-graviton vertex. *Physics Letters*, 41 B(4):533–535, October 1972.
- [47] S. Deser. Scale invariance and gravitational coupling. *Annals of Physics*, 59:248–253, 1970.
- [48] S. Deser. Improvement versus stability in gravity-scalar coupling. *Physics Letters*, 134 B 6:419, January 1984.
- [49] A. Edery, A. A. Méthot, and M. B. Paranjape. Gauge choice and geodetic deflection in conformal gravity. *astro-ph/0006173*, 2000.
- [50] A. Edery and M. B. Paranjape. Classical tests for Weyl gravity: Deflection of light and time delay. *Physical Review D*, 58(024011):1–8, 1998. astro-ph/9708233.
- [51] A. Edery and M. B. Paranjape. Causal structure of vacuum solutions to conformal (Weyl) gravity. *General Relativity and Gravitation*, 31(1031), 1999. astro-ph/9808345 v2 (25th february 1999).
- [52] A. A. Elliott, R. W. Hellings, and J. K. Miller. PPN gamma results from the NEAR conjunction. 1998. Bulletin of the American Astronomical Society, 191st A.A.S. Meeting, 1997, vol. 29, nb. 48.09, p1289.
- [53] T. M. Eubanks, J. O. Martin, B. A. Archinal, F. J. Josties, S. A. Klioner, S. Shapiro, and I. I. Shapiro. Advances in solar system tests of gravity. 1999. ftp://casa.usno.navy.mil/navnet/postscript/prd_15.ps.

- [54] V. L. Fitch, J. H. Jr Taylor, E. G. Adelberger, G. W. Elverum, D. G. Hoog, F. E. Low, J. C. Mather, R. E. Packard, R. C. Richardson, S. L. Shapiro, M. W. Strovink, C. M. Will, R. D. Taylor, S. G. Campbell, and A. C. Logan. Task Group on Gravity Probe B. Review of Gravity Probe B. Technical report, Space Studies Board, Board on Physics and Astronomy, National Research Council, Washington D. C., National academy, 1995. <http://www.nas.edu/ssb/gpbmenu.html>.
- [55] E. S. Fradkin and A. A. Tseytlin. Renormalizable asymptotically free quantum theory of gravity. *Physics Letters B*, 104:377–381, 1981.
- [56] E. S. Fradkin and A. A. Tseytlin. Renormalizable asymptotically free quantum theory of gravity. *Nuclear Physics B*, 201(5):469–491, 1982.
- [57] M. Froeshlé, F. Mignard, and F. Arenou. Determination of the PPN parameter γ with the hipparcos data. Proceedings from the Hipparcos Venice 97 symposium. In session 1: Description of the Hipparcos and Tycho catalogues; <http://astro.estec.esa.nl/SA-general/Projects/Hipparcos/venice.html>.
- [58] J.-M. Gérard and I. Mahara. Asymptotic solutions to a tensor-scalar theory of gravity. *Physics Letters B*, 346:35–40, March 1995.
- [59] J.-M. Gérard and I. Mahara. The attractor mechanism in the minimal tensor-scalar theory of gravity. *Modern Physics Letters*, pages 631–637, 1997. UCL-IPT November 1996.
- [60] J.-M. Gérard and Y. Wiaux. Gravitational dipole radiations from binary systems. *Physical Review D*, 66(024040), 2002. [gr-qc/0109062](http://arxiv.org/abs/gr-qc/0109062).
- [61] G. Giampieri. Relativity experiments in the solar system. 1995. Proceedings of the XI Italian Conference on General Relativity and Gravitational Physics, Trieste (Italy), Sept-26-30-1994; [astro-ph/9504098](http://arxiv.org/abs/astro-ph/9504098) April.
- [62] G. F. Giudice, R. Rattazi, and J. D. Wells. Graviscalars from higher-dimensional metrics and the curvature-Higgs mixing. *Nuclear Physics B*, 595:250–276, 2001. [hep-ph/0002178](http://arxiv.org/abs/hep-ph/0002178) v2.
- [63] S. Godier and J.-P. Rozelot. Private communication, 2001.
- [64] S. A. Grossman and R. Narayan. Gravitationally lensed images in ABDEL 370. *Astrophysical Journal*, 344:637–644, September 1989.
- [65] T. Han, J. D. Lykken, and R.-J. Zhang. Kaluza-Klein states from Large Extra-Dimensions. *Physical Review D*, 59:10 5006, April 1999. [hep-ph/9811350](http://arxiv.org/abs/hep-ph/9811350) v4 (2000).
- [66] X.-G. He, G. C. Joshi, and B. H. J. Mc Kellar. Gravitational lensing and extra-dimensions. [hep-ph/9908469](http://arxiv.org/abs/hep-ph/9908469), August 1999.
- [67] H. Hoekstra, H. K. C. Yee, and M. D. Gladders. Current status of weak gravitational lensing. [astro-ph/0205205](http://arxiv.org/abs/astro-ph/0205205), May 2002.
- [68] L. Iess, G. Giampieri, J. D. Anderson, and B. Bertotti. Doppler measurements of the solar gravitational deflection. *Classical and Quantum Gravity*, 16:1487–1502, 1999.
- [69] A. I. Janis, E. T. Newman, and J. Winicour. Reality of the Schwarzschild singularity. *Physical Review Letters*, 20(16):878–880, April 1968.
- [70] K. J. Johnston. Full-Sky Astrometric Mapping Explorer: FAME. Technical report, United States Naval Observatory, 1999. <http://www.usno.navy.mil/FAME/> see Publications: FAME Concept Study Report (1999).
- [71] B. F. Jones. Gravitational deflection of light: solar eclipse of the 30th June 1973. II Plate reductions. *Astronomical Journal*, 81(6):455–463, June 1976.
- [72] J. Julve and M. Tonin. Quantum gravity with higher derivative terms. *Nuovo Cimento B*, 46(1):137–152, 1978.
- [73] S. A. Klioner. Practical relativistic model of microarcsecond astrometry in space. [astro-ph/0107457](http://arxiv.org/abs/astro-ph/0107457) v2, 2001. To appear in *Astronomical Journal*.
- [74] S. A. Klioner and S. M. Kopejkin. Microarcsecond astrometry in space: relativistic effects and reduction of observations. *Astronomical Journal*, 104(2):897–913, 1992.
- [75] S. A. Klioner and M. H. Soffel. Relativistic celestial mechanics with PPN parameters. *Physical Review D*, 62(024019), 2000. [gr-qc/9906123](http://arxiv.org/abs/gr-qc/9906123).
- [76] S. M. Kopejkin. Propagation of light in the stationary field of multipole gravitational lens. *Journal of Mathematical Physics*, 35(5):2587–2601, 1996.
- [77] J. R. Kuhn. Private communication, 1998.
- [78] D. E. Lebach, B. E. Corey, I. I. Shapiro, M. I. Ratner, J. C. Webber, A. E. E. Rogers, J. L. Davis, and T. A. Herring. Measurements of the solar gravitational deflection of radio waves using Very Long Baseline Interferometry. *Physical Review Letters*, 75(8):1439–1442, August 1995.

- [79] D. L. Lee, A. P. Lightman, and W.-T. Ni. Conservation laws and variational principle in metric theories of gravity. *Physical Review D*, 10:1685–1700, 1974.
- [80] L. Lindegren and M. A. C. Perryman. GAIA: Global Astrometric Interferometer for Astrophysics. Proceedings from the Hipparcos Venice 97 symposium. In session 12: Prospects of Microarcsec Astrometry: the Project; <http://astro.estec.esa.nl//SA-general/Projects/Hipparcos/venice.html>.
- [81] L. Lindegren and M. A. C. Perryman. GAIA: Global Astrometric Interferometer for Astrophysics. *Astronomy Astrophysics Supplement Series*, 116:579–595, 1996.
- [82] P. D. Mannheim. Microlensing, Newton-Einstein gravity, and conformal gravity. *astro-ph/9412007*, December 1994. UCON-94-10.
- [83] P. D. Mannheim. Open questions in classical gravity. *Foundations of Physics*, 24(4):487–511, April 1994.
- [84] P. D. Mannheim. Conformal cosmology and the age of the universe. *UCONN 95-08*, December 1995.
- [85] P. D. Mannheim. Local and global gravity. *Foundations of Physics*, 26(12):1683–1709, December 1996. gr-qc/9611038.
- [86] P. D. Mannheim. Private communication, August 2002. University of Connecticut.
- [87] P. D. Mannheim and D. Kazanas. Exact vacuum solution to conformal Weyl gravity and galactic rotation curves. *Astrophysical Journal*, 342:635–638, July 1989.
- [88] P. D. Mannheim and D. Kazanas. General structure of the gravitational equations of motion in conformal Weyl gravity. *Astrophysical Journal*, 76(Supplement Series):431–453, June 1991.
- [89] R. Mansouri and F. Nasserri. A model universe with variable space dimension: its dynamics and wave function. *IPM/P-99/7*, February 1999.
- [90] R. H. McKenzie. A gravitational lens produces an odd number of images. *Journal of Mathematical Physics*, 26(7):1592–1596, July 1985.
- [91] F. Mignard. Private communication, May 2002. CERGA Department, Observatoire de la Côte d’Azur (OCA).
- [92] F. Mignard. Private communication, July 2002. CERGA Department, Observatoire de la Côte d’Azur (OCA).
- [93] C. Misner, K. S. Thorne, and J. A. Wheeler. *Gravitation*. W. H. Freeman and company, 1973.
- [94] T. Muta. English translation of Kaluza’s paper. *Dep. of Phys. of Hiroshima University, Hiroshima 730 JAPAN*, (HUPD-8401), March 1984.
- [95] R. Narayan. Lectures on gravitational lensing. Technical report, Harvard-Smithsonian Center for Astrophysics, October 1997. astro-ph/9606001 v2.
- [96] B. Paczynski. Gravitational microlensing of the galactic bulge stars. *Astrophysical Journal*, 371:L63–L67, April 1991.
- [97] R. Pello, J.-F. Le Borgne, G. Soucail, and Y. Mellier. A straight gravitational image in ABDEL 2390: a striking case of lensing by a cluster of galaxies. *Astrophysical Journal*, 366:405–411, January 1991.
- [98] A. Perez-Lorenzana. Theories in more than four dimensions. *AIP Conference Proceedings*, 562:53–85, 2001. hep-ph/0008333.
- [99] V. Perlick. On Fermat’s principle in General Relativity. *Classical and Quantum Gravity*, 7:1319–1331, March 1990.
- [100] V. Perlick. On Fermat’s principle in General Relativity II. The conformally stationary case. *Classical and Quantum Gravity*, 7:1849–1867, 1990.
- [101] V. Perlick. Infinite dimensional Morse theory and Fermat’s principle in General Relativity I. *Journal of Mathematical Physics*, 36(12):6915–6928, December 1995.
- [102] V. Perlick. Criteria for multiple imaging in Lorentzian manifolds. *Classical and Quantum Gravity*, 13:529–537, 1996.
- [103] S. Perlmutter, S. Gabi, G. Goldhaber, A. Goobar, D. E. Groom, I. M. Hook, A. G. Kim, M. Y. Kim, J. C. Lee, R. Pain, C. R. Pennypacker, I. A. Small, R. S. Ellis, R. G. McMahon, B. J. Boyle, P. S. Bunclark, D. Carter, M. J. Irwin, K. Glazebrook, H. J. M. Newberg, A. V. Filippenko, T. Matheson, M. Dopita, and W. J. Couch. Measurements of the cosmological parameters Omega and Lambda from the first seven supernovae at $z \geq 0.35$. *Astrophysical Journal*, 483:565–581, July 1997.
- [104] M. A. C. Perryman, L. Lindegren, and C. Turon. The scientific goals of the GAIA mission. Proceedings from the Hipparcos Venice 97 symposium. In session 11: Prospects of Microarcsec Astrometry: the Science; <http://astro.estec.esa.nl//SA-general/Projects/Hipparcos/venice.html>.
- [105] D. Peterson. Private communication, January 2000. SUNY, NY, USA.
- [106] D. Peterson and M. Shao. Space Interferometer Mission (SIM, NASA): The scientific basis for the Space

- Interferometry Mission. <http://sim.jpl.nasa.gov/discussion/experiments>.
- [107] S. Pireaux. Etude de solutions particulières d'une théorie invariante conforme de la gravitation. Juin 1997. Graduate thesis, Université catholique de Louvain (UCL).
- [108] S. Pireaux. Etude de la déflexion de la lumière comme test d'une théorie de la gravitation (DEA). Master's thesis, Université catholique de Louvain (UCL), Juin 1998.
- [109] S. Pireaux and J-P. Rozelot. Solar quadrupole moment and purely relativistic gravitation contributions to Mercury's perihelion advance. *Astrophysics and Space Sciences*, (284):1159–1194, 2003. astro-ph/0109032.
- [110] R. D. Reasenberg, I. I. Shapiro, P. E. MacNeil, R. B. Goldstein, J. C. Breidenthal, J. P. Brenkle, D. L. Cain, T. M. Kaufman, T. A. Komarek, and A. I. Zygielbaum. Viking relativity experiment: verification of signal retardation by solar gravity. *Astrophysical Journal*, 234:L219–L221, December 1979.
- [111] S. Refsdal and J. Surdej. Gravitational lenses. *Reports on Progress in Physics*, 56:117–185, 1994.
- [112] R. Reinhard. Ten years of fundamental physics in ESA's space science programme. *ESA Bulletin*, 98(8), June 1999.
- [113] G. W. Richter and R. A. Matzner. Second-order contributions to gravitational deflection of light in the parametrized Post-Newtonian formalism. *Physical Review D*, 26, 1982.
- [114] G. W. Richter and R. A. Matzner. Second-order contributions to gravitational deflection of light in the parametrized Post-Newtonian formalism. II. Photon orbits and deflections in three dimensions. *Physical Review D*, 26(10):2549–2556, November 1982.
- [115] D. S. Robertson and W. E. Carter. Relativistic deflection of radio signals in the solar gravitational field measured with VLBI. *Nature*, 310:572–574, August 1984.
- [116] D. S. Robertson, W. E. Carter, and W. H. Dillinger. New measurements of solar gravitational deflection of radio signals using VLBI. *Nature*, 349:768–770, February 1991.
- [117] D. K. Ross and L. I. Schiff. Analysis of the proposed planetary radar reflexion experiment. *Physical Review*, 141(4):1215–1218, January 1966.
- [118] C. Rovelli. Loop Quantum Gravity. *Living Reviews in Relativity*, (1):1, 1998. gr-qc/9710008.
- [119] J-P. Rozelot. Measurement of the Sun's changing sizes. 2804:241, 1996. SPIE, Missions to the Sun, Denver, Colorado (USA), 8-9 August 1996.
- [120] J-P. Rozelot and J. Rösch. Le soleil change-t-il de forme? *Comptes Rendus de l'Académie des Sciences de Paris*, t 322, IIb:637–644, 1996.
- [121] J-P. Rozelot and J. Rösch. An upper bound to the solar oblateness. *Solar Physics*, 172:11–18, 1997.
- [122] S. Röser. DIVA - Beyond Hipparcos and towards GAIA. *Annual Scientific Meeting of the Astronomische Gesellschaft*, pages 37–106, 1998. Heidelberg, September 14-19, 1998.
- [123] S. Röser. DIVA - A space-born Fizeau interferometer for global astrometry and photometry. Working on the fringe. *ASP Conference Series*, 194, 2000.
- [124] S. Röser. Private communication, January 2000. Astronomische Rechen-Institut, Heidelberg, Germany.
- [125] S. Röser, U. Bastian, K. S. De Boer, E. Hog, C. Schalinski H. P. Röser, E. Schilbach, C. De Vegt, and S. Wagner. DIVA : towards microarcsecond global astrometry. *ESA-SP 402*, May 1997. Proceedings from the Hipparcos Venice 97 symposium. In session 12: Prospects of Microarcsec Astrometry: the Projects; <http://astro.estec.esa.nl/SA-general/Projects/Hipparcos/venice.html>.
- [126] E. Samain. Proposition de recherche scientifique spatiale: Télémétrie Inter-Planétaire Optique (TIPO). Technical report, Observatoire de la Côte d'Azur (OCA), CERGA Département, 2001.
- [127] E. Samain. Private communication, April 2002. CERGA Département, Observatoire de la Côte d'Azur (OCA).
- [128] A. Serna, J.-M. Alimi, and A. Navarro. Convergence of scalar-tensor theories towards General Relativity and primordial nucleosynthesis. *Classical and Quantum Gravity*, 19:857–874, 2002. gr-qc/0201049.
- [129] K. S. Stelle. Renormalization of higher order derivative quantum gravity. *Physical Review D*, 16(4):953–969, 1977.
- [130] T. J. Sumner. Fundamental physics in space: UK scientific aims and opportunities in the future. Technical report, UK Community in "Fundamental Physics in Space", 2000. http://icstar5.ph.ic.ac.uk/Research/dm_fundp/fpinuk_final.pdf.
- [131] System and Technology Study Report. BepiColombo. An interdisciplinary Cornerstone Mission to the planet Mercury. *ESA-SCI*, 1:21–24, 35–38, April 2000.
- [132] G. A. Tammann, A. Sandage, and A. Saha. Ho from type Ia supernovae. *astro-ph/0010422*, October 2000. To be published in "A decade of HST Science", Eds. M. Livio, K. Noll, M. Stiavelli (Cambridge University Press).

- [133] M. S. Turner. Dark matter, dark energy and fundamental physics. *astro-ph/9912211*, December 1999. To be published in the proceedings of "Physics in Collision", Ann Arbor, MI, 24-26th June 1999, Eds. M. Campbell, T. M. Wells (World Scientific, NJ).
- [134] S. G. Turyshev, J. D. Anderson, and R. W. Hellings. Relativistic gravity theory and related tests with a Mercury Orbiter mission. *gr-qc/9606028*, 1996.
- [135] K. S. Virbhadra. Janis, Newman, Winicour and Wyman solutions are the same. *International Journal of Modern Physics A*, 12(27):4831–4835, 1997.
- [136] K. S. Virbhadra, D. Narasimha, and S. M. Chitre. Role of the scalar field in gravitational lensing. *Astronomy and Astrophysics*, 337:1, 1998. *astro-ph/9801174*.
- [137] H. von Klüber. The determination of Einstein's light-deflection in the gravitational field of the Sun. *Vistas in Astronomy*, 3:47–77, 1966.
- [138] D. Walsh, R. F. Carswell, and R. J. Weymann. 0957+561 A, B: Twin quasistellar objects or gravitational lens? *Nature*, 279:381–384, 1979.
- [139] J. Wambsganss. Gravitational lensing in astronomy. *Living Reviews in Relativity*, 1998.
- [140] S. Weinberg. *Principles and applications of the General Theory of Relativity*. John Wiley and sons, 1972.
- [141] J. D. Wells, G. F. Giudice, and R. Rattazzi. Quantum gravity and extra dimensions at high energy colliders. *Nuclear Physics B*, 544:3–38, 1999.
- [142] C. M. Will. *Theory and Experiments in Gravitational Physics, revisited edition*. Cambridge University Press, 1993.
- [143] C. M. Will. The confrontation between General Relativity and experiments. *Living Reviews*, 4, May 2001. www.livingreviews.org/Articles/Volume4/2001-4will.
- [144] J. G. Williams, D. H. Boggs, J. O. Dickey, and W. M. Folkner. Lunar laser tests of gravitational physics. *World Scientific*, pages 1797–1798, 2002. Proceedings of the 9th Marcel Grossmann 2000.
- [145] M. Wyman. Static spherically symmetric scalar fields in General Relativity. *Physical Review D*, 24(4):839–841, August 1981.

APPENDIX A: Conventions

Orders of magnitude and present estimate of cosmological parameters

1 parsec = 3.0856 10 ¹⁶ m		
1 arcsec \simeq 1/206255 rad		
$G_N = 6,672\,59(85) \cdot 10^{-11} \text{ m}^3 \text{ kg}^{-1} \text{ s}^{-2}$		from [14]
$M_{Sun} = 1.98892(25) \cdot 10^{30} \text{ kg}$		from [14]
$M_{Milky\ Way} = 1.8 \cdot 10^{11} M_{Sun}$		from [93]
$a_B = 7,56 \cdot 10^{-16} \text{ J K}^{-4} \text{ m}^{-3}$		from [14]
$H_0 = 100 h_0 \text{ km s}^{-1} \text{ Mpc}^{-1} = (9,778\,13)^{-1} \cdot 10^{-9} h_0 \text{ years}^{-1}$		from [133]
with $h_0 \in]0,55; 0,75[$		
$T_{CMB\ 0}^\circ = 2,728 \pm 0,002 \text{ K}$		from [14]
$\Omega_{dust\ 0\ \text{exp}} \in [0,3; 0,5]$	present-time pressure-less matter density	} from [133]
$\Omega_\Lambda\ 0\ \text{exp} \in [0,6; 1]$	present-time cosmological density	
$\Omega_m\ 0\ \text{exp} \equiv 1 - \Omega_k\ 0\ \text{exp} \in [0,8; 1,2]$	present-time matter density	

Tensorial calculus

Our sign convention for the metric is (+, -, -, ...).

The coma, “ \prime_μ ” or “ ∂_μ ”, denotes the usual derivative, while “ $|_\mu$ ” denotes the covariant derivative with respect to coordinates x^μ and the metric $g_{\mu\nu}$.

Equally, we adopt the dot “ $\dot{\bullet} \equiv \frac{d}{d\tau}$ ” for the proper time derivative and the larger dot “ $\bullet \equiv \frac{d}{dt}$ ” for the time coordinate.

The apostrophe, “ $'$ ”, is for the derivative with respect to the radial coordinate.

The box symbol, “ \square ”, is used for the Dalemberertian with respect to the metric, “ $\square \equiv |_\sigma |_\sigma$ ”.

Finally, the Latin indices from the lower part of the alphabet are reserved for the spatial coordinates only (i.e.: $i, j, k, l = 1, 2, 3$); the Greek indices are used for space-time coordinates (i.e.: $\mu, \nu, \rho, \sigma = 0, 1, 2, 3$); and we use Einstein’s summation convention for each type of indices, between an upper and a lower identical indice with respect to the appropriate metric.

The Minkowskian flat space-time metric is $\eta_{\mu\nu}$.

Generalities about light deflection

We have adopted the following convention for the sign of the deflection angle written as $\hat{\alpha}$: a positive sign is for a convergent lens (bending towards the gravitational deflector) while a negative sign means a divergent lens (bending away from the gravitational deflector).

The angular positions of the image, ϑ_I , and of the source, ϑ_S , are taken as positive angles unless the possibility of considering positive and negative values is noted by an arrow sign “ \rightarrow ”; and “sg()” means the sign of “()”.

Usually, we shall use r to denote the Schwarzschild radial coordinate and ρ for the isotropic coordinate. General radial coordinates are denoted as q .

Normally, the Greek letters $\alpha, \beta, \gamma, \delta$ and ε , are reserved for the Eddington-Robertson-Schiff parameters, unless used as indices for the space-time dimensions.

MTS/SITS theories

$\Upsilon = a/2$ is the constant parameter that characterizes the static spheric asymptotically flat solution to MTS/SITS theories in the Einstein frame.

TS theories

Quantities in the Einstein frame are designed by “ \sim ”, while the other ones are in the Jordan frame.

The symbols Σ or σ are reserved for the gravitational scalar field in the Einstein frame, and Φ or φ for the one in the Jordan frame. ϕ , Ψ , $F^{\mu\nu}$ design the matter fields, respectively scalar, fermionic and electromagnetic.

We will note respectively the cosmological scale factor as \mathfrak{R} , the conformal transformation factor as A , and the scalar coupling to matter as α_{TS} . When we write α_{BD} , this means the *constant* coupling of Brans-Dicke.

When doing some cosmological evolution, we distinguish the different reference times using subscripts, like t_l for the beginning of the radiation era, t_{eq} for the end of the radiation era (when dust and radiation densities are equal -equilibrium-), and t_0 for the present time. Or alternatively, we use the cosmic time \tilde{p} , and in particular, \tilde{p}_{BBN-eq} , the cosmic time elapsed since the relevant epochs prior to Big-Bang Nucleosynthesis till the end of the radiation era.

A subscript “ $_r$ ” is for quantities evaluated during the radiation era, while “ $_d$ ” is for the dust era.

LED theories

The number of extra-dimensions is given by d . Quantities in the $(4 + d)$ -dimensional space-time coming from the $(4 + d)$ -Hilbert-Einstein action are designated by “ $\hat{}$ ”, with the exception of $\hat{\alpha}$ which is the light deflection angle in a 4-dimensional space-time.

Latin indices from the upper part of the alphabet are used for the total $(4 + d)$ -dimensions (i.e.: $s, u, v, w = 0, 1, 2, 3, \dots, 3 + d$). The lower part of the Latin alphabet is reserved for the usual three dimensional space, while Greek indices are reserved for the usual 4-dimensional space-time. We also use Greek indices with an upper bar for the extra-dimensions only (i.e.: $\bar{\mu}, \bar{\nu}, \bar{\rho}, \bar{\sigma} = 3 + 1, \dots, 3 + d$).

The $(4 + d)$ -dimensional space-time part of the coordinates that live in the non compactified space is noted x^μ as usual; the other part that lives on the compactified extra-dimensions is noted as $y^{\bar{\mu}}$, this part is thus cyclic because the compactification is made on a torus.

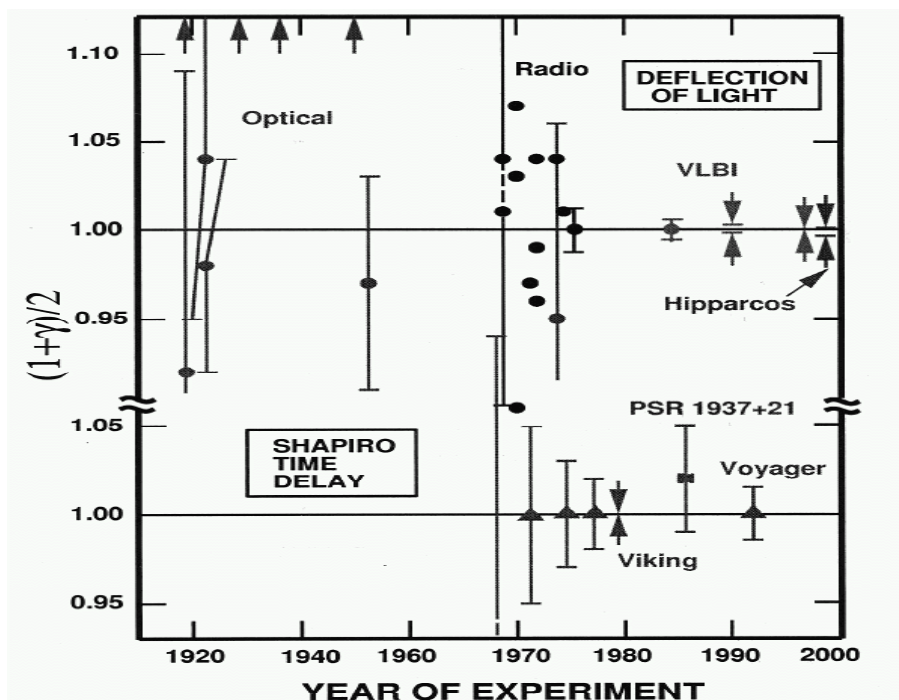
The coupling of the massless scalar mode is written as α_{LED} and that of the massive scalar modes as β_{LED} .

The Minkowskian metric in $(4 + d)$ -dimensions is η_{uv} and the one restricted to the extra-dimensions is $\eta_{\bar{\mu}\bar{\nu}}$.

The Weyl theory

β_W, γ_W and k_W are the constant parameters that characterize the three parameter family of static and spherically symmetric solutions to the Bach equations (in vacuum) in the Weyl theory.

APPENDIX B: Fact sheets of γ -tests through light deflection and other experiments

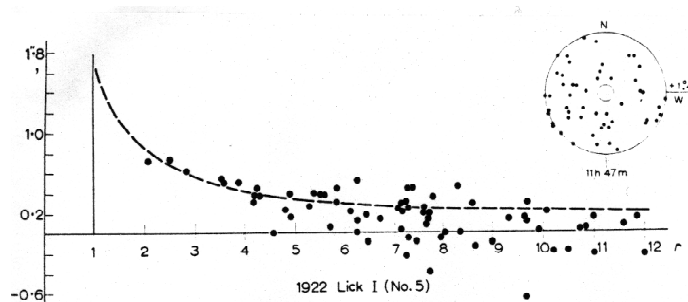


Different measurements constraining the value of the Post-Newtonian parameter γ , representing the departure of gravitational light bending from Newtonian gravity. Its general relativistic value is 1. The figure shows the value derived with the Hipparcos optical astrometric satellite, which has reached a precision of 0.1%. The arrows in the upper part of this graph denote anomalously large values from the early solar eclipse observations. VLBI observations of the light deflection angle leading to the best precision (about 0.01%) so far are illustrated. Comparison is also made with the Viking spacecraft which, thanks to Shapiro time-delay measurements, yielded an agreement with General Relativity within 0.1%. This figure is extracted from reference [143].

1 In the optical waveband

Experiment	<i>Solar eclipses</i>
Description	<p>Those experiments took advantage of the solar eclipse to observe relative angular position of stars in the solar neighborhood;</p> <p>Photographic plates were taken at \neq locations (eclipse plates \equiv star field containing the eclipse location, and comparison/check plates \equiv star field 10° to the south, where gravitational bending is considered to be negligible) and at different times of the year (eclipse-epoch fields \equiv fields taken during the eclipse, and night time plates \equiv fields taken at night, a few months after the eclipse).</p> <p>A subsequent comparison of the same stellar field on the eclipse and on the night plates would lead to the measurement of light deflection, while comparison fields during the eclipse or night time would serve for calibration of the instruments scale factors. (This independent determination of the scale factors was not always possible because the check plates were not (always) reliable, even though several different methods were used to obtain them).</p> <p>For the 1973 experiment, plates were taken with the same telescope, on the 30th June (eclipse in Chinguetti, Mauritania) and in November. Measurements were made on Galaxy II comparator at the Royal Greenwich Observatory, and on a PDS micro-photometer at the University of Texas.</p> <p>The light deflection angle was obtained with least squares adjustments to a GR model.</p>
1st intended goal	To measure the gravitational deflection due to the Sun and test GR.
How it happens to be measuring γ	Through change in the apparent position of the stars close to the Sun, where the effect is the strongest.
Start-End	Sporadic experiments in 1919, 1920... the last one in 1976, for a total of ~ 9 experiments.
Advantages	The first confirmation of General Relativity.
Drawbacks	<p>Scarcity of the solar eclipses (and an eclipse is of max. duration of 7 minutes; most of them being shorter). Thus a short total observing time in order to make absolute measurements.</p> <p>Different eclipse experiments were not repeated with the same instruments.</p> <p>Observations have to be made at the location of the eclipse: so they are made with a rough temporary station and sometimes, political/weather conditions prevent them.</p> <p>During a same experiment, different exposures of the same field had different instrumental scale values (mainly due to different setting of the focus, the tilting of the telescope and photographic emulsions) => delicate calibration of scaling factors of the instruments.</p> <p>During the eclipse, the Sun has to pass close enough to some suitable stars (of sufficient magnitude), as the bending signal decreases with the distance and the scaling errors increase with the distance from the center (Sun) of the photographic plate.</p> <p>Intrinsic difficulty of observing at small distances from the Sun (increasing brightness of the solar corona during the eclipse).</p> <p>(...)</p>

<p>(...) Drawbacks</p>	<p>The full maximum value of 1.75" light deflection (at the solar limb) is thus not measured, but extrapolated from a few measurements at larger distances from the Sun. Einstein's theoretical curve being hyperbolic, a small change in the scaling errors or others would lead to different predictions for γ, even though stemming from the same data.</p> <p>It experiences the perturbations from the atmosphere, the lack of all-sky visibility, the gravitational and thermal flexure of telescopes, like all ground-based astronomical observatories (↔ satellites).</p>
<p>Precision</p>	<p>Very large error generally >10% and in average 30%. The precision was just sufficient to distinguish between Newton's law and GR.</p> <p>Experiment of 1973: $\gamma = 0.95 \pm 0.11$, or $\hat{\alpha} = 1.66'' \pm 0.18''$, extrapolated at the solar limb.</p>
<p>Main cause of errors</p>	<p>Delicate calibration of scaling factors.</p>
<p>References</p>	<p>Jones [71] Von Klüber [137] and references therein.</p>



Light deflection measured by the Lick expedition (1922) versus the star distance to the Sun in solar radii [137].



Eclipse experiment of 1922 by the Lick expedition [137].

Experiment	<i>High Precision PARallax Collecting Satellite (Hipparcos Satellite from ESA)</i>
Description	<p>Space optical satellite mission performing an astrometric survey. Equipped with a novel “beam combining technique” (a two-part mirror) which brought the light from the 2 fields of view (separation 58° and $0.9 \times 0.9^\circ$) to a common focal surface, achieving thus large/small field measurements simultaneously. The satellite did sweep out great circles over the celestial sphere, spinning ($T = 2$ hours) with a continuous slow change in its rotation axis, in order to scan the complete celestial sphere several times during the mission \equiv Hipparcos scanning mode. Though initially it was designed to have a geostationary orbit (failure).</p>
1st intended goal	<p>It is a pioneering astrometric space experiment to measure precisely the position, parallaxes and proper motions of stars ($\pm 120\,000$ stars to a precision of ± 2 to 4 marcsec planned and an actual precision of 1 marcsec achieved), plus astrometric and color (B-V) photometric properties of some additional 400 000 stars (an actual precision of 20 – 30 marcsec achieved) (Tycho experiment). A rotation free or “quasi-inertial” system is then represented by relating the final catalogue to observations of extragalactic objects, and a link to the radio reference frame is provided by direct/indirect observations of radio stars/quasars by VLBI. The first aim was to monitor the Earth motion.</p>
How it happens to be measuring γ	<p>It also provides stringent new tests of GR (including lensing): as the very accurate positional measurements of Hipparcos require the inclusion of stellar aberration corrections, as well as the treatment of light bending due to the gravitational field of the Sun and the Earth (the dominant effect). GR is then assumed and deviations from it are measured ($1 - \gamma$).</p>
Start-End	<p>Launched on 8th August 1989. Planned operational lifetime of 2.5 years. Actual operational lifetime > 3 years: communication lost on 15th August 1993. Final Hipparcos-Tycho Catalogue completed in August 1996, published in June 1997 (ESA).</p>
Advantages	<p>It does not experience the perturbations from the atmosphere, the lack of all-sky visibility, the gravitational and thermal flexure of telescopes (thanks to a controlled thermal environment), like all ground-based astronomical observatories (\leftrightarrow VLBI). All differential angular measurements are at large angles from the Sun (47 to 133°) (\leftrightarrow eclipses) which allows a better randomisation of the systematic errors thanks to the large coverage in elongation. Also, the coronal bending is weaker at such angles. Moreover, optical waves are less affected by coronal bending than radio waves (\leftrightarrow VLBI). Measurements with the same instrument (well calibrated all over the sky) were made at many different orientations and different epochs, thus the parallaxes are absolute and regional or systematic errors in position/annual proper motion are expected to be $< \text{marcsec}$. It is the first <i>optical</i> measurement of γ without the need for eclipses. It is a pioneering experiment which demonstrated that Global Space Astrometry was feasible.</p>

Drawbacks	<p>The measurements are at large angles from the gravitational deflector (45° avoidance angle for the Sun), thus the signal (deflection) is weaker (\leftrightarrow eclipses).</p> <p>The individual accuracy was obtained only when the mission was fully completed and the accuracy on a special target could not be \nearrow by \nearrow the observing time, nor could special targets be selected as the scanning law was fixed, unlike what is possible with pointing missions (\leftrightarrow SIM).</p>
Precision	<p>It results in $\gamma = 0.997 \pm 0.003$ ($\sim 10^{-3}$ precision) based on multiple observations of $\pm 12 \cdot 10^4$ stars (limiting mag. (V) ~ 12, completeness (V) 7.3 – 9.0), with individual accuracies of 1 – 2 mas.</p>
Main cause of errors	<p>A correlation between the deflection and parallactic displacements (parallax zero point).</p>
References	<p>Hipparcos homepage [6] Froeshle <i>et al.</i> [57]</p>

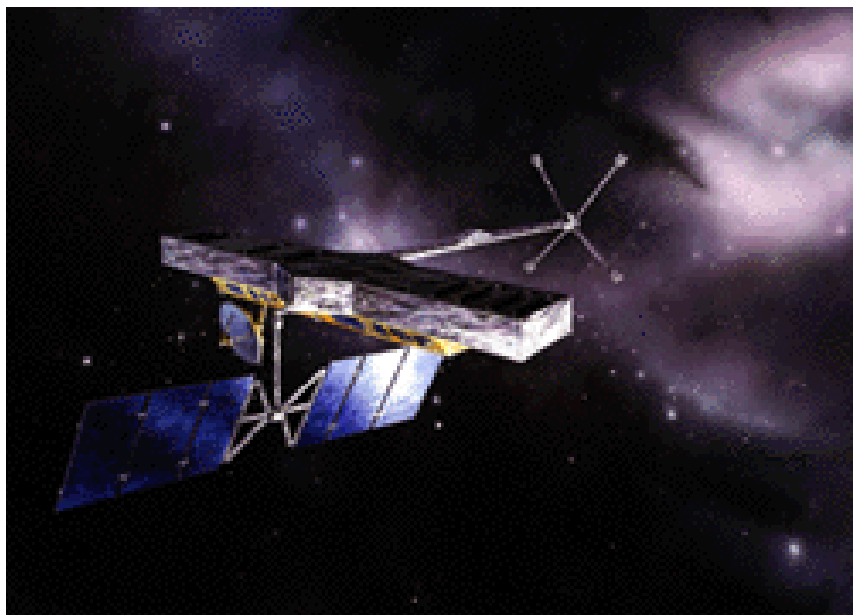


Hipparcos Satellite.

Experiment	<p style="text-align: center;"><i>Full sky Astrometric Mapping Explorer (FAME) previously coordinated by NASA, as a MIDEX mission, with the U.S. Naval Observatory and several other institutions, but financial support from NASA was withdrawn in October 2002. Several changes in FAME are discussed to lower the costs and revive the FAME project.</i></p>
Description	<p>Small, low cost, astrometric survey satellite, equipped with a telescope looking at 2 fields of view separated by 81.5°, with CCDs used in a TDI method. Waveband: 550-850 nm. The scanning law is analogous to Hipparcos.</p>
1st intended goal	<p>To fill the gap between Hipparcos and GAIA missions. To provide positions, proper motions, parallaxes, photometry.</p>
How it happens to be measuring γ	<p>In the same implicit way as Hipparcos does.</p>
Start-End	<p>Launch uncertain. Planned operational lifetime of 2.5 (minimal mission) or 5 years (extended mission). Results uncertain.</p>
Advantages	<p>Same advantages as Hipparcos over ground-based experiments (\leftrightarrow VLBI). Multiple observations with the same instruments (\leftrightarrow eclipses). Low cost mission. It will complement the observational program of the pointing SIM instrument.</p>
Drawbacks	<p>The measurements are at large angles from the gravitational deflector (previously 45° avoidance angle for the Sun, now changed to $35 \pm 5^\circ$), thus the signal (deflection) is weaker (\leftrightarrow eclipses). Same drawbacks as Hipparcos in comparison with pointing missions (\leftrightarrow SIM). Individual accuracy not as good as SIM.</p>
Precision	<p>It should measure light deflection not only due to the Sun, but also to Jupiter and Saturn. It should result in $\sim 0.005\%$ precision with 1σ uncertainty on γ (crude analysis for an extended mission, based on previous avoidance angle and assuming a single measurement uncertainty of 1 marcsec at $V=9$, as well as no correlation between γ and estimates of other parameters), multiple observations of $\pm 40 \cdot 10^6$ stars within our galactic neighborhood (mag. $(V) \in]5, 15[$), with individual accuracies better than Hipparcos. For example, for $V = 9$: individual positions $\simeq 50 \mu\text{arcsec}$, and $500 \mu\text{arcsec}$ for $V = 15$; photometry $\sim 10^{-3}$ mag.</p>
Main cause of errors	<p>Systematic errors: pixel variations/detector read noise for faint stars, fewer observations for brightest stars, photon noise for fainter stars ($V \sim 10 - 14$).</p>
References	<p>FAME homepage [2] Johnston [70]</p>

Experiment	<i>Deutsches Interferometer für Vielkanalphotometrie und Astrometrie (DIVA from Germany)</i>
Description	<p>The first time an homogeneous astrometric sky survey will be performed in at least 6 wavelength bands in the optical regime.</p> <p>A small satellite equipped with, as main instrument, a beam combining mirror analogous to Hipparcos, which brings the light from 2 simultaneous fields of view (separation $\sim 100^\circ$ and $0.6^\circ \times 0.6^\circ$) to a common focal surface.</p> <p>Spectral dispersion in a direction to the direction of the scan is enabled by a diffraction grating on the folding mirror.</p> <p>It will operate in a similar revolving scanning mode as Hipparcos on a highly eccentric orbit, with a 24 hour revolution, and an apogee at about 70 000 km.</p>
1st intended goal	<p>To fill the gap between Hipparcos and GAIA missions.</p> <p>To measure positions, motions and parallaxes of $35 \cdot 10^6$ stars, plus spectrophotometry.</p> <p>This should allow learning about the structure of the Galaxy, star forming regions, extragalactic objects, kinematics of stars clusters/associations/LMC/SMC, cosmic distance scale, etc.</p>
How it happens to be measuring γ	<p>In the same implicit way as Hipparcos does.</p>
Start-End	<p>Launch in 2004.</p> <p>Planned operational lifetime of 2 years.</p> <p>Results in 2008.</p>
Advantages	<p>Same advantages as Hipparcos over ground-based experiments (\leftrightarrow VLBI).</p> <p>Multiple observations are made with the same instruments (\leftrightarrow eclipses).</p> <p>Individual observations are 5 times more precise \leftrightarrow Hipparcos.</p> <p>Fringe dispersion enables simultaneous astro-/photo-metric measurements with the same equipment.</p> <p>It will probe a larger volume of our Galaxy: 300 times more objects \leftrightarrow Hipparcos.</p> <p>The survey is unbiased from any a priori selection/input catalogue, thanks to an on board real-time object detection (\leftrightarrow Hipparcos).</p> <p>It is a low cost space mission (10% of Hipparcos), successor of Hipparcos, an important step towards GAIA that will allow intermediate results and test data reduction methods for GAIA.</p>
Drawbacks	<p>The measurements are at large angles from the gravitational deflector (45° avoidance angle for the Sun), thus the signal (deflection) is weaker (\leftrightarrow eclipses).</p> <p>Same drawbacks as Hipparcos in comparison with pointing missions (\leftrightarrow SIM).</p> <p>For a short mission length, the scanning law gives a coverage of the sky which is not completely homogeneous.</p>

Precision	It should result in $\sim 10^{-4}$ precision on γ , based on multiple observations of $\pm 35 \cdot 10^6$ stars (limiting mag. (V) ~ 17.2 , completeness to at least (V) ~ 15), with individual accuracies ± 5 times better than Hipparcos. For example for V=10, K0 stars: parallaxes ~ 0.19 marcsec, proper motions ~ 0.24 marcsec/year, photometry ~ 0.0007 mag. For more than 100 000 stars, its observations could be combined with Hipparcos to lead to an accuracy of $\sim 0.1 - 0.2$ marcsec/year on proper motions.
Main cause of errors	Attitude determination, instrument calibration; photon noise for bright stars, readout noise for fainter stars.
References	DIVA homepage [1] Röser [122, 123, 124, 125]



SIM satellite (NASA).

Experiment	<i>Space Interferometric Mission (SIM from NASA's Origin Program)</i>
Description	<p>First pointing spacecraft mission to use optical (400-1000 nm) interferometry. Complementary to GAIA mission.</p> <p>Equipped with 3 colinear, long-baseline, Michelson stellar interferometers (2 for precise measurement of the spacecraft attitude and one for science targets) mounted on a 10-meter long boom. SIM field of view is 15° with a basic reach of about 25 kpc.</p> <p>Equipped with an achromatic on-axis nulling technique (precision 10^{-4} at 5000 Å) to block out light from bright stars to observe the faint environment around them. It allows rotational synthesis imaging V resolution ~ 10 marcsec at 500 nm.</p> <p>It allows wide-angle astrometry, by creating an astrometric reference grid with a precision of $\sim 4 \mu\text{marcsec}$, a model of the positions and motions of particular objects that evenly covers the entire sky (± 4000 stars, quasars, of magnitude 13 to 20, and at least one object by 10 square degrees). Relative angles between objects are not directly measured, but interrelated time delays are.</p> <p>Will observe the grid a few times/year ($\sim 25\%$ of mission time) to recalibrate.</p> <p>Will operate in an Earth trailing solar orbit, slowly drifting away from the Earth at ± 0.1 AU per year.</p> <p>Equipped with propulsion systems that will allow scientist to change/choose its pointing direction for different science targets (with pointing axis $> 45^\circ$ from the Sun to protect the viewing optics).</p>
1st intended goal	<p>To measure precisely the position, parallaxes and distances of stars throughout the Galaxy ($\pm 10^5$ science and grid targets), to probe nearby stars for Earth-sized planets (nulling technique, good resolution in imaging), study time criteria targets (variables, binaries...) and complex sources (multiple points, extended sources...), improve the knowledge of the gravitational potential of the Galaxy and evaluate the rotation curve.</p> <p>The first point will determine the composition, formation and evolution of our galaxy, by providing tests to the various theories and models.</p>
How it happens to be measuring γ	<p>In the same implicit way as Hipparcos does.</p> <p>Choosing the pointing direction of the spacecraft would allow an additional active measuring of the change in angular separation of light sources due to the gravitational bending of light.</p>
Start-End	<p>Launch in 2009.</p> <p>Calibration period of 6 months after launch.</p> <p>Planned operational lifetime of 5 years.</p>

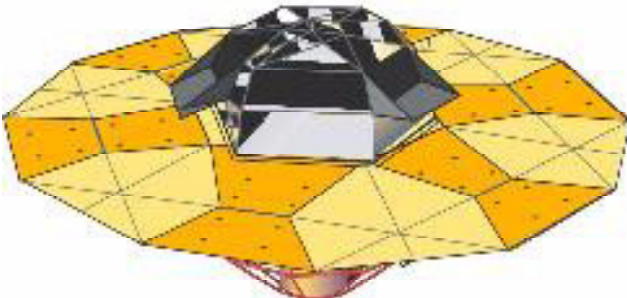
Advantages	<p>Same advantages as Hipparcos over ground-based experiments (\leftrightarrow VLBI).</p> <p>Multiple observations are made with the same instruments (\leftrightarrow eclipses).</p> <p>Ability to point at a single source for an extended period of time, unlike survey missions. Scientists can choose the pointing direction if their experiment is voted, an active measurement of gravitational light deflection, detection of microlensing events, is thus possible (\leftrightarrow Hipparcos, DIVA, GAIA).</p> <p>Individual observations are much more precise (\leftrightarrow Hipparcos) and the possibility to point at a single source for a longer period, together with real-time monitoring of the baseline, allow higher accuracy on targets so faint ($V \sim 20$) they cannot even be detected by GAIA. It can reach similar individual accuracies as survey missions (where the accuracy is obtained when the mission is fully completed) but in one single observation (\leftrightarrow Hipparcos, DIVA, GAIA).</p> <p>Ability to serve as a potential test bed for new technology developments (nulling capability).</p>
Drawbacks	<p>The measurements are at large angles from the Sun (pointing axis $> 45^\circ$ from the Sun), thus the signal (deflection) is weaker (\leftrightarrow eclipses).</p> <p>It is not constantly obtaining data as it scans the sky: time is limited by pointing manoeuvres and settling time (200 s for a 12 magnitude measurement, 14 hours at magnitude 20)(\leftrightarrow Hipparcos, GAIA). A large fraction of the mission time will also be devoted to maintaining the grid.</p>
Precision	<p>A factor 10 or 100 more accurate than Hipparcos.</p> <p>Fainter limiting magnitude ($V \sim 20$) and better individual accuracy even than GAIA.</p> <p>It should be sensitive to light bending by Jupiter and the other massive planets. Solar J_2 might be detected, as well as frame dragging from the rotation of the Sun and planets.</p> <p>Determination of distances in the Galaxy with a precision of 10 % out of 25 kpc: parallaxes $\sim 4 \mu\text{arcsec}$, proper motions $\sim 1 - 2 \mu\text{arcsec/year}$.</p> <p>In small angles/differential astrometry ($< 15^\circ$), the individual accuracies are $1 \mu\text{arcsec}$ over a small 1° field. At larger angles ($> 15^\circ$), the precision on absolute positions is $\sim 4 \mu\text{arcsec}$.</p> <p>With such a precision, light modulation effects due to gravitational lensing by MACHOs must be considered.</p>
Main cause of errors	<p>Unmodelled errors, mostly field dependent errors in the metrology fiducials.</p>
References	<p>SIM homepage [9]</p> <p>SISWG report [13]</p> <p>Boders <i>et al.</i> [26]</p> <p>Peterson [105]</p> <p>Peterson and Shao [106]</p>

Experiment	<i>Global Astrometric Interferometer for Astrophysics Satellite (GAIA from ESA)</i>
Description	<p>Space optical satellite performing an astrometric survey complementary to Hipparcos. Equipped with two astrometric viewing directions (separation 106° and $1700 \times 700 \text{ mm}^2$, either using a beam combiner, like Hipparcos, in front of an interferometer; or several interferometers with baselines set at a fixed angle to each other). Its payload is also composed of multicolor photometric instruments and velocity spectrometers.</p> <p>It employs interferometry (single baseline \Rightarrow one dimensional angular measurements in optical/near-infrared) to enhance resolution and hence astrometric accuracy.</p> <p>It should operate in a spinning ($T \sim$ hours) Lissajous-type, eclipse free orbit around the L2 point ($1.5 \cdot 10^6 \text{ km}$ from Earth) of the Sun-Earth system, characterized by a very high observing efficiency (since the Sun, the Earth and Moon are behind the instrument field of view) and low radiation environment. It should allow a continuous scanning of the whole sky.</p>
1st intended goal	<p>To improve on Hipparcos results in terms of accuracy, object number, limiting magnitude. To determine the composition, formation and evolution of our galaxy, by providing tests to the various theories and models. This will be achieved by providing a stereoscopic, kinematic and photometric map (an accurate set of reference directions) of more than one billion stars in our Galaxy and throughout the Local Group.</p> <p>Additional results shall include the detection and characterization of tens of thousands of extra-solar planetary systems, a comprehensive survey of objects (ranging from huge number of minor bodies in our solar system, through galaxies in the nearby universe, to some 10 millions of distant quasars)...</p>
How it happens to be measuring γ	In the same implicit way as Hipparcos does.
Start-End	<p>It should be launched before 2012 in ESA's "Horizon Plus" program.</p> <p>Planned operational lifetime of 5 years.</p> <p>Results are expected in about 8 to 10 years after launch.</p>
Advantages	<p>Same advantages as Hipparcos over ground-based experiments (\leftrightarrow VLBI).</p> <p>Multiple observations with the same instruments (\leftrightarrow eclipses).</p> <p>Individual observations much more precise (\leftrightarrow Hipparcos).</p> <p>It will probe a larger volume of our Galaxy: a large fraction of the Milky Way within its parallax horizon, including much of the halo, and even touching on the nearest companion galaxies, such as the MCs (\leftrightarrow pointing missions like SIM, previous Hipparcos astrometric mission for which $< 0.1 \%$ of the volume of the Galaxy was probed by direct distance measurements).</p> <p>Observations are at smaller angles from the Sun (35° avoidance angle) (\leftrightarrow Hipparcos, DIVA, SIM), which increases the deflection signal.</p> <p>(...)</p>

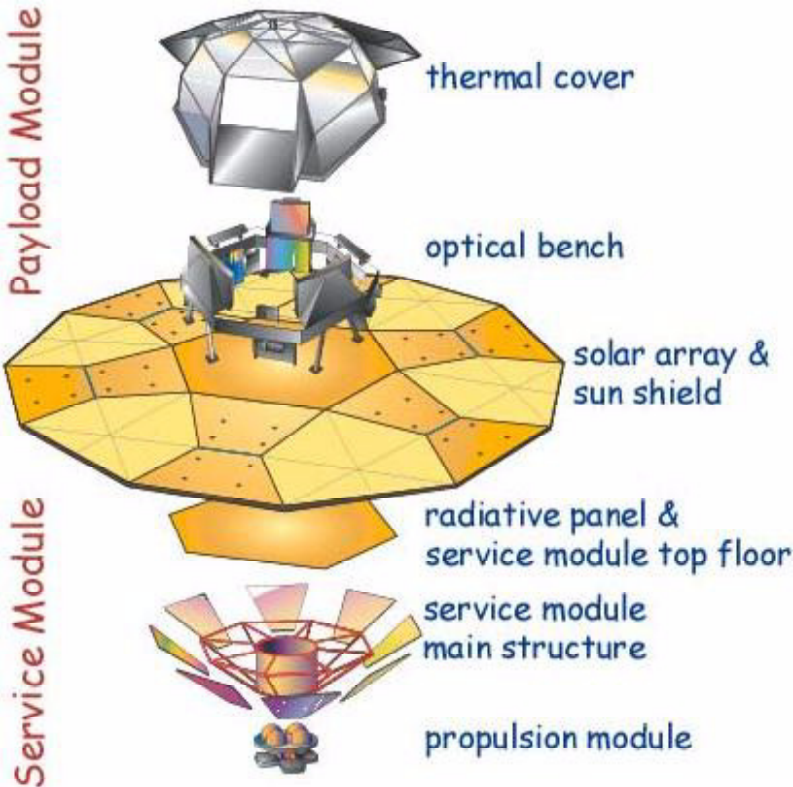
<p>(...) Advantages</p>	<p>The limiting magnitude is sufficiently faint to allow a <i>direct</i> link with the extragalactic system by observation of quasars to establish the inertial reference frame (↔ Hipparcos). The basic angular variations of the beam combiner (a source of errors in angular positions) are reduced/monitored, thanks to a powerful set of laser metrology.</p>
<p>Drawbacks</p>	<p>The measurements are at large angles (35° avoidance angle) from the Sun (↔ grazing incidence is possible for the planets), thus the signal (deflection) is weaker (↔ eclipses). Same drawbacks as Hipparcos in comparison with pointing missions (↔ SIM).</p>
<p>Precision</p>	<p>It will extend the domain of observations by two orders of magnitude in the length scale (now $10^9 - 10^{21}$ m) and six orders of magnitude in the deflector mass scale (now $1 - 10^{14}$ solar masses). For example, it should be sensitive to light bending by the Earth. It should result in a precision of about $5 \cdot 10^{-7}$ (or better) on γ, based on multiple observations of about $35 \cdot 10^6$ ($V=15$) to $3 \cdot 10^8$ ($V=18$) stars (limiting magnitude and completeness (V) $> 15 - 16$), at wide angles from the Sun, with individual measurement accuracies of $5 - 20 \mu\text{arcsec}$. This will go along with multi-color, multi-epoch photometry of each object. As a result too, distance and kinematical motions of tens of millions of objects should be known with an accuracy such that direct (trigonometric distance to galactic center) estimates would be accurate to 10% at 10 kpc, and transverse motions to 1 km/s at 20 kpc. At this level of accuracy, light modulation effect due to gravitational lensing by MACHOs and possible metric perturbations due to gravitational waves must also be considered. Also, subtle effects will start to become apparent: quadrupole moment of the gravitational deflectors and the “frame dragging” effect of their motions and rotations.</p>
<p>Main cause of errors</p>	<p>Still a correlation between the deflection and parallactic displacements.</p>
<p>References</p>	<p>GAIA homepage [3] GAIA Study Report [15] Lindgren and Perryman [80, 81] Perryman <i>et al.</i> [104]</p>



The GAIA satellite orbit.



GAIA satellite.



GAIA satellite, split picture of the different payload components.

Experiment	<i>Télemétrie Inter-Planétaire Optique (TIPO)</i> <i>coordinated through OCA/CERGA (France)</i> <i>a proposal to be submitted to CNES in response to a call for mission proposals for "Mars Sample Return".</i>
Description	One way (Earth - Mars orbiter) laser telemetry. The Mars orbiter is equipped with an ultra-stable rubidium clock (stability in frequency: $6.5 \cdot 10^{-13} T^{-1/2}$ with $T < 10\,000$ s or $T < 100\,000$ s if the oscillator frequency is corrected; precision in frequency: 10^{-12} or respectively 10^{-14}), a dater and an optical receptor with an aperture of 100 mm pointing towards the Earth to be used when orbiting Mars. There is an identical optical receptor on the first level of the vehicle to be used during the Earth-Mars journey. The laser is a doubled NdYag 532 nm providing pulses at a frequency of ~ 10 Hz.
1st intended goals	Scientific: <ul style="list-style-type: none"> - validate optical interplanetary telemetry, - Mars orbit determination, - Mars' mass determination, - study electromagnetic wave propagation, - measure PN parameter γ, - measure solar and Martian atmospheres, - validate future telemetric studies with more precise clocks (10^{-16} in ν) Technological developments.
How it happens to be measuring γ	Time-delay measurements: short laser pulse signals sent from the Earth are recorded by precise clocks on board of a Mars orbiter and dated. This set of dates is downloaded via the usual Orbiter-Earth link, and compared with the set of dates of Earth emissions. The signature of the relativistic time delay is superimposed to the orbit signature in particular. The experiment will be carried out around the period of the solar conjunction with Mars (at two solar radii) on 5th December 2008.
Start-End	Orbiter to be launched in 2007. Start of Mars orbit mission in September 2008.
Advantages	
Drawbacks	
Precision	$2.5 \cdot 10^{-5}$ on γ for $T < 10\,000$ s, or $7 \cdot 10^{-6}$ for $T < 100\,000$ s (rough estimate based solely on the accuracy of clocks, neglecting the errors in orbit determination).
Main cause of errors	Errors in the orbit determination.
References	Samain [126, 127]

Experiment	<i>Astrodynamical Space Test of Relativity using Optical Devices (ASTROD) a proposal submitted to ESA in response to “Call for Mission Proposals for 2 Flexi-Missions F2/F3”.</i>
Description	A desirable implementation is 2 spacecrafts in separate solar orbits, carrying a payload of a proof mass, 2 telescopes, 2 1-2W lasers, laser detectors, a stable clock, and a drag-free system together with an earth reference system. However, a minimal project for the mission, mini-ASTROD, has also been proposed, with only one spacecraft ranging optically with ground stations.
1st intended goal	Testing the relativistic gravity with 3-6 orders of magnitude improvement (γ , β , G). Detect and observe gravitational waves from massive black holes and galactic binary stars in $\Delta\nu \in [50 \mu\text{Hz}, 5 \text{mHz}]$, as well as background gravitational waves. High precision measurements of solar system parameters (J_2_{Sun} , masses, \vec{J}_{Sun}).
How it happens to be measuring γ	Through time-delay measurements using the same principle as the SORT project. (Atomic Clock Ensemble in Space) on the IIS (International Space Station) by 2003-2004.
Start-End	The project has been proposed, not yet accepted. Normal lifetime of the mission: 3 years, with possibility to extend to 8 years.
Advantages	Laser ranging extended to the whole solar system (\leftrightarrow LLR only) using a dragfree spacecraft dramatically improves GR tests and allows many applications: solar physics, measurement of J_2_{Sun} that contributes to light deflection, etc.
Drawbacks	
Precision	Certainly $10^{-6} - 10^{-7}$ on γ and possibly 10^{-9} if the stability of the laser clocks can be improved to 10^{-18} , and the range data is used.
Main cause of errors	As the stability of clocks and ranging improves, the limitations of the precision on γ will be mainly due to the atmosphere. Monitoring of atmospheric effects and ground motion through two-ways tracking, or using either an Earth satellite or a spacecraft near the Earth- Sun Lagrange point might help eliminate atmospheric effects from time-delay measurements.
References	Bec-Borsenberger <i>et al.</i> [22]

Experiment	<i>Solar Orbit Relativity Test (SORT) coordinated through ESA</i>
Description	Rely on drag-free control and high precision accelerometers.
1st intended goal	Measuring the light deflection and the time delay.
How it happens to be measuring γ	Time-delay measurements: laser signals sent from the Earth are recorded by precise clocks on board 2 satellites orbiting the Sun on separate orbits. This time-delay variation is recorded over a time interval to minimize the systematic errors. Light deflection experiment through interferometric measurement on Earth of the angle between 2 light flashes emitted from the 2 satellites orbiting the Sun. This project has led to the development of the PHARAO clock (Projet d'Horloge Atomique par Refroidissement d'Atomes en Orbite) and of T2L2 (Transfer de temps par Lien Laser) with a predicted accuracy of ~ 30 ps, that should be tested on the ACES project (Atomic Clock Ensemble in Space) on the IIS (International Space Station) by 2003-2004.
Start-End	Only after 2010.
Advantages	
Drawbacks	
Precision	10^{-7} on γ .
Main cause of errors	
References	Reinhard [112]

2 In the radio waveband

The VLBI γ -estimates in the following tables are either based on a relatively small number of observations at small angles from the Sun, during the quiet phase of the solar cycle (VLBI I) [78]; or on a larger number of observations collected for other purposes⁴³, generally at larger angles from the Sun (VLBI II). But, as we quote from reference [78], “...*(There is a plan) to combine the independent data obtained from VLBI I and VLBI II in order to lower substantially the uncertainty in γ . Collaboration is also investigated with the Jet Propulsion Laboratory for an improved version of the VLBI I experiment that would utilize several compact reference sources surrounding (on the sky) an occulted source, and employ more and more sensitive antennas. (...) (this) should yield a result for gravitational deflection several folds more accurate than the one presented here*”.

⁴³ Like for the “POLar-motion Analysis by Radio Interferometric Surveying” (POLARIS) and the “International Radio Interferometric Surveying” (IRIS), which are projects conducted by the National Oceanic and Atmospheric Administration; or the “Crustal Dynamic Project” (CDP) launched by the National Aeronautic and Space Administration. Notice that, in their publication of 1984 [115], Roberston *et al.* also included results from the “Monitor Earth Rotation and Intercompare the Techniques of observation and analysis” project (MERIT).

Experiment	<i>Very Long Baseline Interferometry (VLBI) type I (original classical experiments) coordinated through the International VLBI Service for Geodesy and Astrometry (IVS)</i>
Description	<p>Ground-based radio-interferometry.</p> <p>Over a period of 1-2 weeks, a set of VLBI antennas tracks 2 or more radio sources (usual angular separation $\pm 5 - 10^\circ$) around the time one of them is occulted (or nearly) by the Sun. The classical experiment consists of observing 3C273B (reference source) and 3C279, 10° apart, 1 or 2 weeks before and after the occultation of 3C279 which occurs around 8th October each year. (The quasar 3C48 and the group O111+02, O119+11 and O116+08 were also used in other measurements).</p> <p>The sources are observed simultaneously in at least 2 widely separated frequency bands (e.g., 2 and 8, 23 GHz) in order to correct the measured additional differential delays in the antennas resulting from the bending effect in the solar corona. It also helps to guard against frequency-specific nulls in the fringe visibility of either source.</p> <p>The antennas used were the 40 m and one of the 27 m \emptyset at the Owens Valley Radio Observatory, CA, USA, and the 37 m and 18 m \emptyset antennas at the Haystack Observatory, MA, USA. Two antennas are used (each larger antenna at 23 GHz, and smaller antennas at 2, 8 GHz) at each site because no single antenna was equipped for simultaneous observations in 3 frequency bands.</p> <p>Both observatories use the Mark-III VLBI system for data acquisition and correlation.</p>
1st intended goal	Specifically designed to measure gravitational light deflection through the apparent displacement of a chosen light source with respect to another reference light source.
How it happens to be measuring γ	<p>Data obtained simultaneously at the same frequency from 2 antennas, each on different sites, are cross-correlated to estimate the difference in the phase of the signal as a function of time (\equiv fringe phase). Group delays (\equiv the derivative of the fringe phase with respect to the angular frequency) are used instead of phase delays (\equiv the fringe phase divided by the angular frequency), even though the second ones are inherently more precise, they have narrowly spaced ambiguities stemming from the 2π ambiguities in the fringe phase.</p> <p>A parametrized theoretical model of the delays is then fitted to the measurements in order to obtain γ. This is an active determination.</p>
Start-End	
Advantages	Large bending signal (\leftrightarrow VLBI II).
Drawbacks	<p>Smaller data sets (\leftrightarrow VLBI II).</p> <p>It does experience the perturbations from the atmosphere, baryometric pressure loading, gravitational and thermal flexure of telescopes... Hence, at some point, improvements in measuring γ will depend critically on the ability of modelling those effects (\leftrightarrow satellites).</p> <p>Observations were made with antennas that had different characteristics.</p>

Precision	$\gamma = 0,9996 \pm 0,0017$ ($\sim 10^{-3}$ precision), corresponding to a deflection $0,9998 \pm 0,0008$ times that predicted by GR.
Main cause of errors	Uncertainties in the knowledge of pole position, time delays due to Earth atmosphere and to the difference in the atomic-clock readings at the two observational sites. However, in general, uncertainties on γ are more sensitive to those factors in the experiment that affect the delays differently on different days (e.g. delays due to the atmosphere), and are virtually insensitive to factors that affect the delays in the same way each day (e.g. delays related to the observational site).
References	Creyn [32] Lebach <i>et al.</i> [78] Will [143]



VLA array structure.

Experiment	<i>Very Long Baseline Interferometry (VLBI) type II coordinated through the International VLBI Service for Geodesy and Astrometry (IVS)</i>
Description	<p>Ground-based radio-interferometry.</p> <p>A cooperation between more than 29 observatories (between 1980 and 1990; since then, more might have joined in the various programs), working on the projects POLARIS, IRIS, and CDP, and involving routine application of VLBI observations devoted to geodesy.</p> <p>All use the Mark-III VLBI system for data acquisition and correlation.</p> <p>Typically, an experiment lasts 24 hours and involves observations of 20-50 sources spread over as much of the sky as can be seen from the observing sites.</p>
1st intended goal	To monitor the polar motion, Earth rotation, construct a geodetic network to study plate tectonics.
How it happens to be measuring γ	<p>The observing schedules were not planned to optimize the determination of γ but fortunately, a large set of radio sources used laid near the ecliptic and thus had small Sun angles at certain time of the year. The change in angular separation between two or more radio sources was thus recorded. Moreover, these observations, in dual X-S frequency (enabling removal of deflection due to the solar corona and the Earth ionosphere), have the requisite angular resolution and are broadly distributed at different angles from the Sun: a set of 342 810 group-delay observations, 74 radio sources, 214 observations at an angle from the Sun $< 3^\circ$ and 592 observations at $< 6^\circ$.</p> <p>Data from multiple experiments spaced over a year or more can be combined and thus changes in the apparent source positions can be measured, even for sources that never come close to the Sun.</p> <p>Least-squares adjustments of the \neq parameters (including γ, but also source coordinates, baseline coordinates, polar motion and the Earth rotation parameters, clock error coefficients, atmospheric Smith-delay parameters) are then made to determine γ. The determination is implicit.</p>
Start-End	The data taken into account by D.S. Robertson <i>et al.</i> in their article of 1991 comes from observations between 1980 and 1990. The project is still working with more than 20 years of activity now.
Advantages	<p>Over almost the entire celestial sphere (\leftrightarrow eclipses).</p> <p>The project is still running! The set of observations is enlarging (\leftrightarrow eclipses). With time, we might expect a more precise measurement of γ.</p> <p>The apparent displacement of the light sources is 1 year periodic, which allows to decrease the correlation between γ and other parameters in the fitted solution (mostly source coordinates). The usual sources of systematic errors for VLBI observations (atmosphere, clock effects station and source coordinates errors) are really weakly correlated with γ estimates.</p> <p>(...)</p>

<p style="text-align: center;">(...) Advantages</p>	<p>Measurements are more accurate thanks to:</p> <ul style="list-style-type: none"> - a longer baseline (mainly $3 \cdot 10^3$ km in the 1984, $7 \cdot 10^3 - 10^4$ km in the 1990 results), - improved data processing software (modelling of atmospheric refraction; adjustments in tectonic plate velocities, to the Earth tide Love numbers, nutation, relativistic propagation of the radio-wave in the Earth gravitational field), - dual band X-S frequency allows to remove solar corona and Earth ionospheric deflection, - improved instruments (double spanned bandwidth, and eightfold increase in the recorded bandwidth and an improved delay/phase-calibration equipment). <p>Basing the determination of γ on the observation of many light sources leads to very little correlation between γ and the source parameters (\leftrightarrow original classical VLBI).</p> <p>The number of observatories involved is increasing (improved sky coverage):</p> <ul style="list-style-type: none"> - observatories from the southern hemisphere are joining (southern hemisphere radio sources not yet included in these 1991 results), - new observing stations. <p>The next sunspot minimum should be accompanied with reduced solar corona activity, allowing observation closer to the solar limb.</p>
<p style="text-align: center;">Drawbacks</p>	<p>It does experience the perturbations from the atmosphere, errors in the nutation model used to reduce the observations, baryometric pressure loading, gravitational and thermal flexure of telescopes... Hence, at some point, improvements in measuring γ will depend critically on the ability of modelling those effects (\leftrightarrow satellites).</p>
<p style="text-align: center;">Precision</p>	<p>$\gamma = 1.000 \pm 0.002$ ($\sim 10^{-4}$precision) in results given by [116], or according to [143], $\frac{1+\gamma}{2} = 0.99992 \pm 0.00014$ for the Sun. The precision since 1991 has increased since the number N of geodetic experiments has increased. However, only 50% accuracy is reached for the light deflection by Jupiter. D.S. Robertson <i>et al.</i> foresee an inevitable improvement in measurements by a factor 2 or 5 in the decade (from 1991!), or maybe a full order of magnitude.</p> <p>Even though the angular positions of the sources are only accurate to ~ 1 marcsec (the accuracy obtained from a few geodetic experiments is much worse than that from only one classical VLBI experiment), it is the very large number of geodetic experiments that decrease the error, simply by means of root-N (\leftrightarrow VLBI type I).</p>
<p style="text-align: center;">Main cause of errors</p>	<p>Refraction of the radio-waves in the solar corona, at small angles from the Sun, leads to an additional bending correction which is stronger in the radio than in the optical waveband (\leftrightarrow Hipparcos, GAIA), thus observations are collected during solar quiet periods.</p> <p>However, the main problem at large angles lies in effects like unmodelled atmosphere refraction, despite their small correlation with γ; together with relative time offset between stations clocks.</p>
<p style="text-align: center;">References</p>	<p>Robertson and Carter [115, 116] Will [143]</p>

Experiment	<i>VLBI Space Observatory Program (VSOP) coordinated through JPL Space Very Long Baseline Interferometry project (NASA) and several collaborations</i>
Description	The project associates space telescopes to the existing VLBI network of Earth observatories (40 telescopes from more than 15 countries in 1999) to create a virtual radio telescope > 3 times the Earth diameter. A Japanese satellite, HALCA, was launched into an elliptical Earth orbit to co-observe with the international collaboration of radio telescopes.
1st intended goal	Routine radio science observations with scientific goals such as: <ul style="list-style-type: none"> - high resolution imaging of Active Galactic Nuclei (AGN), - monitoring structural changes in superluminal sources, - measuring proper motion as a function of z in AGN, - distribution of spot sizes in OH maser sources, - high resolution imaging of radio stars.
How it happens measuring γ	In the same way recent VLBI observations did.
Start-End	<ul style="list-style-type: none"> - HALCA (Japan) launched in 1997, - Radioastron (Russia) to be launched in 2002, - VSOP2 (Japan) to be launched in 2007, 10 times more sensitive than HALCA, - ALFA (Astronomical Low Frequency Array), a cluster of small satellites operating as a single radio telescope, far from Earth, - ARISE (Astronomical Radio Interferometry between Space and Earth), JPL project to be launched in 2008, - 30 meter antenna on board the Space Station Freedom (ESA) for 2010, - Milimetron (Russia), - (...)
Drawbacks	
Advantages	Increasing precision over VLBI terrestrial results. The elliptic orbit of HALCA provides a wide range of distances between the satellite and the Earth, allowing high quality image of radio sources.
References	Space VLBI homepage [10] US Space VLBI homepage [11] VSOP homepage [12]

3 Other experiments measuring γ

The PN parameter γ of course does not solely contribute to light deflection, but also to the gravitomagnetic frame dragging effect/Lense-Thirring effect $\propto (\gamma + 1 + \frac{\alpha_1}{4})$, to the de Sitter precession $\propto (\gamma + \frac{1}{2})$, to the time delay of radio signals $\propto (\gamma + 1)$, to the precession of celestial bodies $\propto (2 + 2\gamma - \beta)$, or to the Nordtvedt effect testing the Weak and Strong Equivalence Principles $\propto \eta = (4\beta - \gamma - 3)$ [143]... As such, various tests in the past, like ranging data using the time delay to landers (Viking [110], etc) or spacecrafts (NEAR [52]), the precession of Mercury and Icarus, lunar laser ranging..., have been used or are still used. However, VLBI experiments using light deflection or time delay so far provide the best determination of γ . In the future, some experiments will improve on the present determination of γ by other means than the change in apparent position of a light source (preceeding paragraph), see the following table.

Proposed space missions leading to an improvement in the estimation of γ			
References	Method	Mission	Expected precision on γ
[25] [61] [68]	Doppler measurement of the Solar gravitational deflection, the first time this method is used	Cassini launched in 1997, experiment in 2002-2003	$10^{-4} - 10^{-5}$
[5] [15] [54]	relativity gyroscope experiment, geodetic precession measurement	Gravity Probe B (2002)	$6 \cdot 10^{-5}$
[8] [131] [134]	output of orbit determination of the orbiter, time-delay and Doppler-shift measurements	Mercury Orbiter, within BepiColombo (2007/2009) chosen as the 5th or 6th Cornerstone Mission of the Horizon 2000 Scientific Plan of ESA	$2.5 \cdot 10^{-6}$
[112] [130]	Projet d'Horloge Atomique par Refroidissement d'Atomes en Orbite (PHARAO clock), a swiss hydrogen maser clock to provide a long term frequency standard, associated with the IIS, to form the Atomic Clock Ensemble in Space (ACES) for time-delay measurements	International Space Station (IIS) (2004/2005)	$1 \cdot 10^{-5}$

- Massive, helicity-2, KK propagator, see expressions (1.40) and (1.46):

$$\overset{-\text{KK } n}{\text{O}}_{\mu\nu}(q)$$



$$iG_{(\vec{n} \neq 0)}^{\mu\nu, \alpha\beta}(q) = i \frac{\eta^{\mu\alpha} \eta^{\nu\beta} + \eta^{\mu\beta} \eta^{\nu\alpha} - \frac{2}{3} \eta^{\mu\nu} \eta^{\alpha\beta}}{q^2 - m_n^2 + i\varepsilon}$$

- Massive gravitational scalar-field propagator, see expressions (1.40) and (1.46):

$$q$$



$$iG_{(\vec{n} \neq 0)}(q) = i \frac{1}{q^2 - m_n^2 + i\varepsilon}$$

External lines

The normalization factor ($\frac{1}{\sqrt{2V} \text{Energy}}$) where V is the volume of space, times the polarization matrix for photons (ε_r^α) are used to write the external lines of the

- Matter massive scalar field:

$$\Psi_{m k} \xrightarrow{k} \bullet \frac{1}{\sqrt{2V} \omega_k}$$

- Electromagnetic field (photon):

$$\gamma_{p,r} \xrightarrow{\varepsilon_\lambda^\alpha(p)} \bullet \frac{\varepsilon_r^\alpha(p)}{\sqrt{2V} \omega_p}$$

Vertices

We have seen, in the linearized action (1.40), that the interaction of the massive helicity-2 Kaluza-Klein states with matter reduces to:

$$-\sqrt{\frac{\kappa}{2}} \sum_{\vec{n} \neq 0} \int dx^{(4)} \left(h^{(\vec{n})}{}_{\mu\nu} T_m^{\mu\nu} + \beta_{LED} \Phi^{(\vec{n})} T_m \right),$$

while for zero-mode graviton and scalar field, according to (1.38), it is given by

$$-\sqrt{\frac{\kappa}{2}} \int dx^{(4)} \left(h_{\mu\nu}^0 T_m^{\mu\nu} + \alpha_{LED} \Phi^0 T_m \right).$$

The expression of the electromagnetic-field action,

$$I_m^{(phot.)} = \int d^{(4)}x \sqrt{-g} \left(-\frac{1}{4} g^{\mu\nu} g^{\rho\sigma} F_{\mu\nu} F_{\rho\sigma} \right),$$

leads to the energy momentum for a photon

$$T_{m \mu\nu}^{(phot.)} = - (g^{\rho\sigma} F_{\mu\rho} F_{\nu\sigma}) + \frac{1}{4} g_{\mu\nu} (g^{\mu\nu} g^{\rho\sigma} F_{\mu\nu} F_{\rho\sigma}) \quad \text{with } F_{\mu\nu} = \partial_\mu A_\nu - \partial_\nu A_\mu;$$

while from the matter action for a massive scalar field Ψ_m ,

$$I_m^{(scal.)} = \int dx^{(4)} \sqrt{-g} \left(\frac{1}{2} \Psi_{m,\mu} \Psi_m^{\cdot\mu} - \frac{1}{2} m_\Psi^2 \Psi_m^2 \right),$$

one deduces the following tensor:

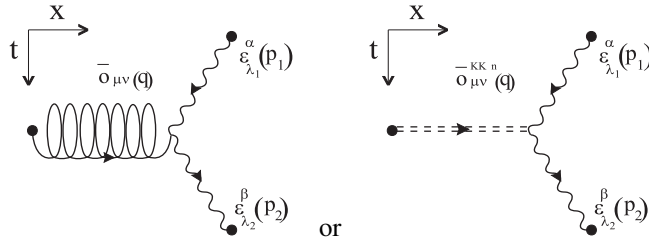
$$T_{m\mu\nu}^{(scal.)} = \frac{1}{2} \left(-\Psi_m^{\cdot\sigma} \Psi_{m,\sigma} + m_\Psi^2 \Psi_m^2 \right) g_{\mu\nu} + \Psi_{m,\mu} \Psi_{m,\nu}.$$

Consequently, to obtain the corresponding vertices, one just needs to proceed through the following steps:

1. Fourier transform the respective linearized interaction terms,
2. symmetrize over the initial and final states $1 \leftrightarrow 2$,
3. associate the appropriate coupling constant $-\sqrt{\frac{\kappa}{2}}$, $-\alpha_{LED} \sqrt{\frac{\kappa}{2}}$ or $-\beta_{LED} \sqrt{\frac{\kappa}{2}}$ to each vertex, plus a factor $-i$.

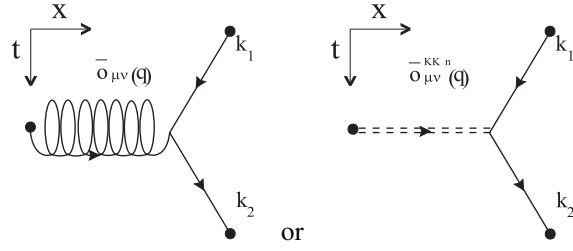
The result is given by the following expressions, for a photon of polarization $\varepsilon_r^\alpha(p)$ and 4-momentum p^μ , or a massive scalar field of mass m_Ψ and 4-momentum k^μ .

- Photon – helicity-2 gravitational fields vertices:



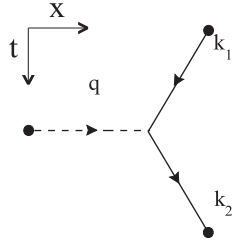
$$\begin{aligned}
 V_{\alpha,\beta,\rho\sigma}(p_1, p_2) &\equiv (-i) \left(-\sqrt{\frac{\kappa}{2}} \right) \left[\begin{array}{l} + \left\{ \begin{array}{l} -p_{1\alpha} p_{2\beta} \eta_{\rho\sigma} \\ -p_{2\alpha} p_{1\beta} \eta_{\rho\sigma} \end{array} \right\} + \left\{ \begin{array}{l} +p_{1\alpha} \eta_{\beta\sigma} p_{2\rho} \\ +p_{2\alpha} \eta_{\beta\rho} p_{1\sigma} \end{array} \right\} \\ + \left\{ \begin{array}{l} +\eta_{\mu\alpha} p_{2\nu} p_{1\beta} \\ +\eta_{\mu\beta} p_{1\nu} p_{2\alpha} \end{array} \right\} + \left\{ \begin{array}{l} -\eta_{\mu\alpha} \eta_{\nu\beta} (p_1 \cdot p_2) \\ -\eta_{\mu\beta} \eta_{\nu\alpha} (p_1 \cdot p_2) \end{array} \right\} \\ -\eta_{\alpha\beta} (p_1 \cdot p_2) \eta_{\rho\sigma} \\ -\eta_{\alpha\beta} p_{2\rho} p_{1\sigma} \end{array} \right] \\
 &= (-i) \left(-\sqrt{\frac{\kappa}{2}} \right) \left[\begin{array}{l} +\eta_{\mu\nu} (\eta_{\alpha\beta} p_1 \cdot p_2 - p_{1\beta} p_{2\alpha}) \\ + \left\{ \begin{array}{l} -p_1 \cdot p_2 \eta_{\mu\alpha} \eta_{\nu\beta} + \eta_{\nu\beta} p_{1\mu} p_{2\alpha} + \eta_{\nu\alpha} p_{1\beta} p_{2\mu} - \eta_{\alpha\beta} p_{1\mu} p_{2\nu} \\ + (\mu \longleftrightarrow \nu) \end{array} \right\} \end{array} \right].
 \end{aligned}$$

- Matter massive scalar field – helicity-2 gravitational fields vertices:

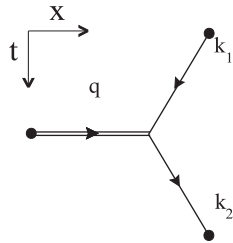


$$V_{\mu\nu}(k_1, k_2) \equiv (-i) \left(-\sqrt{\frac{\kappa}{2}} \right) \left[-\eta_{\mu\nu} k_1 \cdot k_2 + \eta_{\mu\nu} m_{\Psi}^2 + (k_{1\mu} k_{2\nu} + k_{1\nu} k_{2\mu}) \right].$$

- Matter massive scalar field – gravitational scalar field vertices:



$$V^{(\vec{n}=0)}(k_1, k_2) = (-i) \left(-\alpha_{LED} \sqrt{\frac{\kappa}{2}} \right) \left[-2(k_1 \cdot k_2) + 4m_{\Psi}^2 \right],$$



$$V^{(\vec{n} \neq 0)}(k_1, k_2) = (-i) \left(-\beta_{LED} \sqrt{\frac{\kappa}{2}} \right) \left[-2(k_1 \cdot k_2) + 4m_{\Psi}^2 \right].$$

2 Light deflection process in LED theories

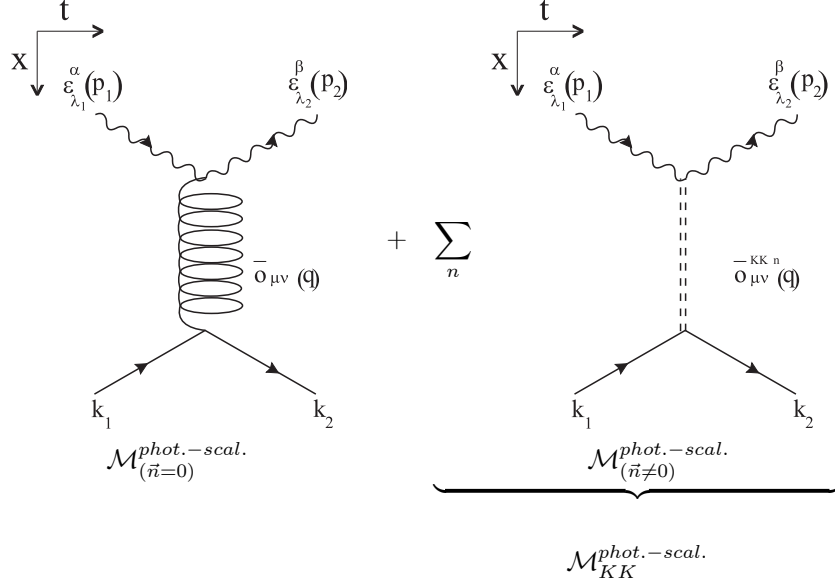
The corresponding diagrams

Light deflection can be seen as the scattering of a photon (γ) onto a gravitational potential represented by a massive scalar field (the Sun for example, Ψ_m), and mediated by the gravitational interaction:

$$\gamma_{p_1} + \Psi_{mk_1} \xrightarrow{\text{gravity}} \gamma_{p_2} + \Psi_{mk_2}.$$

However, among the KK states, only the helicity-2 and scalar states couple to matter by construction. The photon stress tensor being traceless and the scalar modes coupling only through the trace of the matter fields, solely the helicity-2 will contribute to the cited process.

Also, the massive graviton diagrams are analogous to the one associated with the usual massless graviton. Hence, we can represent light deflection by the following Feynman diagrams:



with

- the photon, γ_p ,
- the gravitational potential, Ψ_{mk} ,
- $\mathcal{M}_{(\vec{n}=0)}^{phot.-scal.}$ mediated by the massless helicity-2 graviton,
- $\mathcal{M}_{(\vec{n}\neq 0)}^{phot.-scal.}$ mediated by the helicity-2 KK massive states number n ,
- $\mathcal{M}_{KK}^{phot.-scal.}$, the contribution of all massive helicity-2 KK states,
- the transferred energy momentum, $q^\mu = p_2^\mu - p_1^\mu = k_2^\mu - k_1^\mu$.

The amplitude

From the diagrams and the Feynman rules, we obtain the following amplitude for the light deflection process:

$$\begin{aligned}
 \mathcal{M}_{LED}^{phot.-scal.} &= \mathcal{M}_{(\vec{n}=0)}^{phot.-scal.} + \mathcal{M}_{KK}^{phot.-scal.} \\
 &= \text{incoming-outcoming lines of massive scalar} \\
 &\quad * \text{vertex of massive scalar} * \text{gravitational propagators} * \text{vertex of photon} \\
 &\quad * \text{incoming-outcoming lines of photon} \\
 &= \frac{1}{\sqrt{2V\omega_{k_1}}} \frac{1}{\sqrt{2V\omega_{k_2}}} \\
 &\quad * \left[V_{\mu\nu}(k_1, k_2) * \left\{ G_{(\vec{n}=0)}^{\mu\nu, \alpha\beta}(q) + \sum_n G_{(\vec{n}\neq 0)}^{\mu\nu, \alpha\beta}(q) \right\} * V_{\alpha\beta, \rho\sigma}(p_1, p_2) \right] \\
 &\quad * \frac{\varepsilon_{r_1}^\rho(p_1)}{\sqrt{2V\omega_{p_1}}} \frac{\varepsilon_{r_2}^{*\sigma}(p_2)}{\sqrt{2V\omega_{p_2}}}.
 \end{aligned}$$

In the gravitational propagators, the $(\eta^{\mu\nu}\eta^{\alpha\beta})$ -terms will not contribute, because of the null trace of the photon:

$$0 = T^{(phot.)} \equiv \eta^{\alpha\beta} T_{\alpha\beta}^{(phot.)} \xrightarrow{\text{Fourier transform}} \eta^{\mu\nu} \eta^{\alpha\beta} * V_{\alpha\beta, \rho\sigma} = 0.$$

The amplitude thus reduces to

$$\begin{aligned}
\mathcal{M}_{LED}^{phot.-scal.} &= \frac{1}{\sqrt{2V\omega_{k_1}}} \frac{1}{\sqrt{2V\omega_{k_2}}} \\
&* \left[V_{\mu\nu}(k_1, k_2) * (-i) [\eta^{\mu\alpha}\eta^{\nu\beta} + \eta^{\mu\beta}\eta^{\nu\alpha}] \left\{ \frac{1}{q^2} + \sum_n \frac{1}{q^2 - m_n^2} \right\} * V_{\alpha\beta, \rho\sigma}(p_1, p_2) \right] \\
&* \frac{\varepsilon_{r_1}^\rho(p_1)}{\sqrt{2V\omega_{p_1}}} \frac{\varepsilon_{r_2}^{*\sigma}(p_2)}{\sqrt{2V\omega_{p_2}}}, \\
&= \frac{1}{\sqrt{2V\omega_{k_1}}} \frac{1}{\sqrt{2V\omega_{k_2}}} \frac{1}{\sqrt{2V\omega_{p_1}}} \frac{1}{\sqrt{2V\omega_{p_2}}} \\
&\quad \varepsilon_{r_1}^\rho(p_1) * \varepsilon_{r_2}^{*\sigma}(p_2) \\
&\quad * \left(-i 4 \frac{\kappa}{2} \right) * \left\{ \frac{1}{q^2} + \sum_n \frac{1}{q^2 - m_n^2} \right\} * \\
&\quad \left[\begin{aligned}
&+ \eta_{\rho\sigma} \{ (k_1 \cdot p_1)(k_2 \cdot p_2) + (k_1 \cdot p_2)(k_2 \cdot p_1) - (k_1 \cdot k_2)(p_1 \cdot p_2) \} \\
&+ (p_1 \cdot p_2) \{ k_{1\rho} k_{2\sigma} + k_{2\rho} k_{1\sigma} \} \\
&+ (k_1 \cdot k_2) \{ p_{2\rho} p_{1\sigma} \} \\
&- 1 \left\{ \begin{aligned}
&+ p_{2\rho} k_{2\sigma} (k_1 \cdot p_1) + k_{2\rho} p_{1\sigma} (k_1 \cdot p_2) \\
&+ k_{1\rho} p_{1\sigma} (k_2 \cdot p_2) + p_{2\rho} k_{1\sigma} (k_2 \cdot p_1) \end{aligned} \right\}
\end{aligned} \right] \left. \vphantom{\frac{1}{\sqrt{2V\omega_{k_1}}}} \right\} A_{LED}^{phot.-scal.} \left. \vphantom{\frac{1}{\sqrt{2V\omega_{k_1}}}} \right\} A_{LED}^{phot.-scal.}.
\end{aligned}$$

Sum and average over the polarization (helicity) of photons

Seeing that the incoming photon is not polarized, we need to sum the amplitude over the two possible polarizations of the incoming photon (\sum_{pol}). Moreover, we must average over the polarizations of the outgoing photon as we do not measure it ($\frac{1}{2} \sum_{pol}$). This leads to

$$\begin{aligned}
\overline{|A_{LED}^{phot.-scal.}|^2} &= \frac{1}{2} \sum_{\substack{pol \ \varepsilon_1 \\ pol \ \varepsilon_2}} |A_{LED}^{phot.-scal.}|^2 = \frac{1}{2} \sum_{\substack{pol \ \varepsilon_1 \\ pol \ \varepsilon_2}} \left(\varepsilon_{1\mu} \varepsilon_{2\nu}^* A_{LED}^{phot.-scal. \ \mu\nu} \right) \left(\varepsilon_{1\rho} \varepsilon_{2\sigma}^* A_{LED}^{phot.-scal. \ \rho\sigma} \right)^* \\
&= \frac{1}{2} A_{LED}^{phot.-scal. \ \mu\nu} A_{LED}^{phot.-scal. \ * \ \rho\sigma} \underbrace{\sum_{pol \ \varepsilon_1} \varepsilon_{1\mu} \varepsilon_{1\rho}}_{-\eta_{\mu\rho}} \underbrace{\sum_{pol \ \varepsilon_2} \varepsilon_{2\nu}^* \varepsilon_{2\sigma}^*}_{-\eta_{\nu\sigma}} \\
&= \frac{1}{2} A_{LED}^{phot.-scal. \ \mu\nu} A_{LED}^{phot.-scal. \ * \ \mu\nu}.
\end{aligned}$$

Using the fact that $p_i^2 = 0$ for the photon and $k_i^2 = m_\Psi^2$ for the scalar field, we find

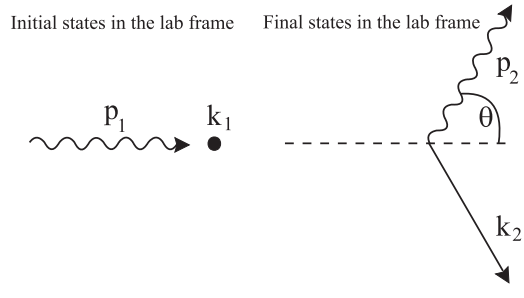
$$\begin{aligned}
\overline{|\mathcal{M}_{LED}^{phot.-scal.}|^2} &= \underbrace{\frac{1}{2V\omega_{k_1} 2V\omega_{p_1}}}_{V^2 * \text{incoming flux}} * \underbrace{\frac{1}{2V\omega_{k_2} 2V\omega_{p_2}}}_{V^2 * \text{outcoming flux}} \\
&* \frac{1}{2} \left(4 \frac{\kappa}{2} \right)^2 * \left\{ \frac{1}{q^2} + \sum_n \frac{1}{q^2 - m_n^2} \right\}^2 \\
&* \left[\begin{aligned}
&+ 8(p_1 \cdot p_2)^0 \{ (k_1 \cdot p_1)(k_2 \cdot p_2)(k_1 \cdot p_2)(k_2 \cdot p_1) \} \\
&- 4(p_1 \cdot p_2)^1 m_\Psi^2 \{ (k_1 \cdot p_1)(k_1 \cdot p_2) + (k_2 \cdot p_2)(k_2 \cdot p_1) \} \\
&+ 2(p_1 \cdot p_2)^2 \{ m_\Psi^4 \}
\end{aligned} \right] \left. \vphantom{\frac{1}{2V\omega_{k_1} 2V\omega_{p_1}}} \right\} \overline{|A_{LED}^{phot.-scal.}|^2};
\end{aligned}$$

while the 4-momentum conservation law $\delta^4((k_1+p_1) - (k_2+p_2))$ leads to

$$\overline{|A_{LED}^{phot.-scal.}|^2} = 4 \left(4\frac{\kappa}{2}\right)^2 * \left\{ \frac{1}{q^2} + \sum_n \frac{1}{q^2 - m_n^2} \right\}^2 * \begin{bmatrix} +(p_1 \cdot p_2)^0 \left\{ (k_1 \cdot p_1)^2 (k_1 \cdot p_2)^2 \right\} \\ -(p_1 \cdot p_2)^1 m_\Psi^2 \left\{ (k_1 \cdot p_1) (k_1 \cdot p_2) \right\} \\ +(p_1 \cdot p_2)^2 \left\{ \frac{m_\Psi^4}{4} \right\} \end{bmatrix} .$$

In the lab frame where the Sun is initially at rest

In a particular frame where the massive scalar field, the Sun, is initially at rest,



Initial states in the lab frame Final states in the lab frame

$$\begin{aligned} p_1^\mu &= (\omega_{p_1}, \vec{p}_1 = \omega_{p_1} \cdot \vec{z}_0) \\ p_2^\mu &= (\omega_{p_2}, \vec{p}_2 = \omega_{p_2} \cdot \vec{z}_0) \\ k_1^\mu &= (\omega_{k_1} = m_\Psi, 0) \\ k_2^\mu &= (\omega_{k_2}, \vec{k}_2 = \vec{p}_2 - \vec{p}_1) \end{aligned} \quad (C.1)$$

where \vec{z}_0 is a unit vector in the direction of the incoming photon, m_Ψ is the solar mass, ω_{p_1} (ω_{p_2}) is the energy of the incoming (outcoming) photon, θ is the angle between the momentum of the outcoming photon and that of the Sun after interaction, and ω_{k_1} (ω_{k_2}) is the total energy of the Sun before (after) interaction.

The following momentum product reduces to

$$(p_1 \cdot p_2) = \omega_{p_1} \omega_{p_2} (1 - \cos \theta)$$

and can be replaced in the preceding expression for the amplitude:

$$\overline{|A_{LED}^{phot.-scal.}|^2} = 4 \left(4\frac{\kappa}{2}\right)^2 * \left\{ \frac{1}{q^2} + \sum_n \frac{1}{q^2 - m_n^2} \right\}^2 * m_\Psi^4 \begin{bmatrix} +1 \left\{ \omega_{p_1}^2 \omega_{p_2}^2 \right\} \\ -\omega_{p_1} \omega_{p_2} (1 - \cos \theta) \left\{ \omega_{p_1} \omega_{p_2} \right\} \\ +\omega_{p_1}^2 \omega_{p_2}^2 (1 - \cos \theta)^2 \left\{ \frac{1}{4} \right\} \end{bmatrix} ,$$

$$\text{with } \omega_{k_2} = \sqrt{m_\Psi^2 + \omega_{p_1}^2 + \omega_{p_2}^2 - 2\omega_{p_1} \omega_{p_2} \cos \theta} .$$

Weak angle and massive deflector approximation

If we suppose that the deflection is weak,

$$\sin \theta \simeq \theta ,$$

and we further assume a very massive scalar field (solar mass), so that we may consider that the energy of the photon is conserved as the scalar particle experiences almost no recoil, the following approximations are valid:

$$\begin{aligned} \omega_{p_1} &\simeq \omega_{p_2} \equiv \omega_p , \\ q^2 &\simeq -\omega_p^2 \theta^2 , \\ (1 - \cos \theta) &\simeq \theta^2 . \end{aligned} \quad (C.2)$$

We shall thus neglect the terms proportional to θ^2 and $(p_1 \cdot p_2)^x$ with $x \geq 1$ in the amplitude. This leads to

$$\overline{|A_{LED}^{phot.-scal.}|^2} \simeq +16 \cdot 64\pi^2 G^2 m_\Psi^4 \left\{ \frac{1}{\theta^2} - \omega_p^2 \Delta_d(q^2) \right\}^2,$$

$$\text{with } \begin{cases} \Delta_d(q^2) \equiv \sum_{n \neq 0} \frac{1}{q^2 - m_n^2}, \\ \vec{n} = (n_1, n_2, \dots, n_l), \text{ the wave vector with } n_i = -\infty, \dots, +\infty, \\ n \equiv |\vec{n}|, \text{ the wave number,} \\ \kappa \equiv \frac{8\pi G}{c^4}, \text{ the gravitational coupling in 4-dimensions,} \\ \text{where } G \neq G_N \text{ a priori.} \end{cases} \quad (\text{C.3})$$

3 Cross-section of LED light - massive scalar-field scattering

The differential cross-section

Let us define

$$d\sigma \equiv \text{incoming flux} * \int d\Pi_2 * \overline{|A_{LED}^{phot.-scal.}|^2},$$

where the phase space integral is given by

$$\int d\Pi_2 \equiv \int \int \underbrace{\frac{dp_2^3}{(2\pi)^3} \frac{1}{2\omega_{p_2}}}_{\text{outcoming photon}} \underbrace{\frac{dk_2^3}{(2\pi)^3} \frac{1}{2\omega_{k_2}}}_{\text{outcoming scalar}} \underbrace{(2\pi)^4 \delta^4(k_2 + p_2 - k_1 - p_1)}_{\text{energy-momentum conservation}}.$$

We can calculate this phase space integral, that is, integrate the outcoming flux on the phase space of the outcoming particles ($\frac{V dp_2^3}{(2\pi)^3}$ and $\frac{V dk_2^3}{(2\pi)^3}$), using the energy-momentum conservation law:

$$\begin{aligned} \int d\Pi_2 &= \int \frac{dp_2^3}{(2\pi)^3} \frac{1}{2\omega_{p_2}} \frac{1}{2\omega_{k_2}} (2\pi) \delta(\omega_{k_2} + \omega_{p_2} - m_\Psi - \omega_{p_1}) \\ &= \int \frac{|\vec{p}_2| d|\vec{p}_2| d\Omega_2}{(2\pi)^3} \frac{1}{4\omega_{p_2}\omega_{k_2}} (2\pi) \delta(\omega_{k_2} + \omega_{p_2} - m_\Psi - \omega_{p_1}) \\ &= \int \frac{\omega_{p_2} d\omega_{p_2} d\Omega_2}{(2\pi)^3} \frac{1}{4\omega_{p_2}\omega_{k_2}} (2\pi) \delta(\omega_{k_2} + \omega_{p_2} - m_\Psi - \omega_{p_1}) \\ &= \int \frac{\omega_{p_2} d\Omega_2}{(2\pi)^2} \frac{1}{4} \frac{1}{\omega_{p_2} - \omega_{p_1} \cos \theta + \omega_{k_2}} \\ &= \frac{1}{8\pi} \int d\cos \theta \frac{\omega_{p_2}}{m_\Psi + \omega_{p_1}(1 - \cos \theta)}, \end{aligned}$$

$$\text{with } \begin{cases} \omega_{k_2} = \sqrt{m_\Psi^2 + \omega_{p_1}^2 + \omega_{p_2}^2 - 2\omega_{p_1}\omega_{p_2} \cos \theta}, \\ \Omega_2 (d\Omega_2 = \sin \theta d\theta d\varphi), \text{ the solid angle around } \vec{p}_2. \end{cases}$$

In the laboratory frame previously described by (C.1), we find the energy of the outgoing photon:

$$k_2^2 = (k_1 + p_1 - p_2)^2 \Rightarrow \frac{1}{m_\Psi + \omega_{p_1}(1 - \cos \theta)} = \frac{\omega_{p_2}}{\omega_{p_1} m_\Psi}.$$

In addition, if we use the weak angle and massive field approximation (C.2), we get

$$d\sigma = \frac{1}{2m_\Psi 2\omega_p} * \frac{1}{8\pi} \int d\cos \theta \frac{\omega_p}{m_\Psi} * \left| A_{LED}^{phot.-scal.} \right|^2.$$

We recall that the differential cross-section is the probability of scattering per unit of time for $\frac{\vec{p}_2 - \vec{p}_1}{|p_2 - p_1|}$ fixed. It is given by

$$\frac{d\sigma}{d\Omega_2} = \frac{1}{2m_\Psi 2\omega_{p_1}} * \frac{1}{2\pi} \frac{1}{8\pi} \frac{\omega_{p_2}^2}{m_\Psi \omega_{p_1}} * \left| A_{LED}^{phot.-scal.} \right|^2.$$

This thus leads to the following result in the weak angle and massive deflector approximations:

$$\frac{d\sigma}{d\Omega_2} \simeq +16 G^2 m_\Psi^2 \left\{ \frac{1}{\theta^2} - \omega_p^2 \Delta(q^2) \right\}^2. \quad (C.4)$$

The cross-section

To recover the angular cross-section,

$$\sigma(\theta) \equiv \frac{d\sigma}{d\theta}, \quad (C.5)$$

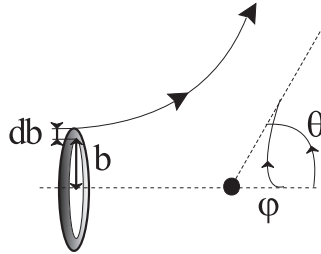
we just need to remember that $d\Omega_2 \simeq \theta d\theta d\varphi$, and integrate over the angle φ . Doing so, we find

$$\sigma(\theta) \simeq +32\pi G^2 \frac{m_\Psi^2}{\theta^3}.$$

4 Light deflection angle in LED theories

The impact parameter, the scattering angle and the light deflection angle

The scattering angle, θ , is linked to the impact parameter b by the following reasoning



$$\left(\begin{array}{c} \# \text{ incident particles with} \\ \text{an impact parameter } \in [b, b + db] \end{array} \right) = \left(\begin{array}{c} \# \text{ particles scattered at an angle} \\ \in [\theta, \theta + d\theta] \end{array} \right)$$

$$\Leftrightarrow \text{Intensity} * 2\pi b db = -\text{Intensity} * \frac{d\sigma}{d\Omega_2} \int_\varphi d\Omega_2$$

$$\Leftrightarrow \int b db = - \int \frac{d\sigma}{d\Omega_2} \sin \theta d\theta$$

which leads, in the small angle approximation, to

$$\begin{aligned} \frac{b^2}{2} &\simeq - \int 16 G^2 m_\Psi^2 \left\{ \frac{1}{\theta^2} - \omega_p^2 \Delta_d(q^2) \right\}^2 \theta d\theta, \\ b^2 &\simeq +16 G^2 m_\Psi^2 \left\{ \frac{1}{\theta^2} + 4 \omega_p^2 \Delta_d(q^2) \ln\theta - \omega_p^4 \Delta^2(q^2) \theta^2 \right\}, \\ b &\simeq +4 G m_\Psi \frac{1}{\theta} \left\{ 1 + 2 \omega_p^2 \Delta_d(q^2) \theta^2 \ln\theta \right\}, \end{aligned}$$

using the result (C.4) previously obtained for the differential cross-section.

Inverting this last expression, we get

$$\theta \simeq + \frac{4Gm_\Psi}{b} \left\{ 1 + 2 \omega_p^2 \Delta_d(q^2) \left(\frac{4Gm_\Psi}{b} \right)^2 \ln\left(\frac{4Gm_\Psi}{b} \right) \right\}.$$

We still need to remember that the scattering angle, θ , is the angle between the directions of the momentum of the incident and that of the outgoing photon; while, $\hat{\alpha}$, the light deflection angle, is the angle between the incoming and outgoing directions of the momentum of the scattered particle for a target at rest. Consequently, in the particular chosen lab frame, where the scalar field is massive and thus stays at rest, the angle θ is equal to the light deflection angle $\hat{\alpha}$. Hence, we have demonstrated expression (4.7) with the mass of the deflector given by $m_\Psi \equiv M$.

It is interesting to recall that this result for the light deflection angle contains the particular case of BD and GR theories. Indeed, there exist no massive states in those theories, hence $\Delta_{d\,TS/GR} \equiv 0$; the gravitational constant G is given by (1.48) with $\alpha_{BD} \equiv \alpha_{LED}$ from (1.37); and the corresponding Brans-Dicke parameter, ϖ , is found in (1.39). GR is recovered for $\alpha_{BD} \rightarrow 0$ or $\varpi \rightarrow \infty$.

Estimation of $\Delta_d(q^2)$ for LED theories

We now have to estimate the sum over the massive propagators ($\vec{n} \neq 0$) given in (C.3), for the case that interests us, *i.e.* for $q^2 < 0$ (space like propagators (C.2)). For $d=0$, it is of course null.

When $d=1$, the vector mode reduces to $\vec{n} = n_1$ and the sum over the massive propagators can be computed explicitly. However, one has to be cautious to remove the zero mode contribution (first term in the following). We obtain the expression given in (4.7) for $\Delta_{d=1}$:

$$\begin{aligned} \Delta_{d=1}(q^2 = -Q^2) &= -\frac{1}{Q^2} + \sum_{n_1=-\infty}^{n_1=+\infty} \frac{1}{q^2 - m_{n_1}^2} = +\frac{1}{Q^2} - \sum_{n_1=-\infty}^{n_1=+\infty} \frac{1}{Q^2 + m_{n_1}^2} \quad (\text{C.6}) \\ &\stackrel{(1.44)}{=} +\frac{1}{Q^2} - \frac{1}{Q^2} \frac{RQ}{2} \coth\left(\frac{RQ}{2}\right) \\ &\stackrel{\text{QR,small}}{\simeq} +\frac{1}{Q^2} - \frac{1}{Q^2} \left(1 + \frac{R^2 Q^2}{12}\right) \\ &\simeq -\frac{\pi^2}{3(GM_s^3)^2}, \end{aligned}$$

where the expression for the gravitational coupling in 4-dimensions obtained from the $(4+d)$ -action reduction 66 ,

$$G = (4\pi)^{d/2} \Gamma(d/2) R^{-d} M_s^{-(2+d)}, \quad (\text{C.7})$$

was used in the last step.

For $d>1$, we note that massive KK states with mass m_n given by (1.44) are quasi degenerated in mass because if the radius of compactification, R , is a submillimeter scale in LED theories, the separation between two consecutive masses, proportional to $1/R$, is, on its side, much smaller than the other physical scales in our problem. Consequently, we can approximate the discrete sum by a continuous integral. There exists a number $dr^{(d)}$ of Kaluza-Klein states in

the mass interval $[m_n, m_n + dm_n]$ with $r \equiv n$, so to give

$$\begin{aligned}\Delta_d(q^2 = -Q^2) &\simeq -\text{zero mode contribution} + \int_0^\infty dr^{(d)} \frac{1}{q^2 - m_n^2} \\ &\simeq -\text{zero mode contribution} - \int_0^\infty dr^{(d)} \frac{1}{Q^2 + m_n^2} \\ &\simeq -\text{zero mode contribution} - \int_0^\infty \frac{R^d m_n^{d-2}}{(4\pi)^{n/2} \Gamma(d/2)} dm_n^2 \frac{1}{Q^2 + m_n^2} \\ &\simeq -\text{zero mode contribution} - 2 \frac{R^d q^{d-2}}{(4\pi)^{d/2} \Gamma(d/2)} \int_0^\infty \frac{y^{d-1} dy}{1+y^2},\end{aligned}$$

where $y \equiv m_n/Q$.

To remove the zero mode contribution, we integrate from the minimum mass, $m_{\min} \stackrel{(1.44)}{\equiv} 2\pi/R$; and because the above integral diverges logarithmically for $d > 1$, we insert a cut off at $m_n = M_s$, the mass scale of the theory. We obtain

$$\Delta_d(q^2 = -Q^2) \stackrel{(C.7)}{\simeq} \frac{2}{GM_s^4} \left(\frac{Q^2}{M_s^2} \right)^{d/2-1} \left\{ I_d\left(\frac{M_s}{Q}\right) - I_d\left(\frac{m_{\min}}{Q}\right) \right\}, \quad (C.8)$$

$$\text{where } \begin{cases} I_d(x) \equiv - \int_0^x \frac{y^{d-1} dy}{1+y^2}, \\ = \begin{cases} -\frac{1}{2} \ln(x^2 + 1) & \text{for } d = 2, \\ (-1)^{d/2-1} \left[\sum_{k=1}^{d/2-1} \frac{(-1)^k}{2k} (x)^{2k} + \frac{1}{2} \ln(x^2 + 1) \right] & \text{for } d > 2 \text{ even,} \\ (-1)^{(d-1)/2} \left[\sum_{k=1}^{(d-1)/2} \frac{(-1)^k}{2k-1} (x)^{2k-1} + \arctan(x) \right] & \text{for } d > 2 \text{ odd.} \end{cases} \end{cases}$$

In the scattering process that we envisaged here to model light deflection, $M_s \gg Q = |p_2 - p_1|$ and $M_s \gg m_{\min}$. Using (C.8) and (C.7) in this approximation leads us to the expression for $\Delta_{d>1}(q^2)$ given in (4.7).

Note that a calculation with the integral for $d = 1$, without the cutoff,

$$\begin{aligned}\Delta_{d=1}(q^2 = -Q^2) &\simeq + \int_{-\infty}^{-n_1 \min} \frac{dn_1}{q^2 - m_{n_1}^2} + \int_{+n_1 \min}^{+\infty} \frac{dn_1}{q^2 - m_{n_1}^2}, \\ &= - \int_{-\infty}^{-n_1 \min} \frac{dn_1}{Q^2 + m_{n_1}^2} - \int_{+n_1 \min}^{+\infty} \frac{dn_1}{Q^2 + m_{n_1}^2}, \\ &\stackrel{(1.44)}{=} -2 \frac{R}{2\pi} \int_{+m_{n_1} \min}^{+\infty} \frac{dm_{n_1}}{Q^2 + m_{n_1}^2}, \\ &= -\frac{R}{2Q} + \frac{R}{\pi Q} \arctan\left(\frac{\pi}{Rq}\right) \stackrel{\text{QR small}}{\simeq} -\frac{R^2}{2\pi^2},\end{aligned}$$

gives us an idea of the approximation done when comparing this latter result with (C.6). The approximation seems better when integrating from $m_{\min}/2$, which leads to $-R^2/\pi^2$, closer to the exact result of (C.6).